

# UNCLASSIFIED

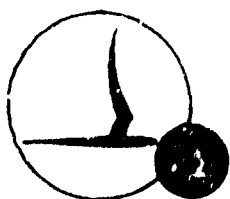
AD NUMBER
AD819971
NEW LIMITATION CHANGE
TO Approved for public release, distribution unlimited
FROM Distribution authorized to U.S. Gov't. agencies and their contractors; Administrative/Operational Use; 1963. Other requests shall be referred to Army Air Mobility Research and Development Lab., Fort Eustis, VA.
AUTHORITY
USAAMRDL ltr, 4 May 1971

THIS PAGE IS UNCLASSIFIED

AD819971



# **CAL/TRECOM SYMPOSIUM**



## **PROCEEDINGS Vol II**

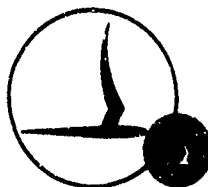
**Dynamic  
Load Problems  
Associated  
with  
Helicopters  
and V/STOL  
Aircraft**



**JUNE 26-28  
STATLER HILTON BUFFALO N.Y.**



# CAL/TRECOM SYMPOSIUM



## PROCEEDINGS Vol II

**Dynamic  
Load Problems  
Associated  
with  
Helicopters  
and V/STOL  
Aircraft**

\*

**JUNE 26-28**

**STATLER HILTON BUFFALO N.Y.**

STATEMENT #2 UNCLASSIFIED

This document is subject to special export controls and each transmittal to foreign governments or foreign nationals may be made only with prior approval of

*H. Carter, Jr.*

Statements and opinions contained herein are those of the authors and are not to be construed as reflecting the views of the Department of the Army or the cosponsors of this Symposium--The U. S. Army Transportation Research Command or Cornell Aeronautical Laboratory, Inc.



## TABLE OF CONTENTS

### Volume II

10. A Review of the Structural Dynamic Characteristics of the XC-142A Aircraft  
Mr. A. L. Head, Jr., Chance Vought Corporation
11. Propeller Whirl Flutter Considerations for V/STOL Aircraft  
Wilmer H. Reed III, and Robert M. Bennett,  
NASA, Langley Field, Virginia
12. High-Speed Shafting for Power Transmission in Aircraft  
J. E. Vorhees, J. B. Day, and R. G. Dubensky,  
Batelle Memorial Institute
13. Dynamic Torsional Problems in VTOL Drive Trains with Universal Joints  
R. Bossler, W. G. Flannelly, Kaman Aircraft
14. Recent Work at the Royal Aircraft Establishment on Helicopter Dynamic Loads, with particular reference to High Blade Incidence Problems  
A. E. Clarke, Naval Air Department, R.A.E. Bedford,  
England
15. Some Results from the Army Low Altitude, High-Speed Flight Program (Man-Machine)  
John E. Yeates, TRECOM, Virginia
16. Human Factor Problems Associated with Low Altitude High-Speed (LAHS) Flight  
H. E. Rawson, and B. Schohan, North American Aviation,  
Inc., Columbus, Ohio
17. Effect of Gust Alleviation System on Dynamic Airloads  
J. D. Balducci, F. L. Adams, and M. A. Schwartzberg,  
Autonetics
18. An Analytical Investigation of Aircraft Loads Induced by Rough Terrain Landings  
Fred C. Allen, and Lane B. Mosby, Douglas Aircraft Company

**A REVIEW OF THE STRUCTURAL  
DYNAMIC CHARACTERISTICS OF THE  
XC-142A AIRCRAFT**

**A.L. Head, Jr.,  
Chance Vought Corporation**

A REVIEW OF THE  
STRUCTURAL DYNAMIC CHARACTERISTICS  
OF THE XC-142A AIRCRAFT

by  
A. L. READ, JR.

Supervisor, Structures Dynamics Group

Chance Vought Corp.

Dallas, Texas

For Presentation at  
The Symposium on "Dynamic Load Problems Associated  
with V/STOL Aircraft" in Buffalo, New York,  
June 26-27, 1963. The Symposium is Jointly Sponsored  
Cornell Aeronautical Laboratory, Inc, and the Army  
Transportation Corp (TRECOM).

# A REVIEW OF THE STRUCTURAL DYNAMIC CHARACTERISTICS OF THE XC-142A AIRCRAFT

A. L. Head, Jr., Supervisor

Structures Dynamics Group

Chance Vought Corp.

## 1.0 INTRODUCTION

The XC-142 Aircraft is a tilt wing VTOL vehicle designed to demonstrate the all-weather operational suitability of VTOL transport aircraft. The airplane has superior STOL as well as VTOL capabilities. It features a large cargo compartment to transport a payload of 8,000 pounds for VTOL missions while cruising at 250 knots. The limit velocity is 400 knots.

The airplane is powered by four T64-GE-6 wing mounted engines driving four propellers and a tail rotor through an interconnected shafting system. The wing is of moderately high aspect ratio mounted high on the fuselage, and can be tilted through an angle of 100 degrees for the hovering and transition mode. The wing incorporates full span double slotted flaps. Independently operated split ailerons are mounted on the outboard sections of the flaps. Leading edge slats for stall suppression are incorporated on the outboard side of each engine nacelle to compensate for the angle of attack induced by the propeller slipstream in these areas. The vertical tail is a conventional fin and rudder arrangement centrally located on the fuselage and supporting the all-moving horizontal tail assembly.

Figures 1 and 2 show the airplane in the conventional flight mode and the hover mode, respectively.

Inherent in the design of this type of aircraft are many formidable dynamic, aeroelastic, and acoustic challenges. Consequently, considerable effort has been expended during the design phase of this aircraft to define clearly the major dynamic, aeroelastic, and acoustic design requirements. Stringent weight guarantees

have required that structural optimization studies be conducted from a stiffness viewpoint as well as from a strength viewpoint. This means that each part of the structure is designed to withstand the critical design loads for a minimum weight.

This paper will review some of the more interesting dynamic and acoustic challenges faced during the design of the XC-142A Aircraft. These challenges are classified into three areas as follows: flutter and vibration, dynamic response, and acoustics. Each of these general areas is subdivided as discussed hereinafter. Required test programs are also indicated.

## 2.0 FLUTTER AND VIBRATION

The philosophy of design for flutter utilized on the XC-142A Aircraft is essentially the same as that given in reference (1). The basic objective of this philosophy is to produce a design that has the required flutter margin for the least weight. The required flutter margin can be defined as follows: At any flight condition within the flight envelope, flutter must not occur within a 15 percent margin on either equivalent airspeed or Mach number. To attain the basic objective of the above philosophy, a good balance between analytical and experimental efforts must be established and scheduled to provide the right answers at the right time.

### 2.1 Analytical Program

Each major component of the aircraft is first analyzed individually. Then, the components are coupled together to form either symmetric or antisymmetric analyses of the complete airplane. Basically, a modal type of analysis is employed where appropriate vibration modes are used as generalized coordinates in Lagrange's equations-of-motion to define the various dynamical systems. Individual components are then coupled together using modal coupling techniques to define the complete airplane.

The airforces acting on each airfoil are based on modified subsonic, two-dimensional, unsteady, aerodynamic theory. The modification used is one that forces the two-dimensional theory to yield the correct spanwise and chordwise pressure distributions per unit angle-of-attack at zero frequency. In this way, correct static aerodynamic performance is achieved while the theoretical frequency dependence is retained at other than static conditions.

The unsteady airforces acting on the propellers are based on quasi-steady assumptions using static propeller derivatives as a base.

The resulting equations of motion are solved on an IBM-7090 computer to determine critical flutter conditions. Important parameters are varied to determine their effect on flutter.

## 2.2 Analytical Results

The empennage of the XC-142A presents no state-of-the-art problems from a flutter viewpoint. To illustrate some of the analytical results obtained, the results of the all-moving horizontal tail coupled with the symmetric airframe analysis are presented. Figure 3 shows horizontal tail flutter velocity and frequency as a function of its uncoupled pitching frequency. This figure is a summary flutter plot that is obtained by cross plotting data from damping versus flutter velocity plots such as shown in Figure 4. Figure 4 is the conventional "v-g" plot. It shows, for a particular dynamic configuration at a particular altitude, the damping characteristics of the system as a function of velocity. Also shown is the flutter frequency versus velocity. An incipient flutter condition exists where the damping goes to zero. Figure 3 serves the function of determining the stiffness requirements of the horizontal tail pitch actuator.

The wing of the XC-142A does present a state-of-the-art problem. Both conventional flutter and propeller whirl flutter considerations are important.

The equations-of-motion that define both of the above types of flutter simultaneously require the inclusion of a large number of degrees-of-freedom to adequately represent the coupled system. This gives rise to state-of-the-art problems associated with the solution of the equation. Further, the number of parameters that need to be varied is greatly increased. The size of the problem makes parametric studies unwieldy and expensive. Consequently, the component method of analysis is used extensively. Basic engine-gearbox support requirements are determined from flutter analyses of the engine-gearbox-propeller combination including local wing flexibility. Conversely, basic wing flutter requirements are determined assuming the engine-gearbox-propeller combination to be rigidly affixed to the wing. This technique of analysis yields preliminary design information. The complete wing-engine-gearbox-propeller combination is then coupled together and analyzed, minimizing the number of parameters that need to be varied in the completely coupled system:

A schematic drawing of the engine-gearbox mounting system is shown as Figure 5. This mounting system features a multi-redundant strut arrangement. The philosophy of design for this mounting system requires that the system be operative when any one joint is failed. That is, the failure of any one joint or of any one member shall not produce a catastrophic aircraft failure. Consequently, dynamic failure analyses are required consistent with the above design philosophy.

As stated previously, component analyses are conducted for the engine-gearbox-propeller combination supported on local wing constraints. These analyses are truly propeller whirl type flutter analyses. The objective of these analyses is to determine design requirements considering both failed and soft-mounted configurations. Many iterations are required to clarify all aspects of the design requirements. Consequently, typical results are presented as Figures 6 and 7 to illustrate the

important features of such analyses. Figure 6 is a damping versus flutter velocity plot that shows the effect of strut failures on flutter velocity. This plot pertains to an optimum-strength (no isolator) configuration. Figure 7 is a damping versus flutter velocity plot that shows the effect on flutter velocity of various degrees of soft-mounting. Three conclusions can be drawn from Figures 6 and 7 as follows: strut failures tend to reduce flutter speed, soft-mounting reduces flutter speed, and damping is very important. Usually, a structural damping coefficient of 0.02 can be expected for normal aircraft structures, whereas a value of 0.06 can be expected for soft-mounts employing rubber. As shown in Figure 7, a little damping goes a long way in propeller whirl flutter considerations.

An example of the results of a completely coupled wing-engine-gearbox-propeller combination flutter analysis is shown as Figure 8. This is a damping versus velocity plot that shows the effect of power variation (propeller advance ratio variation) on flutter speed. Power variation has a very small effect on flutter. As a matter of interest, the analysis from which Figure 8 is derived contains 27 degrees-of-freedom. Both conventional airforces on the airfoil and propeller airforces are included in the analysis. The flutter characteristics of the healthy wing are summarized in Figure 9. This is a velocity versus Mach number plot obtained from cross plotting data such as shown in Figure 8. Maximum power, cruise power, and no-power conditions are shown. Again, power setting has very little effect on flutter. The no-power condition corresponds to a windmilling propeller.

All analytical results obtained to date indicate that the XC-142A Aircraft is flutter free to the required margin.



### 2.3 Flutter Model Design and Testing

To implement the philosophy of design for flutter, a flutter model program for the complete aircraft is in progress. A 1/10-scale, dynamically similar model is designed for testing in the Vought Low Speed Wind Tunnel. To complement the analytical program and to facilitate the comparison of analytical and experimental results, the model program is divided into three phases as follows: wing tests, empennage tests, and complete aircraft tests. The wing and empennage components are designed to be assembled into the complete aircraft model. As indicated, the components are first tested individually consistent with the analyses that are available. Then, the components are assembled into a complete aircraft model and are tested as a unit.

A very high degree of dynamic simulation is achieved in the model. As usual the first three to four surface vibration modes and frequencies are accurately simulated for each surface. Aileron and rudder degrees of freedom are also simulated. However, certain aspects of the detailed simulation deserve special mention as follows: the fundamental propeller blade mode is simulated, the engine-gearbox mounting system is simulated in detail both dynamically and geometrically, struts in the mounting systems can be removed to simulate failure conditions, the propellers are interconnected with a shafting system, the in-plane modes of the wing are simulated, and the first three symmetric and antisymmetric modes of the fuselage are each simulated.

The dynamically similar model design extends the state-of-the-art in modeling technology in several aspects of the simulation. The model is to be used for both flutter testing and for steady-state response testing. The response of the airframe to propeller unbalance is to be determined both in still air and in various flight conditions. This work is to be the subject of a paper that will

be presented at the forthcoming Symposium on Aeroelastic and Dynamic Modeling Technology in Dayton, Ohio, September, 1963.

Currently, the wing tests are partially completed. These test clear the healthy wing to the required flutter margin. Failure configurations are being run in the tunnel. The empennage tests are scheduled during July, and no problems are anticipated. Finally, the complete aircraft model is scheduled for testing during August. During these aircraft tests the model will be flown in the tunnel constrained by a cable. Fore-and-aft translation and roll are constrained by the mounting system. The model is trimmed by the all-moving horizontal tail which is controllable from outside the tunnel.

No tests of any transition configurations are planned. During hover and transition the velocities are relatively small and no flutter-type instabilities are anticipated.

### 3.0 DYNAMIC RESPONSE

The dynamic response loads due to both transient and steady-state excitations provide some very interesting problems on the XC-142A Aircraft. Only a few of these problems are discussed herein. They are: aircraft response due to gust, aircraft response due to propeller unbalance, and shafting response due to shaft unbalance.

#### 3.1 Gust Response

Gust response loads combined with maneuver loads usually produce critical design loads for low load-factor aircraft. Further, the loading spectrum during the life of an aircraft is strongly influenced by gust loading. This, in turn, determines the environment for fatigue. It is, therefore, very important to determine the gust loads as accurately as possible. Two basic analytical approaches to the gust response problem are utilized on the XC-142A Aircraft.

One is a discrete gust analysis; the other is a power-spectral-density (PSD) gust analysis. The discrete gust analysis is based on the assumption that the aircraft will encounter a single "1-cosine" gust of a 50 feet per second amplitude. The wave length of the gust is varied to produce the maximum loading possible. The PSD gust analysis is based on a statistical definition of the atmosphere. Treating the gust velocity distribution as a random variable, the probability of encountering a gust of a given amplitude is defined for various atmospheric conditions. Many papers discussing the relative merits of discrete and PSD gust analyses are available in the literature. For example, see reference (2). Only a few of the major points are discussed below.

The discrete gust analysis based on a "1-cosine" velocity distribution has been used in aircraft design for years. It has the advantage of being simple to apply, and it has a powerful experience factor in its favor. However, followed to an arbitrary extreme, it can give quite unrealistic design loads. For instance, if the wing is designed to a "1-cosine" gust critically phased to give maximum response in the fundamental normal bending mode, should the fundamental in-plane mode also be tuned with another critically phased gust? This criterion leads to the superposition of peaks in the determination of wing normal response loads and in-plane response loads, and the two conditions cannot occur simultaneously. The same argument can be made with respect to other surfaces. The wave length of the gust necessary to tune each mode is different. Therefore, peaks do not superimpose in general. Much weight can be forced into a design using this discrete criterion blindly.

On the other hand, the PSD type of analysis provides a much more rational approach to the problem but lacks the experience factor associated with its use. Both methods of analysis are being used on the XC-142A Aircraft, and the results are being compared. In general, the PSD approach is providing lower design loads.

Figure 10 is the result of a typical PSD analysis showing the number of exceedances of wing root bending moment that might be expected during the life of the XC-142A Aircraft.

### 3.2 Aircraft Response to Propeller Unbalance

The airframe response to propeller unbalance is important for two basic reasons. One reason is the steady-state response loads that must be used in the design of the structure. The other reason is the human factors consideration in occupied areas. Extensive response analyses are required to define the response of the airframe. The studies conducted on the XC-142A Aircraft are consistent with the definition of the dynamical systems used for corresponding flutter analyses.

As shown in Figure 7, the propeller whirl flutter velocity is markedly reduced as the mounting system is softened. On the contrary, it is desirable to soften the mounting systems to permit vibration isolation of the airframe from the once-per-revolution (1P) propeller loads. The requirements to prevent propeller whirl flutter and to provide vibration isolation are incompatible and in some cases are mutually exclusive. This problem is aggravated further on the XC-142A due to motion limitations at the intersection of the gearbox and the cross shafting that interconnects each gearbox. Strict motion limits are required at this intersection to prevent excessive loading in the high-speed shaft. This requirement is also incompatible with 1P isolation requirements. Due to these incompatibilities, no 1P isolation is provided in the form of soft isolators. Significant 1P isolation is provided in the basic design of the mounting system, however. The next possibly significant propeller exciting forces occur at 4P. Several isolator designs to produce 4P isolation are considered. Further analysis reveals that 4P isolation is also unfeasible. Consequently, after 14 months of extensive analysis, it is concluded that all isolation achieved must be inherent in the basic design of the mount structure.

To see this problem in proper perspective, the results of several of the final analyses are shown in Figures 11, 12, and 13. Figure 11 is a frequency response curve showing strut loads per inch-pound (in-lb) of propeller unbalance versus propeller rotational speed. (Refer to Figure 5 for identification of strut numbers.) In Figure 11, the unbalance is on one side only. The variation of strut loads for several configurations is shown. An optimum-strength (no isolator) configuration actually produces less strut loading in the 1P range than does a design to isolate 4P excitations. This is due to the fact that the addition of resilient material to produce 4P isolation drops a 22 cps peak to 18 cps, placing it in the 1P operating band. The 1P operating band extends from 15 cps to 20 cps. Similar analyses for very soft mounts significantly reduces strut loading in the 1P band, but these soft-mount designs cannot be tolerated due to motion limitations as previously discussed.

Figure 12 is a frequency response curve for the 4P isolator design showing the effect of strut failure on loads. In most struts, the loads increase due to the failure of other struts; however, the increase is not dramatic. This is due to the multiple redundancy of the mounting system.

The basic optimum-strength (no isolator) configuration is designed to place the predominately pitching frequency of the propeller at about 12 cps. The predominately yawing frequency of the propeller is about 22 cps. Thus, the 1P operating band is avoided in this configuration. Following the generally accepted criterion for 1P isolation, the isolator design should place the boiler-plate frequencies in pitch and yaw at 70 percent of the 1P frequency. This would be about 11 cps for the XC-142A Aircraft. This criterion is essentially met in the pitch mode for the optimum-strength configuration. It is not met in the yaw mode.

Figure 13 is a frequency response curve for the fuselage showing both vertical and lateral acceleration per in-lb of propeller unbalance versus

propeller rotational speed. There are some fairly large peaks in the 1P operating band. On the brighter side, there are also some fairly low valleys. The philosophy here is this: should a pilot find that he is operating on a peak, he can vary the propeller speed slightly and get into a valley.

Currently, a very conservative philosophy of combining loads due to unbalance of different propellers is in use. In essence, a philosophy of superposition of peaks is employed. This is highly unlikely. At this time, a statistical basis for combining the loads is being developed.

### 3.7 Shafting Dynamics

The high-speed shafting utilized on the XC-142A Aircraft is extending the state-of-the-art for shafting applications. A philosophy of design is used that requires that no objectionable vibrations exist in the entire shafting system. The wing cross shafting speed is approximately 8000 rpm. The tail rotor drive speed is 6000 rpm. To meet the requirements of the above design philosophy the minimum shafting whirling frequency that can be tolerated is 125% of the normal operating shaft speed. To illustrate the type of analysis performed Figure 14 is presented. Displayed are the first five mode shapes and frequencies of an unacceptable tail rotor drive configuration. Design changes are now incorporated into the design to raise the minimum critical whirling frequency to the required value. In addition to whirl frequency calculations, the torsional characteristics of the complete shafting system are known. The response of the shafting system due to torsional transients and the stability characteristics of the closed-loop system involving the shafts and the governors are all part of the shafting dynamics work already accomplished.

Early in the design of the above shafting system, the decision to use a subcritical system was made. A subcritical system required the least developmental work and posed a lesser risk in the design. It is by no means certain, however, that a subcritical design is more nearly optimum than is a supercritical design.

On the contrary, a supercritical design has many desirable features. For instance, the tolerances pertaining to eccentricity and misalignment of the shafts can be greatly increased. Basically, a supercritical design allows the shaft to be isolated from the support structure. Future developmental work will undoubtedly include a very serious evaluation of a supercritical shaft design.

#### 4.0 ACOUSTICS

High intensity noise is a major design consideration for XC-142A Aircraft. Both structure and personnel are affected. There are four major noise sources as follows: main propulsion system, tail rotor, aerodynamic noise, and internally generated noise. The main propulsion system includes propeller noise and exhaust noise. By far the principal external noise sources are the main propellers and the tail rotor. The tip speed and power combinations yield very high sound pressure levels. Figure 15 shows sound pressure level contours over the exterior of the airplane for a STOL condition. The frequency spectrum of this external noise contains very strong discrete frequency components associated with propeller blade passage frequency. Analysis and measurement show that most of the acoustic energy is contained in the first three harmonics of the propeller blade passage frequency.

The impingement of acoustic energy on structure causes the structure to respond dynamically. Response loads are induced in the structure, causing fatigue problems. The philosophy of design adopted requires that the structural fatigue problem be solved while achieving the most sound attenuation possible. Interior sound-proofing treatment will be determined after interior sound pressure levels are measured on the first airplane.

Consistent with the stated philosophy extensive analytical and experimental programs are being conducted to develop design criteria for the outer covering of the airplane. The most critical area is the fuselage side walls in the vicinity

of the propeller plane. Both sheet-stringer and sandwich types of design are evaluated. The sandwich structure evaluated is Metalite. The faces are aluminum while the interior is balsa wood. Metalite is much better from an acoustic standpoint than an equivalent-weight, sheet-stringer design. It has superior fatigue and attenuation characteristics. Metalite construction is now used over a large area of the fuselage.

#### 5.0 TEST PROGRAMS

In addition to some of the tests previously indicated, extensive dynamic testing programs will be conducted on the aircraft and its components to verify design information included in the various analyses. For instance, each component of the aircraft will be ground-vibration tested to determine mode shapes and frequencies. Prior to first flight, the complete airplane will be suspended and vibration tested to determine coupled modes and frequencies.

Output impedance tests of each servo-actuator will show whether or not control surface impedance requirements are met. To verify LP loadings a comprehensive test program is planned on the engine test stand. Strut loading will be measured.

A simulator accurately simulating all wing dynamics and containing the actual engine, propeller, shafting system, and controls is under construction at Moffett Field, California. This simulator is called the Propulsion Integrated Test Stand (PITS). Comprehensive tests are planned on the PITS to determine strut loading, whirl frequencies, and transient response characteristics. Any dynamic problems related to the propulsion systems will manifest themselves prior to first flight.

During the 50-hour ground run of the first airplane all important dynamic quantities will be measured again. Sound pressure levels inside and outside the structures will also be measured. Finally, all of the quantities will be recorded in flight. Flight flutter tests are scheduled. No doubt some dynamical problems will occur during the flight test program, but the analytical and experimental

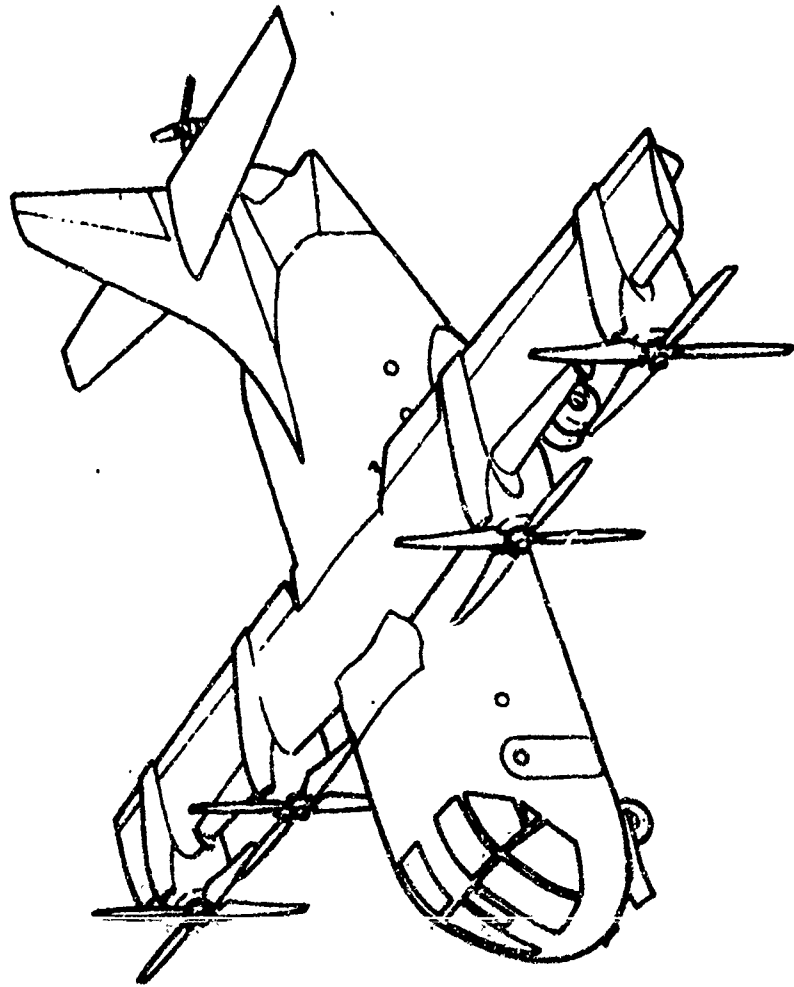


programs previously conducted will provide a sound base for the solution of any potential dynamical problems.

### References

1. "A Philosophy of Design for Flutter," A. L. Head, Jr., Proceedings of the National Specialists Meeting on Dynamics and Aeroelasticity, Nov. 6-7, 1958, Sponsored by the Institute of the Aeronautical Sciences
2. "Application of Power Spectral Methods in Airplane and Missile Design," K. R. Thorsen and Q. R. Bohme, Journal of the Aero/Space Sciences, Vol. 27, No. 2, pp. 107-116, February, 1960

# C142A AIRPLANE CONVENTIONAL MODE



# XC142A AIRPLANE HOVER MODE

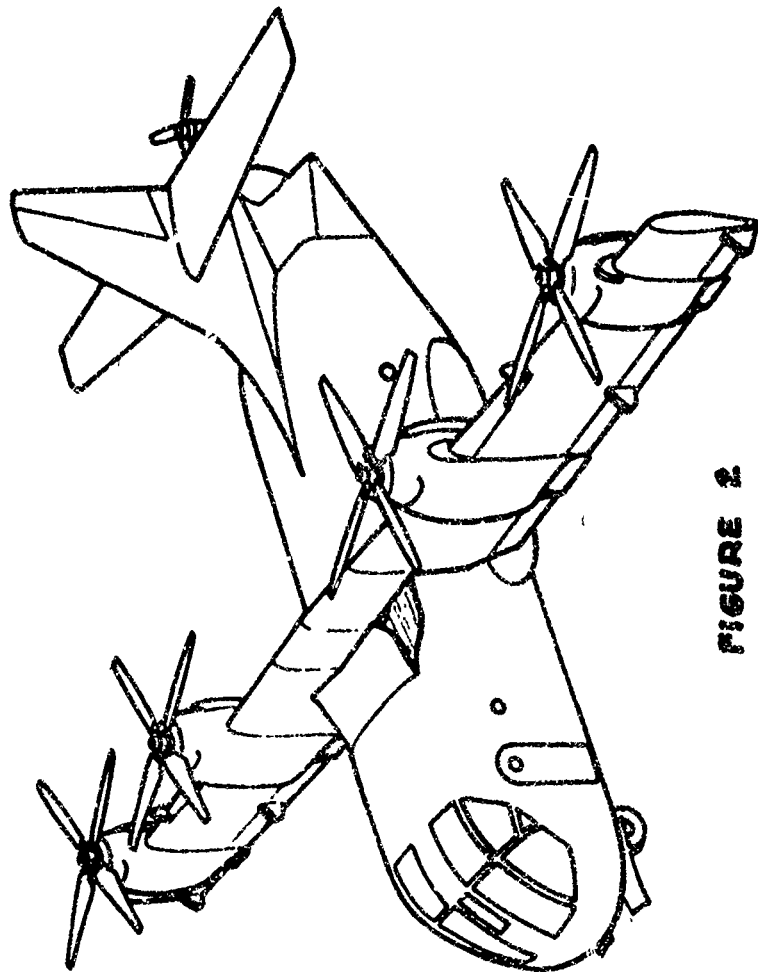
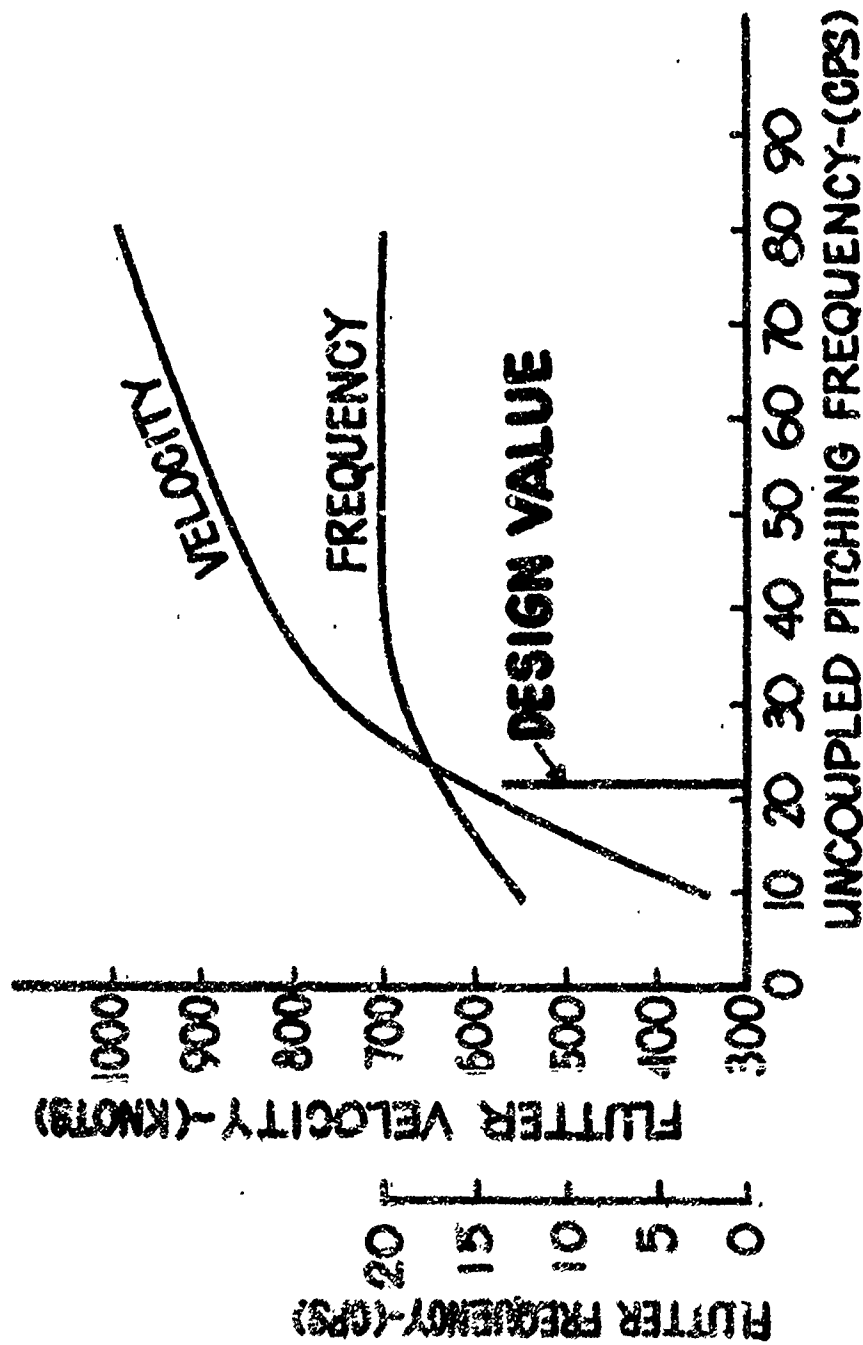


FIGURE 2

# **XCM42A HORIZONTAL TAIL FLUTTER VELOCITY VS. HT PITCHING FREQUENCY 02 STRUCTURAL DAMPING**



**FIGURE 3**

# XC142A HORIZONTAL TAIL

DAMPING VS VELOCITY FREQUENCY VS VELOCITY

0.2 STRUCTURAL DAMPING MACH 0.7 ACTUATOR FREQ = 20 CPS

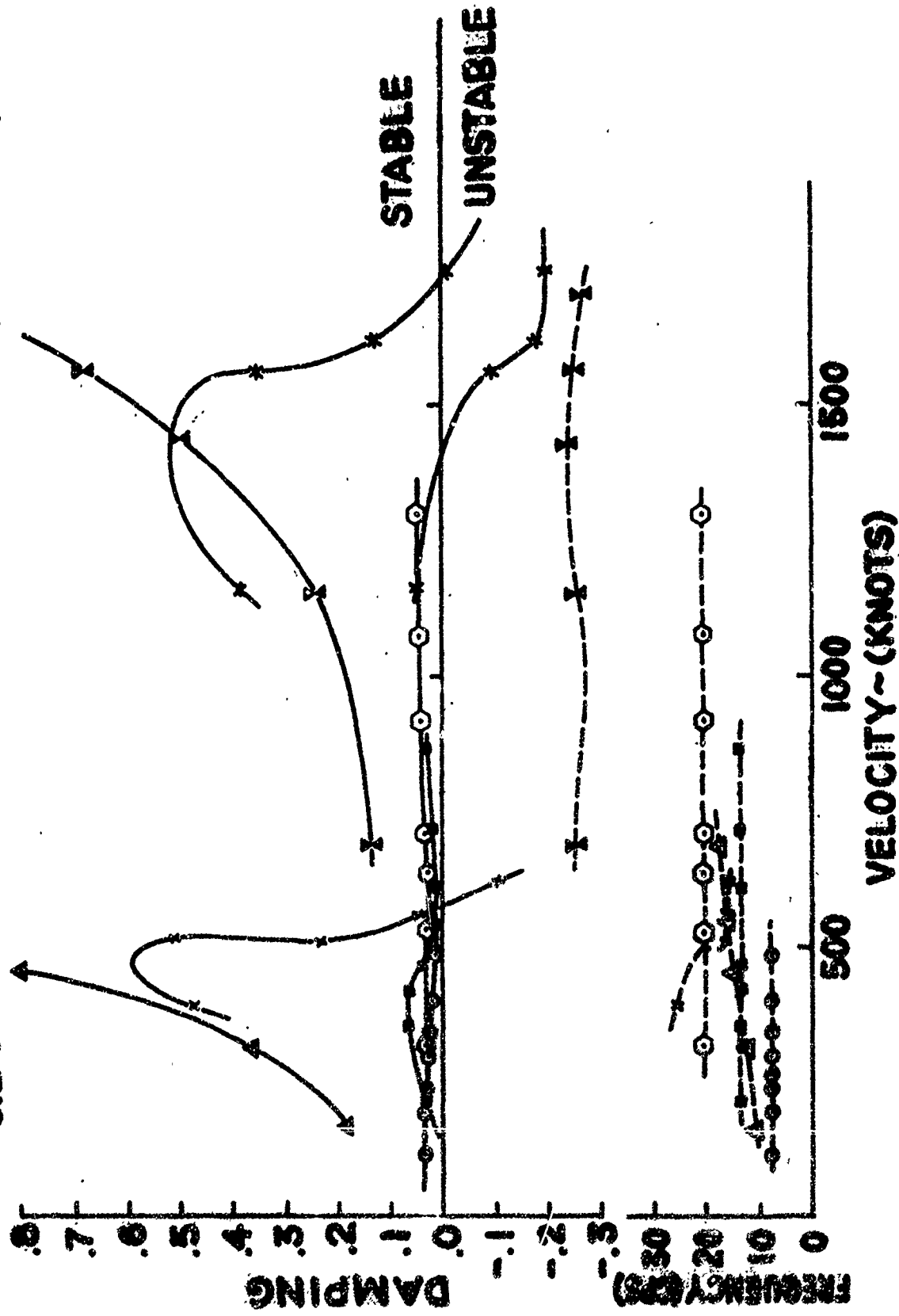


FIGURE 4

# XC142A

## ENGINE MOUNT DESIGN

### RELATIVE STRUT LOADING DUE TO PROP UNBALANCE

± (UP)

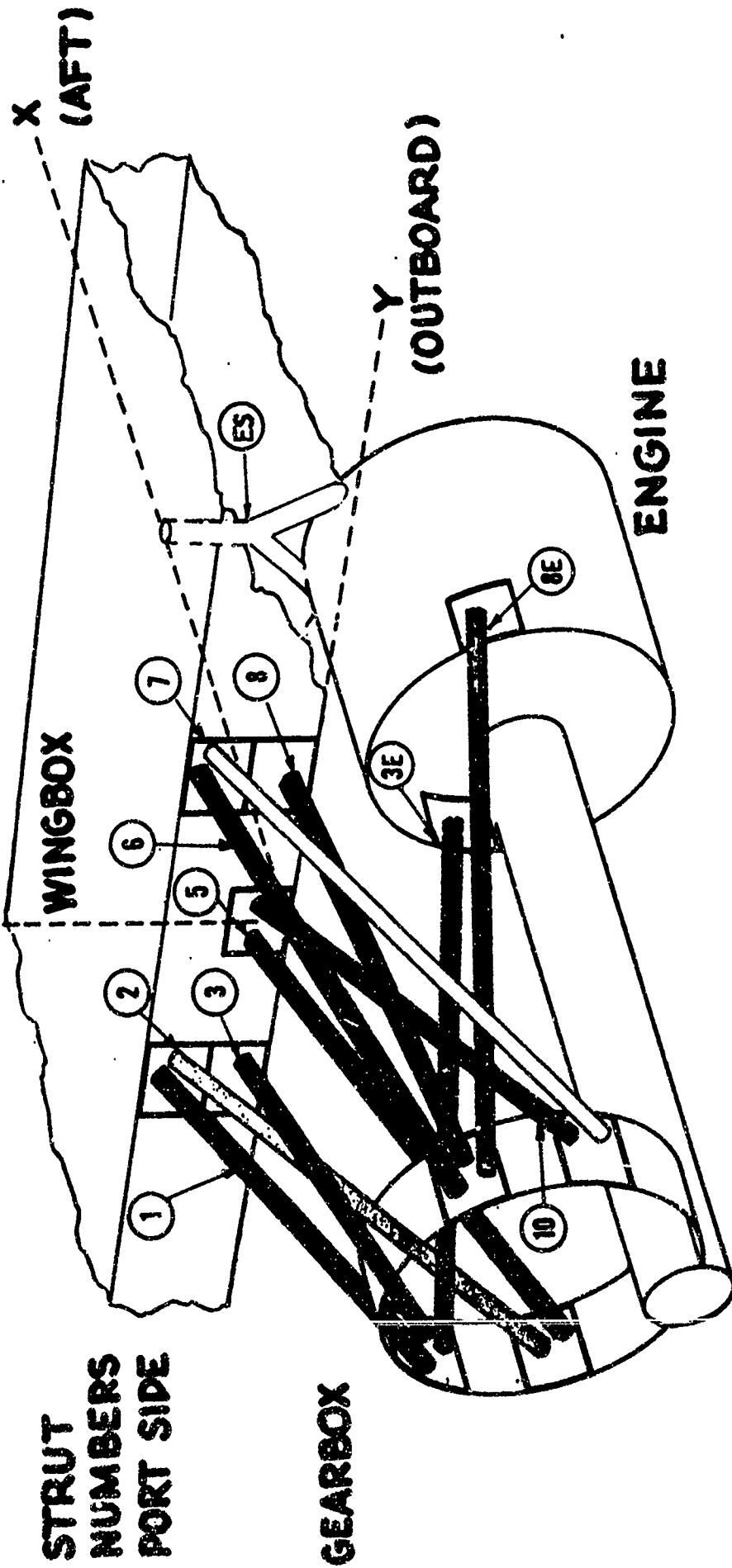
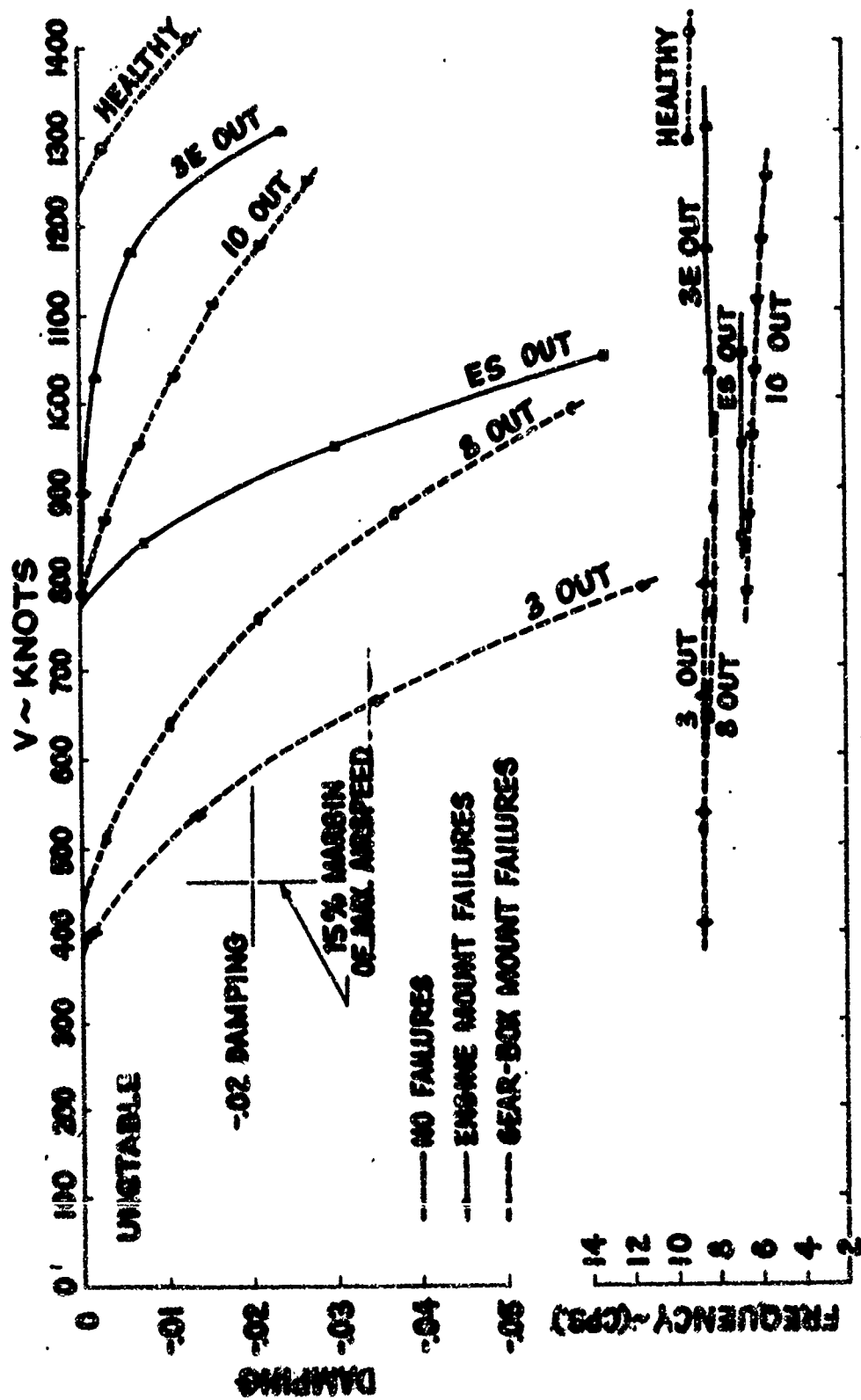


FIGURE 5

# **XC142A ENGINE-GEARBOX-PROPELLER DAMPING VS. FLUTTER VELOCITY OPTIMUM-STRENGTH STRUT FAILURES**



**FIGURE 6**



# XC 142A ENGINE-GEARBOX-PROPELLER DAMPING VS. FLUTTER VELOCITY SHOCK MOUNT STIFFNESSES AS SHOWN-NO FAILURES

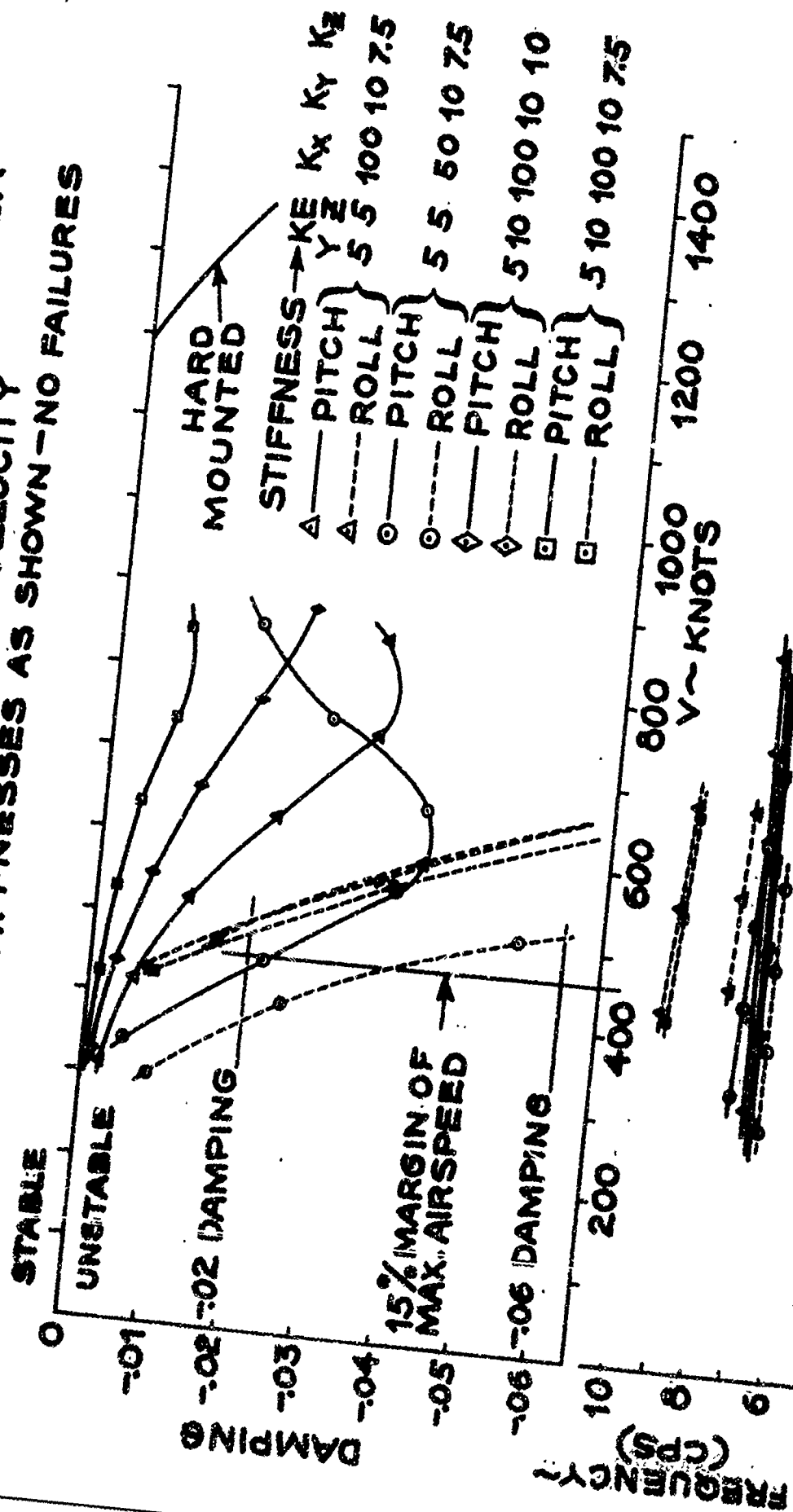


FIGURE 7

# XC 142A

WING - ENGINE - GEARBOX

DAMPING VS VELOCITY - - FREQUENCY VS VELOCITY  
MAXIMUM POWER CONDITION

V = 300 KTS

VELOCITY ~ KNOTS

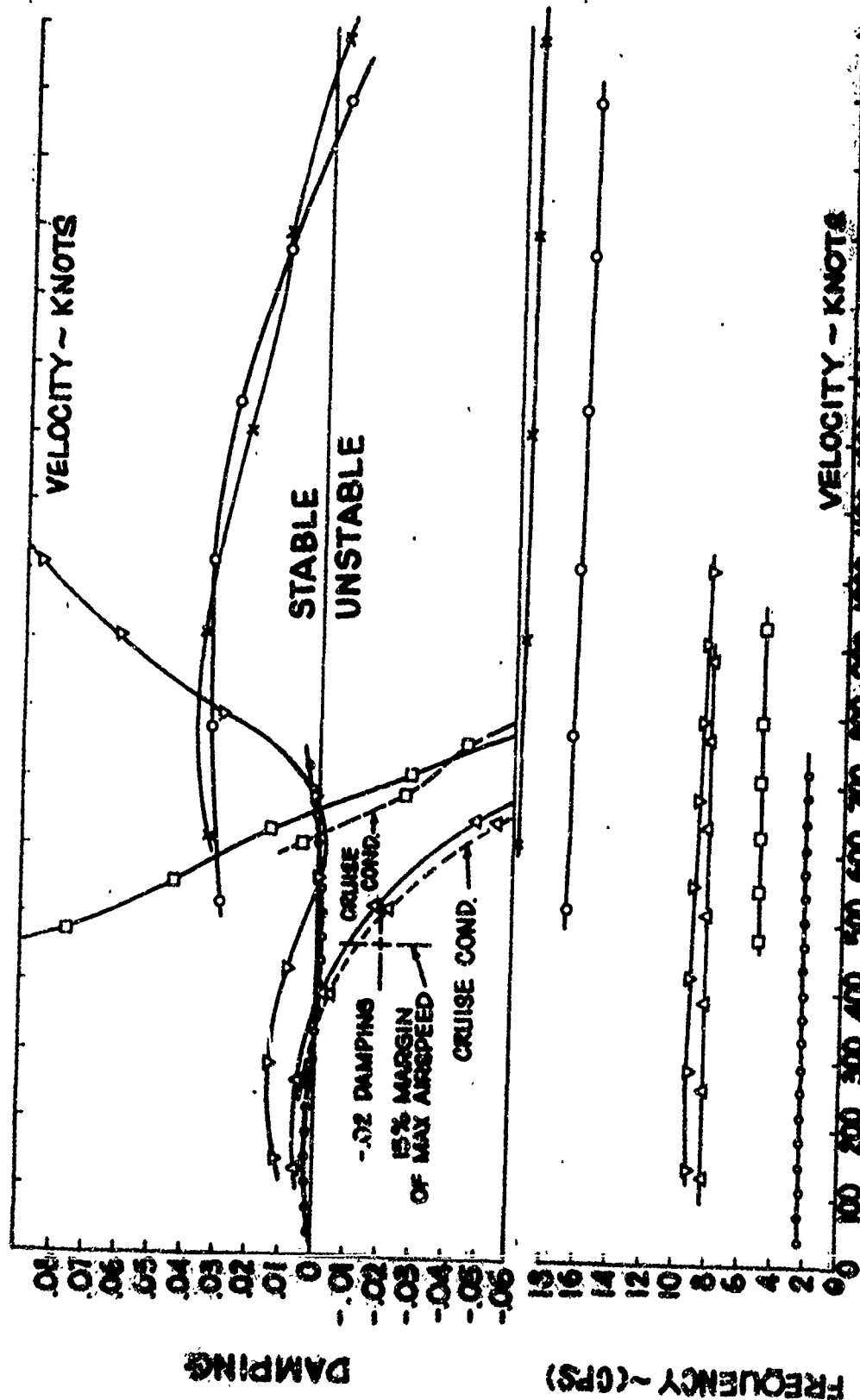
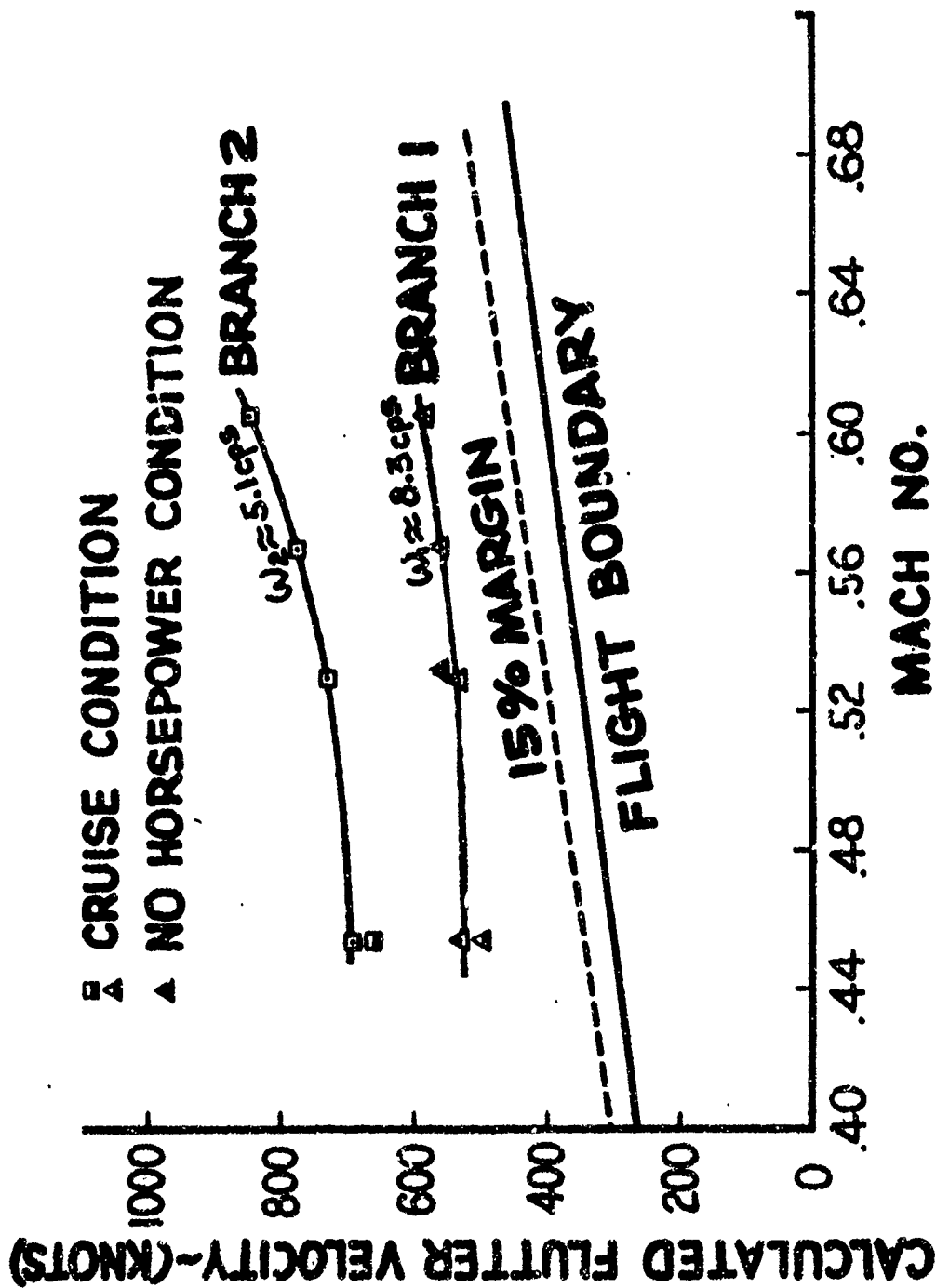


FIGURE 8

# **XCI42A WING** **FLUTTER VELOCITY VS. MACH NUMBER** **MAXIMUM POWER CONDITION, .02 DAMPING**



**FIGURE 9**

# XC142A AIRPLANE POWER SPECTRAL DENSITY

## GUST ANALYSIS

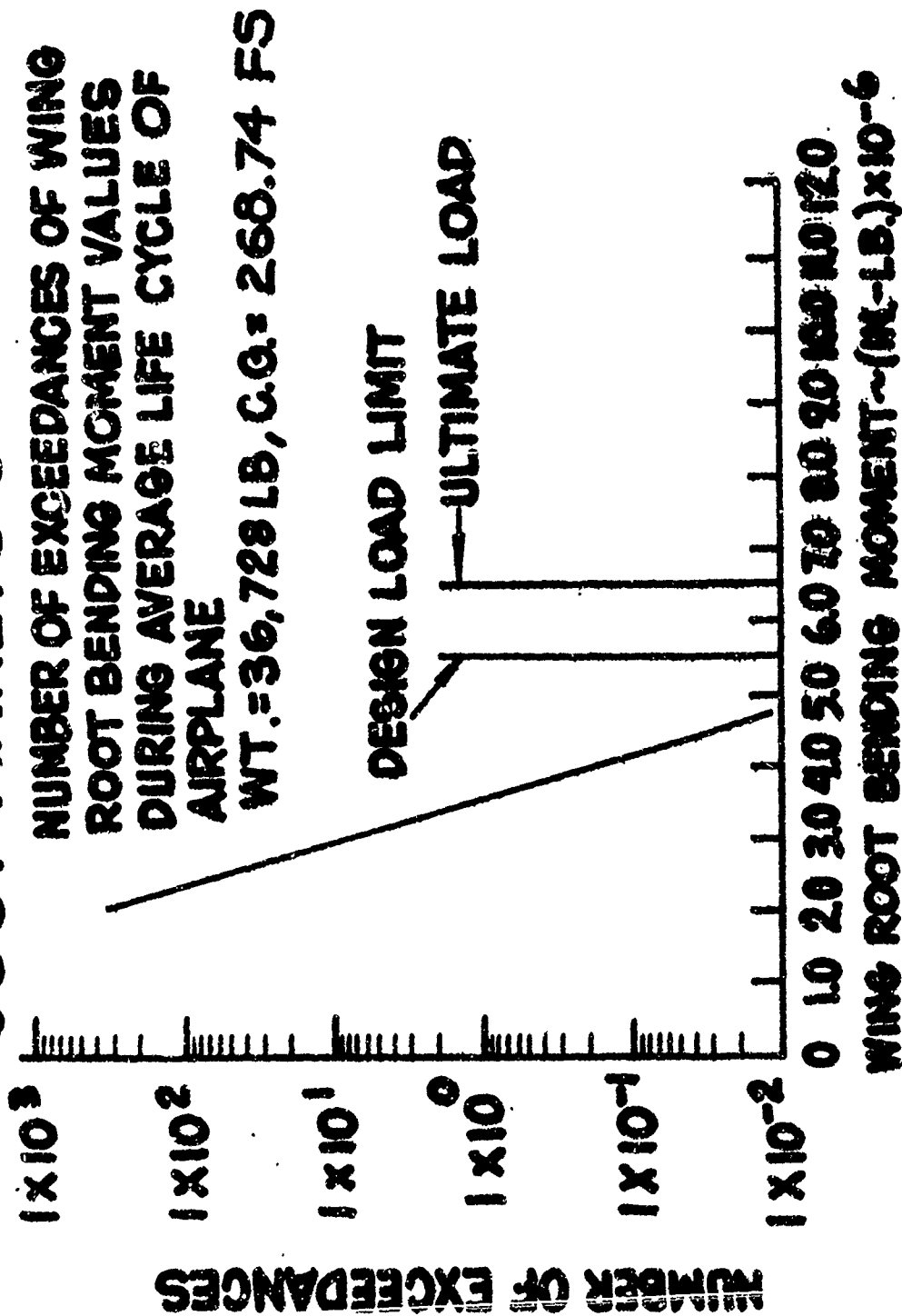
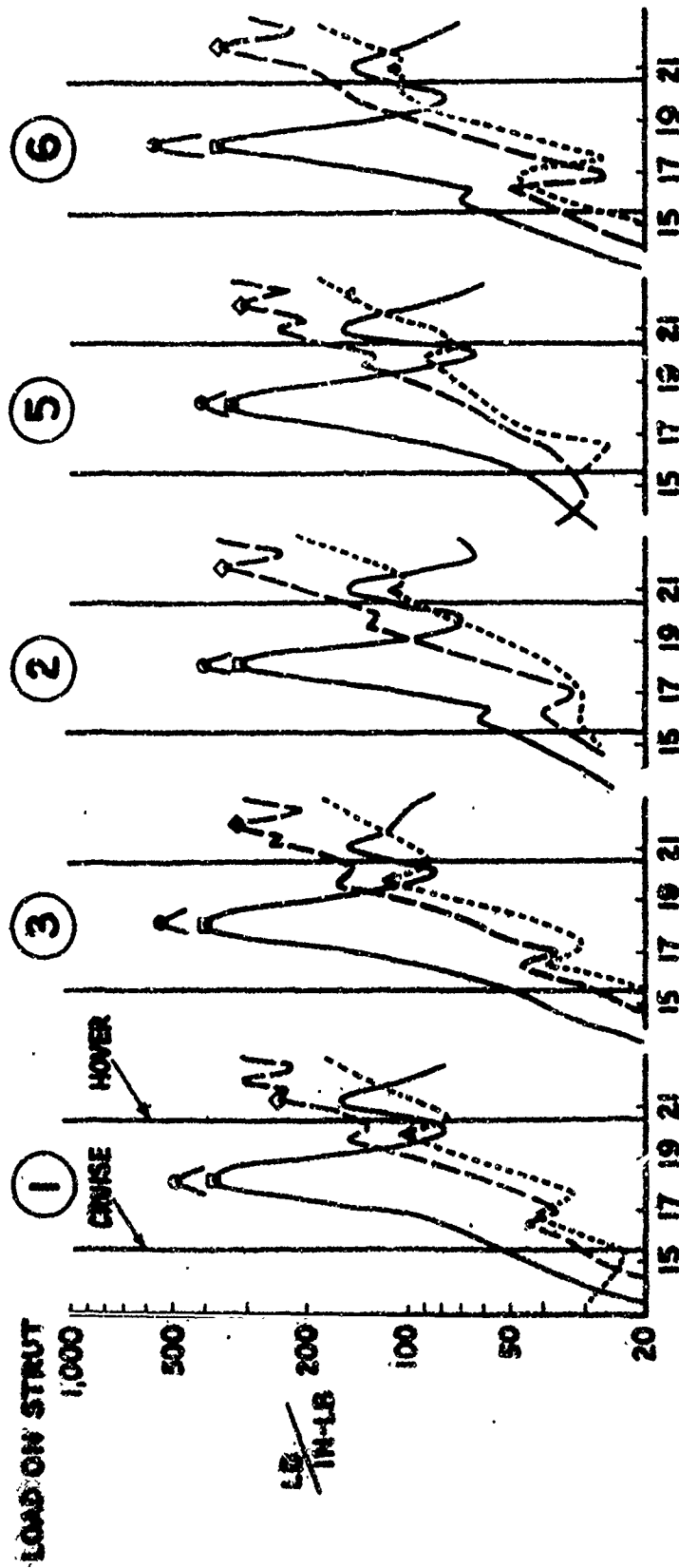


FIGURE 10

# **XCI42A ENGINE MOUNT** **INBD STRUT LOADS (LBS) PER PROP UNBALANCE (IN-LB) INBD SAME SIDE** **WING DOWN**

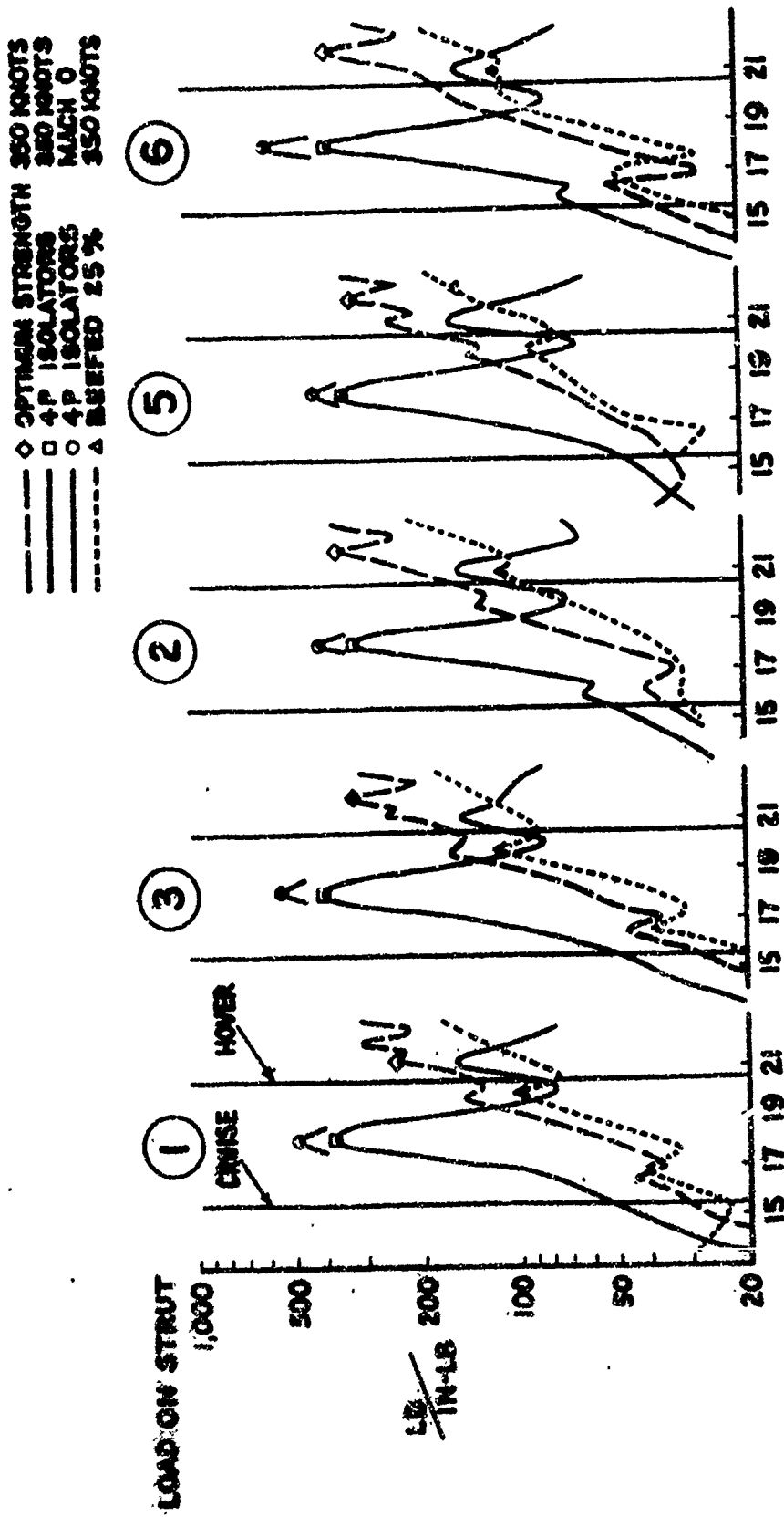
- ◇--- OPTIMUM STRENGTH 350 KNOTS
- 4P ISOLATORS 350 KNOTS
- 4P ISOLATORS MACH 0
- △--- BEEFED 25 % 350 KNOTS



**FREQUENCY ~ CPS**  
**FIGURE 11**

XCI42A ENGINE MOUNT

# INBD STRUT LOADS (LBS) PER PROP UNBALANCE (IN-LB) INBD SAME SIDE WING DOWN



FREQUENCY ~ CPS  
FIGURE 11

# XC142A

INBOARD STRUT LOADS PER IN-LB INBOARD PROP UNBALANCE  
WITH INBOARD STRUT FAILED - WING DOWN - SYMMETRIC - 4P ISOLATED

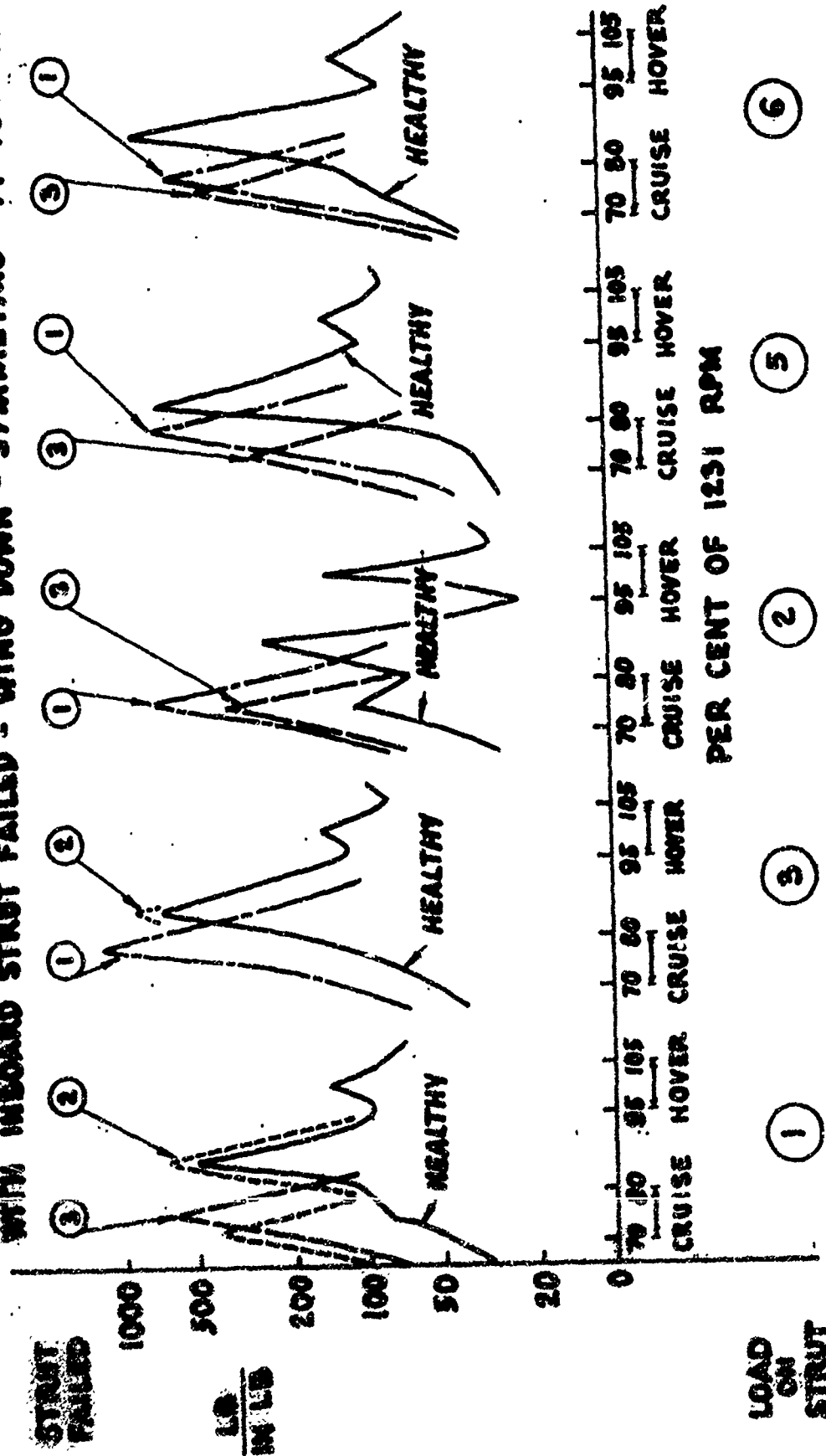
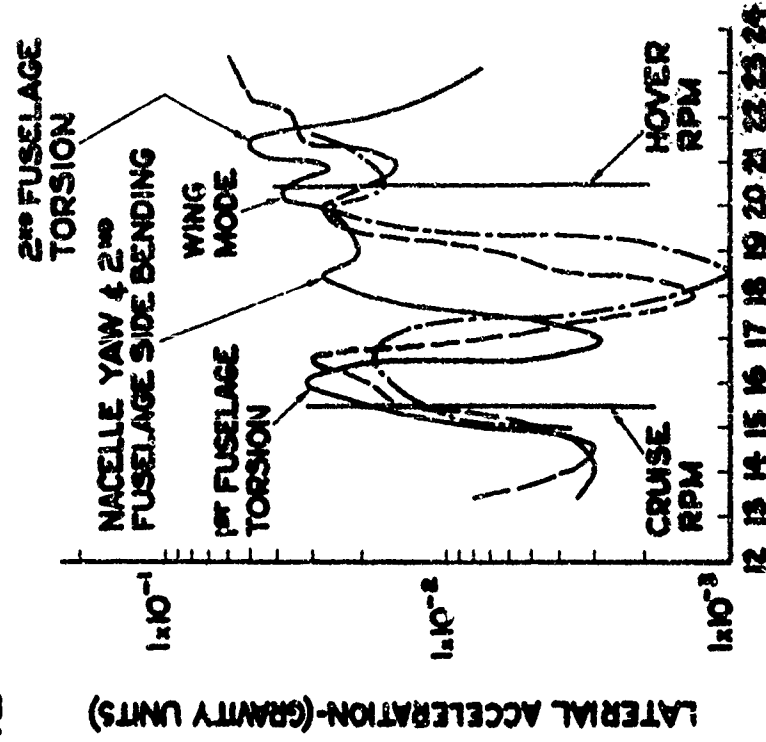
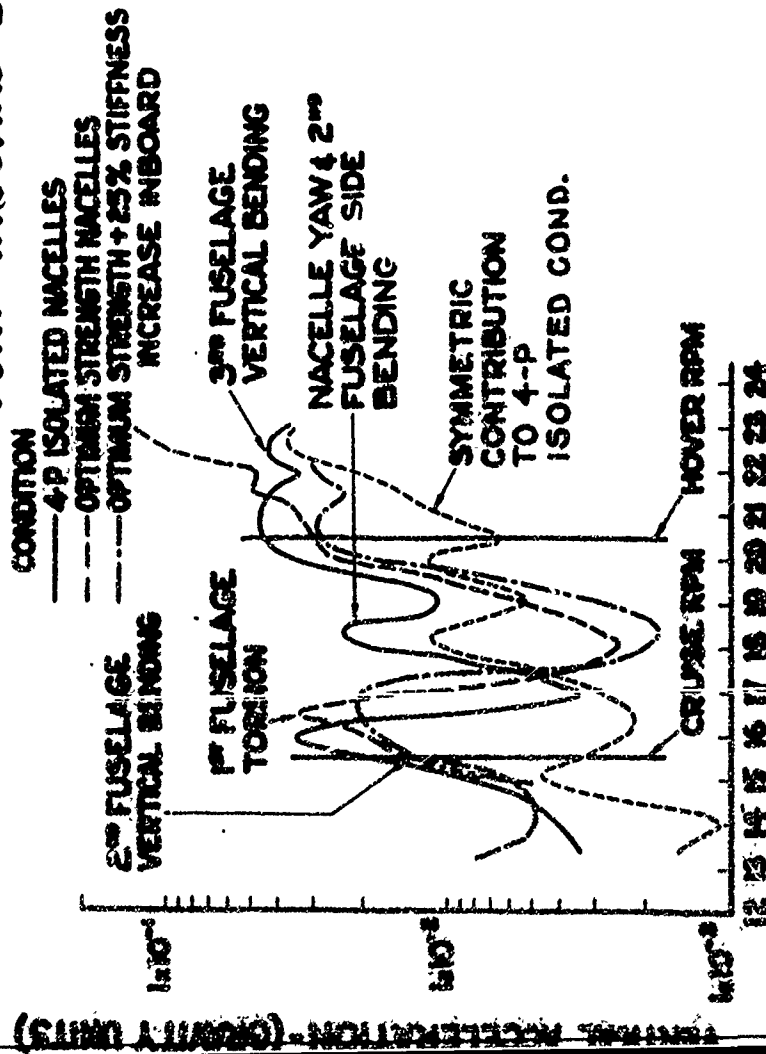


FIGURE 12

# XC142A

## ENVELOPE OF FUSELAGE ACCELERATIONS FROM FUSELAGE STATIONS 130 THRU 400 FOR A ONE INCH-POUND PROPELLER UNBALANCE ON THE

### PORT INBOARD ENGINE



FREQUENCY ~ (CPS.)

FIGURE 13



# XC142A TAIL PROPELLER SHAFTING VIBRATION MODE SHAPES

STIFFNESS OF ALL SUPPORTS

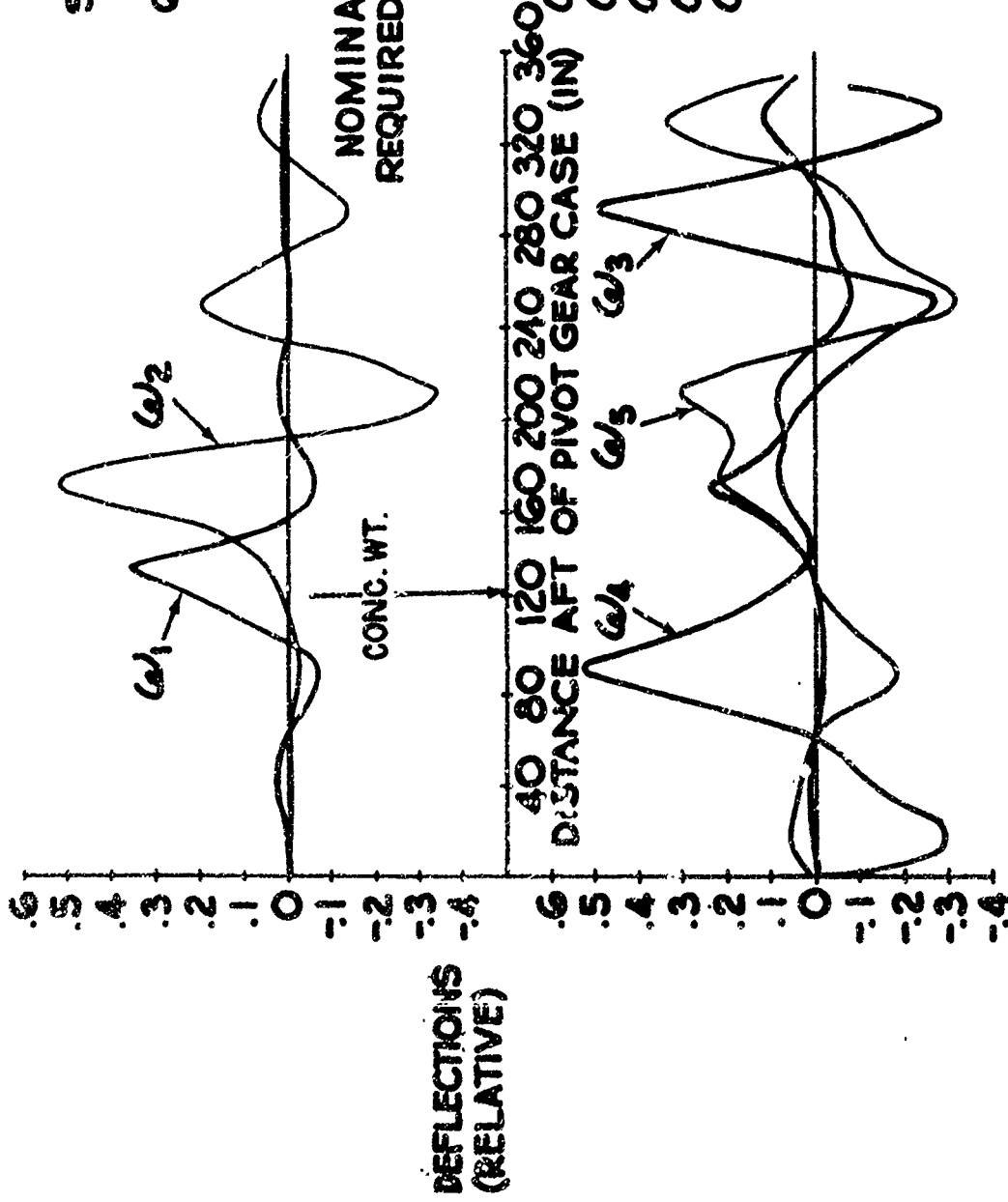
= 16,700 LB/IN.

GLB CONCENTRATED WEIGHT

12 IN. AFT FUSE STA 450

NOMINAL SHAFT SPEED = 6050 RPM

REQUIRED CRITICAL SPEED = 8500 RPM



$\omega_1 = 88$  CPS = 5280 RPM

$\omega_2 = 158$  CPS = 9480 RPM

$\omega_3 = 162$  CPS = 9710 RPM

$\omega_4 = 171$  CPS = 10,270 RPM

$\omega_5 = 171$  CPS = 10,270 RPM

FIGURE 14

# XC142A AIRPLANE

## PROFILES OF SOUND PRESSURE LEVELS:

STOL (DB, RE: 0.0002 DYNES/CM<sup>2</sup>)  
 VELOCITY NEAR ZERO, 2700 HP/PROPELLER  
 RPM=1230, HELICAL TIP SPEED=MACH 0.9

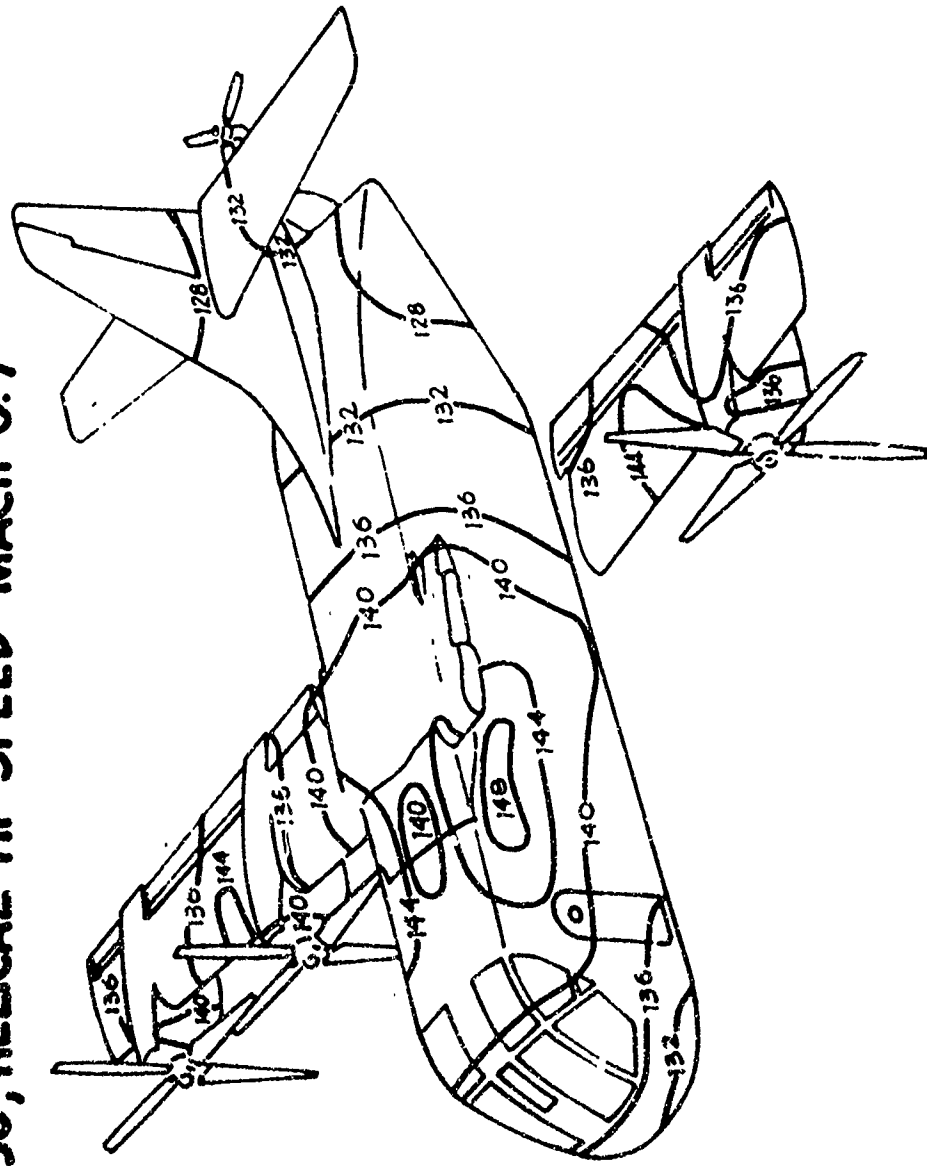


FIGURE 15

**PROPELLER WHIRL FLUTTER CONSIDERATIONS  
FOR V/STOL AIRCRAFT**

**Wilmer H. Reed, III and Robert M. Bennett**

**NASA, Langley Field, Virginia**

PROPELLER WHIRL CONSIDERATIONS FOR

V/STOL AIRCRAFT

By Wilmer H. Reed III and Robert M. Bennett  
NASA Langley Research Center

For Presentation at the CAL-TRECOM Symposium on  
Dynamic Loads Problems Associated With Helicopters  
and V/STOL Aircraft, Buffalo, New York,

June 26-27, 1963

PROPELLER WHIRL FLUTTER CONSIDERATIONS FOR  
V/STOL AIRCRAFT

By Wilmer H. Reed III and Robert M. Bennett

ABSTRACT

Recent studies of propeller whirl flutter conducted at the NASA Langley Research Center are reviewed and extended to encompass operating conditions peculiar to V/STOL aircraft. The extension of previous work involves consideration of angle of attack, propeller thrust, and flapping blades. Experimentally determined whirl flutter boundaries using both measured and theoretical propeller derivatives are compared with theory. As a related dynamic problem, the response of propeller-nacelle systems to random atmospheric turbulence is analyzed.

PROPELLER WHIRL FLUTTER CONSIDERATIONS FOR  
V/STOL AIRCRAFT

By Wilmer H. Reed III and Robert M. Bennett

INTRODUCTION

The purpose of this paper is to review recent work on propeller whirl conducted at NASA Langley Research Center, to extend these studies to include V/STOL aircraft operating conditions, and to consider a related problem - the dynamic response of a propeller-powerplant system to random atmospheric turbulence.

Until about 3 years ago the phenomenon known as propeller whirl flutter fell into the category of an interesting but academic problem of little practical concern. The possibility that a precession-type instability could develop in a flexibly mounted aircraft propeller-powerplant system was mentioned in a 1938 paper by Taylor and Browne (ref. 1) which dealt primarily with the problem of vibration isolation. Following this paper, Wright Field personnel and other groups made propeller whirl flutter calculations for new aircraft as a matter of routine. The procedure was eventually abandoned, however, when it was found that in all cases considered very large margins of safety were indicated. Then in 1960, intense interest was focused on the problem as a result of two Lockheed Electra accidents. Wind-tunnel investigations conducted in the Langley transonic dynamics tunnel indicated that if stiffness in the engine support structure was severely reduced, say through damage, propeller whirl was possible; in the undamaged condition

the aircraft had an adequate margin of safety. The solution was to modify the Electra with sufficient redundant structure to preclude a large loss of stiffness from a single failure. Because of these experiences with the Electra and the sometimes radical departures from conventional methods of installing propeller-powerplant systems - especially on V/STOL configurations - propeller whirl stability has once again become a design consideration on new propeller aircraft.

During and since the Electra investigation several generalized studies of propeller whirl have been published by the NASA. These studies show the influence of various parameters affecting the stability of a simplified representation of propeller-powerplant systems. References 2, 3, and 4 analyze the whirl stability of an isolated propeller system which is assumed to be flexibly mounted to a rigid back-up structure; more recently, unpublished experimental data have been obtained for a similar system wherein both propeller aerodynamic derivatives and whirl stability boundaries were measured. These investigations were concerned primarily with operating conditions representative of high-speed (low angle-of-attack) flight. Under such conditions it can be shown that, from the standpoint of whirl stability, the effects of mean angle of attack and thrust of the propeller are relatively unimportant and can therefore be neglected. This leaves open the question of propeller whirl stability on V/STOL aircraft during the high-thrust, high-angle-of-attack transition maneuver. Thus, one of the aims of this paper is to extend the previous generalized studies to include the effects of thrust and high mean angles of attack.

# SYMBOLS

$b_{0.75R}$	propeller chord at 0.75 blade radius
$B$	number of propeller blades
$C_m$	propeller pitching-moment coefficient
$\bar{C}_m$	total pitching-moment coefficient about pitch axis of system (see eq.(8))
$C_n$	propeller yawing-moment coefficient
$C_T$	thrust coefficient, $\frac{T}{\rho \left(\frac{U}{2\pi}\right)^2 (2R)^4}$
$C_Y$	propeller side-force coefficient
$C_Z$	propeller vertical-force coefficient
$e$	offset of blade hinge axis
$h_{\theta\bar{v}}, h_{\theta\bar{w}}$	response in $\theta$ due to unit impulse in $\bar{v}$ and $\bar{w}$ , respectively
$H$	moment-of-inertia ratio, $\frac{\pi I_x}{I_y}$
$H_{\theta\bar{v}}, H_{\theta\bar{w}}$	frequency-response functions giving response in $\theta$ to unit sinusoidal inputs in $\bar{v}$ and $\bar{w}$ , respectively
$I_x$	mass moment of inertia of propeller about axis of rotation
$I_y$	mass moment of inertia of propeller-powerplant system about pitch axis
$J$	propeller advance ratio, $\frac{JU}{\Omega R}$
$k, k_\theta$	reduced-frequency parameters, $k = \frac{\omega R}{U}$ , $k_\theta = \frac{\omega_\theta R}{U}$
$l$	distance from plane of propeller to pitch axis
$L$	scale of atmospheric turbulence
$R$	propeller radius
$S_\theta$	rotational stiffness of powerplant mount about pitch axis



$t, \tau, T$  time  
 $u(t), v(t), w(t)$  longitudinal, lateral, and vertical components  
of turbulence velocity  
 $\bar{v}, \bar{w}$  flow angles due to turbulence,  $\bar{v} = \frac{v}{U}, \bar{w} = \frac{w}{U}$   
 $\bar{V}(\omega), \bar{W}(\omega)$  Fourier transforms of  $v(t)$  and  $w(t)$ , respectively  
 $\alpha$  angle of attack of propeller  
 $\beta$  geometric blade angle at  $0.75R$  measured from propeller  
plane of rotation  
 $\zeta$  viscous damping ratio  
 $\theta, \psi$  geometric pitch and yaw angles  
 $\theta_g, \psi_g$  effective pitch and yaw angles in turbulent flow  
(see eq. (9))  
 $\Theta(\omega)$  Fourier transform of  $\theta(t)$   
 $\kappa$  density-inertia ratio,  $\frac{\rho R^5}{I_y}$   
 $\rho$  air density  
 $\sigma^2$  mean-square value of turbulence velocity component  
 $\tau$  nondimensional time,  $\frac{Ut}{R}$   
 $\Phi_\theta, \Phi_{\theta w}$  power spectra and cross spectra, where subscripts denote  
the associated time histories  
 $\Omega$  propeller rotational frequency  
 $\omega$  circular frequency

Subscripts:

q        differentiation with respect to  $\theta'$   
r        differentiation with respect to  $\psi'$   
 $\theta$        pitch direction  
 $\psi$        yaw direction

Primes denote differentiation with respect to  $\tau$ .

Partial derivatives are denoted by double subscripts;

for example,  $C_{m\theta} = \frac{\partial C_m}{\partial \theta}$ ,  $C_{mq} = \frac{\partial C_m}{\partial q}$ , and so forth.

## DYNAMIC SYSTEM

A schematic diagram of the idealized propeller-powerplant system to be considered in this paper is shown in figure 1. The system is mounted on two springs,  $S_\theta$  and  $S_\psi$ , located a distance  $l$  behind the plane of the propeller. These springs permit small angular deflections  $\theta$  and  $\psi$  of the propeller axis from its equilibrium position which is inclined at an arbitrary angle  $\alpha$  from the free stream. Damping, which in an actual system would be introduced by hysteresis or friction in the mounts, fuel lines, electrical conduits, etc., is here simulated by equivalent viscous damping  $\zeta_\psi$  and  $\zeta_\theta$ . Other variables shown in the figure are the airstream velocity  $U$  and, the rotational speed of the propeller  $\Omega$ .

## MECHANISM OF WHIRL FLUTTER

Let us briefly review some basic aspects of propeller whirl flutter. The dynamic behavior of a propeller-powerplant system is governed by an interaction of the aerodynamic and gyroscopic moments on the rotating propeller, the inertia forces of the propeller-powerplant system, and the damping and elastic forces in the mount structure. If the propeller is replaced by an equivalent nonrotating mass and the aerodynamic forces are neglected, natural vibrations of the system about the pitch axis can occur independently of those about the yaw axis. On the other hand, if the propeller is replaced by an equivalent rotating mass, or flywheel, the associated gyroscopic moments prevent the occurrence of independent motions in

either pitch or yaw so that the natural vibrations of the system are characterized by a precession or wobbling motion of the rotation axis. The variation of these so-called "precession" modes with rotational speed of the flywheel is illustrated in figure 2 for a system having symmetrical stiffness in pitch and yaw. Note that as the angular velocity  $\Omega$  of the flywheel is increased, the frequency of one mode increases while that of the other decreases. As illustrated by the sketches on the right of the figure, the flywheel shaft follows a circular path for each mode. For the higher frequency mode the direction of precession is the same as that of rotation and is thus referred to as the "forward" mode; alternatively, for the lower frequency mode the direction of precession is opposite that of rotation and is referred to as the "backward" mode. These modes can only be stable, for there is no mechanism by which the flywheel can add energy to the system.

Let the flywheel be replaced by a propeller having the same angular momentum. Now when precession occurs, aerodynamic forces and moments are generated due to angle-of-attack changes on blade elements of the propeller. These forces and moments are governing factors that determine whether the precession modes of a given system will damp out following a disturbance, such as a gust, or will build up with time until the structure fails or its motion becomes limited by the presence of nonlinearities. It has been found that on conventional propellers whirl flutter invariably occurs in the backward whirl mode.

The generalized propeller whirl studies of references 2, 3, and 4 show trends for many parameters that affect the stability of the system shown in figure 1. It is beyond the scope of this paper to summarize these trends; however, one type of stability-boundary plot is particularly enlightening and will be discussed with the aid of figure 3. This figure shows the pitch and yaw stiffness required for stability for three values of structural damping (the physical properties of the system treated are tabulated in reference 3 under system 2A with  $J = 1.8$ ). Both whirl-flutter and static-divergence boundaries are presented. An important feature shown, which appears to be characteristic of most propeller whirl systems, is the pronounced sensitivity of the stability boundaries to small changes in structural damping when the damping is near zero. Thus, to assume zero structural damping for a propeller system, as is often done as a measure of conservatism in conventional wing flutter analyses, would probably lead to an unduly low estimate of the whirl flutter speed. Note also that the shapes of the whirl boundaries are likewise highly dependent on damping.

#### COMPARISON OF THEORY AND EXPERIMENT

To enable a better evaluation of theoretical methods for predicting whirl flutter, some experimental data have been obtained on a model which closely resembles the idealized mathematical model treated in references 2, 3, and 4. The model is shown in figure 4 and its physical properties are given in table I under

system 1. These data, obtained by Bland and Bennett (ref. 5), include measurements of both static aerodynamic propeller derivatives and whirl-flutter boundaries. Typical results from the study are presented in figure 5, which shows the viscous damping required to prevent flutter plotted against a nondimensional velocity ratio.

The calculated stability boundaries shown for comparison are based on three sets of propeller aerodynamic derivatives: theoretical derivatives evaluated by the methods of Ribner (ref. 6) and Houbolt and Reed (ref. 3), and the actual derivatives that were measured on the model (the damping derivative  $C_{m_q}$  was not measured, so it was calculated by the method of ref. 6).

It can be seen from the figure that the calculations based on measured derivatives are in excellent agreement with the experimental data, while those based on theoretical derivatives predict somewhat lower flutter velocities than were observed. Similar comparisons between theory and experiment were also indicated for other values of such system parameters as advance ratio, inertia, and pivot-point location.

#### V/STOL TRANSITION

The propeller of a V/STOL vehicle, such as a tilt-wing aircraft, will undergo large changes in thrust and mean angle of attack during transition from hovering to high-speed flight. Since previous generalized studies (refs. 2, 3, and 4) have been concerned primarily with the high-speed flight regime where angle-of-attack and thrust effects are known to have a negligible influence on whirl stability,

it is of interest to explore the possibility of encountering propeller whirl during low-speed transition maneuvers. For this purpose some whirl stability calculations have been made, utilizing experimental static propeller derivatives obtained by Yaggy and Rogallo in the Ames 40- by 80-foot tunnel for high angle-of-attack and thrust conditions typical of VTOL operations. (See ref. 7, propeller 1.) These derivatives, which were determined graphically from data presented in reference 7, are shown in figure 6 of the present report. It should be noted that since the damping derivative  $C_{mq}$  was not measured in reference 7 it has been necessary to use theoretically determined values and make the assumption that angle-of-attack effects on  $C_{mq}$  are negligible. The system considered in these calculations is identified in table I as system 2.

Figure 7 indicates the effect of angle of attack on the stiffness required to prevent flutter. The curves have been normalized with respect to the stiffness required at zero angle of attack. Little effect of angle of attack is noted for  $\beta = 13.0^\circ$ , which corresponds to a low thrust condition ( $C_T = 0$  at  $\alpha = 0$ ); at  $\beta = 36.5^\circ$ , which represents a high thrust condition ( $C_T = 0.24$  at  $\alpha = 0$ ), a moderate stabilizing effect is present.

The effects of thrust coefficient for angles of attack up to  $30^\circ$  are presented in figure 8 for several values of advance ratio. The figure indicates, as has been shown in previous studies, that propeller thrust effects are negligible for advance ratios representative of high-speed flight ( $J > 2.0$ ). At low forward speeds during

transition, however, thrusting propellers are seen to have a destabilizing influence on whirl flutter.

The combined effects of thrust and angle of attack on the whirl flutter during a hypothetical transition maneuver are illustrated in figure 9. The assumed variations of  $\alpha$  and  $C_T$  with forward velocity are given on the left-hand side of the figure and the associated flutter boundary, in the form of damping required to prevent flutter, is on the right. (Velocity was determined by assuming  $\omega_0 R = 76.8$  so that  $V = \frac{76.8}{k}$  ft/sec.) Shown for comparison is the flutter boundary computed on the basis of  $C_T = 0$  and  $\alpha = 0$ . Although the overall effects of thrust and angle of attack are slightly destabilizing, the large margin of stability at low forward speeds would seem to indicate that propeller whirl problems would not occur during the transition maneuver. It should be pointed out that these conclusions are based on the assumption that  $C_{mq}$  is essentially independent of angle-of-attack changes during transition.

#### FLAPPING HINGES

Propellers with blades hinged to permit flapping in a plane perpendicular to the propeller rotation axis have been proposed for V/STOL applications. Some unpublished data obtained on such a system by E. F. Baird of Grumman Aircraft Engineering Corporation indicated a possible occurrence of whirl flutter in the forward mode as well as the backward mode which is typical of fixed blade designs. In an effort to gain further insight into the problem, we have



conducted a brief exploratory wind-tunnel investigation on a simple model.

The model, shown in figure 10, consists of a windmilling propeller attached to a rod which has freedom to pitch and yaw about a set of gimbal axes. The system has symmetrical stiffness that can be controlled by varying tension in a spring connected axially at the other end of the rod. Each propeller blade is attached to the hub by means of two pins. When both pins are in position the blade is fixed; when one of the pins is removed the other pin becomes a hinge about which the blade is free to flap. (See fig. 10.) In this way the blades can be hinged at either 0.08 or 0.13 of the propeller radius from the spin axis. Other physical properties of the model, identified herein as system 3, may be found in table I.

Whirl-flutter boundaries for the flapping-blade and fixed-blade conditions are presented in figure 11. Both forward and backward whirl instabilities were encountered. The system became unstable in the backward mode for the fixed blade and the 0.13R hinge offset, but instability developed in the forward mode with the smaller hinge offset of 0.08R. Note that for flutter in the backward mode blade flapping had a significant stabilizing influence; just the opposite conclusions are indicated for flutter in the forward mode. In addition to frequency differences (backward whirl occurs at low frequency, forward whirl at high frequency), the two modes behaved differently in other respects. Whereas backward whirl instability was accompanied by divergent motions as predicted by linear theory, forward whirl instability was characterized by amplitude limited motions which could be excited when the disturbing force exceeded a threshold level. The

implication to be drawn from these preliminary studies is that blade flapping, and possibly blade flexibility, can have either strong stabilizing or destabilizing influences on propeller whirl flutter. Additional research is required to further delineate these aspects of the problem.

#### RESPONSE TO RANDOM ATMOSPHERIC TURBULENCE

Previous sections of the paper have dealt with factors that affect the stability of propeller-powerplant systems. A related problem of interest in connection with dynamic loads and fatigue is the response of such systems to gusts and turbulence in the atmosphere. These loads may be significant even though the system is operating well on the stable side of its whirl-flutter boundary.

The gust response problem and a method of analysis is illustrated in figure 12. The free-stream velocity is represented by a mean velocity  $U$ , upon which is superimposed unsteady velocity components  $u(t)$ ,  $v(t)$ , and  $w(t)$ . These time-dependent velocities produce unsteady forces and moments on the propeller which in turn cause pitch and yaw deflections,  $\theta(t)$  and  $\psi(t)$ , of the flexibly mounted system. If turbulence is considered to be a stationary random process, a solution can be obtained for the response of the system to multiple random inputs  $u(t)$ ,  $v(t)$ , and  $w(t)$ . This requires specifications of the power spectra and cross spectra of the inputs, together with a set of frequency-response functions which define the response of the system to sinusoidal variations of the gust velocity components. If the turbulence is considered to be isotropic, the cross-spectrum terms become zero and the equation for the power spectrum of response of the system in, say, pitch can be written

$$\phi_{\theta} = \phi_w \left[ |H_{\theta w}|^2 + |H_{\theta v}|^2 \right]$$

where  $\phi_w$  is the power spectrum of the  $v$  and  $w$  components of turbulence and  $H_{\theta v}$  and  $H_{\theta w}$  represent the response in pitch to unit-amplitude sinusoidal  $v$  and  $w$  inputs. It is assumed that  $H_{\theta u} = 0$ . (For derivation of equations, see appendix.) A graphical indication of the way in which typical power spectra and frequency-response functions for a system might vary with frequency is also shown in figure 12. It should be mentioned that the frequency-response function  $H_{\theta v}$  - that is, the response in a vertical plane due to a horizontal gust input - is a measure of the aerodynamic and gyroscopic coupling produced by the propeller. The two peaks in the frequency-response curve occur at the backward and forward whirl frequencies.

For purposes of illustration, figure 13 shows the calculated response to random turbulence for system 1, whose whirl-flutter boundary was presented in figure 5. The conditions chosen for these calculations are  $\frac{U}{R\Omega_0} = 2.0$  and  $\zeta = .05$ , which, as can be seen in figure 5, fall well within the stable region since the damping required for stability at this  $\frac{U}{R\Omega_0}$  value is  $\zeta = 0.002$ . The analytical expression for the turbulence spectrum assumed in the calculations is the approximation given in reference 8 for isotropic turbulence at high frequencies:

$$\phi_w = \frac{0.521 \sigma^2}{L^{3/2} \left( \frac{\omega}{U} \right)^{5/3}}$$

where  $\sigma^2$  is the mean-square value of  $w$  and  $L$  is the scale of turbulence, assumed here to be 5,000 feet. It was also necessary to specify a propeller radius, which was taken to be  $R = 6.75$  feet for these calculations.

The solid curve in figure 13 represents the power spectrum of the response of the system in pitch. (Since the system was assumed to have symmetrical stiffness, this curve also represents the response in yaw.) The dashed curve shown for comparison indicates the quasi-static response, that is, the response calculated by neglecting the time-dependent inertia, gyroscopic, and damping forces. The relative magnitudes of these two curves at a given frequency indicates the amplification of response due to dynamics of the system. As would be expected, the amplification is highest at frequencies corresponding to the natural whirl modes and becomes sharply attenuated at higher frequencies.

#### CONCLUDING REMARKS

This paper has examined some potential problem areas relating to propeller whirl response and flutter on V/STOL aircraft. From limited studies presented herein on highly idealized systems the following general conclusions are indicated:

1. Calculated whirl-flutter boundaries based on theoretical propeller derivatives are in reasonable agreement with experimental data; those based on measured derivatives are in excellent agreement with experiment.
2. For flight conditions representative of transition maneuvers, the effects of large angle of attack and large thrust coefficient are relatively unimportant from the standpoint of propeller whirl stability.

3. Flapping propeller blades can have significant stabilizing or destabilizing influences on propeller whirl and make possible the occurrence of flutter in the forward whirl mode.

4. Power-spectral-density techniques offer a convenient means of analyzing the response of propeller-powerplant systems to random atmospheric turbulence.

## APPENDIX

### DERIVATION OF EQUATIONS FOR RESPONSE OF PROPELLER-NACELLE TO RANDOM ATMOSPHERIC TURBULENCE

#### Response Equations

The problem considered is that of calculating the dynamic response of a propeller-nacelle system to random fluctuations of the free-stream velocity. The response quantities of interest are the pitch and yaw deflections of the system which is assumed to be flexibly mounted to a rigid backup structure.

Consider the free-stream velocity to be represented by the vector addition of the flight velocity  $U$  and time-varying gust velocities  $u(t)$ ,  $v(t)$ , and  $w(t)$  as is shown in figure 12. It will be assumed that the gust components act uniformly over the propeller disk and that the response induced by the  $u(t)$  component is negligible. Since the analytical procedures are the same for both pitch and yaw, only the pitch response will be treated.

The pitch angle  $\theta(t)$  of the system can be expressed in terms of arbitrary time variations of flow angularity due to gusts,  $\bar{v}(t) = \frac{v(t)}{U}$  and  $\bar{w}(t) = \frac{w(t)}{U}$ , by means of the superposition integral

$$\theta(t) = \int_{-\infty}^{\infty} \bar{v}(\tau) h_{\theta\bar{v}}(t - \tau) d\tau + \int_{-\infty}^{\infty} \bar{w}(\tau) h_{\theta\bar{w}}(t - \tau) d\tau \quad (1)$$

where  $h_{\theta\bar{v}}$  is the response in  $\theta$  to a unit impulse in  $\bar{v}$  and similarly  $h_{\theta\bar{w}}$  is the response to a unit impulse in  $\bar{w}$ . Note that the function  $h_{\theta\bar{v}}$  is a coupling term which describes the response in a vertical plane associated with gusts in the horizontal plane. This term is a result of the aerodynamic and gyroscopic coupling moments on the propeller.

The gust components considered herein are random functions which cannot be expressed explicitly in terms of time, as is required in equation (1). If equation (1) is rewritten in terms of frequency rather than time, however, the problem becomes readily amenable to analysis by power spectral density techniques. (See ref. 8.)

The Fourier transform of  $\theta(t)$  is defined as

$$\Theta(\omega) = \lim_{T \rightarrow \infty} \int_{-T}^T \theta(t) e^{-i\omega t} dt \quad (2)$$

Substitution of equation (1) for  $\theta(t)$  into equation (2) gives

$$\Theta(\omega) = \bar{V}(\omega) H_{\theta\bar{v}}(\omega) + \bar{W}(\omega) H_{\theta\bar{w}}(\omega) \quad (3)$$

where  $\bar{V}(\omega)$  and  $\bar{W}(\omega)$  are Fourier transforms of the flow angles  $\bar{v}(t)$  and  $\bar{w}(t)$ , respectively, and  $H_{\theta\bar{v}}(\omega)$  and  $H_{\theta\bar{w}}(\omega)$  are frequency-response functions which describe the pitch response of the system to unit sinusoidal inputs in  $\bar{v}$  and  $\bar{w}$ .

The power spectrum of the response  $\Phi_\theta(\omega)$  is related to its Fourier transform by the expression

$$\Phi_\theta(\omega) = \lim_{T \rightarrow \infty} \frac{1}{2\pi T} \theta(\omega) \theta^*(\omega) \quad (4)$$

where  $\theta^*$  is the complex conjugate of  $\theta$ . From equation (3) the spectrum of the response then follows as

$$\begin{aligned} \Phi_\theta(\omega) &= \lim_{T \rightarrow \infty} \frac{1}{2\pi T} (\bar{V}H_{\theta\bar{V}} + \bar{W}H_{\theta\bar{W}})(\bar{V}^*H_{\theta\bar{V}}^* + \bar{W}^*H_{\theta\bar{W}}^*) \\ &= \Phi_{\bar{V}} |H_{\theta\bar{V}}|^2 + \Phi_{\bar{W}} |H_{\theta\bar{W}}|^2 + \Phi_{\bar{V}\bar{W}} H_{\theta\bar{V}} H_{\theta\bar{W}}^* + \Phi_{\bar{W}\bar{V}} H_{\theta\bar{W}} H_{\theta\bar{V}}^* \end{aligned} \quad (5)$$

where  $\Phi_{\bar{V}\bar{W}}$  and  $\Phi_{\bar{W}\bar{V}}$  are the cross spectra between  $\bar{V}$  and  $\bar{W}$  components of turbulence. Henceforth it will be assumed that the turbulence is isotropic so that the following simplifications can be introduced

$$\begin{aligned} \Phi_{\bar{V}} &= \Phi_{\bar{W}} \\ \Phi_{\bar{V}\bar{W}} &= \Phi_{\bar{W}\bar{V}} = 0 \end{aligned}$$

Thus equation (5) reduces to

$$\Phi_\theta = \Phi_{\bar{W}} \left[ |H_{\theta\bar{V}}|^2 + |H_{\theta\bar{W}}|^2 \right] \quad (6)$$



### Frequency-Response Functions

The frequency-response functions in equation (6) can be derived by including a sinusoidal gust forcing function on the right-hand side of the equations of motion for the system. For convenience the two-degree-of-freedom symmetrical system considered in reference 2 will be treated as an example. With slight modifications of the notation in reference 2, the equations of motion for the propeller-nacelle system with gust terms included become

$$\begin{aligned}\theta'' + \frac{H}{J} \psi' + 2\zeta_{\theta} k_{\theta} \theta' + k_{\theta}^2 \theta &= (\bar{C}_{m_{\theta}} \theta_g + \bar{C}_{m_q} \theta'_g + \bar{C}_{m_{\psi}} \psi_g + \bar{C}_{m_r} \psi'_g) \\ \psi'' - \frac{H}{J} \theta' + 2\zeta_{\psi} k_{\psi} \psi' + k_{\psi}^2 \psi &= (\bar{C}_{m_{\theta}} \psi_g + \bar{C}_{m_q} \psi'_g - \bar{C}_{m_{\psi}} \theta_g - \bar{C}_{m_r} \theta'_g)\end{aligned}\quad (7)$$

where a viscous-type damping in the mount system has been assumed. The aerodynamic coefficients with bar superscripts denote the total moments about the elastic axes of the system due to aerodynamic forces and moments on the propeller and are defined as follows:

$$\begin{aligned}\bar{C}_{m_{\theta}} &= \kappa \left( C_{m_{\theta}} - \frac{l}{2R} C_{Z_{\theta}} \right) \\ \bar{C}_{m_{\psi}} &= \kappa \left( C_{m_{\psi}} - \frac{l}{2R} C_{Z_{\psi}} \right) \\ \bar{C}_{m_q} &= \kappa \left[ C_{m_q} - \frac{l}{R} \left( \frac{1}{2} C_{Z_q} + C_{m_{\theta}} - \frac{l}{2R} C_{Z_{\theta}} \right) \right] \\ \bar{C}_{m_r} &= \kappa \left[ C_{m_r} - \frac{l}{2R} C_{Z_r} - \frac{l}{R} \left( C_{m_{\psi}} - \frac{l}{2R} C_{Z_{\psi}} \right) \right]\end{aligned}\quad (8)$$

The terms  $\theta_g$  and  $\psi_g$  in equation (7) represent the resultant air-stream angles at the propeller associated with the combined effects of angular deflections of the system plus gust velocities.

$$\begin{aligned}\theta_g &= \theta - \bar{w} \\ \psi_g &= \psi + \bar{v}\end{aligned}\quad (9)$$

Assume a simple harmonic variation in the  $\bar{w}$  gust component and zero disturbance in the  $\bar{v}$  component. The forcing function and the resulting response then become

$$\begin{aligned}\bar{w} &= \bar{w}_0 e^{ik\tau} \\ \bar{v} &= 0 \\ \theta &= \theta_0 e^{ik\tau} \\ \psi &= \psi_0 e^{ik\tau}\end{aligned}\quad (10)$$

where  $k = \frac{\omega R}{U}$  is the nondimensional driving frequency and  $\tau = \frac{Ut}{R}$  is the nondimensional time variable.

Equations (9) and (10) substituted into equation (7) lead to the following pair of simultaneous equations for  $\theta_0$  and  $\psi_0$ :

$$\begin{aligned}(A + iB)\theta_0 + (C + iD)\psi_0 &= (E + iF)\bar{w}_0 \\ -(C + iD)\theta_0 + (A + iB)\psi_0 &= (-C + iK)\bar{w}_0\end{aligned}\quad (11)$$

where with the assumption of structural symmetry  $k_\theta = k_\psi$  and  $I_\theta = I_\psi = I$ , the coefficients in equation (11) are

- 22 -

$$A = k_{\theta}^2 - k^2 - \bar{C}_{m\theta}$$

$$B = (2\zeta k_{\theta} - \bar{C}_{m_q})k$$

$$C = -\bar{C}_{m_{\dot{\psi}}}$$

$$D = \frac{H}{J} - \bar{C}_{m_r}$$

$$E = -\bar{C}_{m\phi}$$

$$F = -\bar{C}_{m_q}k$$

$$K = \bar{C}_{m_r}k \quad (12)$$

The frequency-response functions for  $\theta$  and  $\psi$  are by definition

$$H_{\theta\bar{w}} = \frac{\theta_0}{\bar{w}_0}$$

$$H_{\psi\bar{w}} = \frac{\psi_0}{\bar{w}_0} \quad (13)$$

But since the system under consideration is symmetrical in pitch and yaw the second of equations (13) can be written

$$H_{\psi\bar{w}} = H_{\theta\bar{v}} \quad (14)$$

Thus, from a simultaneous solution of equations (11) for  $\frac{\theta_0}{\bar{w}_0}$  and  $\frac{\psi_0}{\bar{w}_0}$  the frequency-response functions may be expressed in the form of the following complex ratios:

$$\begin{aligned} H_{\theta\bar{w}} &= \frac{A_1 + iB_1}{\Delta_R + i\Delta_I} \\ H_{\theta\bar{v}} &= \frac{A_2 + iB_2}{\Delta_R + i\Delta_I} \end{aligned} \quad (15)$$

or

$$\begin{aligned} H_{\theta\bar{w}}^2 &= \frac{A_1^2 + B_1^2}{\Delta_R^2 + \Delta_I^2} \\ H_{\theta\bar{v}}^2 &= \frac{A_2^2 + B_2^2}{\Delta_R^2 + \Delta_I^2} \end{aligned} \quad (16)$$

where

$$\begin{aligned} A_1 &= AE + C^2 - BF + DK \\ B_1 &= BE + CD + AF - CK \\ A_2 &= CE - AC - BK - DF \\ B_2 &= DE - BC + AK + CF \\ \Delta_R &= A^2 + C^2 - B^2 - D^2 \\ \Delta_I &= 2AB + 2CD \end{aligned}$$

With these frequency-response functions and an assumed form of the spectrum of turbulence (see ref. 8, for example) the spectrum of resulting response of the system can be calculated by means of equation (6).

#### REFERENCES

1. Taylor, E. S., and Browne, K. A.: Vibration Isolation of Aircraft Power Plants. Jour. Aero. Sci., vol. 6, no. 2, Dec. 1938, pp. 43-49.
2. Reed, Wilmer H., III, and Bland, Samuel R.: An Analytical Treatment of Aircraft Propeller Precession Instability. NASA TN D-659, 1961.
3. Houbolt, John C., and Reed, Wilmer H., III: Propeller-Nacelle Whirl Flutter. Jour. Aerospace Sci., vol. 29, no. 3, 1962, pp. 333-346.
4. Sewall, John L.: An Analytical Trend Study of Propeller Whirl Instability. NASA TN D-996, 1962.
5. Bland, Samuel R., and Bennett, Robert M.: Wind-Tunnel Measurement of Propeller Whirl-Flutter Speeds and Static-Stability Derivatives and Comparison With Theory. NASA TN D-1807, 1963.
6. Ribner, Herbert S.: Propellers in Yaw. NACA Rep. 820, 1945.
7. Yaggy, Paul F., and Rogallo, Vernon L.: A Wind-Tunnel Investigation of Three Propellers Through an Angle-of-Attack Range From  $0^\circ$  to  $85^\circ$ . NASA TN D-318, 1960.
8. Houbolt, John C., Steiner, Roy, and Pratt, Kermit G.: Flight Data Considerations of the Dynamic Response of Airplanes to Atmospheric Turbulence. Presented to the Structures and Materials Panel and to the Flight Mechanics Panel, AGARD, Paris, France, July 3-13, 1962.

TABLE I.- SUMMARY OF SYSTEM CHARACTERISTICS.

	System		
	1	2	3
$\frac{I_x}{I_y}$	0.135	0.135	0.583
$\frac{b}{R} 0.72R$	.216	.196	.160
$\frac{l}{R}$	.346	.350	.250
$\kappa$	.0466	.0504	1.76
B	4	3	4
J	2.66	varies	1.1
$8\theta/8\psi$	1.0	1.0	1.0

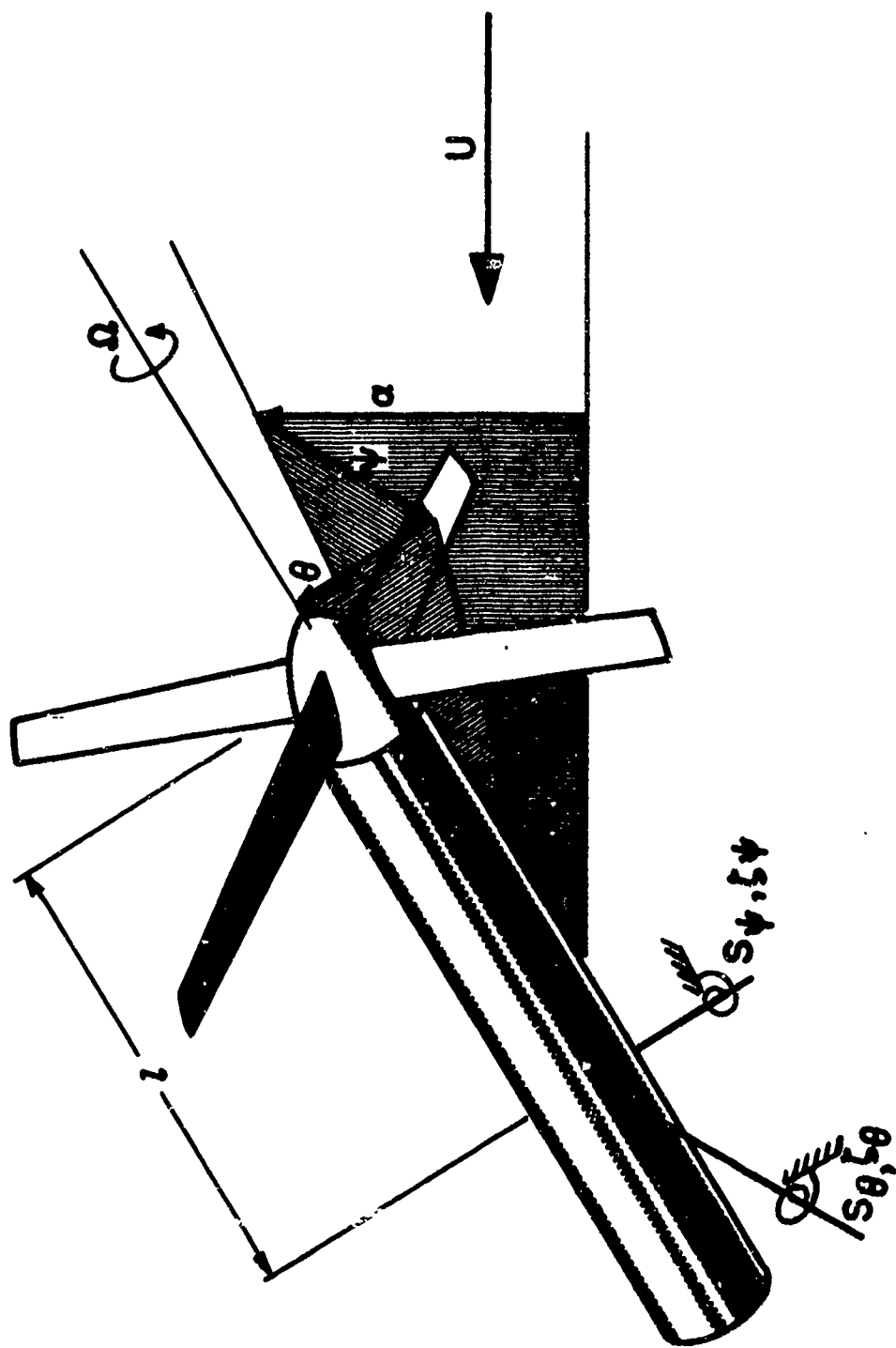
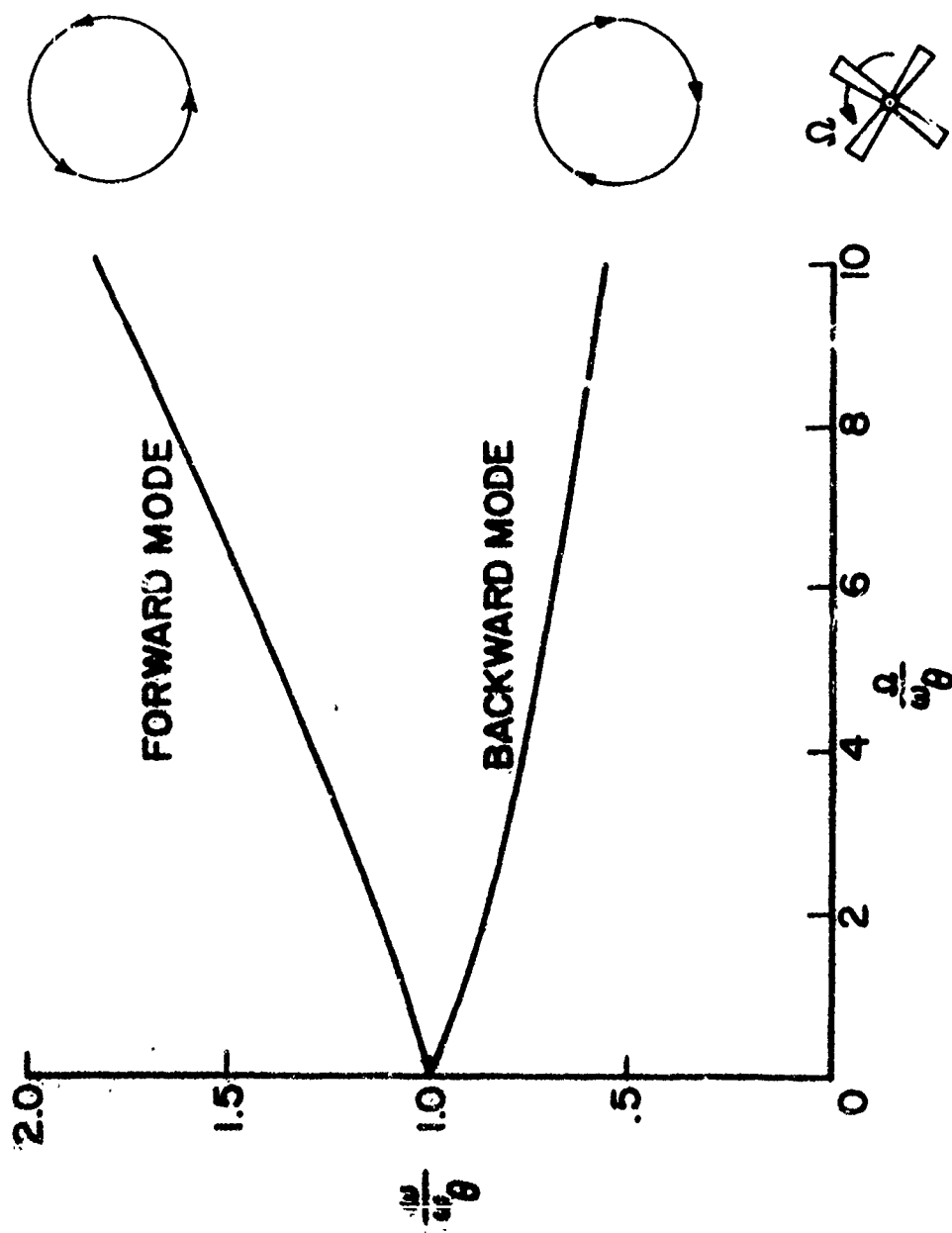


Figure 1.- System considered.

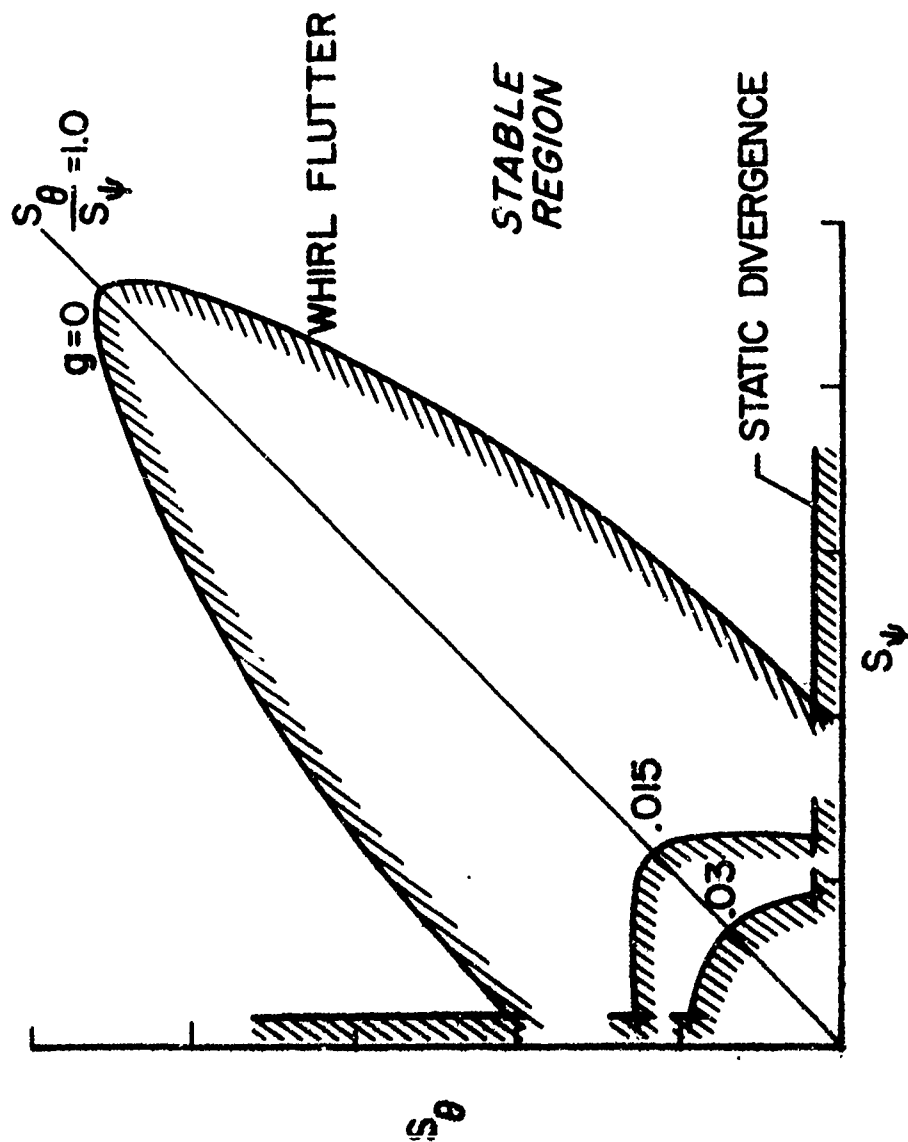
115



NASA

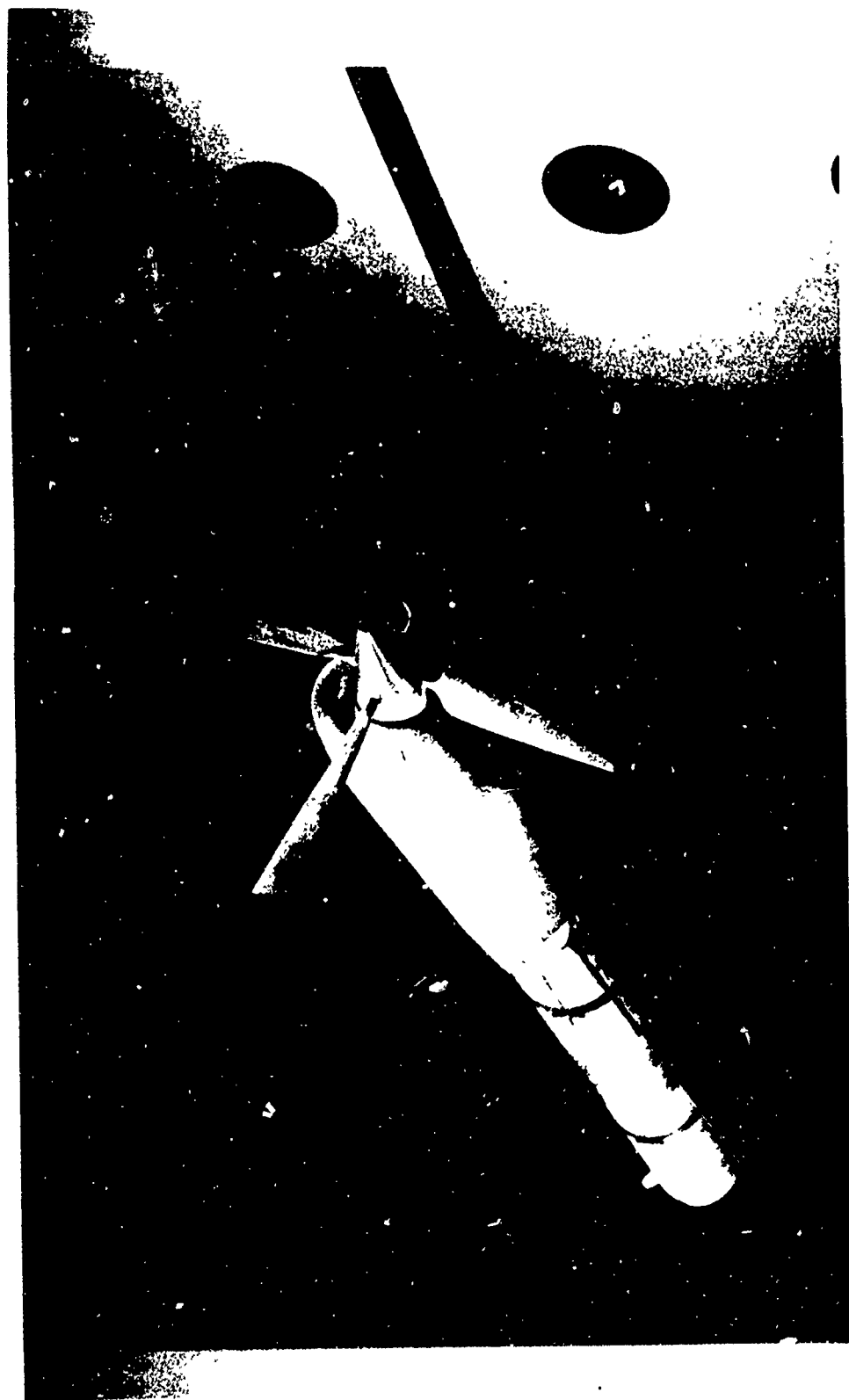
Figure 2.- Natural precession frequencies ( $\omega_\theta = \omega_p$ ).



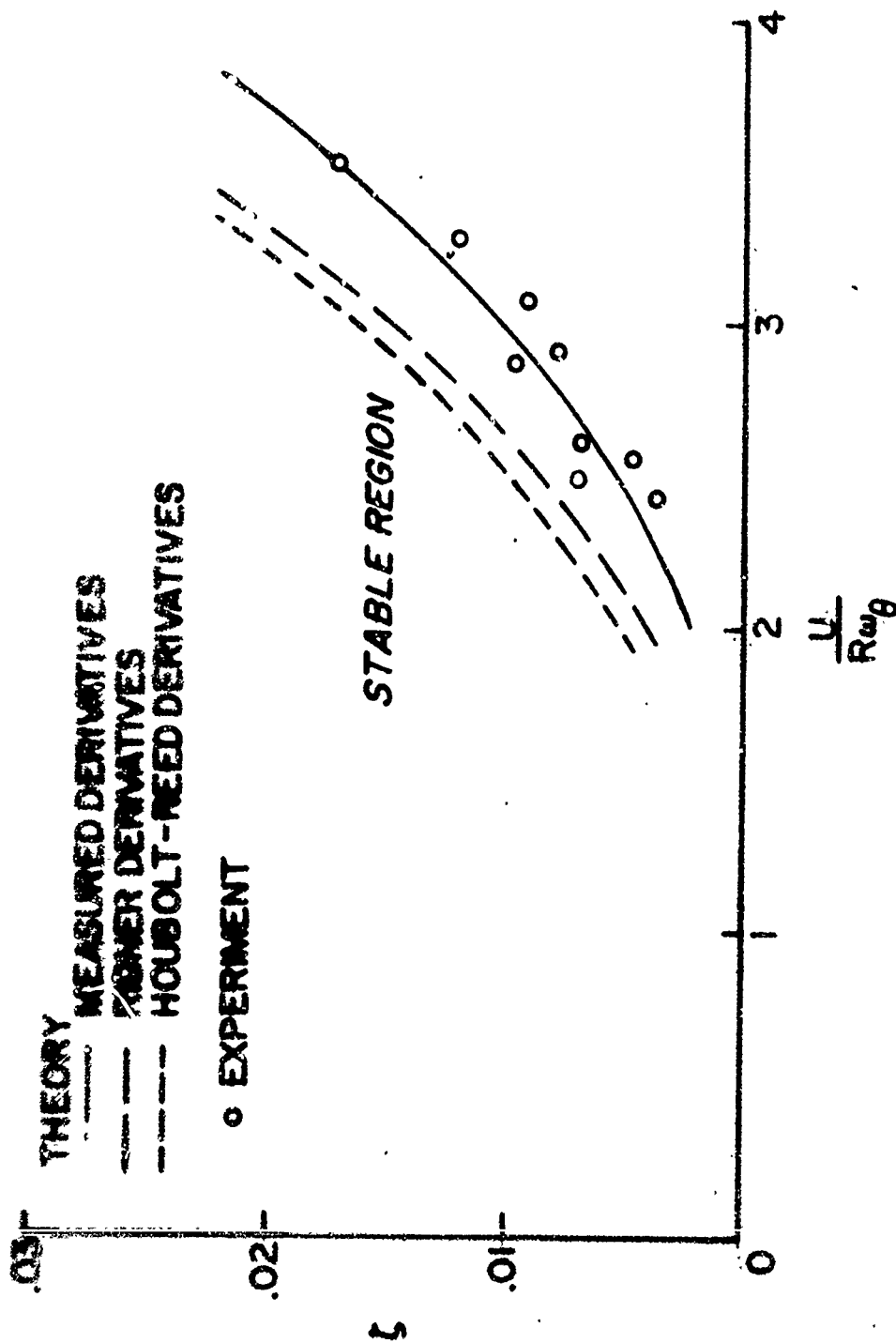


NASA

Figure 3.- Pitch and yaw stiffness required.

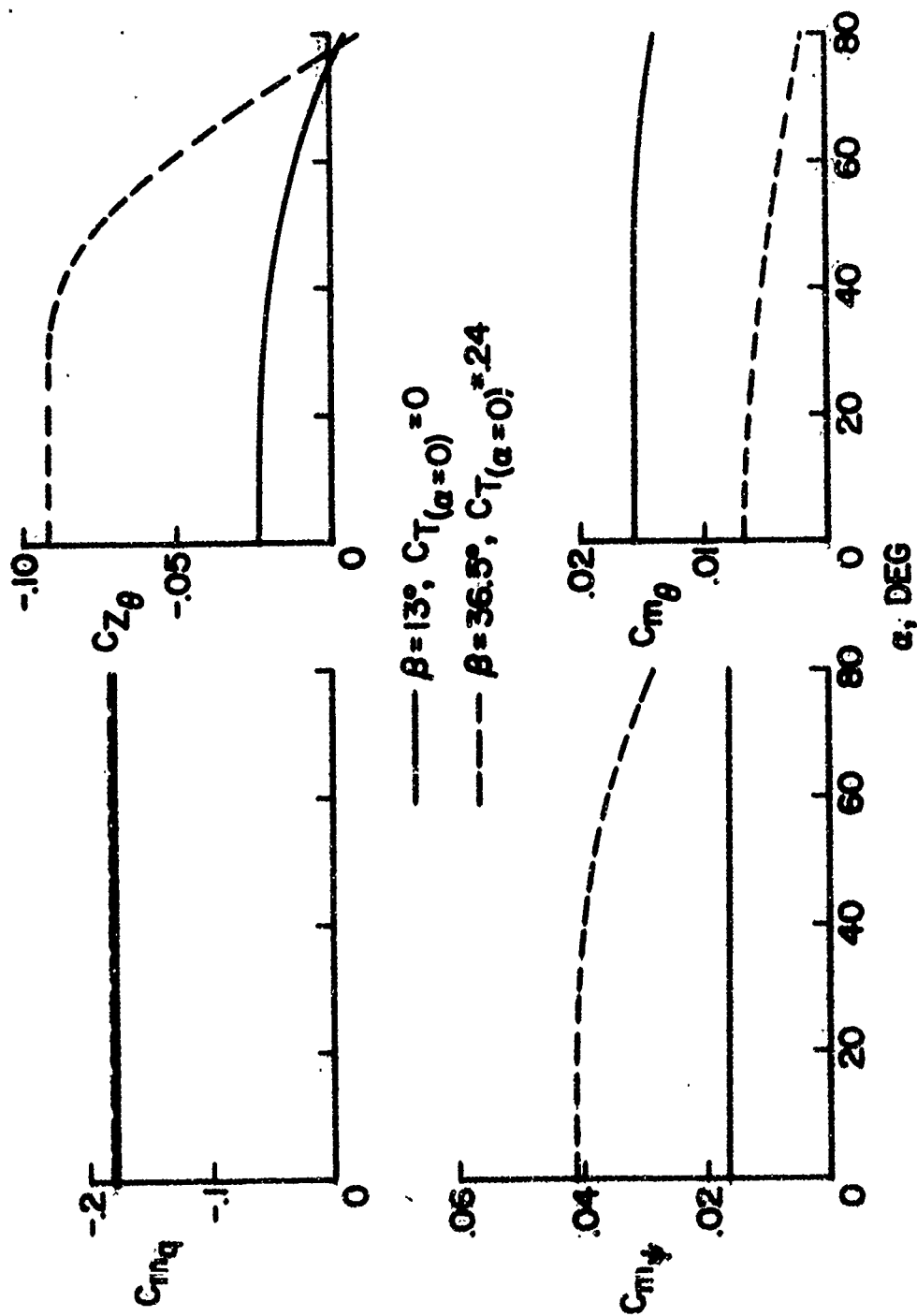


NAS:  
L-61-  
Figure 4.- Model used for measuring stability boundaries and aerodynamic derivatives (system 1).



NASA

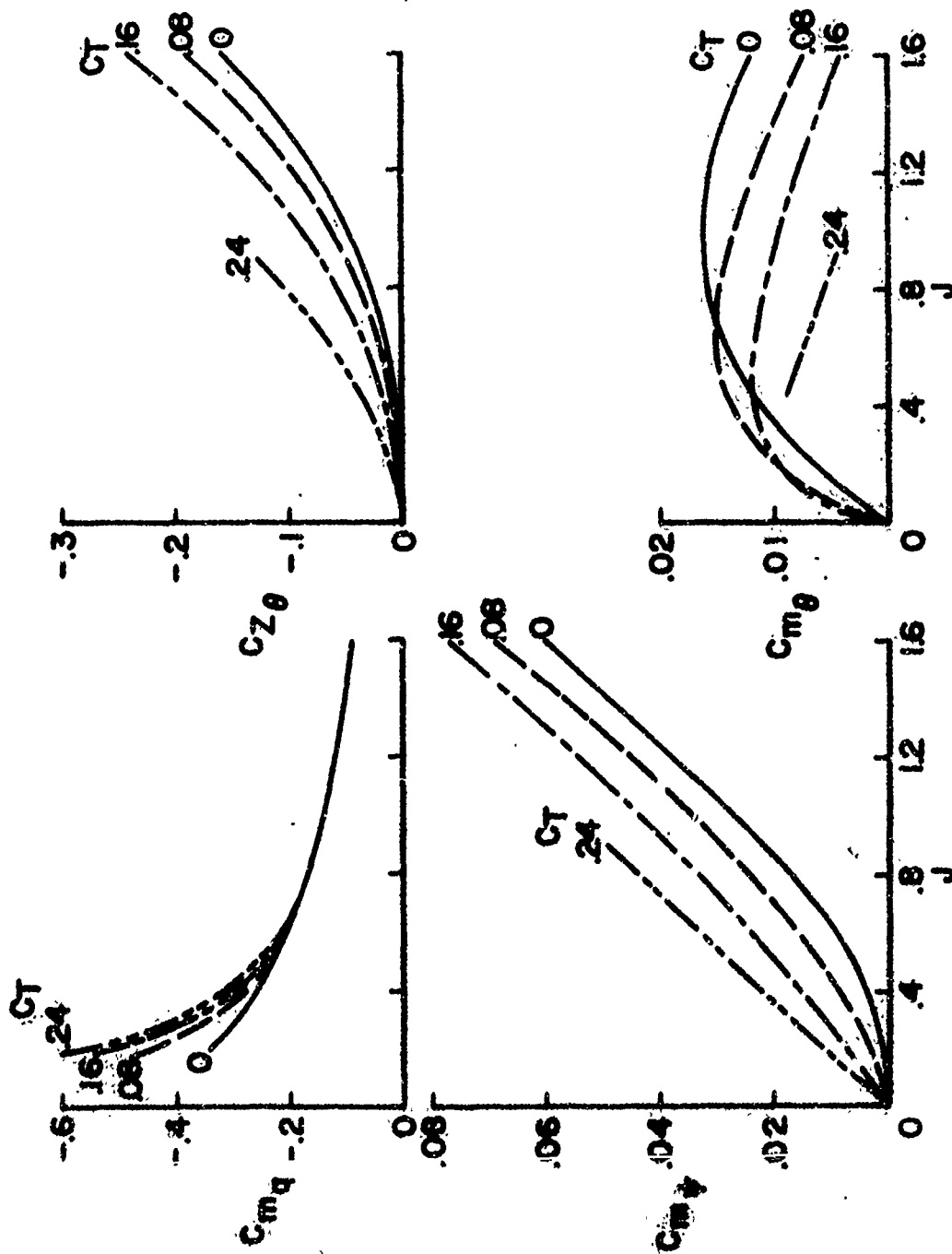
Figure 5.- Comparison of theoretical and experimental whirl flutter boundaries (system 1,  $J = 2.66$ ).



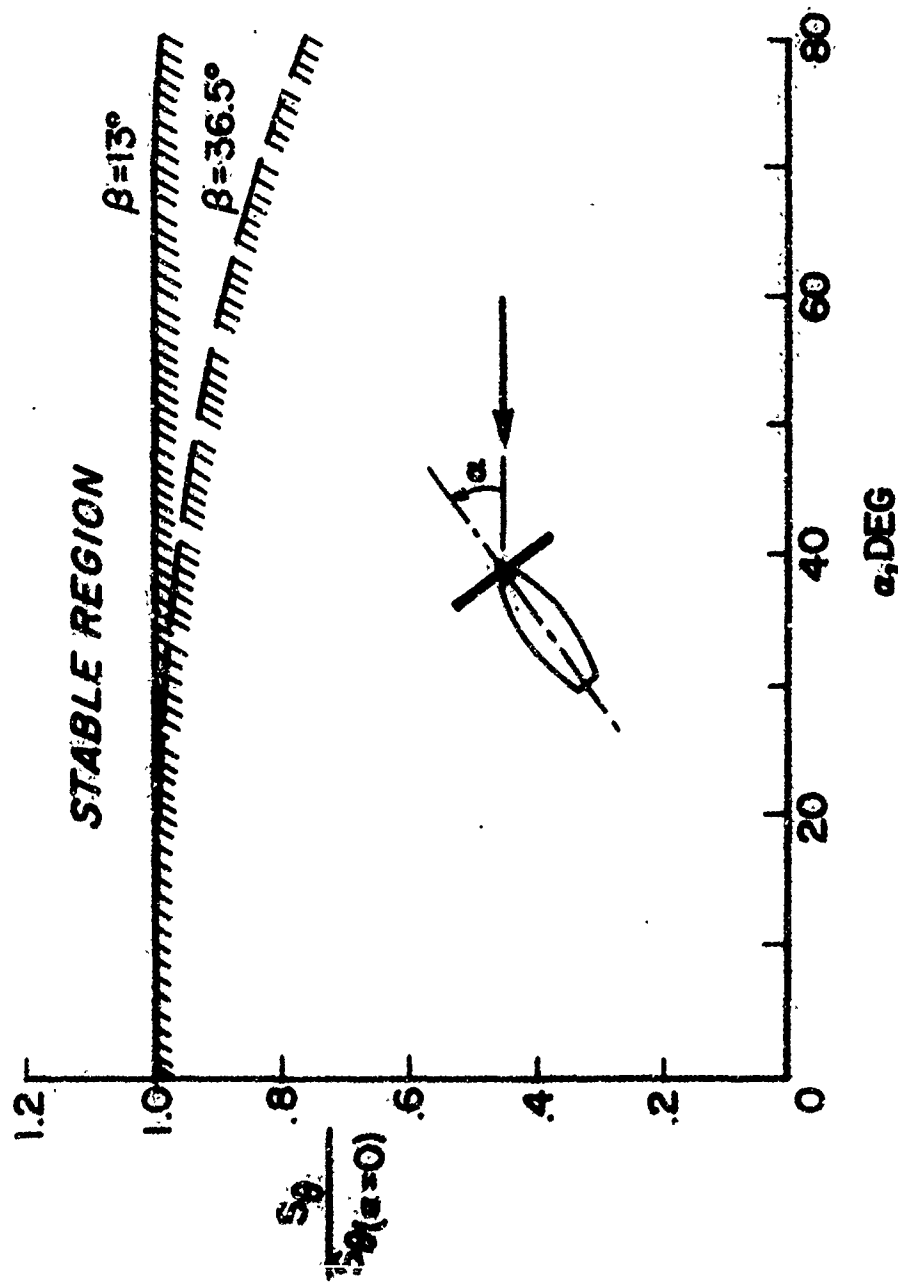
(a) Effect of angle of attack,  $J = 0.75$ .

NASA

Figure 6.- Propeller aerodynamic derivatives used in analysis of transition maneuvers for system 2.

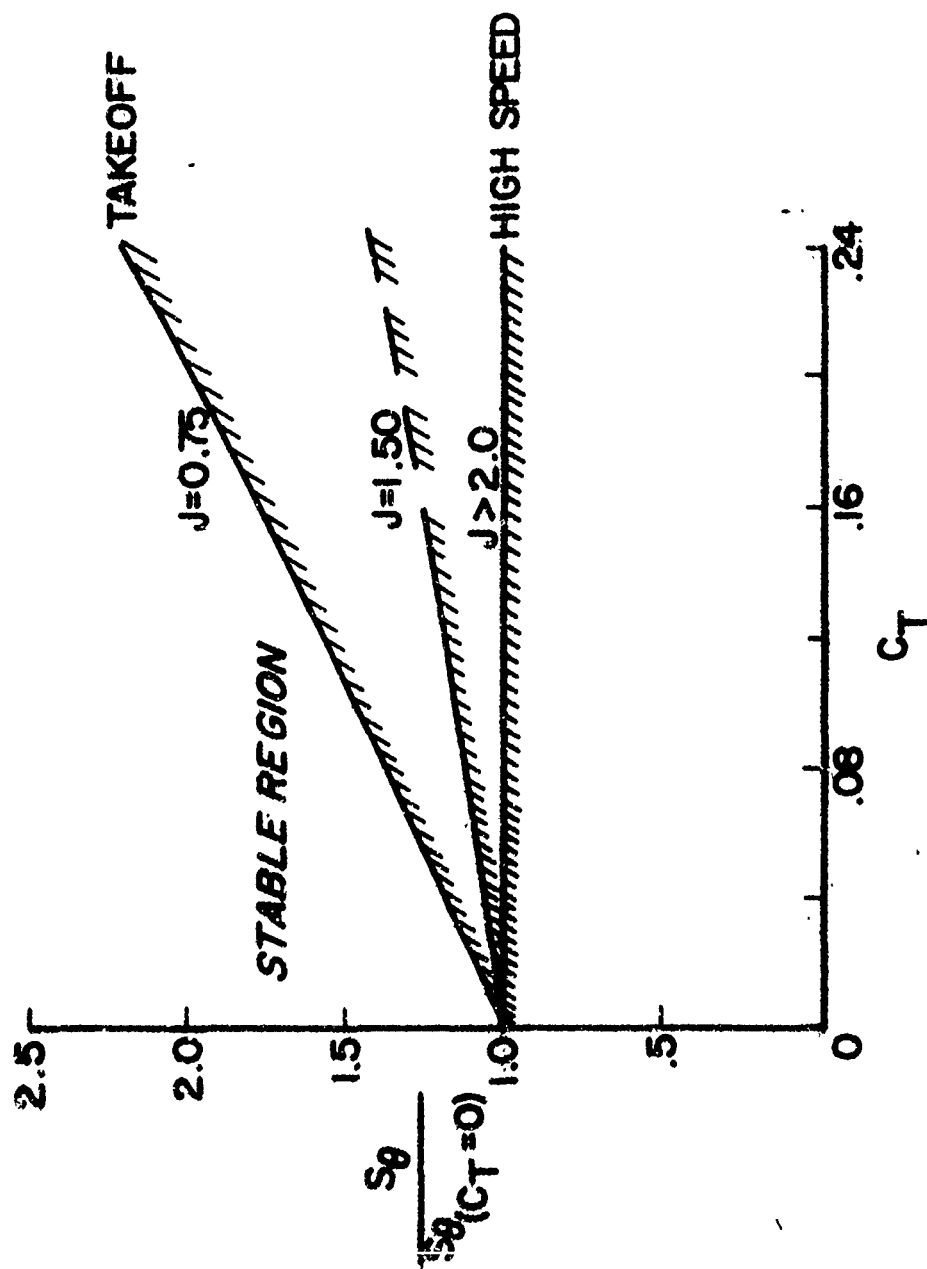


(b) Effect of thrust coefficient for angles of attack less than  $30^\circ$ .



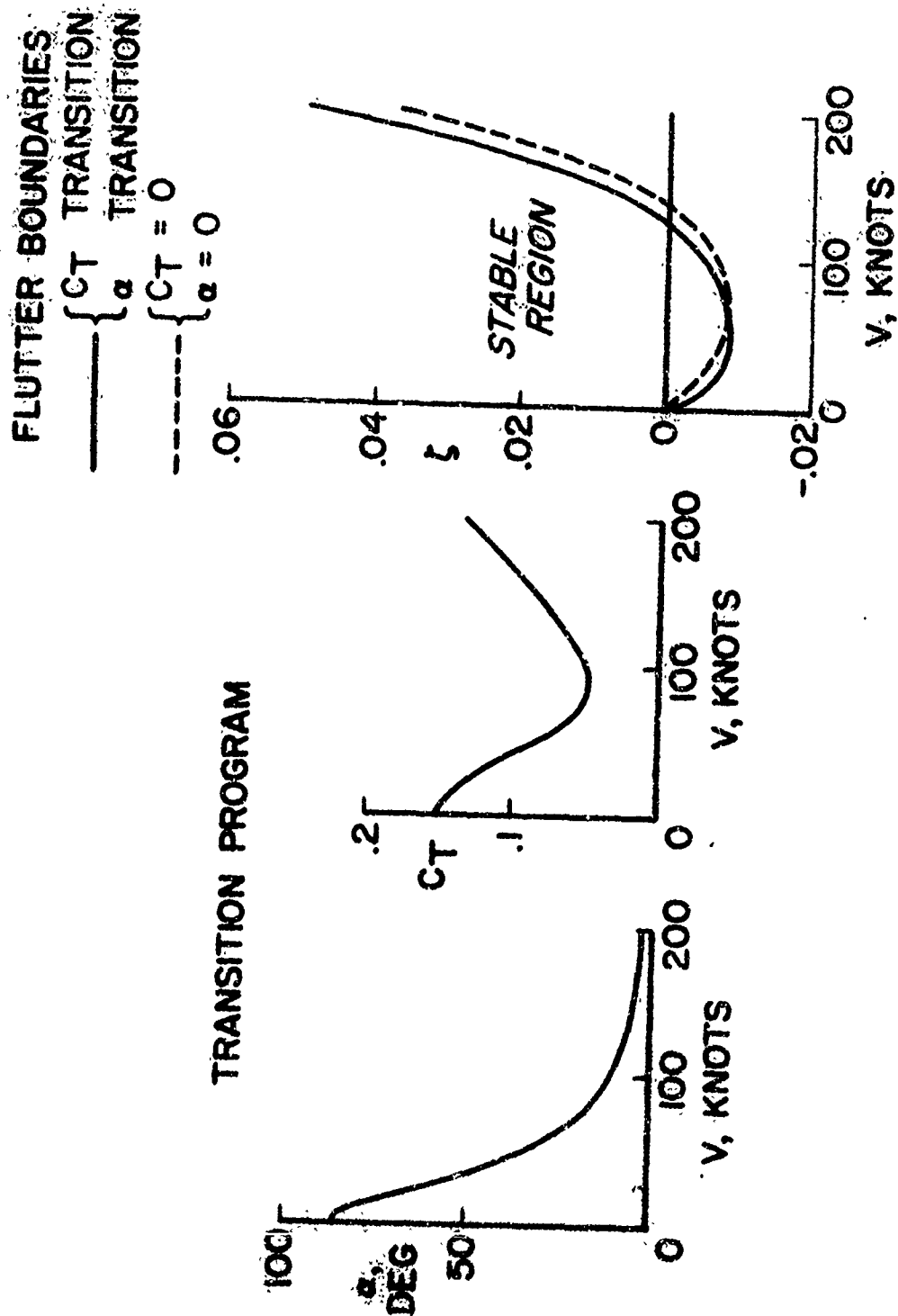
NASA

Figure 7.- Effect of angle of attack at constant blade angle (system 2,  $J = 0.75$ ,  $\xi = 0.05$ ).



NASA

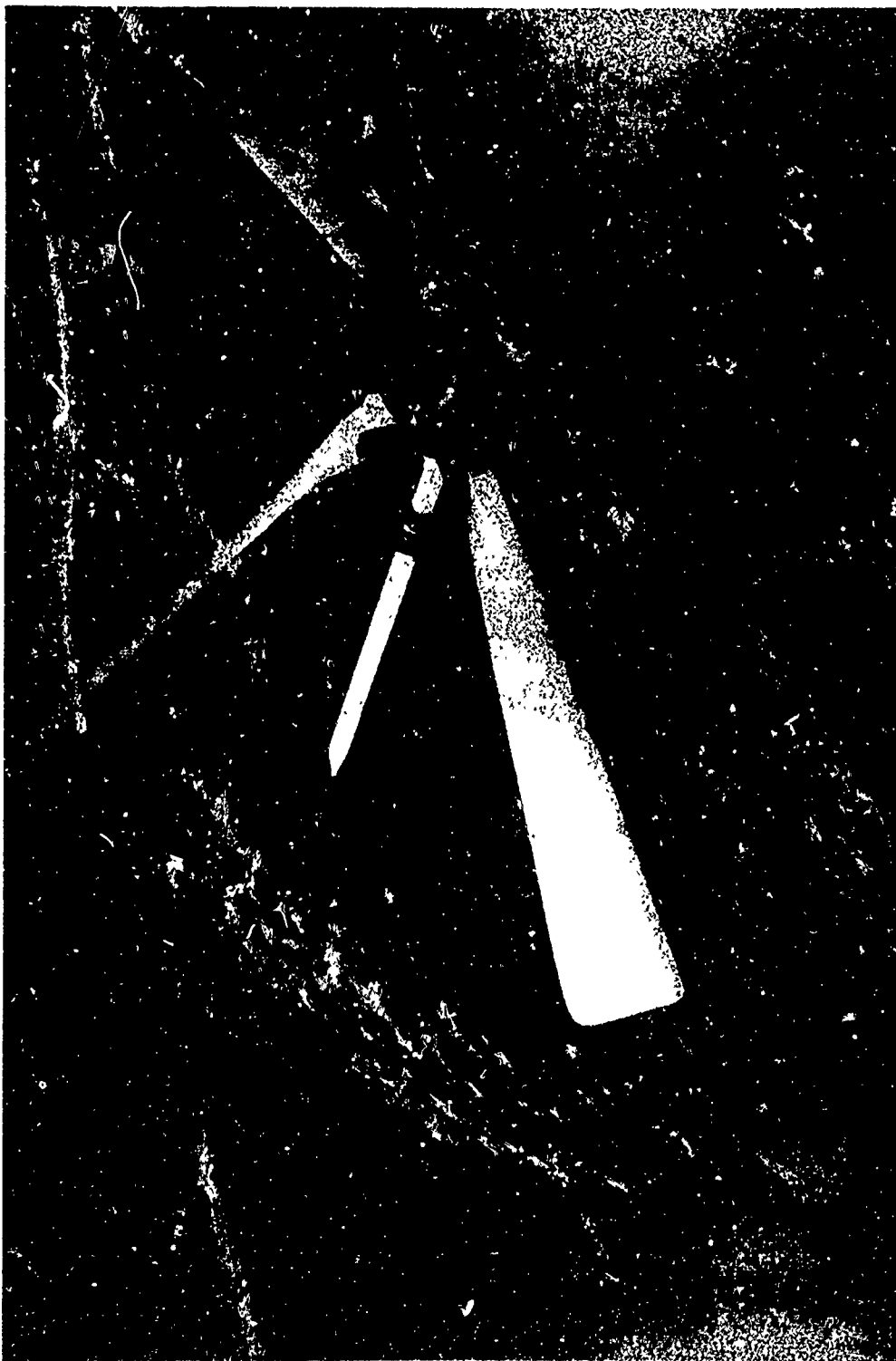
Figure 8.- Effect of thrust coefficient (system 2,  $\xi = 0.05$ ,  $\alpha = 0$ ).



NASA

Figure 9.-- Effect of transition program (system 2,  $0 \leq J \leq 1.5$ ).





NASA  
L-63-247

Figure 10.- Flapping blade propeller whirl model (system 3).

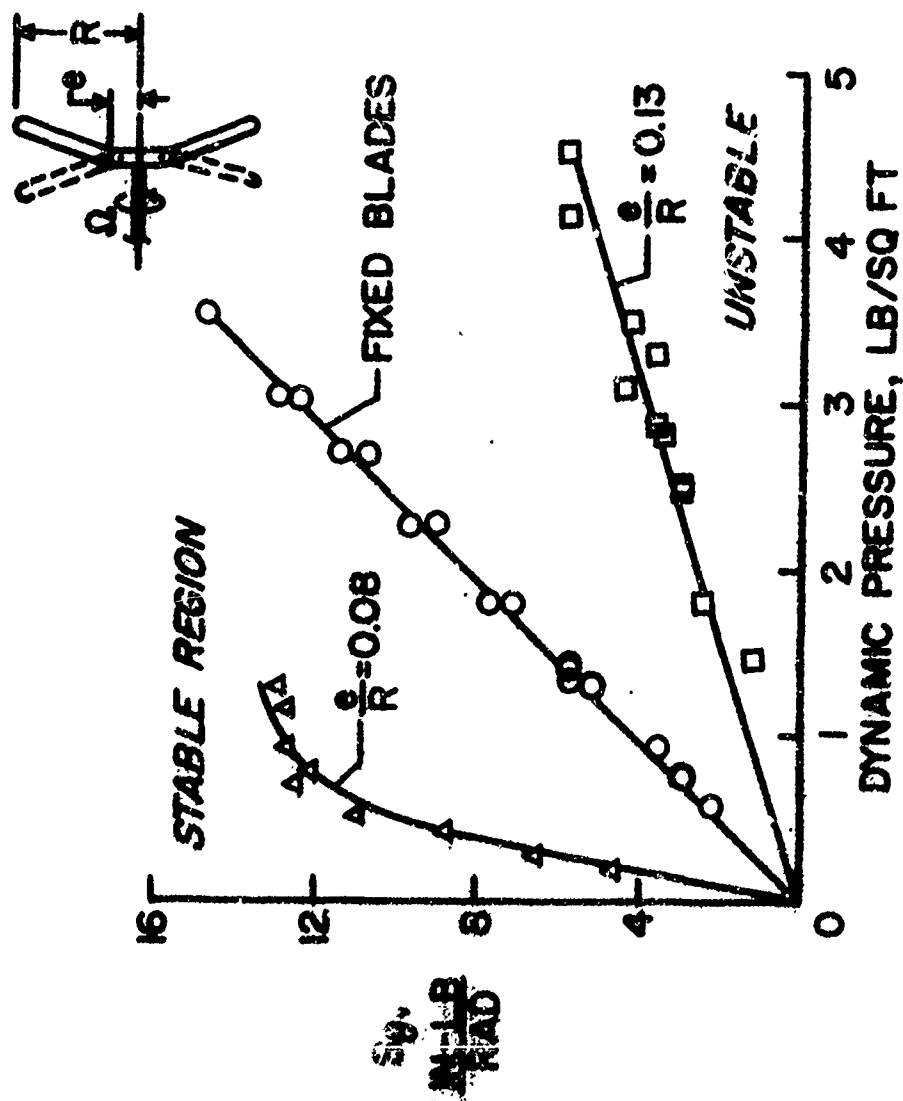
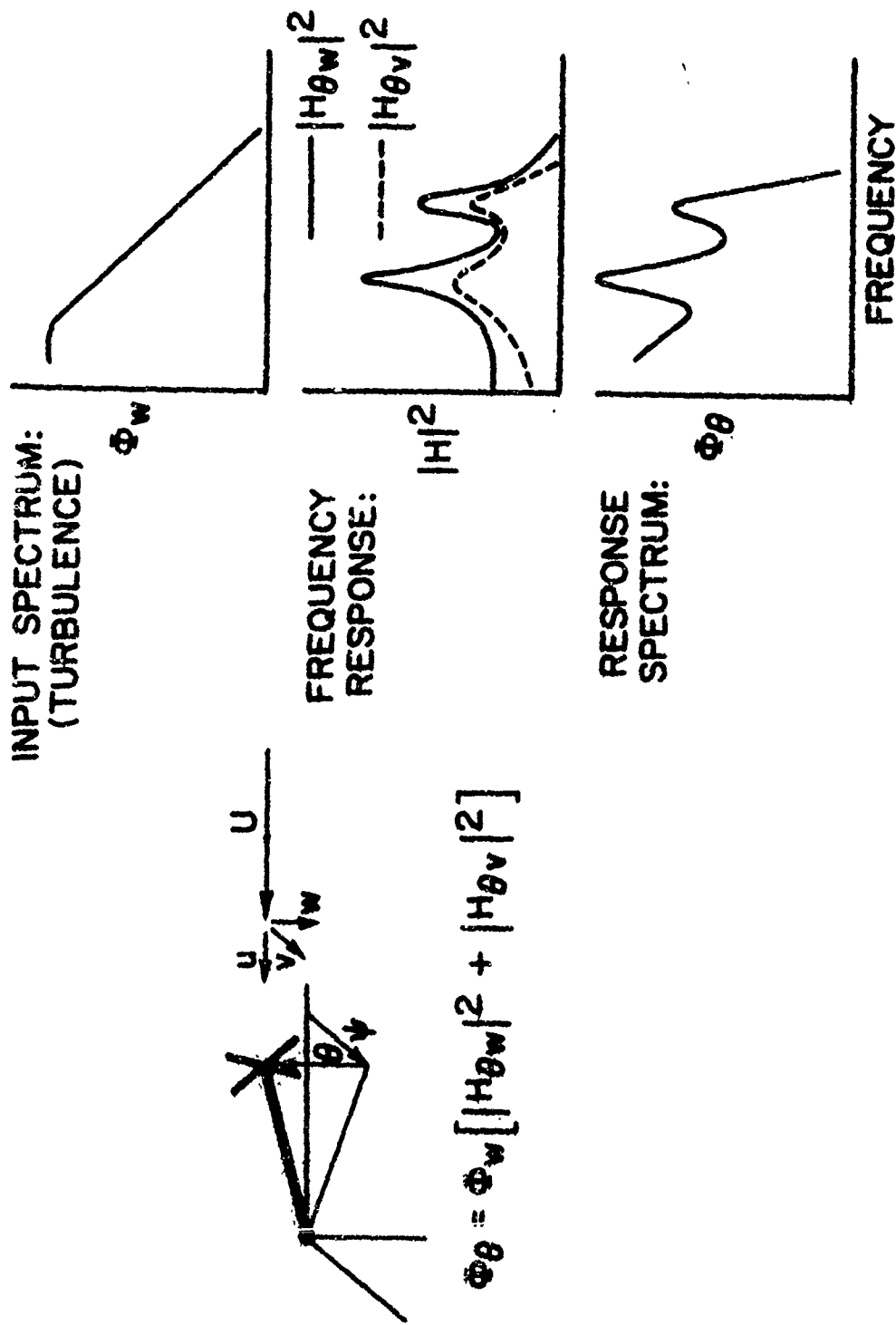


Figure 11.- Effect of flapping hinges (system 3).



NASA

Figure 12.- Response of propeller system to random turbulence.

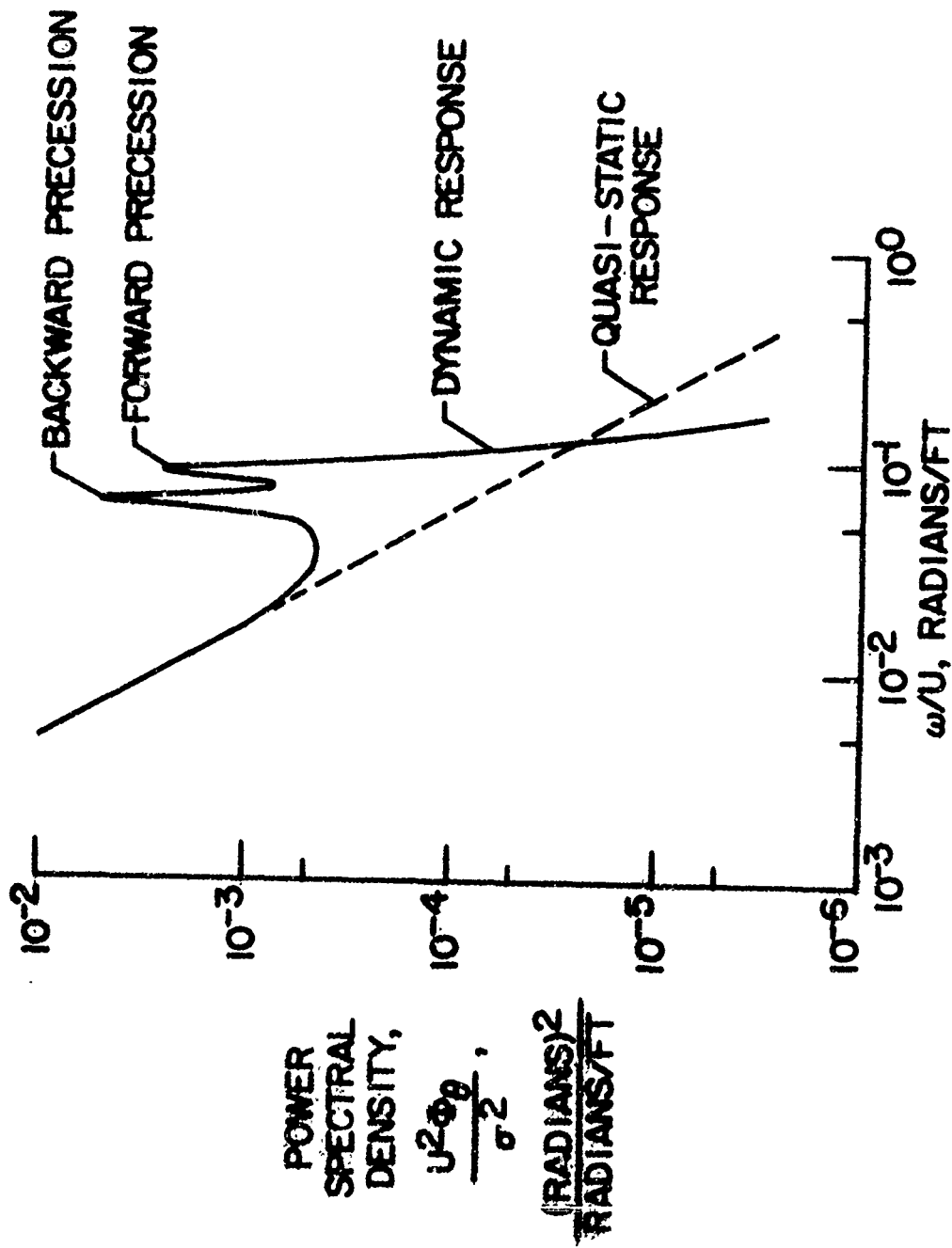


Figure 13.- Pitch angle response to atmospheric turbulence (system 1,  $\zeta = 0.05$ ,  $\frac{U}{R_{\text{eq}}} = 2.0$ ,  $J = 2.66$ ).

**HIGH-SPEED SHAFTING  
FOR POWER TRANSMISSION IN AIRCRAFT**

**J.E. Voorhees, R.G. Dubensky, and J.B. Day**

**Battelle Memorial Institute**

HIGH-SPEED SHAFTING FOR POWER  
TRANSMISSION IN AIRCRAFT

by

J. E. Voorhees,\* R. G. Dubensky,\*\* and J. B. Day\*\*\*

ABSTRACT

In connection with the need for light weight components in military helicopters and STOL and VTOL aircraft, a research program is being conducted by Battelle to determine the merits of hypercritical-speed power transmission shafts. This research has been Sponsored by the Army Transportation Research Command and the Air Force Aeronautical Systems Division.

An analytical study and a model development program have been the basis for determining effectiveness of operating parameters, including the spring constant of flexibly mounted shaft support bearings, the support damping coefficient, support mass, and the location of the supports. A digital computer program was developed to calculate shaft deflections and critical speeds. An analogy to high-frequency electrical transmission lines was developed to aid in the design and placement of shaft dampers.

Recent experimental work has been concentrated upon verifying the dynamic design procedure which was established analytically. Successful shaft operation has been obtained at speeds above the 18th critical speed using commercial quality shafting with two dampers.

\* John E. Voorhees, Group Director, Machine Dynamics Research Group

\*\* R. G. Dubensky, Research Engineer, Machine Dynamics Research Group

\*\*\* J. B. Day, Research Engineer, Machine Dynamics Research Group

Battelle Memorial Institute, Columbus, Ohio

# HIGH-SPEED SHAFTING FOR POWER TRANSMISSION IN AIRCRAFT

by

J. E. Voorhees, R. G. Dubensky, and J. B. Day

## INTRODUCTION

The work on which this paper is based is concerned with damping the lateral vibrations of power transmission shafts running at their critical speeds.

Critical speeds of shafts are those discrete speeds at which centrifugal forces resulting from unbalance overcome the elastic restoring forces in the shaft, causing progressively greater deflections. Operation of a conventionally supported shaft at one of its critical speeds can permanently deform or destroy the shaft and its bearings.

Designers usually plan to operate shafts below their first critical speed to avoid serious problems. This practice carries with it certain penalties:

- (1) Shaft speed may be kept low, requiring high torque and a large shaft to transmit a given horsepower.
- (2) For long shafts, the diameter may be made larger than required for torque loading, merely to raise the first critical speed above the operating speed range.
- (3) In the case of shafts sized for the torque loading, closely spaced bearings may be used to raise the first critical speed of any section of the shaft above the operating speed range. Additional flexible couplings are frequently required when bearings are added.

All of these practices increase the shaft weight. This can be a serious penalty for aircraft applications.

The weight savings which were expected with hypercritical-speed shafting led the Army Transportation Research Command and the Air Force Aeronautical Systems Division to contract with Battelle Memorial Institute for a feasibility study of such shafting. [See reference 1.] The ultimate objective of this study is a manual for the design of hypercritical-speed power transmission shafts for use in helicopters and vertical-takeoff aircraft.

#### RESEARCH PROGRAM

##### Shaft Size vs Critical Speed Relationships

Figure 1 shows the range of shaft sizes and speeds of potential interest in this program. The unshaded area of the figure encloses the sizes and speeds that can be handled experimentally in the present shaft testing machine. These values range from 0.06-inch to 0.5-inch diameter, and up to 50,000 rpm.

The horsepower lines in this figure are drawn for the rather high torsional stress of 50,000 psi merely for example purposes. To take an example, note that a 7/16-inch diameter solid steel shaft could transmit 500 horsepower at 40,000 rpm. If such a shaft were simply supported, however, it could be only 7 inches long and would reach its first critical speed at 40,000 rpm. A 70-inch long, 7/16-inch diameter, solid steel shaft simply supported at its ends would reach its tenth critical speed at 40,000 rpm. The 70-inch shaft would require



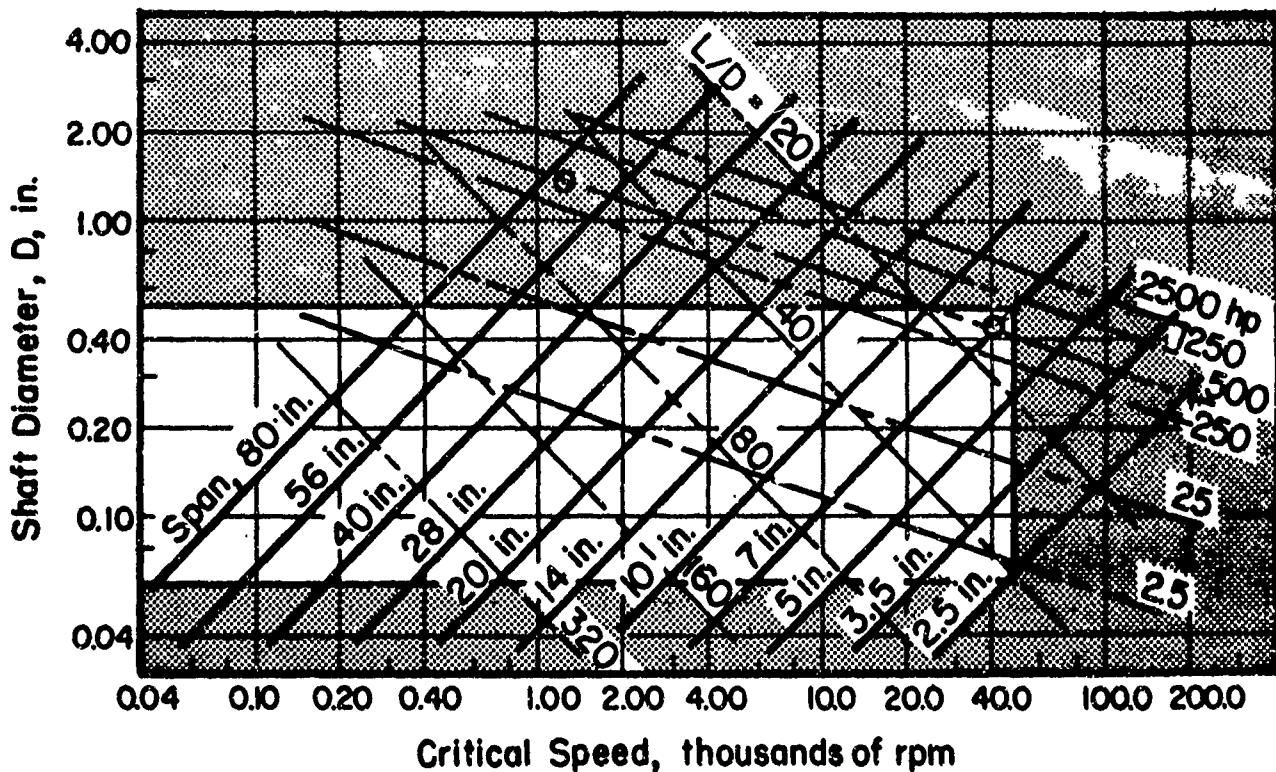


**FIGURE 1. RELATIONSHIPS BETWEEN SHAFT DIAMETER, CRITICAL SPEED, SUPPORT SPACING, AND HORSEPOWER FOR A SIMPLY SUPPORTED SOLID STEEL SHAFT WITH A TORSIONAL STRESS OF 50,000 PSI**

Operating envelope of Battelle high-speed shaft testing machine enclosed by solid line on figure.

nine bearings between its ends to raise its first critical speed to 40,000 rpm. On the other hand, if a 70-inch long, simply supported shaft were sought to transmit 500 horsepower at a speed just below its first critical, it would be approximately 1.4 inches in diameter and would operate under 1200 rpm. These examples serve to illustrate the problems facing a designer of subcritical speed power transmission shafts.

#### Approach to the Problem

Research work on this program was started with the belief that dampers strategically located at bearings along the shaft could extract enough energy of lateral vibration to permit continuous shaft operation at critical speeds. To prove this contention three approaches were followed:

- (1) Digital computer programs were written to compute shaft critical speeds and shaft vibration amplitudes with various bearing and damper assemblies installed.
- (2) A high-speed testing machine was designed and built for laboratory verification of shaft behavior.
- (3) An analogy was developed relating high speed shafts to electrical transmission lines to simplify damper design.

Figure 2 schematically illustrates the testing machine built for this work. The brake head assembly can be located where desired for various shaft lengths. The dampers, or intermediate support bearings, can also be located at any point along the length of a shaft. Guards consisting of very much oversize cast iron pillow blocks are installed along the shaft to protect operating personnel in the event that a shaft should vibrate wildly or even break.

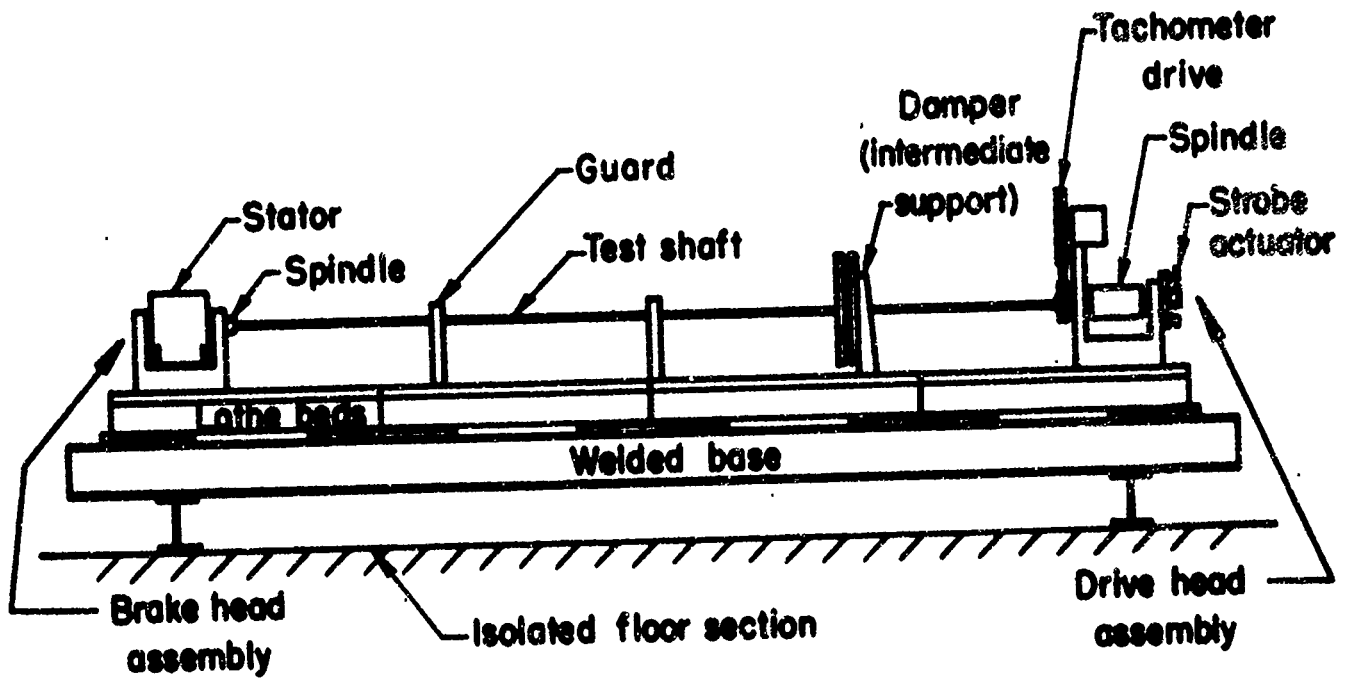


FIGURE 2. SCHEMATIC DIAGRAM OF TEST MACHINE BED AND EQUIPMENT

Figure 3 shows schematically an intermediate support bearing and damper assembly. The ball bearing is clamped to the shaft with a collet assembly. The bearing is also installed in a lightweight housing attached to a thin steel flexure plate which is sandwiched closely between fixed outer plates. The clearance between the flexure plate and fixed plates is adjustable, and is flooded with oil to provide viscous damping of lateral motion of the shaft and bearing assembly. Springs attached to the outer edges of the flexure plate restrain its motion somewhat, and are another variable in the dynamic system.

The testing machine grips both ends of the test shaft in collets, providing essentially fixed end conditions. Figure 4 shows that the shaft critical speeds would have been lower for simply-supported shaft ends than for the fixed end conditions which were used. At the higher-order critical speeds, however, the end conditions have little effect on critical speed.

#### Results of Initial Experiments

Initial experiments were carried out with more-or-less a trial and error approach, in which damping and spring rate at the intermediate bearings, as well as bearing location, were varied widely. Figure 5 shows that as the location of one particular support bearing was varied, the satisfactory operating speed range of the shaft changed substantially. This shaft was solid steel, 1/4-inch in diameter, and 89.3 inches long. Satisfactory operation was here arbitrarily defined as a vibration level sufficiently small that the shaft did not strike the guards which restrained it. This was a peak-to-peak amplitude of 3/8 of an inch.

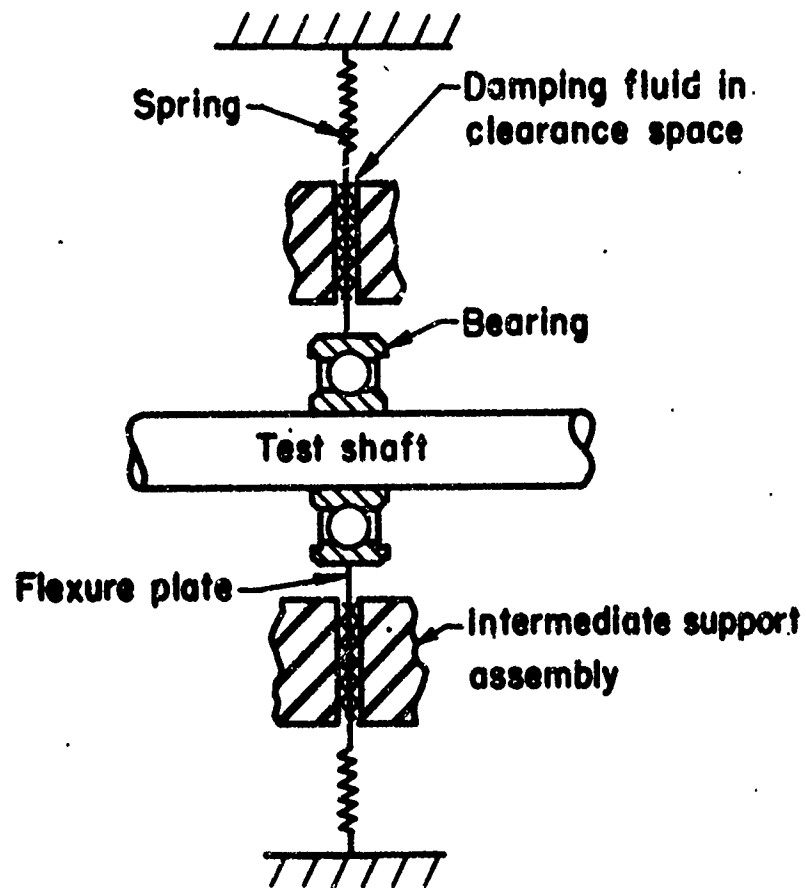


FIGURE 3. SCHEMATIC DIAGRAM OF INTERMEDIATE SUPPORT DAMPER

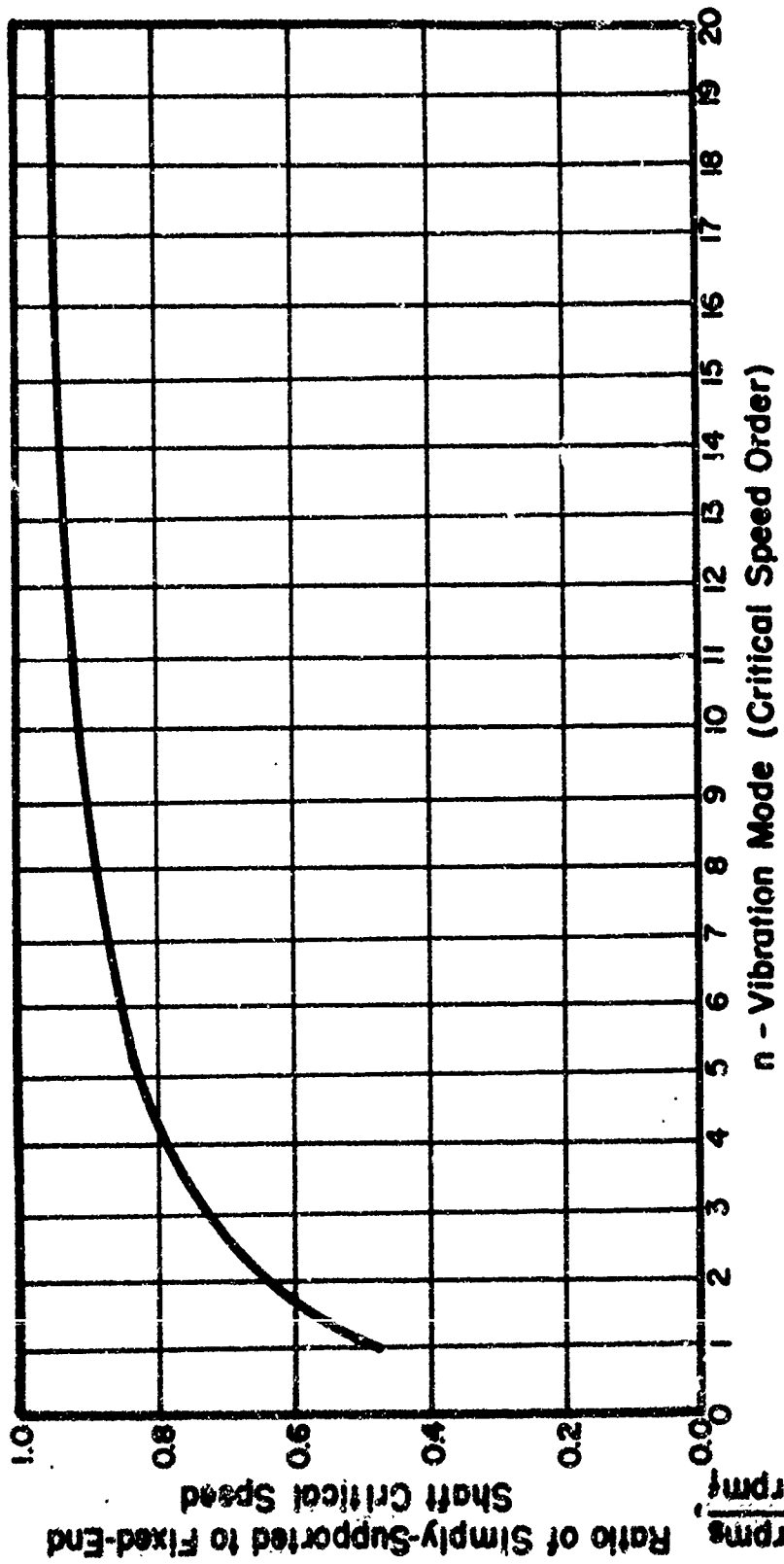


FIGURE 4. CRITICAL-SPEED COMPARISON BETWEEN SIMPLY SUPPORTED AND FIXED-END SHAFTS FOR VARIOUS VIBRATION MODES

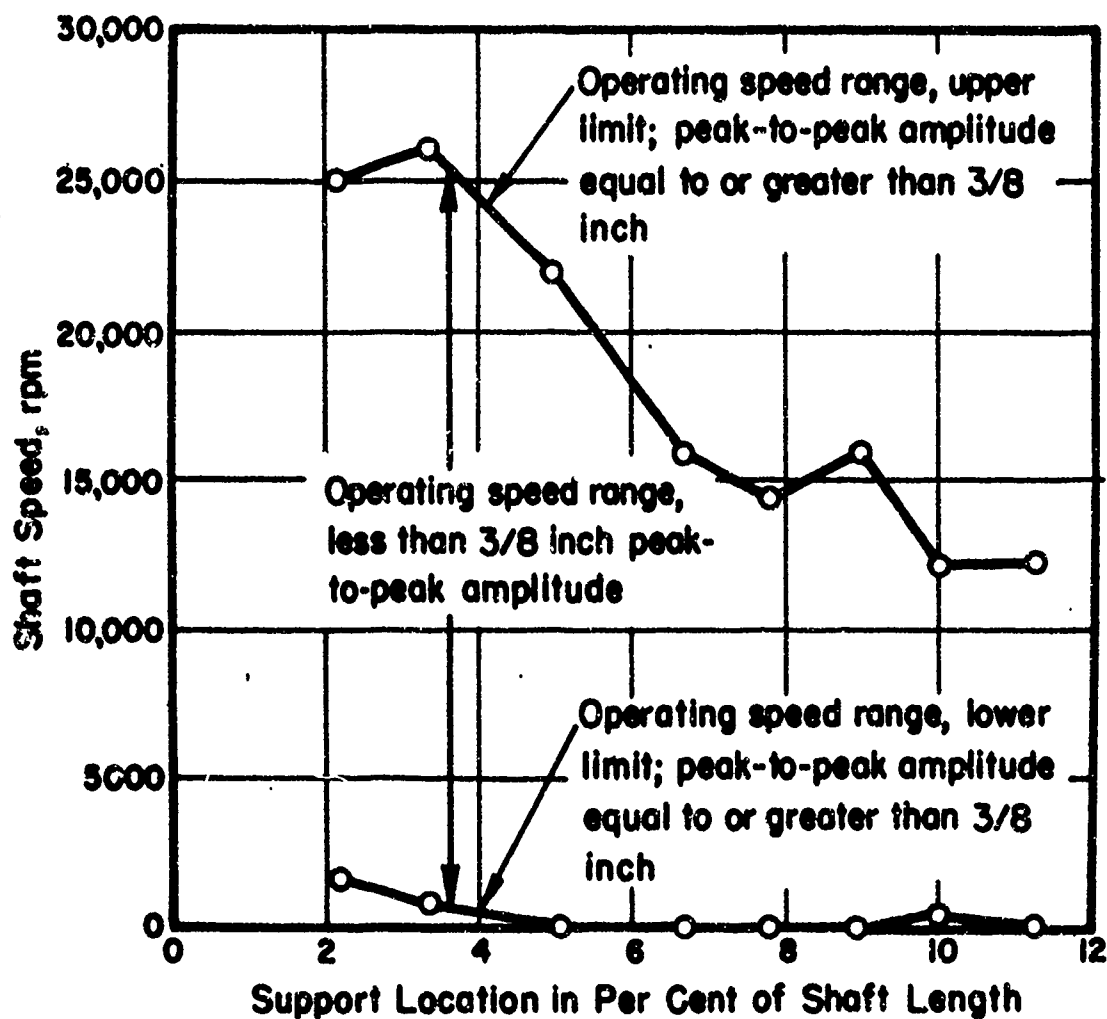


FIGURE 5. SHAFT SPEED VERSUS LOCATION OF A SINGLE DAMPED SUPPORT

$\frac{1}{4}$ -inch diameter, 89.3-inch long steel shaft with clamped ends.

Support Characteristics:  $K = 11.6$  lb/in;  
 $C = 1.73$  lb-sec/in.

Figure 6 shows the results of a series of tests with a similar shaft, but with two dampers installed. The location of one damper was fixed for the tests shown here, while the other damper was moved. Performance varied more widely here than in the single support tests. Figures 5 and 6 represent but a few of many experiments with various shafts and dampers.

Analogy Between High-Speed Shafts and Electrical  
Transmission Lines

Digital computer calculations agreed well with initial laboratory experiments, but little basic understanding of shaft behavior was obtained until a different analysis technique was developed. This technique utilizes an analogy between the mechanical shaft and a high-frequency electrical transmission line.

The differential equation of the bending vibrations of a beam, which also describes the behavior of a rotating shaft, is as follows:

$$EI \frac{\partial^4 y}{\partial x^4} + \frac{PA}{g} \frac{\partial^2 y}{\partial t^2} = 0, \quad (1)$$

or

$$EI \frac{\partial^2}{\partial x^2} \left( \frac{\partial^2 y}{\partial x^2} \right) + \frac{PA}{g} \frac{\partial^2 y}{\partial t^2} = 0, \quad (2)$$

where

A = cross-sectional area, in.<sup>2</sup>

E = modulus of elasticity, lb/in.<sup>2</sup>

I = section moment of inertia, in.<sup>4</sup>



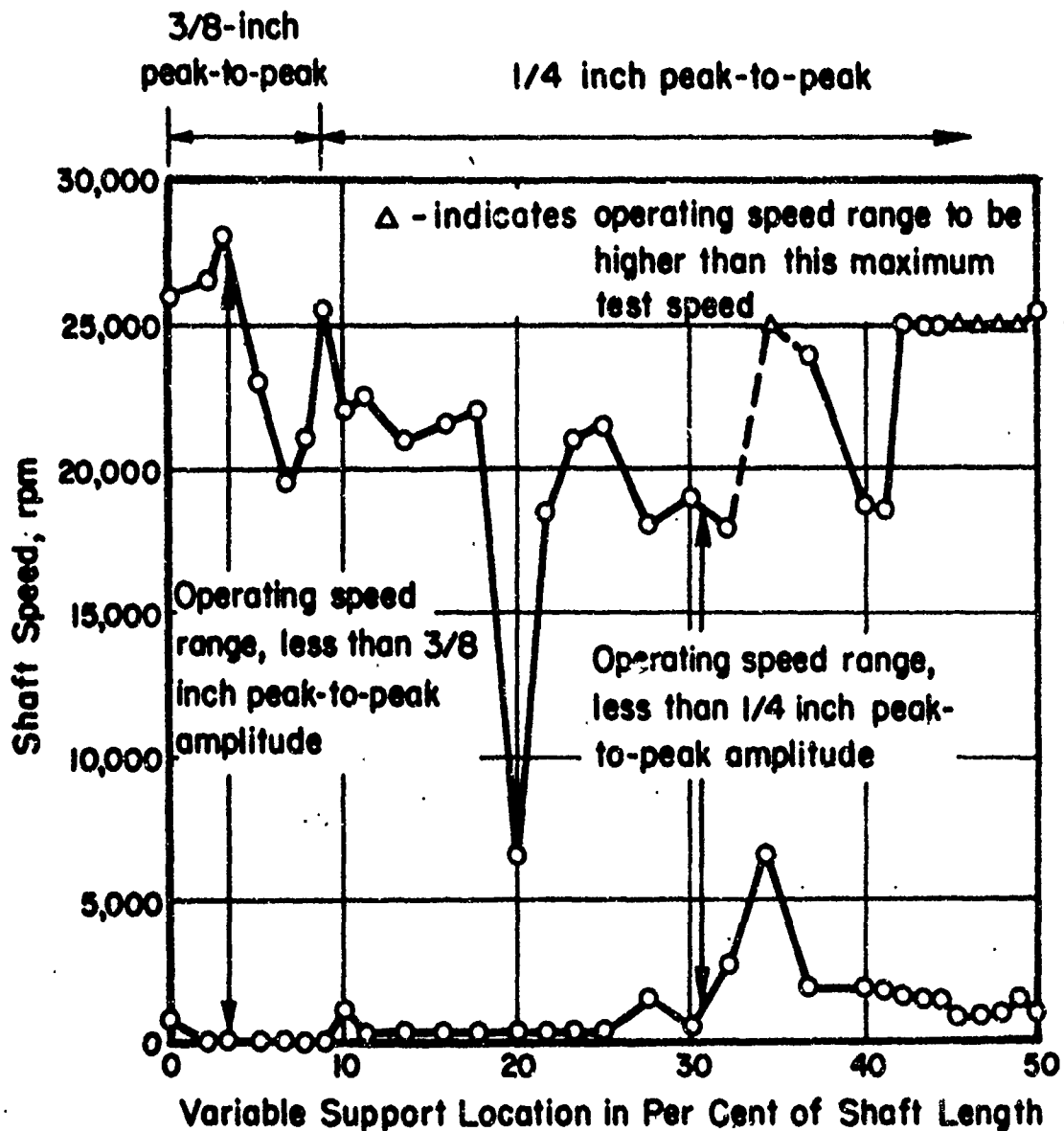


FIGURE 6. SHAFT SPEED VERSUS LOCATION OF ONE DAMPED SUPPORT WITH A FIXED LOCATION OF A SECOND DAMPED SUPPORT

One support fixed at 3.36 per cent from one end, other support varied from other end toward shaft mid-point. 1/4-inch diameter steel shaft. 89.3 inches long with clamped ends. Support Characteristics:  $K=11.6$  lb/in,  $C=1.736$  lb-sec/in.

$P$  = shaft material density, lb/in.<sup>3</sup>

$g$  = acceleration of gravity, 386 in/sec<sup>2</sup>

$y$  = shaft deflection, in.

$x$  = distance along shaft, in.

$t$  = time, sec.

The fourth-order differential equations describing the vibrations of shafts reduce to second-order equations if the shaft deflection curve is assumed to be sinusoidal as it vibrates.

This condition is satisfied by making the following substitution;

$$\frac{\partial^2 y}{\partial x^2} = -k^2 y, \quad (3)$$

where

$k$  = a constant for the particular system, in.<sup>-1</sup>

Substituting (3) in (2) gives:

$$EI k^2 \frac{\partial^2 y}{\partial x^2} = \frac{PA}{g} \frac{\partial^2 y}{\partial t^2} \quad (4)$$

Equation (4) is the ordinary wave equation. The condition  $\frac{\partial^2 y}{\partial x^2} = -k^2 y$  implies that the bending moment is everywhere proportional to the displacement of the shaft. This is almost perfectly true except near the shaft ends. A special treatment of the shaft ends was devised so that analysis procedures used for electrical transmission line calculations could be applied to the shafts.

This treatment of the shaft ends was obtained in the following manner. For any given critical speed order of the fixed-end shaft, a shorter simply-supported shaft can be found which has the same critical speed. The fixed-end shaft is therefore considered equivalent to a simply-supported shaft joined at each end to a short cantilever beam. These short cantilever beams can then be replaced by equivalent lumped masses and springs attached to the ends of the simply supported shafts.

Figure 7 shows the development of the transmission line analogy. Part (a) of the figure represents the shaft schematically. In part (b) of Figure 7 the clamped shaft ends are replaced by equivalent spring-mass combinations. In part (c) of the figure the equivalent electrical quantities are used to represent the damper assemblies as well as the shaft ends.

In calculating the performance of electrical transmission lines it is necessary to know a quantity called the characteristic impedance of the line. For shafts this quantity has been derived to be: [See reference 2]

$$Z_c = 0.0113 f^{1/2} E^{1/4} P^{3/4} (D^2 - d^2)(D^2 + d^2)^{1/4} \quad (5)$$

where

$Z_c$  = shaft characteristic impedance, lb-sec/in.

$D$  = shaft outside diameter, in.

$d$  = shaft inside diameter, in.

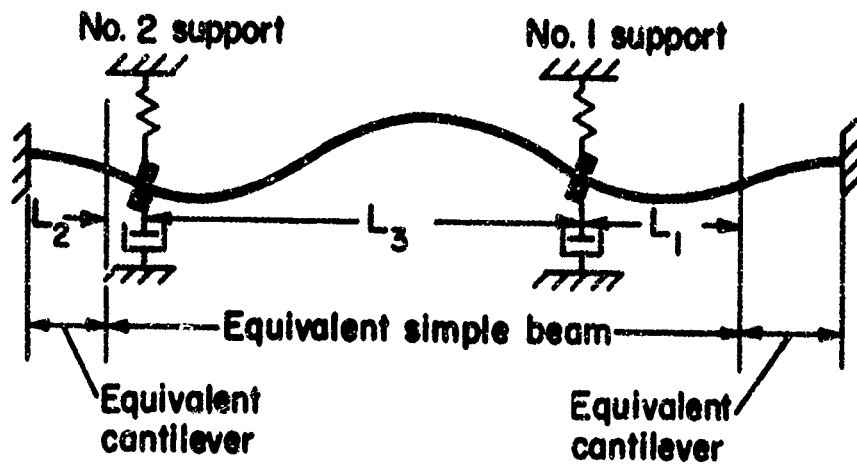
$f$  = shaft rotational speed, rps

For a solid steel shaft equation (5) becomes

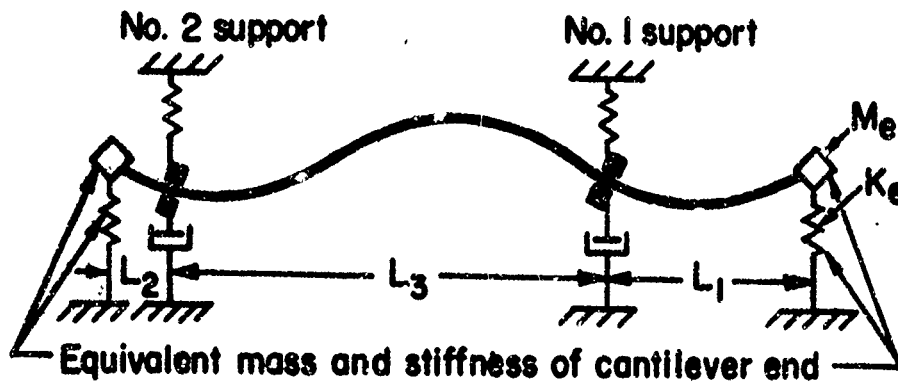
$$Z_c = 0.324 D^2 (Df)^{1/2} \quad (6)$$

In preliminary experiments designed to demonstrate the analogy relationships, superior performance with solid steel shafts was obtained with:

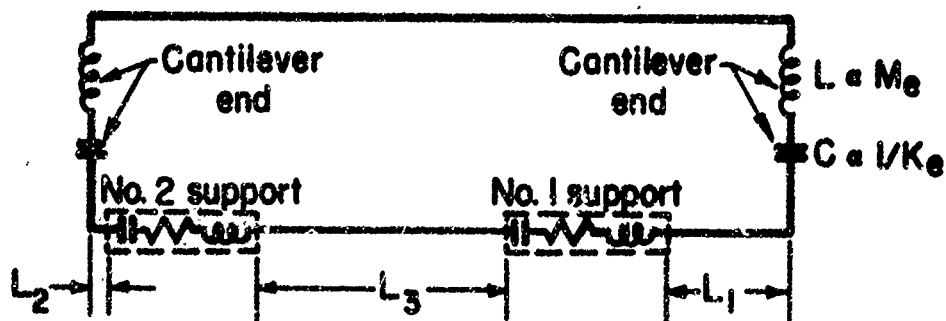
$$Z_c = D^2 (Df)^{1/2} \quad (7)$$



a. General Arrangement of High-Speed Shafts Studied



b. Equivalent Mechanical Representation of High-Speed Shafts



c. Electrical Analogy of High-Speed Shafts

FIGURE 7. DEVELOPMENT OF AN ANALOGY BETWEEN A HIGH-SPEED SHAFT AND AN ELECTRICAL TRANSMISSION LINE

For best impedance matching, or most effective power delivery to a load in an electrical system, the load must appear purely resistive and equal in magnitude to the characteristic impedance of the transmission line. In the shaft system the damper at the intermediate bearing is the load to which vibratory energy is to be delivered. By adjusting the spring rate and mass of the support bearing together with its location, the reactive components of impedance can be cancelled so that the damper can be made to look purely as a dissipative or resistive load at any selected speed.

At other speeds where the damper assembly does not appear as a purely resistive load some degree of increased vibration will be experienced. This is expressed in terms of the Voltage Standing Wave Ratio (VSWR) in electrical transmission lines.

The effectiveness of a damper assembly in suppressing vibration or standing waves can be determined most readily by using the Smith Chart. This is a graphical impedance calculator used by communications engineers. Details of its use will not be given here [See reference 1, pages 41 through 51], but it does permit standing wave ratios to be calculated readily for any damper parameters, and it conveys a feeling for the significance of the various dynamic parameters during the solution of a problem.

#### Dynamic Shaft Scaling Relationships

Numerous successful small-scale high-speed-shaft experiments have been made with damped intermediate supports. To make it possible to achieve similar performance with full-scale shafts a set of modeling equations is needed. The following relationships between dynamic shaft parameters were developed to define the basic properties of all circular shafts of uniform cross section:

$$\text{Characteristic Shaft Weight, } W_s = \frac{\pi}{4} (D^2 - d^2) L \rho, \text{ lb.} \quad (8)$$

$$\text{Characteristic Shaft Lateral Stiffness, } K_s = \frac{3\pi(D^4 - d^4)E}{L^3}, \text{ lb/in.} \quad (9)$$

$$\text{Characteristic Shaft Natural Frequency, } \omega_s = \sqrt{\frac{K_s g}{W_s}}, \text{ rad/sec.} \quad (10)$$

$$\text{Characteristic Shaft Critical Damping Value, } C_s = 2\sqrt{\frac{W_s K_s}{g}}, \text{ lb-sec/in.} \quad (11)$$

The following symbols refer to the intermediate support bearing:

W = weight of bearing plus 1/3 the weight of each support spring, lb.

K = combined spring rate of damper springs, lb/in.

C = support damping coefficient, lb-sec/in.

X =  $\frac{\text{distance between support and shaft end, in.}}{\text{over-all shaft length, L, in.}}$

Four dynamic scaling ratios exist which relate parameters of shafts and their intermediate supports for similar dynamic behavior. Let subscript 1 refer to a shaft configuration of known behavior, and subscript 2 refer to a shaft of different dimensions which is to be dynamically similar to the first shaft. The scaling ratios are then defined as:

$$\frac{W_1}{W_{s1}} = \frac{W_2}{W_{s2}} \quad (12)$$

$$\frac{K_1}{K_{s1}} = \frac{K_2}{K_{s2}} \quad (13)$$

$$\frac{C_1}{C_{s1}} = \frac{C_2}{C_{s2}} \quad (14)$$

$$X_1 = X_2. \quad (15)$$

Knowing the support-to-shaft ratios of equations (12) through (15) for Shaft 1, all that remains is calculating the necessary damper characteristics  $W_2$ ,  $K_2$ , and  $C_2$ , for the diameter, length, and materials of the second shaft. The use of these modeling equations permits scaling the satisfactory operational characteristics of a known shaft configuration to any physically dissimilar situation.

#### Experimental Verification of Electrical Analogy

An example of the application of this design technique to a 138-inch long, 1/2-inch diameter, solid steel shaft is given. The second column of Table 1 lists its first 20 critical speeds with no intermediate support bearings added. It was arbitrarily decided to design a damper for this shaft optimized for the sixth critical speed, 5,330 rpm. The seventh column of Table 1 shows the standing wave ratios determined for one damper optimized for the sixth critical speed.

When high values of standing wave ratio were calculated at the first, fourth, and ninth criticals, as indicated in column seven, the decision was made to add a second damper, optimized for the fourth critical speed. The fourth column of Table 1 shows Standing Wave Ratios for the second damper alone. Note that one or the other of the two dampers gives a low value of standing wave ratio for every critical speed up to the ninth.

Experimental operation of three different shafts using this pair of dampers verified the predictions of operation. Column nine of Table 1 lists peak-to-peak vibration amplitudes measured on one shaft. The shafts ran smoothly without serious vibration up to 11,000 rpm, at which speed they became audibly noisy. They continued to run over the entire speed range up to 51,000 rpm, approaching the twentieth critical speed. Shaft speed was limited by belt slip

TABLE 1. STANDING WAVE RATIOS FOR 1/2-INCH DIAMETER, 138-INCH LONG SOLID STEEL SHAFT HAVING TWO DAMPED INTERMEDIATE SUPPORTS. ONE SUPPORT DESIGNED FOR OPERATION AT THE SIXTH CRITICAL SPEED, THE OTHER FOR OPERATION AT THE FOURTH CRITICAL SPEED

Critical Speed Mode Number (Stations Along Shaft for Col 10)	Critical Speed, RPM, for Fixed-End Shaft, No Added Supports	Calculated Values of Standing Wave Ratio (VSWR)						Measured Peak-to-Peak Vibration Between Supports, mils (Col 1)	Measured Eccentricity, mils at 24 Stations Along Shaft
		1/2 Optimum Damping for							
		4th Critical	Optimum Damping for 4th Critical	2X Optimum Damping for 4th Critical	1/2 Optimum Damping for 6th Critical	Optimum Damping for 6th Critical	2X Optimum Damping for 6th Critical		
1	285	1.52	3.0	5.96	50.	29.	23.	8 (450 rpm) +	.00197
2	783	3.00	2.7	4.05	5.0	4.5	5.6	28 (1000)	.000
3	1540	40.	20.	12.3	1.2	2.0	4.2	68 (2150)	-.00394
4	2540	1.98	1.0	2.0	34.	19.	10.	48 (3400)	-.0059
5	3800	2.73	1.50	1.90	6.5	3.8	3.8	13 (4900)	-.0059
6	5330	48.	24.	13.0	2.0	1.0	2.2	16 (6000)	-.00783
7	7050	3.5	1.8	1.32	3.9	2.4	2.4	—	-.00688
8	9060	12.	6.2	3.7	18.	8.5	5.3	6 (7500)	-.00688
9	11300	160.	80.	42.	80.	33.	18.	9 (10400)	-.00492
10	13800	6.4	3.4	1.92	3.2	1.7	1.5	8 (12600)	-.00196
11	16800	30.	14.0	7.4	7.5	4.0	2.6	4 (14000)	-.00196
12	19600	14.2	7.5	4.0	32.	15.0	8.0	6 (18500)	.000
13	22800	10.8	5.6	3.03	80.	35.	18.	5 (22000)	-.00196
14	26400	46.	26.	12.0	4.8	2.5	1.3	12 (26000)	-.00196
15	30200	11.5	5.9	3.1	12.	6.0	3.4	5 (30000)	-.00196
16	34100	16.0	8.3	4.35	29.	16.	7.7	5 (36000)	-.00196
17	38400	60.	31.	16.0	200.	160.	120.	—	-.00093
18	42900	9.0	4.6	2.37	5.5	2.8	1.3	—	.000
19	47600	23.	12.	6.3	18.	9.6	4.7	—	+.00295
20	52500	80.	39.	21.	36.	17.	8.2	—	+.00295
21								—	+.00196
22								—	.000
23								—	-.00295
24								—	.000

- 18 -



in the machine, although the rising noise level indicated increasing vibration at the twentieth critical. This would be expected from the high values of VSWR at that speed. It should be clearly stated here that the shafts were operated for prolonged periods at the critical speeds, and not just accelerated past them.

Experiments are now in progress to evaluate the effects of smaller and larger values of damping coefficients over a wide speed range. Columns three and six of Table 1 show calculated values of VSWR for dampers having one-half the so-called "optimum" damping coefficient, and columns five and eight show values of VSWR for dampers of twice the "optimum" damping value. The ninth column gives maximum measured peak-to-peak vibration amplitudes obtained with one shaft and the damping values of columns four and seven. Column ten lists values of initial shaft eccentricity measured at twenty-four stations along the shaft. To interpret these values, read column one as station numbers along the shaft, rather than as critical speed mode number.

The series of experiments in progress to confirm the predictions in Table 1 will serve to:

- (1) Help define optimum damping values. (Present indications are that higher than so-called "optimum" damping values reduce VSWR at speeds away from the design speed.)
- (2) Help define allowable values of VSWR for a given degree of shaft crookedness or eccentricity.
- (3) Indicate the sensitivity of the shaft system to changes in damping coefficient, as from temperature effects on the viscosity of damping fluid.

The maximum allowable value of standing wave ratio has not yet been established for any given shaft parameters and degree of unbalance, nor has its precise physical interpretation for the high-speed shafts been determined. Work now in progress is intended to more fully confirm the findings already presented, as well as to establish what might be termed a set of design rules to simplify the calculations required to establish the critical dynamic parameters of damper location, damping coefficient, spring rate, damper mass, and permissible standing wave ratio.

RANGE OF CRITICAL SPEEDS OF INTEREST FOR  
TANDEM ROTOR HELICOPTER SHAFTING

In order to provide some general guidelines for selecting a critical speed range likely to be encountered in actual applications, a brief study of the relationship of shaft critical speed to engine power in tandem rotor helicopters was made. Based on this limited study, it appears that the speed range most likely in these applications includes speeds up to the tenth critical speed. Speeds up to the sixteenth critical might be encountered under some conditions.

A summary of the design study follows. The following conditions were assumed to apply:

- (1) Only tandem-rotor helicopters were considered.
- (2) One engine per rotor was installed in the aircraft.
- (3) Rotor tip speed was constant at Mach 0.7.
- (4) Transmission shaft length was 60 per cent of rotor diameter.
- (5) All solutions involving changes in shaft materials or diameters were for equal-strength conditions.

- (6) The relationships between rotor rpm, engine rpm, and engine horsepower were assumed to be those shown in graphs supplied by TRECOM.

A generalized equation relating shaft parameters and engine parameters were derived. [See reference 3, Appendix]. The equation was determined first for solid shafts and states the value of mode number to be:

$$n_{\text{solid}}^2 = 8.35 \times 10^8 \left[ \left( \frac{P}{E} \right)^{1/2} (R_g^4 S_s)^{1/3} \right] \left[ \frac{N_e^{4/3}}{(N_2 - 4750)^2 \text{hp}_e^{1/3}} \right] \quad (16)$$

where

$n$  = critical speed mode number

$R_g$  = combining box gear ratio, shaft speed/engine speed

$S_s$  = shear stress in shaft, lb/in.<sup>2</sup>

$N_e$  = engine rpm

$\text{hp}_e$  = engine horsepower

All of the items in the first bracket are shaft design parameters, while the second bracket consists of terms which can be obtained from Figure 8, a plot of engine rpm vs horsepower derived from the data supplied by TRECOM.

Equation (16) can be simplified for consideration of steel and aluminum shafts. In the following equations,  $S_s$  was assumed to be 30,000 psi for steel shafts, and 8,000 psi for aluminum shafts.

$$n_{\text{solid steel}}^2 = \frac{2.51 \times 10^6 R_g^{4/3} N_e^{4/3}}{(N_e - 4750)^2 (\text{hp}_e)^{1/3}} \quad (17)$$

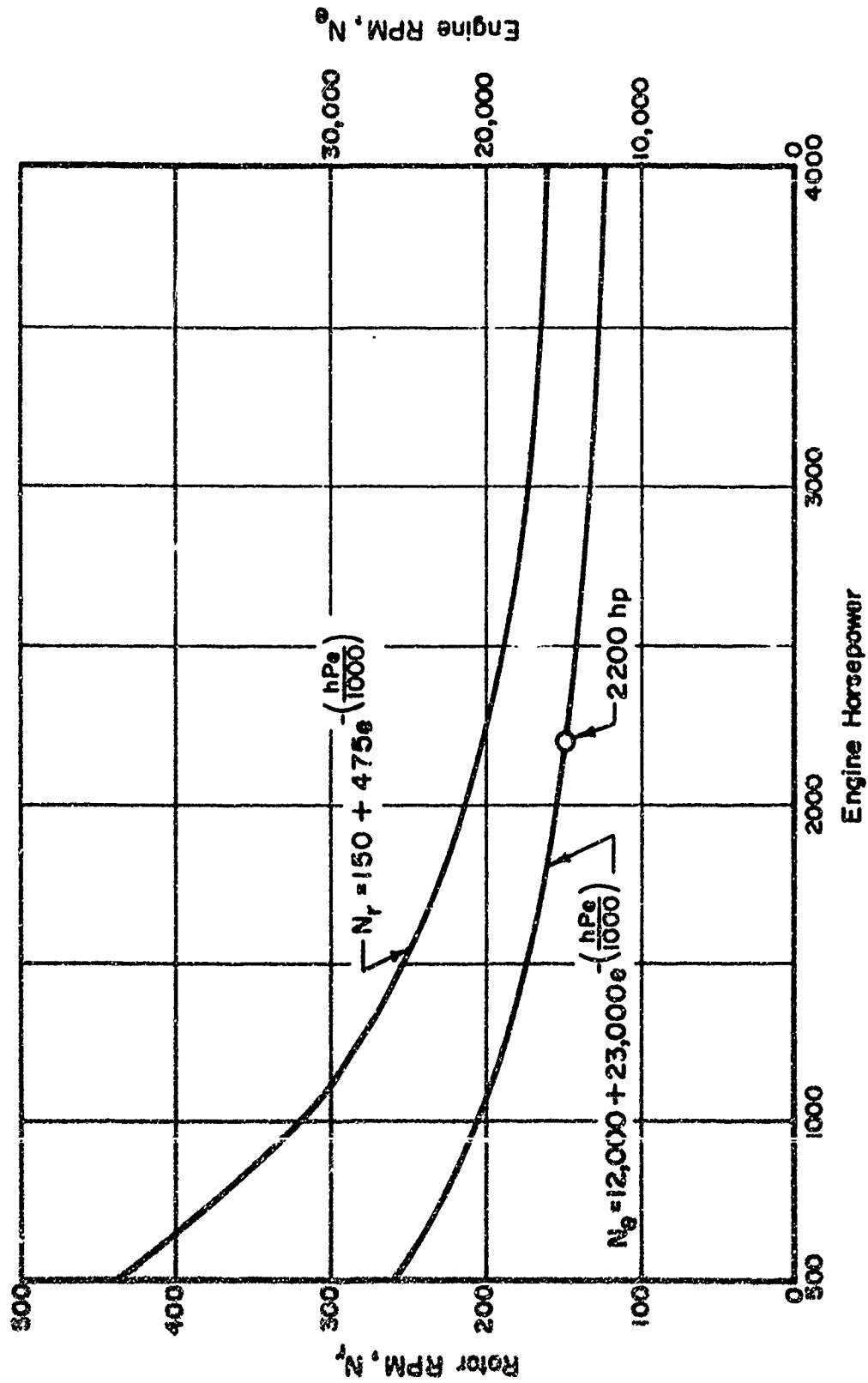


FIGURE 8. ROTOR AND ENGINE SPEED VS ENGINE HORSEPOWER

$$n_{\text{solid aluminum}}^2 = \frac{1.61 \times 10^6 R_g^{4/3} N_e^{4/3}}{(N_e - 4750)^2 (hp_e)^{1/3}} \quad (18)$$

Two other parameters will be of general interest. Since multi-engine machines will probably have combining gear boxes, it seems likely that some speed reductions will be made in these boxes, primarily in the interest of weight reduction. From equation (16), it can be seen that the mode number  $n$  varies as the  $2/3$  power of the gear ratio  $R_g$ . Figure 9 is a plot of this function.

Tubular, rather than solid shafts will probably be used in real applications. Figure 10 shows the relationship between mode number for tubular shafts of equal strength and their inside-to-outside diameter ratios,  $d/D$ .

Figure 11 presents the final relationships between mode number, shaft material, selected gear ratios, and engine horsepower. It can be seen that the mode number does not vary greatly with horsepower.

A typical example should suffice to illustrate the use of the figures. Suppose it is desired to determine the probable mode number for a future application where:

Engine hp - 2200 per engine, 4400 total

Shaft - Aluminum,  $d/D = 0.9$

Combining Box Gear Ratio =  $R_g = 0.6$

From Figure 8,  $N_e = 14,800$  rpm

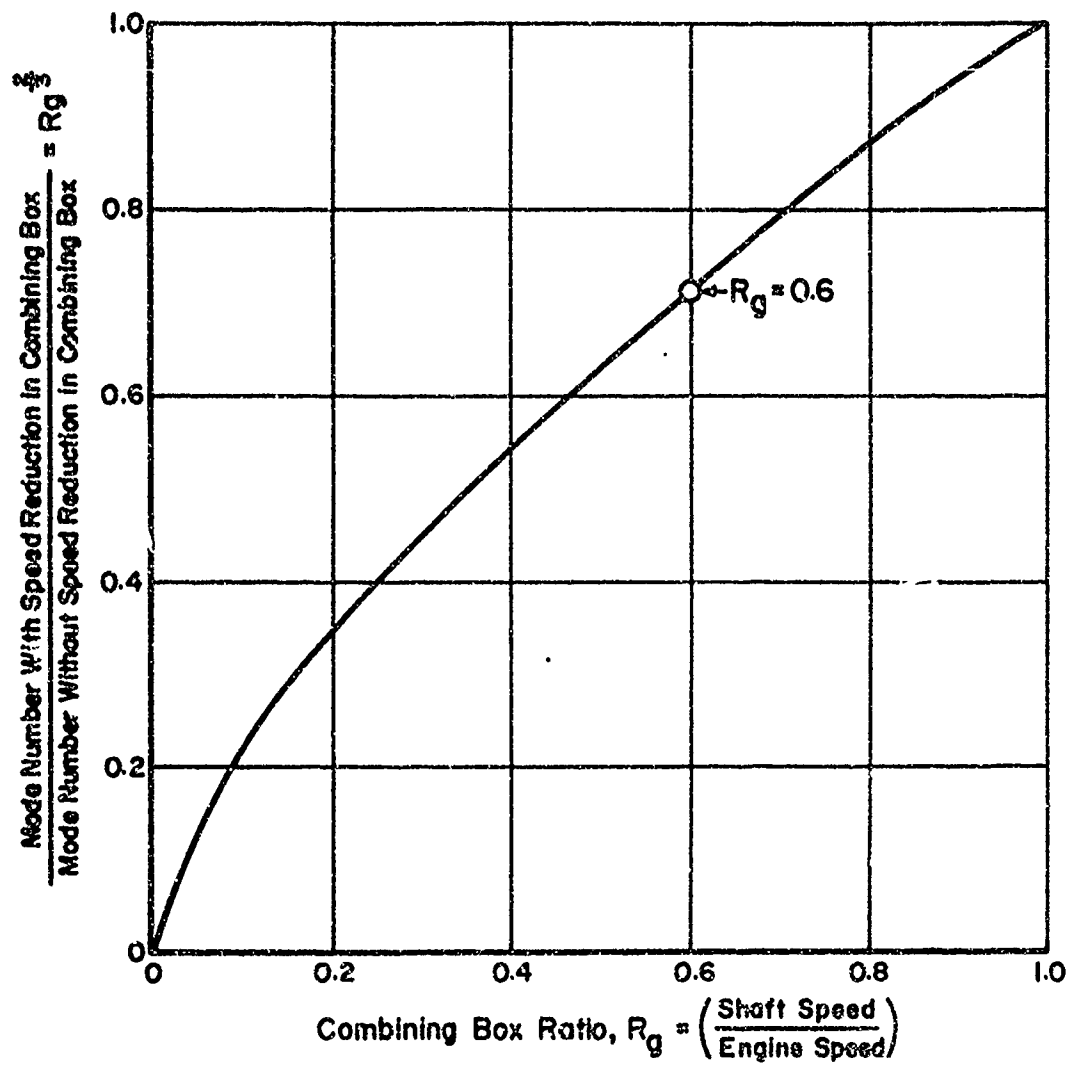


FIGURE 9. EFFECT OF COMBINING-BOX GEAR RATIO ON SHAFT VIBRATION MODE NUMBER

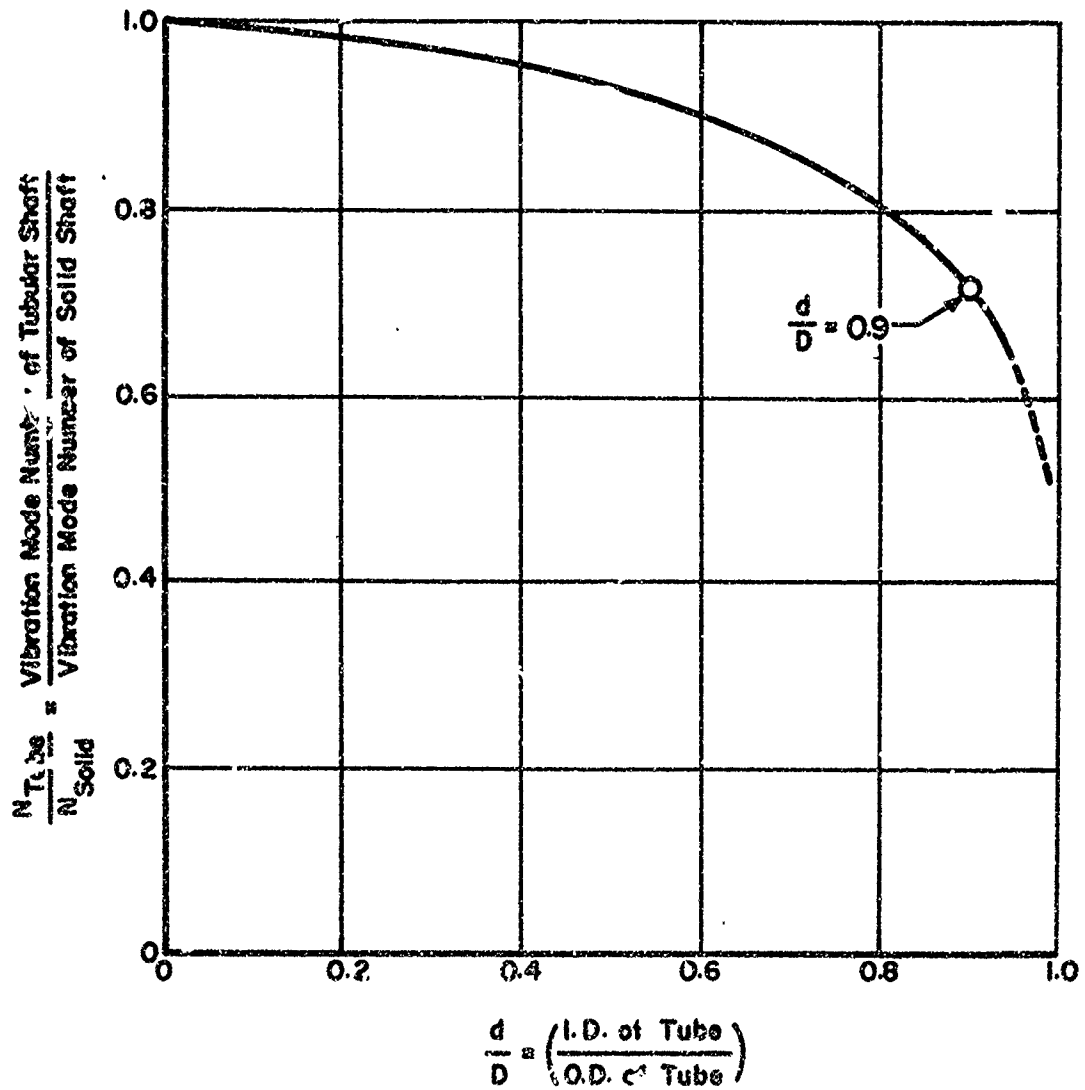


FIGURE 10. EFFECT OF DIAMETER RATIO OF TUBULAR SHAFTS OF EQUAL STRENGTH ON MODE NUMBER

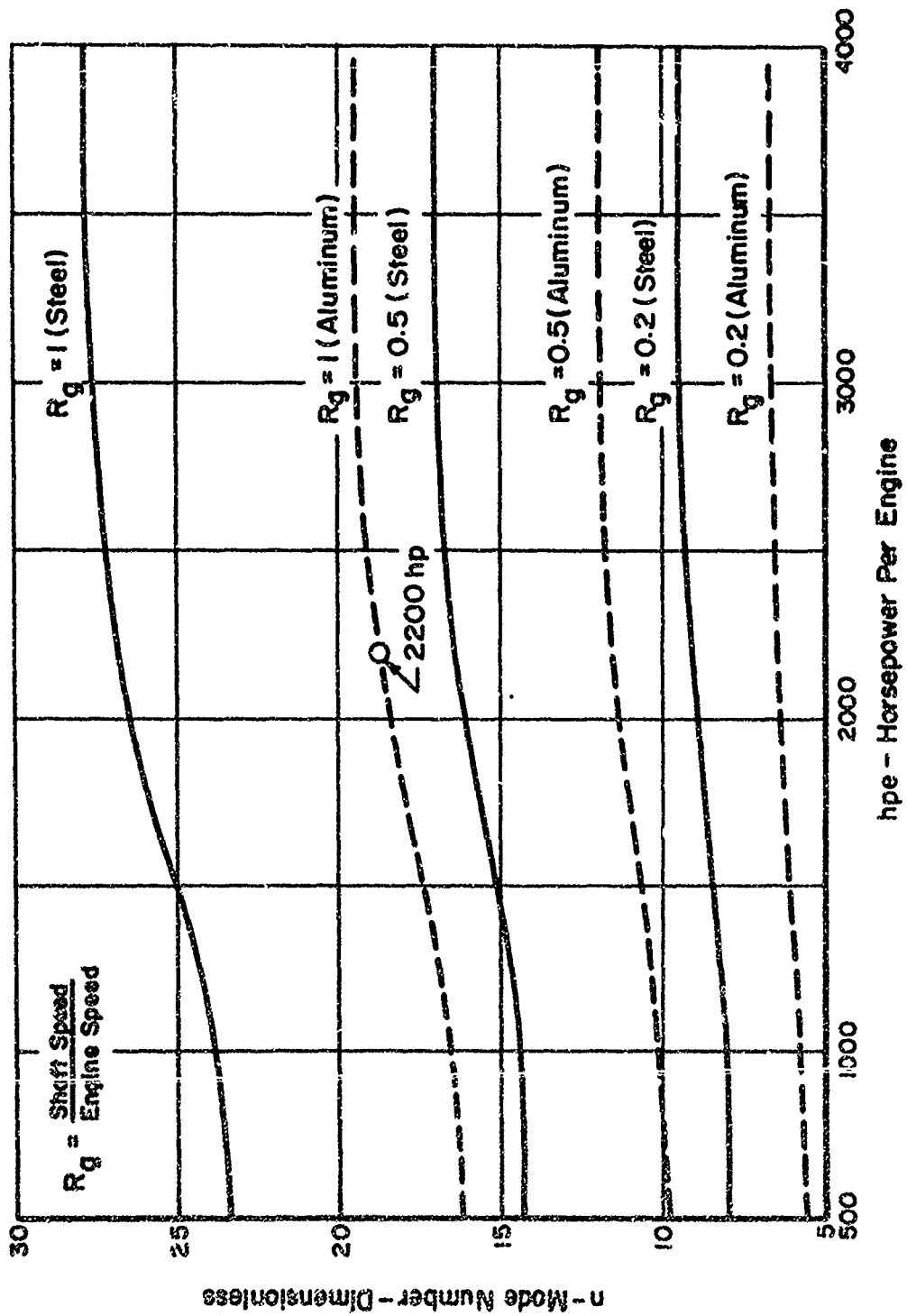


FIGURE 11. SHAFT VIBRATION MODE NUMBER VS HORSEPOWER TRANSMITTED THROUGH SOLID SHAFTS



For a solid aluminum shaft, with  $R_g = 1.0$ , the probable mode number is found from Figure 11 to be 18.7.

The mode number for  $R_g = 0.6$  can be determined by multiplying the factor from Figure 9 by the mode number for  $R_g = 1$ , giving a "geared down" mode number for a solid shaft of  $0.71 \times 18.7$ , or 13.28.

One final step remains - the conversion of the mode number for a solid shaft into that of a tubular shaft whose inside diameter is 0.9 times its outside diameter. Figure 10 provides a conversion factor of 0.72, which when multiplied by 13.28 gives the final answer. The mode number is 9.56, meaning that a shaft with simply-supported ends would operate just above its ninth critical speed in this application.

It might be worthwhile to attempt some generalization on the results obtained. Tubular shafts will almost certainly be used, and a diameter ratio ( $d/D$ ) of 0.9 is conservative. Aluminum is a likely shaft material. Most combining boxes will probably have some reduction built in, and a 2:1 reduction ( $R_g = 0.5$ ) would seem to be a reasonable value. From these assumptions and Figures 10 and 11, the highest probable mode number would be  $11.6 \times 0.72 = 8.35$ , just above the eighth critical speed. Allowing some margin for error, it might be concluded that most practical shaft installations would not involve speeds above the tenth critical, with virtually no practical installations operating above the sixteenth critical speed ( $R_g = 1$ ,  $d/D = 0.8$ ).

It should be restated here that the values of mode number derived above pertain specifically to tandem-rotor helicopters. To date this analysis has not been extended to other types of aircraft. The results obtained for most VTOL/STOL configurations are expected to be similar. Torque reaction rotor drives for

single-rotor helicopters may present an entirely different situation.

### CONCLUSIONS

The most significant findings of the work to date are:

(1) No unusual problems of shaft straightness of balancing have been encountered. In fact, a dynamic straightening effect has been observed in tests as a crooked shaft tends to rotate about its own center of gravity.

(2) Realistic torsional stresses in a shaft appear to have an insignificant effect on lateral vibration. Tests are continuing to fully confirm this.

(3) Fatigue is not expected to be a problem. The shaft deflection curve is static relative to the shaft as the shaft rotates, thus the shaft is not subjected to a stress reversal during each revolution.

(4) The electrical analog of the high speed shafts is a great aid in damper design.

(5) Power dissipation in the dampers appears negligible.

(6) A dynamic scaling procedure has been developed which permits the findings of tests with small shafts to be confidently applied in the design of larger shaft systems.

(7) In most aircraft applications of hypercritical speed shafting it is expected that shafts will not be required to operate at speeds above the sixteenth critical speed.

In summary, it is believed that power transmission by hypercritical speed shafting is practical and can yield important weight benefits in aircraft through the reduction of shaft size and the elimination of many bearings and couplings.

ACKNOWLEDGMENT

The research program during which the information contained in this technical paper was produced was sponsored by the Aeronautical Systems Division, Air Force Systems Command, United States Air Force, Wright-Patterson Air Force Base, Ohio, and the Army Transportation Research Command, Fort Eustis, Virginia.

REFERENCES

1. Dubensky, R. G., Mellor, Jr., C. C., Voorhees, J. E., "Design Criteria for High-Speed Power Transmission Shafts, Part 1. Analysis of Critical Speed Effects and Damper Support Location".\* Technical Documentary Report No. ASD-TDR-62-728, Part 1, August, 1962.
2. Voorhees, J. E., Mellor, Jr., C. C., Dubensky, R. G., "The Control of Shaft Vibrations at Hypercritical Speeds", American Society of Mechanical Engineers, Paper Number 63-MD-30.
3. Day, J. B., Dubensky, R. G., Meacham, H. C., Voorhees, J. E., "Design Criteria for High-Speed Power Transmission Shafts - First Quarterly Report - Phase II",\* Prepared for Aeronautical Systems Division, May, 1963, under Contract No. AF 33(657)-10330.

\* These reports may be obtained from the:

Defense Documentation Center  
Arlington Hall Station  
Arlington 12, Virginia

**DYNAMIC TORSIONAL PROBLEMS  
IN VTOL DRIVE TRAINS  
WITH UNIVERSAL JOINTS**

**R.B. Bossler, W.G. Flannelly**  
**Kaman Aircraft**

## DYNAMIC TORSIONAL PROBLEMS IN VTOL DRIVE TRAINS WITH UNIVERSAL JOINTS

R. B. Bossler, Jr., Mechanical Engineer - Project  
W. G. Flannelly, Dynamics Specialist  
Kaman Aircraft Corporation  
Bloomfield, Connecticut

### INTRODUCTION

The demands for high torque capacity, light weight, long fatigue life and high speed in helicopter and V/STOL drive systems are severe. Some V/STOL aircraft tend to have complex drive arrangements with long shafting which must follow structural flexure, engines and transmissions on elastic foundation and a large number of lumped inertias. Universal joints are required to transmit power from a driving shaft to a driven shaft when the shafts are not in alignment.

For transmitting significant power, the Hooke's Joint is the least expensive universal joint, has large misalignment capability, and experiences of the past 300 years have developed dependability. Because a Hooke's Joint is not a constant speed device, it introduces torsional vibrations into the drive system; because it has moving parts, it requires lubrication and experiences wear. With careful engineering, a VTOL drive system can be designed to take advantage of the many desirable features of the Hooke's Joint without suffering excessively from its limitations.

This paper describes an analytical technique for predicting the dynamic torsional loads and shaft bending moments which result from Hooke's Joint excitations. Procedures for minimizing dynamic loads are suggested and are illustrated with examples of actual situations encountered with hardware. Certain design considerations relevant to dynamic loading are discussed.

## NOMENCLATURE

A	Plane formed by intersecting axes of shafts 1 and 2
B	Plane formed by intersecting axes of shafts 2 and 3
$C_{\theta R}$	Rotating bending moment on the $\theta$ shaft
$C_{\theta F}$	Fixed system bending moment on the $\theta$ shaft
D	Diameter
F	Force
$f_c$	Compressive stress
$I_1$	Mass moment of inertia of the 1 <sup>th</sup> item
$K_{ij}$	Spring rate of shaft between items i and j
P	Load per unit length on needle bearing
Q	Torque
r	Radius of shaft
R	Radius of cross arm
Z	Number of rolling elements
$\alpha$	Angle between intersecting planes A and B, positive when measured clockwise from plane A looking from A joint to B joint
$\beta_i$	Misalignment angle on the i <sup>th</sup> joint
$\beta_e$	Effective misalignment angle, defined by Equation (16)
$\gamma$	Angle between plane B and plane of yoke 3
$\delta$	Phase angle defined by Equation (9)

## NOMENCLATURE

$\Theta$  Angle of shaft rotation

$$\mu = \alpha + \psi$$

$\sigma$  Tensile or compressive stress due to transverse bending

$\tau$  Shear stress

$\phi$  Angle of shaft rotation

$\psi$  Index angle - Angle from the left yoke to the right yoke on shaft 2

$$\omega = 2\Omega$$

$\Omega$  Nominal shaft angular velocity



## KINEMATICS OF HOOKE'S COUPLING

To accommodate both parallel and angular misalignment, it is necessary to have two joints. For discussion purposes in this paper, two Hooke's Joints connected by a shaft will be considered a Hooke's Coupling.

In Figure 1 the angle  $\alpha$  is the angle between Plane A, formed by the intersecting axes of shafts 1 and 2, and Plane B, formed by the intersection of the axes of shafts 2 and 3. The angle between the left and right yokes on shaft 2 is the "index angle"  $\psi$ .

From Figure 2:

$$\tan \phi = \tan \theta \cos \beta_1 \quad \text{Equation (1)}$$

and, similarly for the output joint, with  $\phi' = \phi - \mu$

$$\tan \phi' = \tan \gamma \cos \beta_2 \quad \text{Equation (2)}$$

Differentiating Equation (1) and simplifying gives the velocity of shaft 2 in terms of the velocity of shaft 1:

$$\dot{\theta} = \dot{\phi} \cos \beta_1 (1 - \cos^2 \phi \sin^2 \beta_1)^{-1} \quad \text{Equation (3)}$$

for small angles  $\beta_1$

$$\dot{\theta} - \dot{\phi} \cong \dot{\theta} \frac{\beta_1^2}{2} \cos 2\phi$$

But,  $\theta \cong \Omega$ , therefore,

$$\dot{\theta} - \dot{\phi} \cong \Omega \frac{\beta_1^2}{2} \cos 2\phi \quad \text{Equation (4)}$$

showing that the velocity difference across a joint is a two-per-rev. Differentiating Equation (2) and simplifying gives:

$$\dot{\phi} \cos \beta_2 = \dot{\gamma} [1 - \cos^2(\phi - \mu) \sin^2 \beta_2] \quad \text{Equation (5)}$$

for small angles  $\beta_2$

$$\dot{\gamma} - \dot{\phi} = \Omega \frac{\beta_2^2}{2} \cos 2(\phi - \mu) \quad \text{Equation (6)}$$

Subtracting Equation (6) from Equation (5)

$$\dot{\theta} - \dot{\gamma} = \frac{\Omega}{2} [(\beta_1^2 - \beta_2^2 \cos 2\mu) \cos 2\phi - \beta_2^2 \sin 2\mu \sin 2\phi]$$

which may be written as:

$$\dot{\theta} - \dot{\gamma} = -\frac{\Omega}{2} \sqrt{(\beta_1^2 - \beta_2^2 \cos 2\mu)^2 + \beta_2^4 \sin^2 2\mu} \sin(2\phi - \delta) \quad \text{Equation (7)}$$

Letting  $\omega = 2\Omega$  and noting that  $\phi = \Omega t$  very nearly,

$$\dot{\theta} - \dot{\gamma} = -\frac{\omega}{4} \sqrt{(\beta_1^2 - \beta_2^2 \cos 2\mu)^2 + \beta_2^4 \sin^2 2\mu} \sin(\omega t - \delta) \quad \text{Equation (8)}$$

where

$$\delta = \tan^{-1} \frac{\beta_1^2 - \beta_2^2 \cos 2\mu}{\beta_2^2 \sin 2\mu} \quad \text{Equation (9)}$$

Differentiating Equation (3) and assuming small angle  $\beta$  gives the acceleration:

$$\ddot{\theta} = \ddot{\phi} - \dot{\phi}^2 \beta_1^2 \sin 2\phi \quad \text{Equation (10)}$$

Similarly for Equation (5):

$$\ddot{\gamma} = \ddot{\phi} - \dot{\phi}^2 \beta_2^2 \sin 2(\phi - \mu) \quad \text{Equation (11)}$$

Subtracting Equations (10) and (11) and noting that  $\dot{\phi} \cong \dot{\theta} \cong \Omega$  gives the differential acceleration:

$$\ddot{\gamma} - \ddot{\theta} = \Omega^2 [\beta_1^2 \sin 2\phi - \beta_2^2 \sin 2(\phi - \mu)]$$

Re-arranging terms,

$$\ddot{\gamma} - \ddot{\theta} = \Omega^2 [(\beta_1^2 - \beta_2^2 \cos 2\mu) \sin 2\phi + \beta_2^2 \sin 2\mu \cos 2\phi]$$

which may be written as:

$$\ddot{\gamma} - \ddot{\theta} = \Omega^2 \sqrt{(\beta_1^2 - \beta_2^2 \cos 2\mu)^2 + \beta_2^4 \sin^2 2\mu} \cos(2\phi - \delta)$$

or

$$\ddot{\gamma} - \ddot{\theta} = \frac{\omega^2}{4} \sqrt{(\beta_1^2 - \beta_2^2 \cos 2\mu)^2 + \beta_2^4 \sin^2 2\mu} \cos(\omega t - \delta) \quad \text{Equation (12)}$$

where  $\omega = 2\Omega$

From Equation (1):

$$\tan \theta - \tan \phi = \frac{\beta_1^2}{2} \tan \theta$$

Substituting,

$$\tan \theta - \tan \phi = \frac{\sin(\theta - \phi)}{\cos \theta \cos \phi}$$

and noting that

$\theta \approx \phi$  gives

$$\theta - \phi \approx \frac{\beta_1^2}{4} \sin 2\phi$$

Equation (13)

In like manner, Equation (2) becomes:

$$\gamma - \phi \approx \frac{\beta_2^2}{4} \sin 2(\phi - \mu) - \mu$$

Equation (14)

Subtracting Equations (13) and (14) and simplifying after the fashion of Equation (7):

$$\mu + \theta - \gamma \approx \frac{1}{4} \sqrt{(\beta_1^2 - \beta_2^2 \cos 2\mu)^2 + \beta_2^4 \sin^2 2\mu} \cos(\omega t - \delta)$$

Equation (15)

During the "effective misalignment"

$$\beta_e^2 = \sqrt{(\beta_1^2 - \beta_2^2 \cos 2\mu)^2 + \beta_2^4 \sin^2 2\mu}$$

Equation (16)

the equations for displacement, velocity and acceleration may be written as:

$$(\theta + \mu) - \gamma \approx \frac{\beta_e^2}{4} \cos(\omega t - \delta)$$

Equation (15)

$$\dot{\theta} - \dot{\gamma} \approx -\omega \frac{\beta_e^2}{4} \sin(\omega t - \delta)$$

Equation (8)

$$\ddot{\theta} - \ddot{\gamma} \approx -\omega^2 \frac{\beta_e^2}{4} \cos(\omega t - \delta)$$

Equation (12)

The above three equations describe the important relationships in a Rzele's Coupling, with joints under small-angle misalignment, in a linearized manner suitable for dynamics analysis.

## TORSIONAL DYNAMIC PROBLEMS WITH HOOKE'S COUPLINGS

As shown in Equations (15) and (12), a Hooke's Coupling introduces a two-per-rev torsional acceleration proportional to the square of the effective misalignment and to the square of the R.P.M. Experience has shown that the two-per-rev accelerations of a Hooke's Coupling can produce disastrous results, especially when one of the torsional natural frequencies of the drive system is near two-per-rev of shaft speed.

Consider the series system shown in Figure 3A.

From Equation (15):

$$\theta_A = \frac{\beta_{a12}^2}{4} \cos(\omega t - \delta) + \theta_2$$

From Equations (13) and (14),

$$\theta_B = \theta_3 - \frac{\beta_{B3}^2}{4} \sin \omega t$$

$$\theta_C = \theta_4 - \frac{\beta_{C4}^2}{4} \sin(\omega t - 2\mu)$$

Equation (17)

The Kinetic Energy is:

$$T = \frac{1}{2} I_1 \dot{\theta}_1^2 + \frac{1}{2} I_2 \dot{\theta}_2^2 + \frac{1}{2} I_3 \dot{\theta}_3^2 + \dots + \frac{1}{2} I_N \dot{\theta}_N^2$$

The Potential Energy is:

$$V = \frac{1}{2} K_{12} (\theta_1 - \theta_A)^2 + \frac{1}{2} K_{23} (\theta_2 - \theta_3)^2 + \frac{1}{2} K_{34} (\theta_3 - \theta_C)^2 + \frac{1}{2} K_{45} (\theta_4 - \theta_5)^2 \\ + \frac{1}{2} K_{56} (\theta_5 - \theta_6)^2 + \dots + \frac{1}{2} K_{N-1,N} (\theta_{N-1} - \theta_N)^2$$

Substituting Equation (17) into the Potential Energy equation and solving Lagrange's equations,

$$I_1 \ddot{\theta}_1 + K_{12} (\theta_1 - \theta_2) = K_{12} \frac{\beta_{a12}^2}{4} \cos(\omega t - \delta) \quad \text{Equation (18)}$$

$$I_2 \ddot{\theta}_2 + K_{12} (\theta_2 - \theta_1) + K_{23} (\theta_2 - \theta_3) = -K_{12} \frac{\beta_{a12}^2}{4} \cos(\omega t - \delta) \quad \text{Equation (19)}$$

$$I_3 \ddot{\theta}_3 + K_{23} (\theta_3 - \theta_2) + K_{34} (\theta_3 - \theta_4) = K_{34} \left[ \frac{\beta_{B3}^2}{4} \sin \omega t - \frac{\beta_{C4}^2}{4} \sin(\omega t - 2\mu) \right] \quad \text{Equation (20)}$$

$$I_4 \ddot{\theta}_4 + K_{34} (\theta_4 - \theta_3) + K_{45} (\theta_4 - \theta_5) = -K_{34} \left[ \frac{\beta_{B3}^2}{4} \sin \omega t - \frac{\beta_{C4}^2}{4} \sin(\omega t - 2\mu) \right] \quad \text{Equation (21)}$$

$$I_5 \ddot{\theta}_5 + K_{45} (\theta_5 - \theta_4) + K_{56} (\theta_5 - \theta_6) = 0$$

etc.

$$I_N \ddot{\theta}_N + K_{N-1,N} (\theta_N - \theta_{N-1}) = 0$$

Note that the right-hand sides of Equations (20) and (21) can be expressed in terms of Equation (16),

$$I_3 \ddot{\Theta}_3 + K_{23}(\Theta_3 - \Theta_2) + K_{34}(\Theta_3 - \Theta_4) = K_{34} \frac{\beta_{34}^2}{4} \cos(\omega t - \delta_{34})$$

$$I_4 \ddot{\Theta}_4 + K_{34}(\Theta_4 - \Theta_3) + K_{45}(\Theta_4 - \Theta_5) = -K_{34} \frac{\beta_{34}^2}{4} \cos(\omega t - \delta_{34})$$

provided that the elastic deflection of the shaft is a small angle.

The dynamic response of a system to Hooke's Joint excitations may be illustrated using, for the sake of simplicity, a system consisting of the three inertias shown in Figure 3B.

$$\begin{bmatrix} -I_1 \omega^2 + K_{12} & -K_{12} & 0 \\ -K_{12} & K_{12} + K_{23} - I_2 \omega^2 & -K_{23} \\ 0 & -K_{23} & K_{23} - I_3 \omega^2 \end{bmatrix} \begin{bmatrix} \Theta_1 \\ \Theta_2 \\ \Theta_3 \end{bmatrix} = \begin{bmatrix} K_{12} \frac{\beta_{12}^2 e}{4} \\ -K_{12} \frac{\beta_{12}^2 e}{4} \\ 0 \end{bmatrix} \quad \text{Equation (22)}$$

where a solution of  $\Theta = \Theta \cos(\omega t - \delta)$  is assumed.

The natural frequencies are given by the positive roots of:

$$0 = I_1 I_2 I_3 \omega^4 - \omega^2 [K_{12} I_3 (I_1 + I_2) + K_{23} I_1 (I_2 + I_3)] + K_{12} K_{23} (I_1 + I_2 + I_3)$$

and the maximum vibratory torque in shaft 23 by:

$$K_{23}(\Theta_2 - \Theta_3) = \frac{\omega^2 K_{12} K_{23} I_1 I_3 \frac{\beta_{12}^2}{4}}{I_1 I_2 I_3 \omega^4 - \omega^2 [K_{12} I_3 (I_1 + I_2) + K_{23} I_1 (I_2 + I_3)] + K_{12} K_{23} (I_1 + I_2 + I_3)} \quad \text{Equation (23)}$$

For the misalignments and dynamic parameters ordinarily encountered in V/STOL aircraft, the dynamic loads predicted by Equation (23) will be acceptably low if the operating speed is sufficiently removed from two-per-rev resonance. In certain rare instances, however, the minimum dynamic torque (which is never zero for  $\omega \neq 0$ ) is excessive. Prudence alone dictates, of course, that the drive system should be designed such that none of the torsional natural frequencies occur at two-per-rev, but only through a detailed analysis can the dynamicist prescribe the extent of proximity to resonance which might be dangerous. Avoiding proximity to two-per-rev resonance is becoming more difficult, because of the increased number of degrees of freedom and the

proliferation of Hooke's Couplings sometimes found in multi-engine, multi-rotor V/STOL aircraft. When dealing with existing hardware, it is not always feasible to modify the dynamic response to the extent necessary. In such cases, the dynamic loads may be reduced, or even eliminated, through modification of the effective misalignment.

The ideal condition, as shown by Equation (16), is to have  $\beta_1 = \pm \beta_2$  and  $\mu = 0$  for misalignments other than zero, this is the only arrangement which results in zero effective misalignment. Engines and transmissions are seldom mounted in such a way that  $\beta_1$  and  $\beta_2$  can be varied independently of  $\alpha$ , but the index angle  $\psi$  is usually easily adjusted independently of other variables. The procedure, therefore, is to first manipulate the mounts of the input and output devices to make  $\beta_1$  and  $\beta_2$  as nearly equal as possible then to index the yokes through the angle  $\psi$ . To make this type of adjustment practical, if it ever should be required, all drive systems involving Hooke's Couplings should be designed to have the nominal absolute values of  $\beta_1$  and  $\beta_2$  as nearly equal as possible. Note carefully that with  $\mu = 0$  it is better to have large misalignments equally on each joint than to have moderate misalignment on one joint and zero misalignment on the other. For example, with a given  $\beta_1$ , the dynamic torsional loads with  $\beta_2 = .86 \beta_1$  and  $\mu = 0$  are one-fourth the dynamic loads with  $\beta_2 = 0$ .

When  $\mu = \pi/4$ , the least desirable value, the effective misalignment can be zero only if the misalignment on each joint is zero. With  $\mu = \pi/4$ , the loads resulting from zero misalignment on one joint are 29 per cent lower than the loads resulting from the same misalignment on each joint. If  $\mu = \pi/4$ , there is relatively little to be gained by manipulating misalignments, unless the misalignments on both joints can be substantially reduced. The value of providing indexing capability in the design of the coupling is evident. Fortunately, Hooke's Couplings commonly have a splined connection between the joints to allow for axial deflections. These splined connections allow step adjustment of  $\mu$  to approach the desired phasing. The angle increment per tooth offset is a function of the spline diametral pitch.

## DIFFERENTIAL TORQUE

Considering that a joint cannot store power

$$Q_o \dot{\theta} = Q_\phi \dot{\phi}$$

From Equation (3),

$$Q_o = Q_\phi (1 - \beta^2 \cos^2 \phi)$$

for small angle  $\beta$ . The vibratory torque from one joint is, therefore,

$$Q_\phi - Q_o = Q\beta^2 \cos^2 \phi \quad \text{Equation (24)}$$

Because it is proportional to  $\beta^2$ , the torque difference across a joint is usually negligible.

## SECONDARY COUPLES

When two intersecting torque-carrying shafts are misaligned, a transverse bending moment must exist on either or both shafts to effect equilibrium. The transverse bending moment vector which is transmitted by a Hooke's Joint to a shaft must be perpendicular to the plane of the yoke. In Figure 2, for example, there is a moment vector perpendicular to the left ( $\theta$ ) yoke

$$C_{\theta R} = Q\beta \cos \theta$$

and a moment vector on the right yoke

$$C_{\phi R} = Q\beta \sin \phi \quad \text{Equation (25)}$$

Note that these are one-per-rev rotating bending moments on the shafting. A simplified calculation shows that these secondary moments are not always negligible. In round shafts, the steady shear stress from torque

$$\tau = \frac{Qr}{2I}$$

and the vibratory one-per-rev bending stress

$$\sigma = \frac{C_{\theta R} r}{I} = 2\beta\tau$$

With 3 degrees misalignment, this gives a vibratory bending stress of approximately 10 per cent of the steady shear stress. Such contribution to the fatigue of shafting, combined with vibratory torsion discussed elsewhere in this paper, should not be ignored.

In the fixed system, these secondary couples become two-per-rev moments,

$$C_{or} = Q\beta \cos^2 \theta = \frac{Q\beta}{2} (1 + \cos 2\theta) \quad \text{Equation (26)}$$

The shaft bearings, therefore, react a steady moment and a two-per-rev moment.

#### ILLUSTRATIVE CASES

The schematic of a turbine-powered V/STOL drive system employing fourteen Hooke's Joints is shown in Figure 4. Each joint on the 3000 R.P.M. engine drive shaft (Shaft 1) was designed to have a misalignment of  $2.5^\circ$  with the shaft centerlines almost coplanar ( $\alpha \cong 0$ ).

In the course of research testing of a full-scale test rig, various structural changes were incorporated which resulted in misalignments of  $1.67^\circ$  and  $2.54^\circ$  in the joints on shaft 1, giving an effective misalignment of  $1.86^\circ$ . Bench tests of the sprag-type overrunning clutch revealed that the sprags engaged in a manner that caused elliptical deflections of the clutch outer race proportional to the applied shaft torque. This condition caused the clutch to act as a torsional spring of much lower rate than a structural analysis of the clutch, based on radial loading, would indicate.

An eleven degree-of-freedom torsional analysis was performed which gave a natural frequency of 11755 C.P.M. in the fifth mode. This is almost exactly two-per-rev. It is evident that, with a little simplification of the analysis, this frequency might not have been detected.

To corroborate analysis, and to determine the effect of the torsional damping inherent in the system, a rig run-up test was performed with strain gages on the drive shaft. Results showed a torsional natural frequency at 11400 C.P.M. and vibratory torque (two-per-rev) of +1200 inch-pounds (20 per cent of normal steady torque) in the engine drive shaft. Calculation of the shape of the fifth mode indicated that the vibratory torsion in shaft 2, from the Hooke's Coupling excitation in shaft 1, would be 37 per cent of normal torque. In an attempt to obtain further data, the excessively high two-per-rev torque resulted in failure of the sprag unit.

Deflection of the drive system supporting structure under load precluded assurance that the Hooke's Joint misalignments on shaft 1 could be kept equal. To reduce the resonant amplification, the torsional natural frequencies were shifted by changing the drive shaft from aluminum to steel which resulted in a three-to-one reduction in torsional vibratory loads.



The fact that the high vibratory loadings experienced in this case resulted from an effective misalignment of only  $1.86^\circ$  illustrates the potential seriousness of Hooke's Joint dynamic phenomenon.

In sharp contrast is the case of a certain two-place piston-powered helicopter which had a Hooke's Coupling between its six cylinder engine and transmission. Because the dynamic system was quite simple, there was no difficulty in avoiding dynamic amplification of Hooke's Joint excitations. The joints were deliberately misaligned to eight degrees, in all ships of this model, to avoid false brinnelling by the needle bearings. This arrangement has been successfully employed with no distress throughout the life of the design.

### DESIGN CONSIDERATIONS

The discussion on control of vibratories does not complete the essential information required for successful application of Hooke's Joints. The proportions of the parts affect the dynamic behavior and must be established prior to the dynamic calculations. As noted elsewhere, the life of these couplings is determined by the amount of acceptable wear. The wear, in turn, is determined by the loads and the proportions of the parts which carry these loads. An understanding of the wear mechanism is necessary to proportion the parts for an acceptable life. Therefore, it is felt that a short treatment on load distribution and wear behavior is in order.

The capacity of a universal joint may be divided into two parts, the torque-carrying capacity of the parts other than the bearings and the life capacity of the bearing.

An actual example of a successful design for an aircraft application may illustrate this process. A study was made of the misalignment angles that could be obtained under steady operating conditions. The configurations resulted from the tolerance build-up between transmission and engine locating points plus engine expansion over the temperature range specified. The greatest angle obtained was a  $2.4^\circ$  of which  $2^\circ$  was maximum allowable installation error on each of two joints plus  $0.4^\circ$  for operational misalignment. (The actual installation error is  $1.4^\circ$  maximum, rather than the  $2^\circ$  anticipated.)

A study was made of maneuver misalignments. The greatest anticipated deflection produced a total misalignment of  $4^\circ$  on the individual joint. (A misalignment of this magnitude has never been measured.)

The torque-carrying capacity of the parts other than the bearings were then proportioned. The load schedule was:

- (1) Load from maximum operating torque.
- (2) Limit load = 200 per cent (1).
- (3) Ultimate load = 1.5 (2) = 3 (1) = 300 per cent maximum operating load.

The parts were stress analyzed under two conditions:

- A.  $10^{\circ}$  misalignment, no vibratories.
- B.  $2^{\circ}$  misalignment, 20 per cent vibratory torque assumed.

Case A is a static load condition involving the usual analyses for combined stresses. Case B is a fatigue condition for which stress concentration factors must be applied to the combined stresses. The resultant steady plus alternating stresses were evaluated by conventional methods. This treatment proportioned the yokes, spider (cross), interconnecting shaft, attachment fittings, and attaching hardware.

The proportions of the parts designed by this process were also determined by the desired loads on the bearings. The capacity of the bearings is a dynamic bearing life problem. The bearings in a Hooke's Joint used for significant power transmission are rolling contact bearings. This means eventual failure by rolling contact fatigue. Finite life is dictated by the cyclic compressive loading found in rolling contact bearings.

To digress momentarily, attempts have been made to use sleeve bearings, but success has been elusive. The design conditions include oscillating motion, a centrifugal field affecting lubrication migration and a mean load + an alternating load less than the mean load. This is beyond the present capacity of sliding bearing technology. A way may be found to use sleeve bearing universal joints for significant power transmission. That time is not yet here.

The rolling contact fatigue condition requires the usual bearing life calculation to give a B-10 life for some time limit. The conventional bearing life calculation is not of particular interest unless other forms of distress can be avoided.

There are four sources of distress to be considered: skewing, skidding, true brinelling and false brinelling.

Skewing control requirements are affected by the length/diameter ratio of the rolling cylindrical elements. This discussion will be confined to needle bearings, because of their widespread use in this application. One solution is to use a caged needle bearing, although the contact stresses are higher and the static Brinell capacity is lower. In the example cited, a cage was not used. The crowned rollers had a length/full diameter ratio of approximately 3.5. Skewing was not a problem. Among the contributing factors were a hardened flat thrust washer to react the centrifugal load, close tolerances, hardness level and material selection of inner and outer races, and the nature of the load distribution along the roller length. The last factor is of considerable significance and will appear later.

Skidding appears to be a phenomenon difficult to induce, requiring some combination of high speeds, large angles, lubrication starvation, loose tolerances and a definite sequence of load variation. For a skid to start with the roller at rest, starting friction to slide must be less than starting friction to roll. For a rolling roller to skid, starting friction to slide must be less than rolling friction. For a skidding roller to continue skidding, sliding friction must be less than starting friction to roll. In general, starting friction to slide  $>$  sliding friction  $>$  starting friction to roll  $>$  rolling friction. In addition, a skidding roller will pile up a lubricant wedge simultaneously with a metal pickup under the loaded area. This metal pickup (local welding and tearing) resists further sliding by increasing the co-efficient of friction until starting friction to roll is the path of least resistance. The resultant roll then introduces lubricant to the contacting area. In other words, a skid-relieving mechanism is involved. In the example cited, skidding has never been induced and the effects of skidding have never been observed.

True Brinelling is the third form of distress. Similar to the preceding two forms, it is relatively uncommon and avoidance is not difficult. With true Brinelling, an indentation will be observed, characteristically on the inner race, with displaced material in a raised ridge on either side of the indentation. Obviously, two conditions must exist. The first is an overload and the second is perfect alignment. Given sufficient static capacity, the overload is the result of a vibratory. Very little misalignment is required to increase the area and distribute the overload. There is one source of overload which is not obvious. A crowned roller whose centrifugal load is not reacted by a thrust washer can move radially outward and become cocked in a radial plane when the load distribution applies the highest load at the outboard end of the roller. The roller crown, which was intended to aid in avoiding skidding, introduces a wedging effect as well as reducing the area carrying the load. If the misalignment is small enough, true Brinelling can occur. A zone of true Brinelling versus misalignment is shown on Figure 5.

The last area of distress is false Brinelling. Here an indentation will be found, similar to true Brinelling, but without the raised ridge of displaced metal on either side. The original surface of the bearing race will extend to the edge of the indentation with no evidence of deformation or of deformed metal which has been flattened. False Brinelling results from a concentrated load oscillating over a small area. This is a situation akin to fretting. The ratio of roller diameter to inner race diameter tends to remain fairly constant. This allows the establishment of a range of misalignment within which false Brinelling may occur. Experience determines the variation in probability of false Brinelling. This is shown on Figure 5. The misalignment angle producing the greatest probability of false Brinelling may vary with the lubricant. A fix possible with simple systems is to increase the misalignment angle to avoid the zone of false Brinelling, if it occurs. On one aircraft application, false Brinelling occurred, the universal joints were deliberately misaligned until at 8° the false Brinelling was eliminated.

The wear situation described here has widespread verification in general, although the details vary from case to case. An example is the curve of life versus misalignment angle for universal joints in agricultural applications, shown on Figure 6.

The key to the wear situation in the design phase is in the determination of the Hertz stress. It is here that experience varies most widely from theory.

The classic method of determining the load distribution within a radial bearing may be found in Reference 1, Page 60. This theory, verified by test under ordinary conditions, is that the maximum load carried by a single rolling element may be determined by the Strikeck equation:

$$F_{max} = 5 \frac{F_r}{Z} \quad \text{Equation (27)}$$

where  $F_{max}$  = the maximum load on a rolling element,

$F_r$  = Radial force

$Z$  = Number of rolling elements

5 = A constant, practical for ordinary conditions of operation

This load is then used for a Hertz stress calculation according to the method of Reference 2, Page 288.

The equation is:

$$f_c = .591 \sqrt{PE \frac{D_1 + D_2}{D_1 D_2}} \quad \text{Equation (28)}$$

where

P = F<sub>max</sub>/length of roller = load

E = Modulus of elasticity

D<sub>1</sub> = Diameter of roller

D<sub>2</sub> = Diameter of inner race

Wear indications observed on a great many samples over a long period of time define a load distribution as shown on Figure 7. An envelope is shown which encloses all of many superimposed, observed wear indications. The wear indications on any one sample will not reproduce this pattern, but will lie inside this envelope. It will be observed that this envelope has an area of approximately one-half the projected area. The wear indications on any individual sample are a function of the variation in dimensions of the component parts of that sample. With normal tolerances, the area on an individual sample will be approximately one-third the projected area.

The empirical conclusion reached is that for a Hooke's joint with needle bearings, the determination of the Hertz stress could use a modified Stribeck equation:

$$F_{max} = 15 \frac{F_r}{Z}$$

Equation (29)

## CONCLUSIONS

A drive train with Hooke's Couplings can be built of common materials by known methods and the performance is predictable. The predictable performance includes misalignment capability, angular accelerations, torque and speed capacity, efficiency, temperature limitation, rotating secondary couples and torsional vibratories of known frequency and amplitude.

The conditions which could lead to catastrophic failure are known, recognized, and avoidable.

In general, the life of a Hooke's Joint is a matter of establishing the limit of acceptable wear. This limit is under the influence of the low cost of replacement. Therefore, the cost of reliability is chiefly diligent maintenance.

## REFERENCES

Palmgren, A., "Ball and Roller Bearing Engineering", Third Edition, S.H. Burbank & Company, Inc., Philadelphia, Pennsylvania, 1959, PP 55-60

Roark, R.J., "Formulas For Stress and Strain", Third Edition, McGraw-Hill Book Company, Inc., New York City, New York, 1954, PP 288

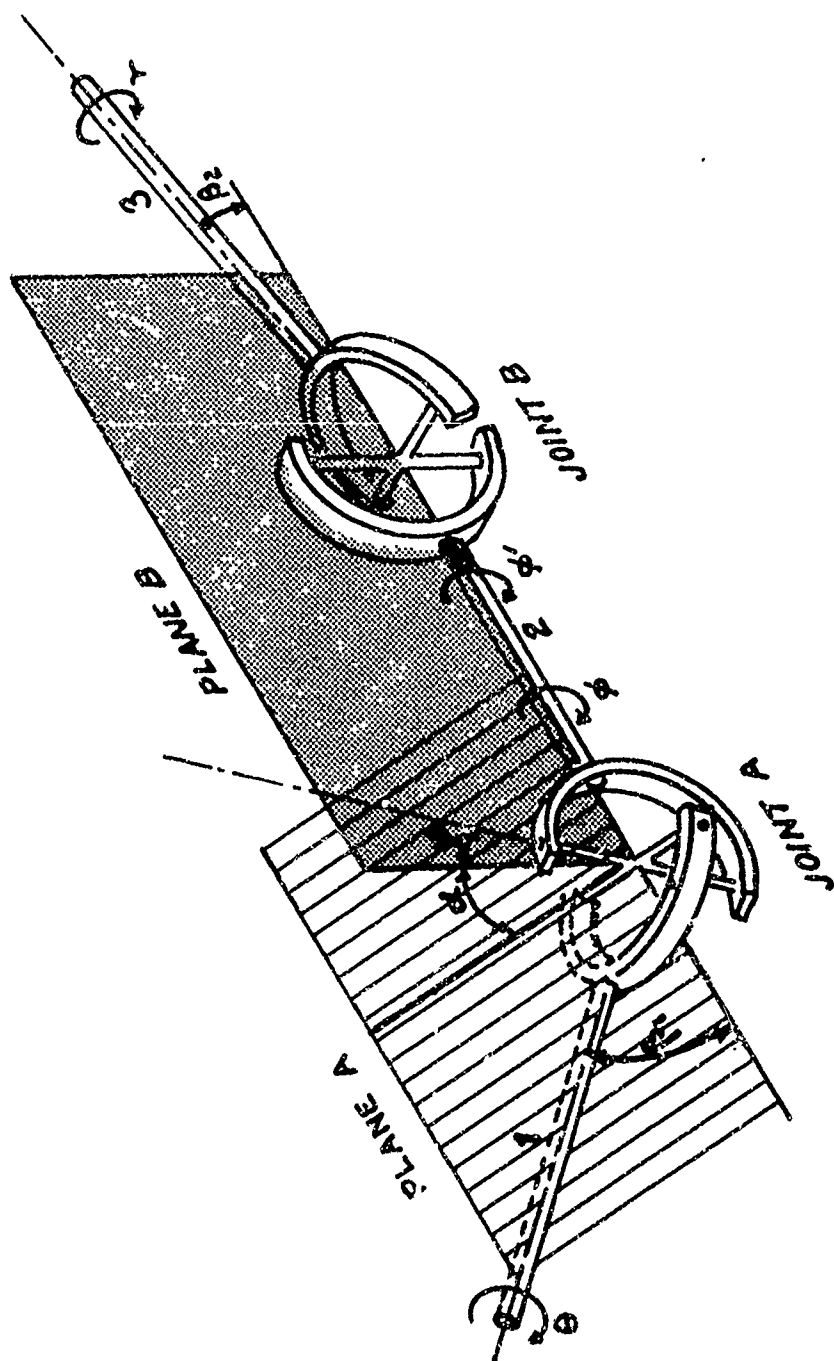


FIGURE 1.

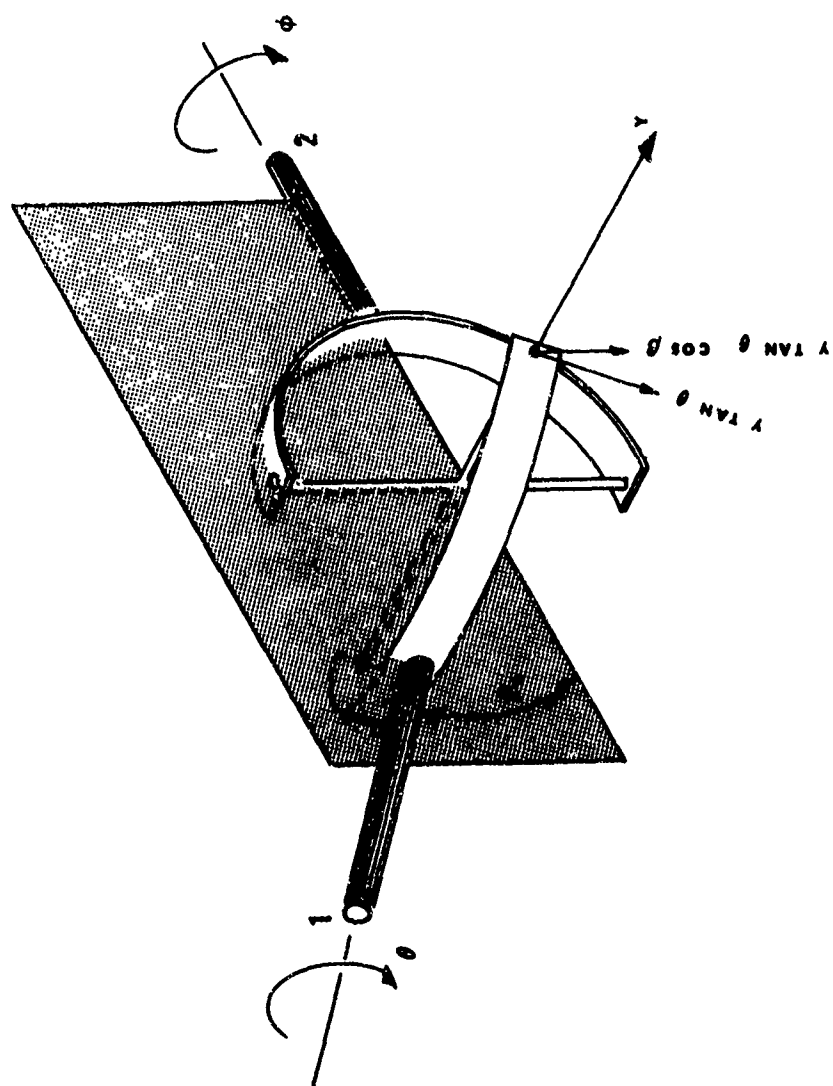


FIGURE 2

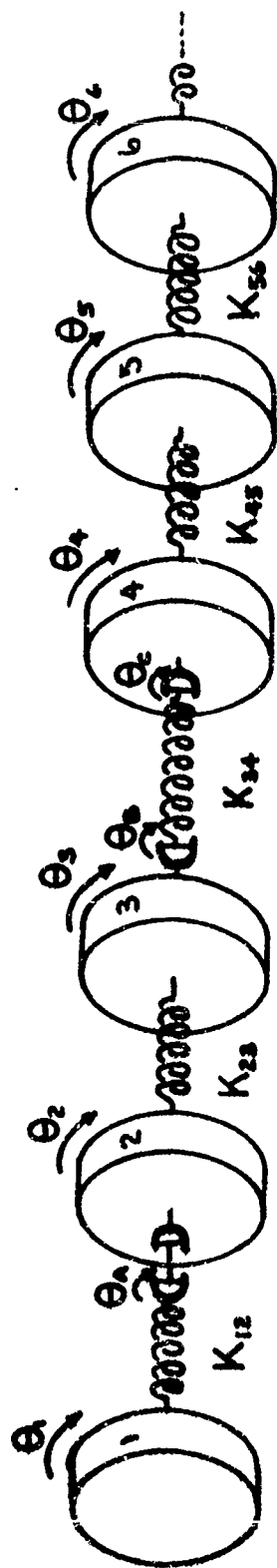


FIGURE 3A

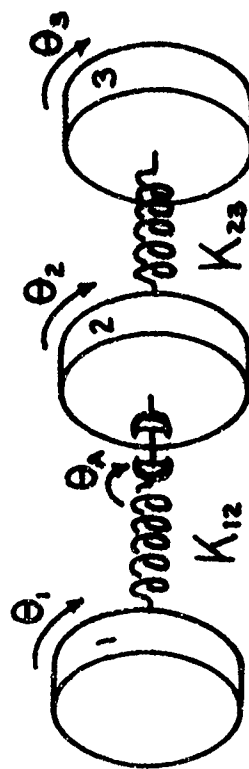


FIGURE 3B



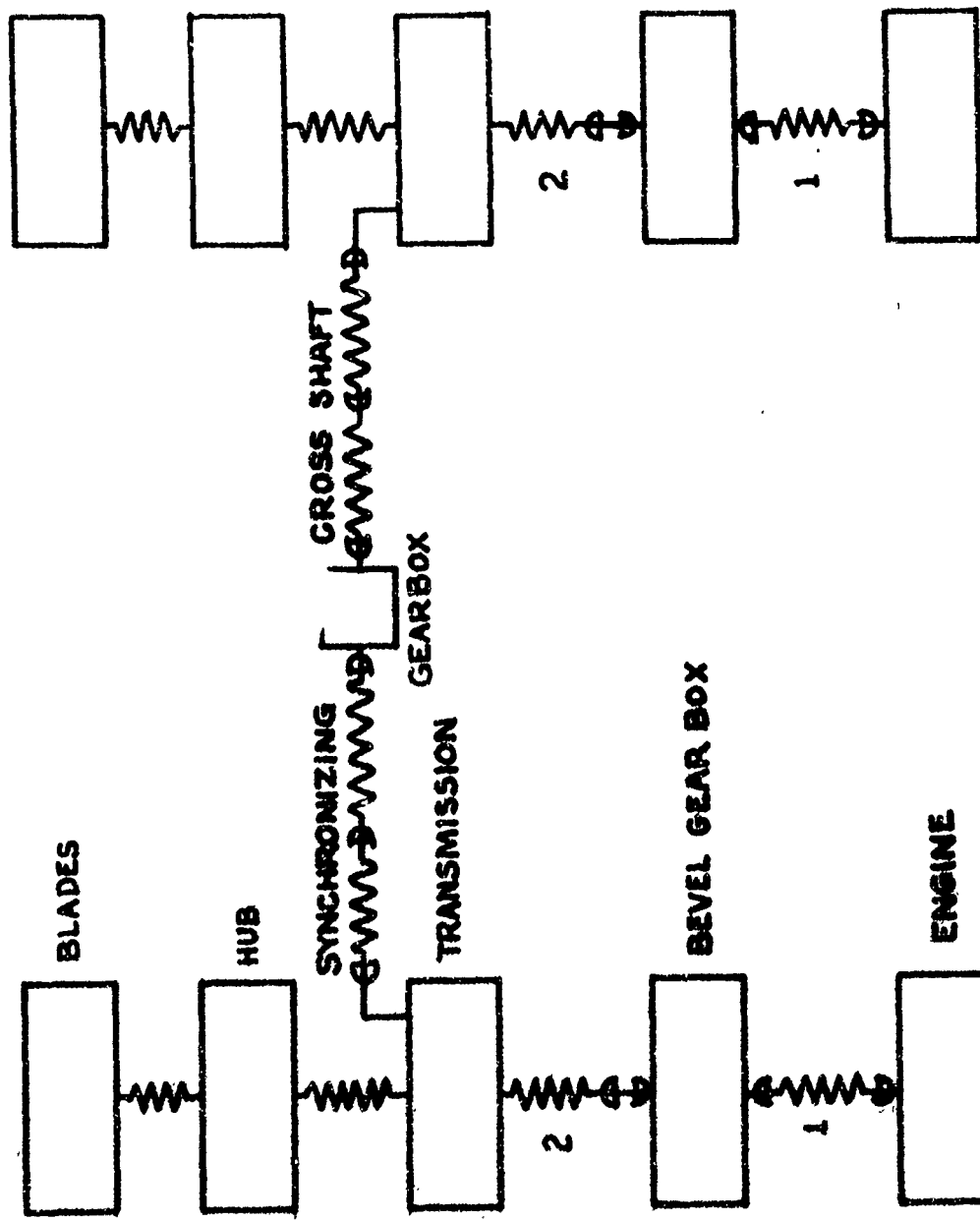


FIGURE 4

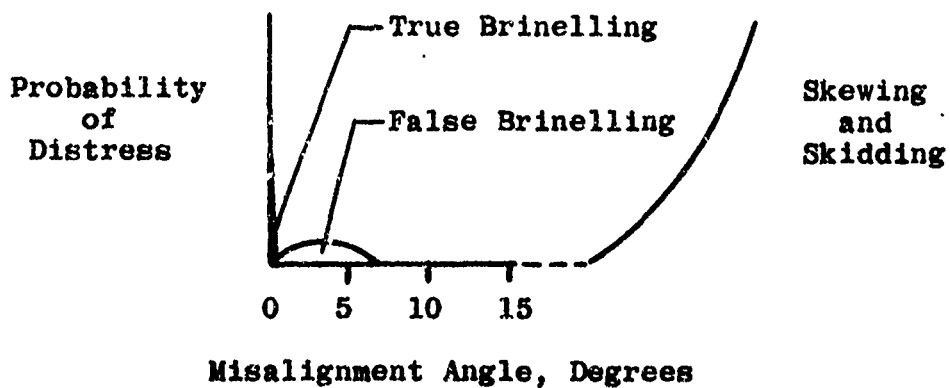


Figure 5. Probability of Distress Versus Misalignment Angle

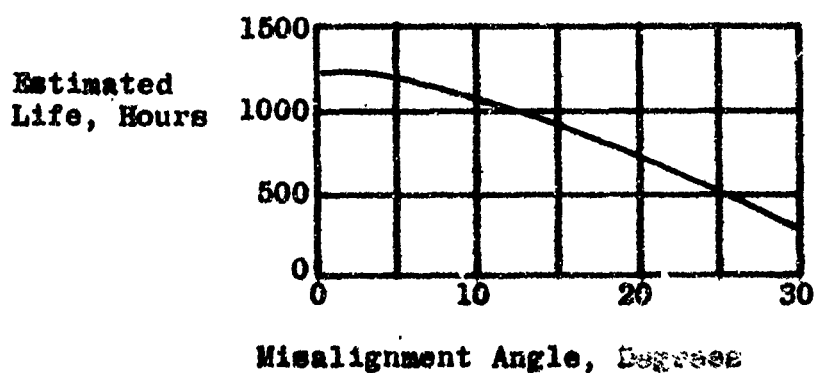


Figure 6. Lift of Agricultural Implement Joints Versus Misalignment Angle

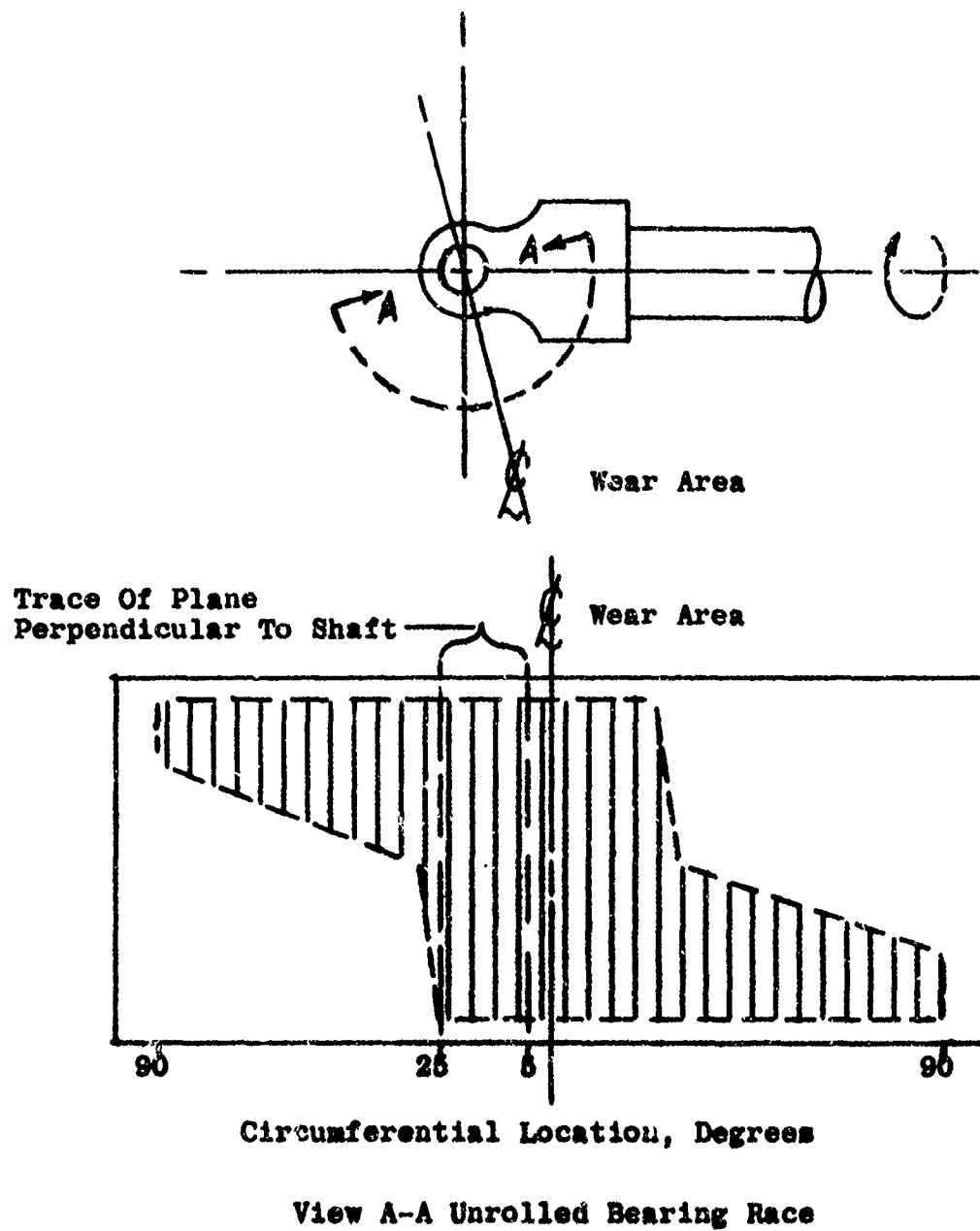


Figure 7. Wear Indication Distribution Envelope

**RECENT WORK AT THE  
ROYAL AIRCRAFT ESTABLISHMENT  
ON HELICOPTER DYNAMIC LOADS,  
WITH PARTICULAR REFERENCE TO  
HIGH BLADE INCIDENCE PROBLEMS**

**A.E. Clarke**

**Naval Air Department, R.A.E.**

**Bedford, England**

**Recent Work at the Royal Aircraft Establishment on  
Helicopter Dynamic Loads, with particular reference  
to High Blade Incidence Problems.**

**by**

**A. E. CLARKE**

**(Naval Air Department, R.A.E. Bedford, England)**

**To be presented at V. T. O. L. Dynamic Loads Symposium,  
held at Buffalo U.S.A., 26-28 June, 1963**

## I. INTRODUCTION

Dynamic loads, which are the subject of this Symposium, have many aspects and it is necessary to narrow the field in any Paper presented. I shall essentially exclude maneuvering flight cases and deal only with dynamic loads associated with the rotor of a helicopter. As the Symposium culminates in a review of outstanding problems to be investigated, you will probably also wish me to describe the relevant programme in the United Kingdom but again I must restrict the survey. I shall only outline work done at R.A.E. and more specifically that carried out either by my own Group or done elsewhere at my request, but this does represent most of the R.A.E. activity on this subject, while excluding some gust investigations. However, a simple review paper tends to be unsatisfactory so I shall not give equal emphasis to the various topics mentioned and propose to discuss high blade incidence problems in greater detail.

## II. ROTOR-FUSELAGE INTERFERENCE

Interference between an articulated rotor and a fuselage has been assessed. Theoretical and experimental work has been carried out by Bramwell and Johnston on the mutual transient interference between rotor blades in hovering conditions and a cylinder, representing a fuselage. Bramwell made the interference mathematics tractable by supposing that the flow about the aerofoil of the blade could be represented by that around a simple two-dimensional vortex. The problem was then reduced to the calculation of pressures and forces on a circular cylinder, in the first instance, in the presence of this vortex. Further, by transformations, the pressures and forces on a square sectioned fuselage and a flat plate representing a wing could also be found. The agreement with experiment was good as shown for the case of pressures on the cylinder in Slide 1. The full curve shows the calculated effect of a two-dimensional vortex and the dotted line adds a correction for blade tip effects. This pressure increment on the fuselage was found to be due mainly to the acceleration terms in the flow equation but the corresponding forces on the blade proved to be small compared with the steady aerodynamic forces.

However, the effects of distortions of the slipstream by the fuselage, i. e. the velocity terms, were found to be significant; typically 20% of the undisturbed pressures for a circular cross section and 30% with a square section. It is worth noting that although the values of the distance parameters were chosen to give reasonable pressures for experimental measurement, the more significant one for blade pressures is that expressed in terms of fuselage dimensions. Hence the 20% increment occurs when the blade is a fuselage radius distant, irrespective within reasonable limits of the ratio of blade chord to fuselage size. Willmer considered the effects on the rotor of flow curvature in forward flight due to the presence of solids of revolution representative of actual fuselages and found these to be relatively small.

### III. CALCULATION OF BLADE LOADINGS

Some of you will be familiar with earlier quasi-static theoretical work by Willmer<sup>1</sup> on the effects on blade loading of shed vorticity. This was not very well received by Industry on the grounds that it was leading to a digital computer programme of great magnitude and complexity, which was still unlikely to give adequate solutions, especially for maneuvering flight cases needed for design purposes. Hence only a limited amount of additional theoretical work has been done on the consequences of time variations in the vortex sheets of the near wake. These were found to be small for the range of blade incidence appropriate to the theory, which is based on the ideas of Jones in R. & M. 2117 "Aerodynamic Forces on Wings in Non-uniform Motion".

### IV. PROBLEMS OF HIGH BLADE INCIDENCE

In view of the criticisms previously referred to, semi-empirical methods of determining blade loadings have also been sought in a combined programme of experimental work and digital computer analysis. The computer programme was initially quite conventional, employing two-dimensional, steady but non-linear aerodynamic section data; spanwise flow effects on drag were included but only constant induced velocity was assumed. The

blades were also assumed to be infinitely stiff and the blades of the model were actually made as stiff as possible; it was established by photography that the torsional deflection at the tip never exceeded  $1^\circ$ . The original intention was to correlate total forces and moments and then go on to more detailed loading exploration, for which purpose a similar rotor with pressure plotting facilities was prepared. However, although the initial correlation was generally good, it became poor when the blade incidence was calculated to exceed  $11^\circ$ . The stalling then predicted was not apparent and hence the aerodynamic assumptions adopted were faulty. This is of particular interest in the dynamic loads context because many of our vibration problems occur in conditions associated with high blade incidence. Furthermore, as helicopter speeds are increased, and this is the object of much work at present, the tendency for such incidences increases and it is very desirable to anticipate and understand potential problem areas. The magnitude of the discrepancy is shown for a typical case in Slide 2 and no significant change in this finding could be observed throughout the range of tip speed ratios covered, up to  $\mu = 0.5$ . Similar results have been reported by Sweet and Jenkins of N.A.S.A.<sup>2</sup> Later work sought to establish the relevant aerodynamics by concentrating on conditions at  $\mu = 0.3$  to minimise the combined effects of flow asymmetry and shed vorticity, but rotor parameters giving very extreme operating conditions have been included to accentuate the interesting conditions. Some of the various steps taken to improve the computations are shown on the slide but we will return to this after they have been described. It will be noted that a theory employing linear aerodynamics without allowance for any stalling actually gives excellent agreement with the experimentally determined thrust but the blade flapping computed by this method did not agree, indicating that the distribution of loading was not correct.

#### Assessment of Causes

For reference, the  $C_L$  contours computed by the basic non-linear aerodynamic theory are illustrated in Slide 3 and have the characteristic of a plateau of relatively high values centered around  $270^\circ$  azimuth. Now let us look at experimental values, and as the pressure plotting rotor was not ready



at the time, previously published results are used. First, Slide 4 shows findings on blade loading obtained by MIT<sup>3</sup> on a small rotor and recast into  $C_L$  contours at R. A. E. by using the component of resultant velocity normal to the blade span. The distribution is quite different, with a ridge of high values at 230-240° azimuth, followed by a less clearly defined tendency for relatively low values at 300° azimuth. Note that the values of  $C_L$  reach 1.3 in regions where the air velocity is sufficiently high for the deduced  $C_L$ 's to be reasonably accurate, although the normally quoted section  $C_L$  max, at this Reynolds Number, is only 0.75. Next, Slide 5 illustrates full scale evidence from N. A. S. A. flight tests on a S58 helicopter. Similar trends are shown with  $C_L = 1.6$  compared with a  $C_L$  max = 1.1 obtained on a portion of a S58 blade in a wind tunnel at full scale speeds. With this evidence, we have to look for aerodynamic phenomena which not only change the distribution of loading in azimuth but give section lift in excess of normal two-dimensional, steady values.

#### Non-Steady Aerodynamics

Knowledge of the blade motions occurring, together with the loading distribution, suggested the possibility of a hysteresis loop in the section lift characteristics. MIT time averaged data<sup>4</sup> on aerofoils oscillating in pitch and in heave did show maximum lift values in excess of the corresponding steady conditions for some sections tested. However, there is regularly little information giving more details on non-steady aerodynamics at high mean incidence. Indeed, only that determined by the United Aircraft Laboratory<sup>5</sup> on an aerofoil oscillating in pitch could be found but this did give the complete form of lift hysteresis. Typical results are given in Slide 6, showing lift compatible with the values noted on the rotor. Also shown is the loop given by an approximating function found by R. A. E. to give a reasonable fit to almost all the experimental results and then used in the computer programme. Note, however, that in spite of the high transient values of  $C_L$ , the steady state data in this case lie in the centre of the hysteresis loop. Thus use of this results in a distribution of  $C_L$  which begins to resemble the experimental cases but which gives only a small increment

in thrust. Speculation remains on the important difference between MIT and United Aircraft findings because one of the arbitrary sections used by the former is generally similar to the NACA 0012 of the other tests. Also, of course, there are other types of non-steady motions of the blade on which there is no detailed information at all.

### Induced Velocity Distribution

The distribution of loading must also be influenced by the non-uniformity of induced velocity which actually exists over the rotor disk. This cannot on its own lead to values of  $C_L$  in excess of the maximum of the section data assumed and so it had to be combined with something other than those normally obtained in a wind tunnel. The first induced velocity distribution considered was that derived by Mangler<sup>6</sup> and confirmed experimentally near the rotor by Heyson and Katzoff<sup>7</sup>. This is symmetrical about the fore and aft axis of the rotor and hence could not be responsible for the characteristics in azimuth observed unless it was combined with the oscillating aerofoil data. The resultant computation certainly showed increased thrust but it still fell far short of the measured value. Mangler's theory strictly relates to an infinite number of blades but MIT had considered a case towards the opposite extreme by analysing their pressure plotting records from a two-bladed rotor through linear aerodynamic theory to get induced velocity at the blade. The previous discussion has suggested certain possible shortcomings in this method but any criticism applies only to a limited, although important, range of azimuth angles. Considering the findings as a whole, there is again symmetry, this time about a skewed axis, and with greater transverse gradient of velocities. The induced velocity at the tip of the retreating blade was eight times the momentum mean value and for the purpose of exploring the possible effects of varying induced velocity, this was particularly valuable as a severe case of such non-uniformity. In order to get the high  $C_L$  values, this distribution was again combined with the oscillating aerofoil data, and as before resulted in thrust considerably less than had been measured, although the general pattern of loading computed looked very similar to the experimental ones.

### Three-Dimensional Section Data

A variety of three-dimensional effects, additional to normal end corrections which had been included in the calculations, might also change section characteristics. For example, the effective sweep angles of the blade could influence the aerodynamics although at  $\mu = 0.3$ , these angles are modest except at inboard stations where the dynamic head is low. Then, the high centrifugal forces might influence the boundary layer. This is a probable cause of the unexpectedly high thrust obtained with propellers at high blade incidences and would seem to be implicit in the NASA synthesised section data<sup>8</sup> derived from hovering tests. These give  $C_{L \text{ max}}$  higher by about 0.15 than the corresponding two-dimensional case but not as high as seen in the experimental rotor lift contours. In order to make some allowance for this, these synthesised data were used in the computer programme in combination with the lift hysteresis and non-uniform induced velocity at the blade. This gave good agreement with experiment both on thrust and flapping, especially when the tendency for slightly high computed thrust at low blade incidence is remembered.

If we return to an earlier slide, (Slide 2) the results of the various processes tried can be seen. Obviously, the assessment has not been a rigorous one due to lack of comprehensive basic information and to uncertainty about whether the various factors are simply additive. It does, however, provide a reasonable basis for experimental work to acquire more data. Various unresolved questions have been referred to already and in addition, discussions with people concerned in the United States indicated some caution about the magnitude of lift augmentation indicated by the synthesised data. The rotors used were large and of typical flexible construction, but in the initial tests on the 00-series of sections at least, aero-elastic distortions were not determined. Thus the field for further experimenting is large and although such work is proceeding, the programme has not been completed as yet.

## V. EXPERIMENTAL EVALUATION OF HIGH INCIDENCE AEROFOIL SECTION DATA

### Three-Dimensional Aerodynamic Tests

Because suitable equipment was readily available, the first tests have sought better understanding of symmetrical three-dimensional aerodynamic effects. A 12 ft. diameter rotor with very stiff blades has been pressure plotted in hovering conditions through the stall and the same blades put in a wind tunnel to give two-dimensional data at the same Reynolds Numbers. The originally planned programme was somewhat curtailed because stalling did not take place simultaneously along the blade span and so some blade flapping occurred before the stall was reached at some survey stations. However, it was established by photography that structural deformations were negligible. In order to show that flow conditions were comparable for corresponding tests, transition was determined in each case by sublimation techniques with which the reaction takes place sufficiently slowly to give no record of the transient run up and run down of the rotor. The next slide, Slide 7, shows that similar flow conditions existed in the two test series and also illustrates the surprising extent of laminar flow on the rotor at 8° collective pitch. This occurred in spite of the facts that the Reynolds Number reached  $1 \times 10^6$  and the surface condition of the blade was far from good. Comparison of the two and three-dimensional results with free transition showed very little difference in the value of  $C_L$  max. obtained although stall was delayed by a few degrees of incidence in the hovering tests. The significance of this is not great because the accuracy of deducing incidence is also diminished in this region. Examination of the pressure records suggested that the strong rearward turbulent separation was moving forward more slowly in the hovering tests. Some evidence of bubble formation was also noted and further explored in the tunnel which did have singularly low turbulence due to 32:1 contraction ratio. Oil flow patterns confirmed a forward bubble. A turbulent boundary layer was induced by carborundum grains around the leading edge of 0.002" and 0.010" nominal sizes in successive tests and turbulence was also introduced into the main windstream by a coarse

screen immediately ahead of the working section. Each case gave somewhat different results with significant changes in  $C_L$  max. and stalling incidence compared with the free transition case but rearward separation was not affected. More specifically, the maximum increment in  $C_L$  max. was approximately 0.2 and stalling incidence varied by approximately  $3^\circ$ . For completeness, the hovering test will be repeated with carborundum grains but it is already reasonably clear that no value of  $C_L$  can be obtained compatible with those observed on rotors in forward flight conditions.

This investigation has brought out yet another uncertainty about the lift data to be used in loading computations. Sections of 10-15% thickness-chord ratio, which are commonly used on helicopters are known to be susceptible to variation in flow conditions but it is not clear whether the 00-series is particularly subject to such problems. Improved methods of constructing blades promise more latitude in aerodynamic design and perhaps the time has come for reappraisal of suitable sections. At the same time, it is desirable to place manufacturing tolerances on a more rational basis. Some work has been done on the latter but there is not time to deal with this.

#### Non-Steady Aerodynamic Tests

Another experimental programme is being done by Moss on an aerofoil oscillating in pitch, using a model of finite aspect ratio but with large end plates. Forces are being measured, partly to complement rather than duplicate U.A.L. work and partly to enable pitching moments to be determined. Only some preliminary exploratory tests have been done so far and the main investigation begins next month but interesting features are already apparent. As expected, considerable random scatter was encountered but two separate regimes could be seen. Usually a hysteresis loop occurred, sometimes at an unexpectedly low lift level, but occasionally the lift followed an extension of the low incidence  $C_L - \alpha$  relationship to give very high lift. As a simple mean of a large number of records, it was found that the ratio of the number of high lift excursions to the number of hysteresis loops increased with the frequency of oscillation. The natural frequency of the rig was changed and the instrumentation was varied but this result was not altered, indicating an

aerodynamic cause. A sample from the results is shown in Slide 8, on which, for clarity of presentation only a high lift case and low lift loop, without interconnection are shown. At the bottom of the slide is a copy of a typical trace showing the lift variations. For this particular frequency of oscillation, which was 4.6 cycles/sec. or 17 chords forward motion per cycle, the high lift excursion occurred once every two or three cycles. This might be another example of the flow problems previously described. The Reynolds Number of this test was  $0.9 \times 10^6$  and it was established that the size of the quasi-static hysteresis loop also shown on the slide diminished as the Reynolds Number was increased above this value. Consequently, the wind speed will be doubled in the next tests. However, a hysteresis loop can be produced by lag in establishing circulation irrespective of other flow phenomena and so additional results are awaited with interest.

## VI. SIGNIFICANCE TO HELICOPTER DESIGN

In spite of an incomplete experimental programme, the implication remains of need to embody non-steady data when considering dynamic load problems associated with high blade incidence. If finally substantiated, it also means that a semi-empirical method of loading analysis will probably have to be retained at least for this particular problem. The hypothesis is well founded on the results of tests done with model rotors but the evidence from more important full scale work is based on analysis of the one case of detailed information available. Since this paper was first drafted, the interesting one presented by Cornell<sup>9</sup> at the 1963 American Helicopter Forum has become available. This attributes all the excess rotor thrust to induced velocity distribution and although details of the theory used are not known, it is evident that comparison was made with a case of excess thrust without exceptional local values of  $C_L$ . The introduction and exploration of augmented section lift adds enormously to the dynamic loads programme and it is suggested that its significance to helicopter design should be assessed by further evaluation of full scale evidence. Any such evidence at tip speed ratios in excess of 0.3, which is characteristic of most current production helicopters, would be particularly valuable.

## VII. CALCULATION OF BLADE DEFORMATIONS

I will conclude by brief reference to a foray into structural matters. The work described has been concerned with aerodynamic problems of stiff blades but it is obviously important to consider the additional consequences of blade flexibility. As aerodynamicists, we are keenly aware of the increasing complexity of this aspect of blade problems and have sought a simplified method of handling structural deformations. Starting with the Raleigh-Ritz principle, Wilde has used Legendre Polynomials as approximations instead of the more usual trigonometric series, because of the similarity between blade behaviour and a chain. These orthogonal functions converge very rapidly but boundary conditions cannot be satisfied in the usual way. Instead, these are handled by placing constraints on the constants associated with the functions rather than by the functions themselves. The method has been found to work well, and to be economical in computer facilities, for blades with uniform mass distribution but non-uniform stiffness, which is a reasonable approximation to many modern blades. At present it is only suitable for assessing the possibilities of resonant conditions between the blade structure and the aerodynamics. However, work is proceeding, using this as a first step and adopting similar techniques, to determine the modes forced by the applied aerodynamics.

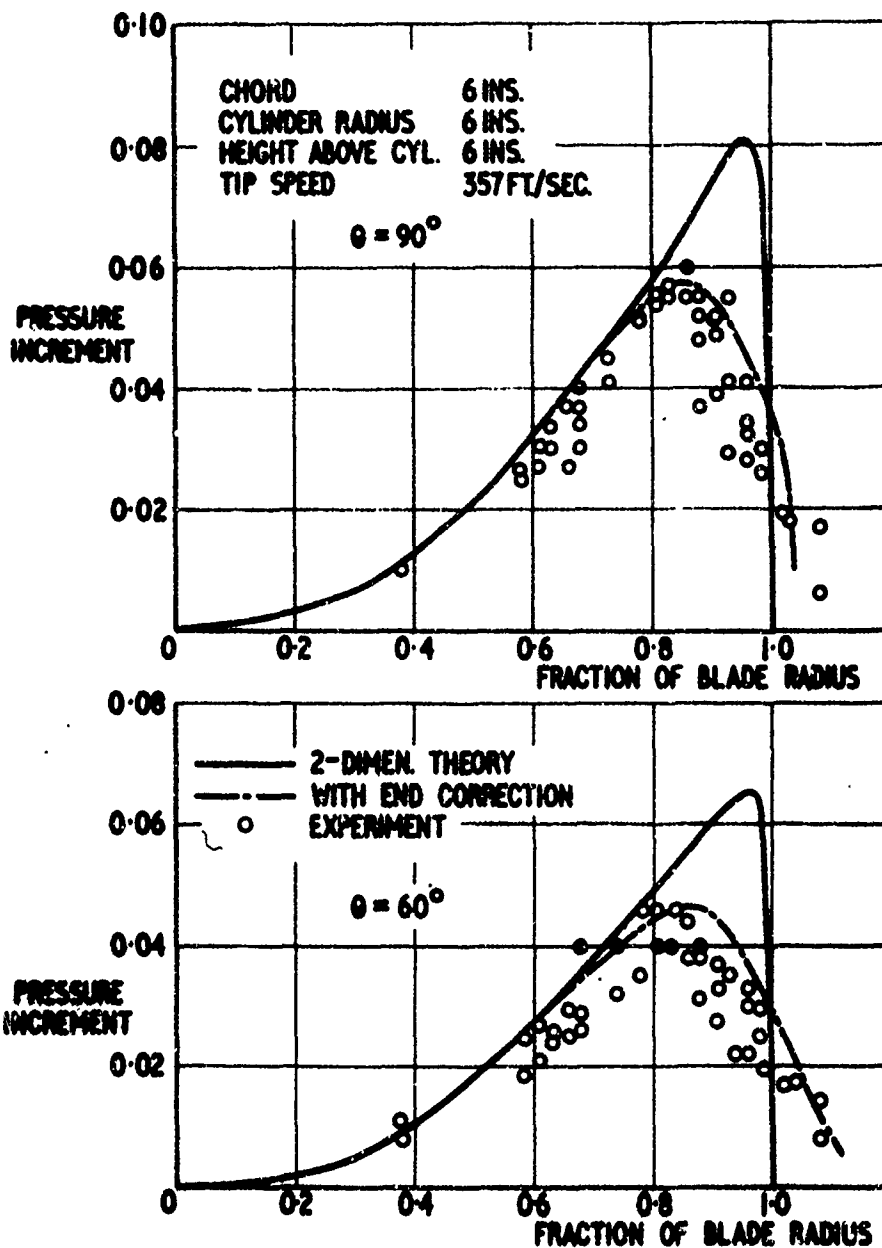
## REFERENCES

1. M.A.P. Willmer      The Loading of Helicopter Rotor Blades in Forward Flight.  
R.A.E. Report Naval 2.      April 1959
2. G.E. Sweet  
J.L. Jenkins      Results of Wind-Tunnel Measurements on a Helicopter Rotor Operating at Extreme Thrust Coefficients and High Tip Speed Ratios.  
Presented at I.A.S. Meeting      Jan. 1963
3. G. Falabella  
J.R. Meyer      Determination of Inflow Distributions for Experimental Aerodynamic Loading and Blade Motion Data on a Model Rotor in Hovering and Forward Flight.  
N.A.C.A. Tech Note 3492      Nov. 1955
4. R.L. Halfman  
H.C. Johnson  
S.M. Haley      Evaluation of High Angle of Attack Aerodynamic Derivative Data and Stall Flutter Prediction Techniques.  
N.A.C.A. Tech Note 2533      Nov. 1951
5. F.O. Carta      Experimental Investigation of the Unsteady Aerodynamic Characteristics of a N.A.C.A. 0012 Aerofoil.  
U.A.L. Report M-1283-1      Aug. 1960
6. K.W. Mangler      Calculation of the Induced Velocity Field of a Rotor.  
R.A.E. Report Aero 2247      Feb. 1948
7. H.H. Heyson  
S. Katzoff      Induced Velocities Near a Lifting Rotor with Non-uniform Disk Loading.  
N.A.C.A. Report 1319      1957



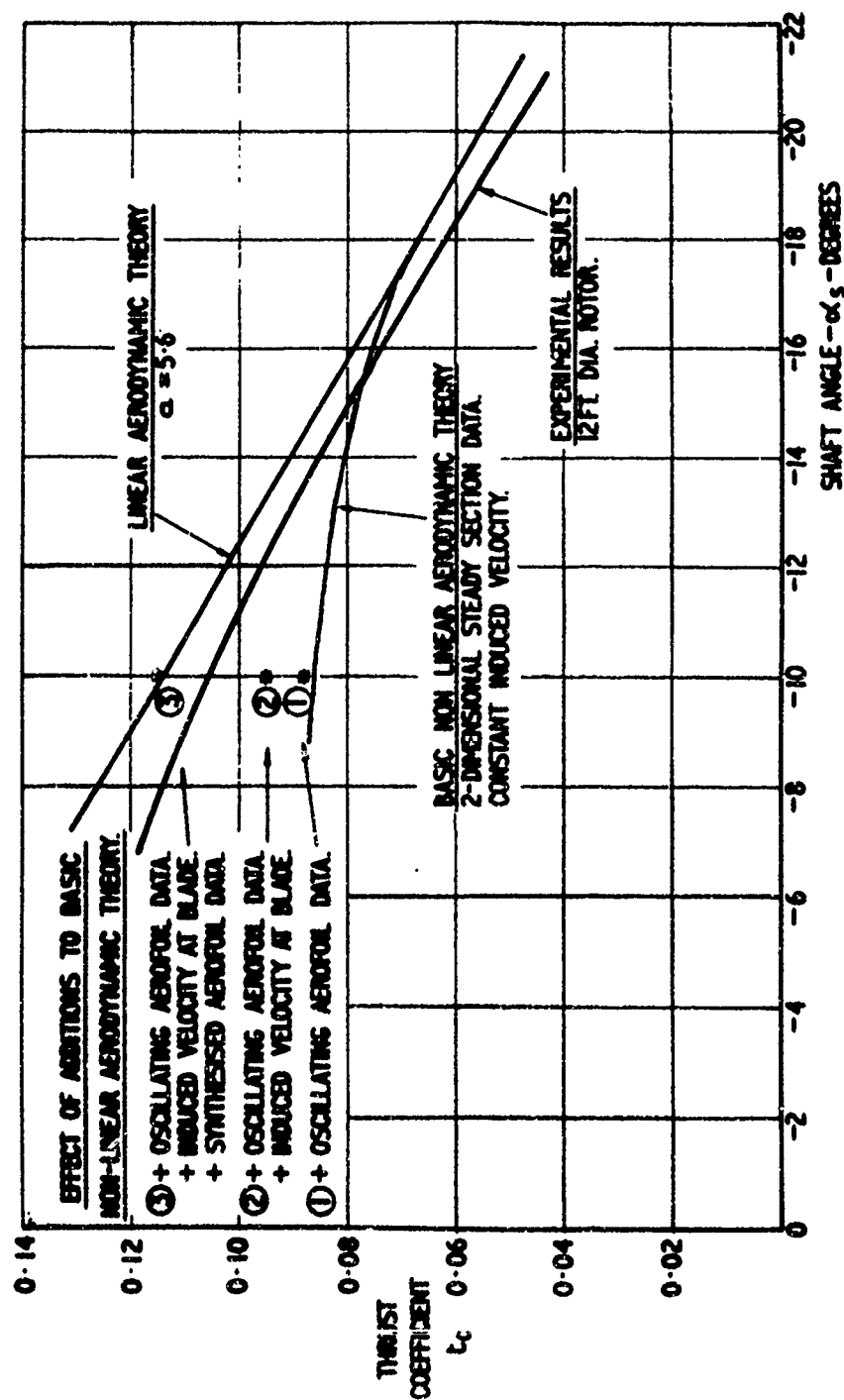
## REFERENCES (CONT.)

8. P. J. Carpenter      Lift and Profile Drag Characteristics of  
N.A.C.A. 0012 Airfoil as Derived from  
Measured Helicopter Rotor Hovering  
Performance.  
N.A.C.A. Tech Note 4357      Sept. 1958
9. R. Piziali      Computed Induced Velocity, Induced Drag,  
F. DuWaldt      and Angle of Attack Distributions for a  
Two-Bladed Rotor.  
Presented at A.H.S. Meeting      May 1963



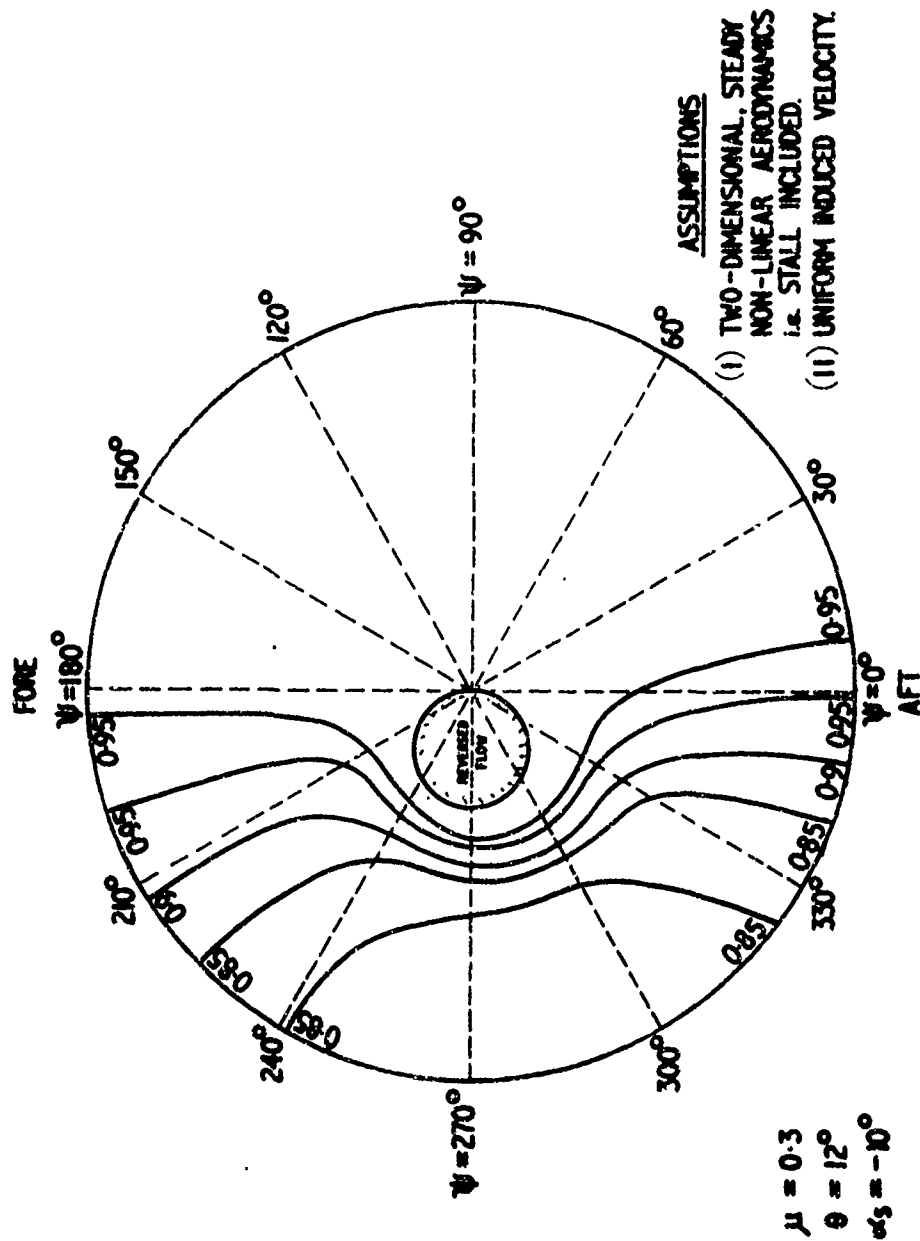
DYNAMIC PRESSURES ON A  
CIRCULAR CYLINDER.

FIGURE 1



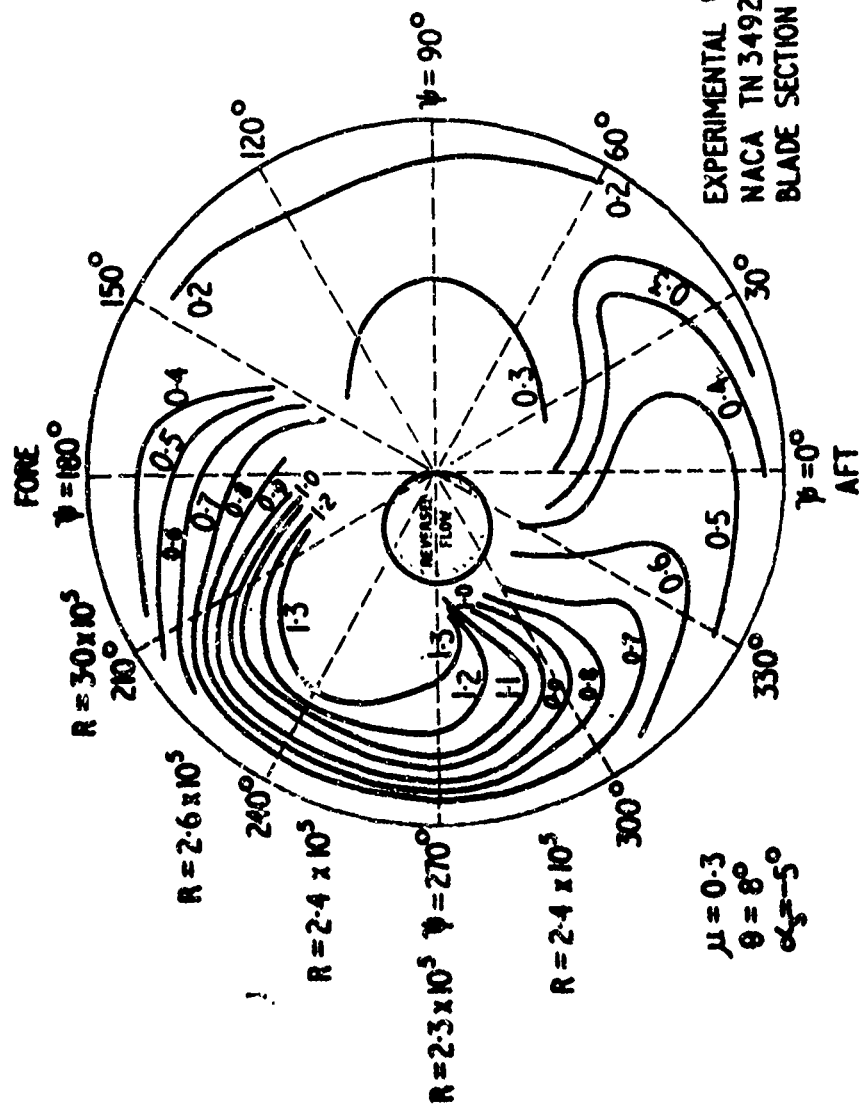
COMPARISON BETWEEN EXPERIMENT AND COMPUTATIONS OF THRUST.

FIGURE 2



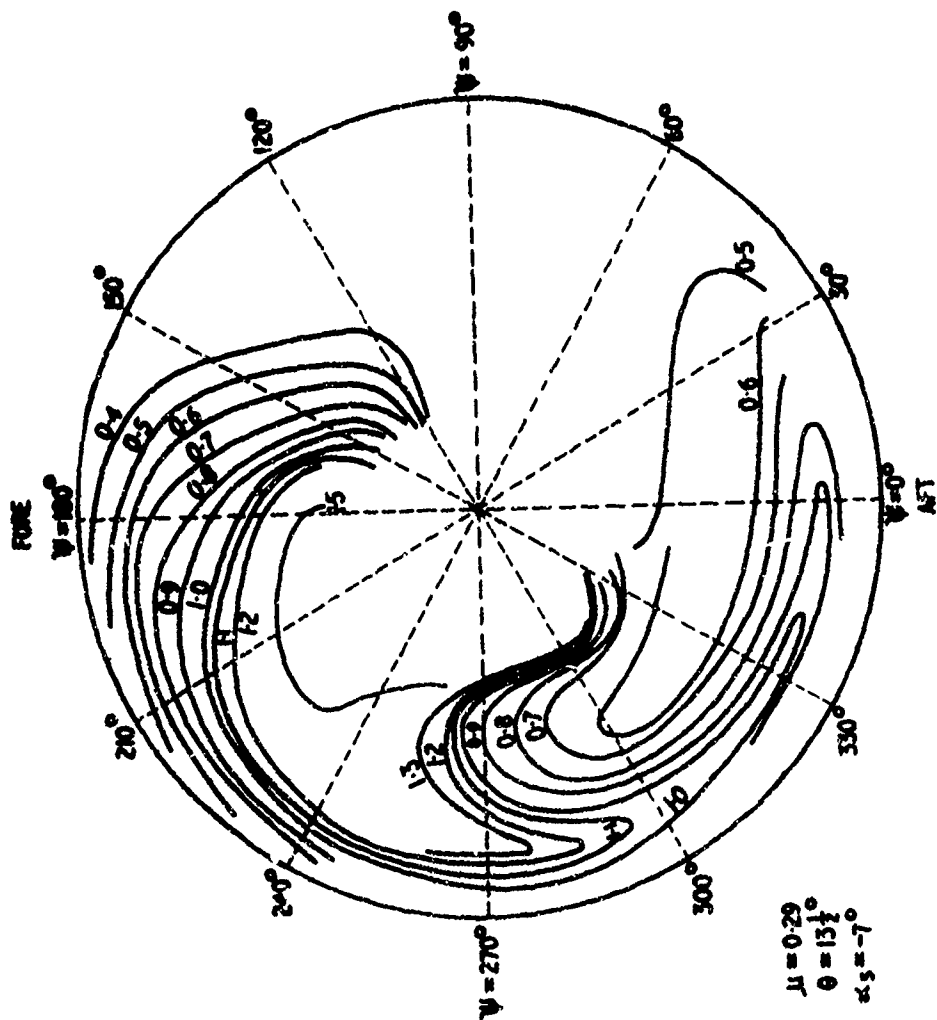
COMPUTED BLADE CL CONTOURS.

FIGURE 3



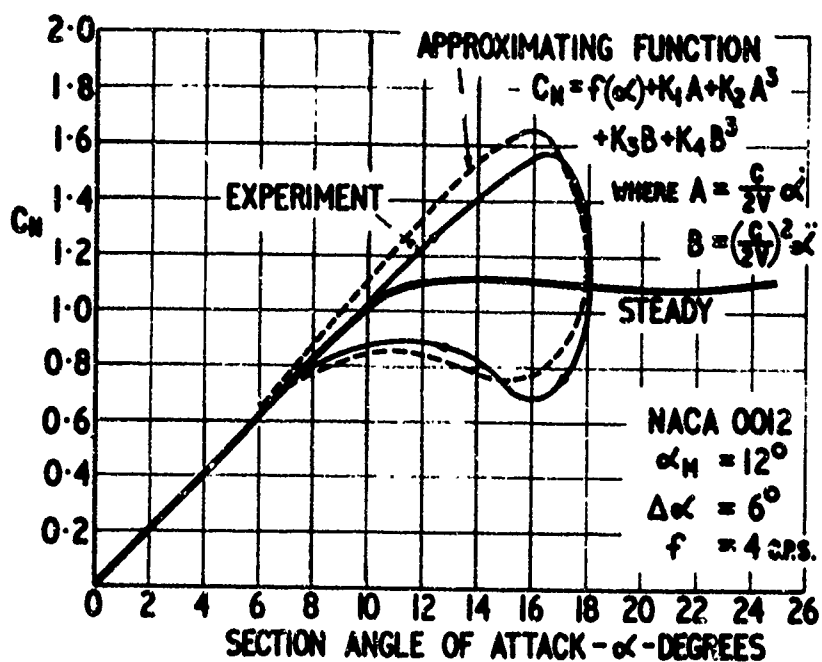
EXPERIMENTAL BLADE  $C_L$  CONTOURS.  
 5 FEET DIAMETER MODEL ROTOR (M.I.T.)

FIGURE 4

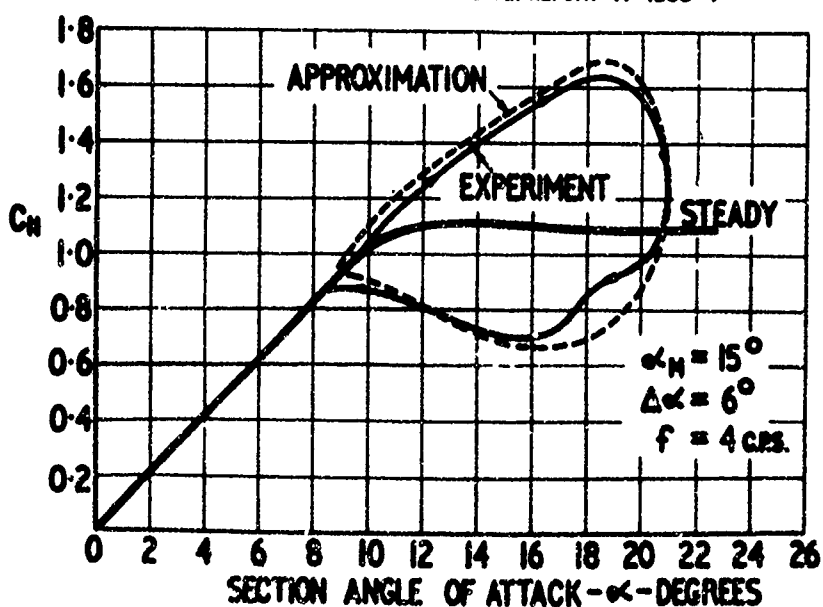


EXPERIMENTAL BLADE  $C_L$  CONTOURS.  
FLIGHT TESTS S58 HELICOPTER (NASA)

FIGURE 5

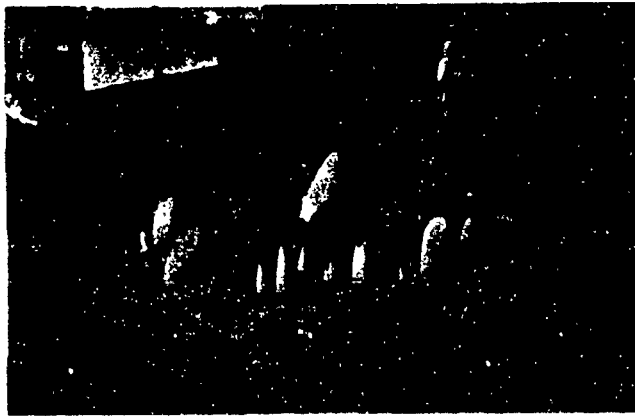


EXPERIMENTAL WORK REF. U.A.L. REPORT M-1283-1



## LIFT HYSTERESIS FROM PITCH OSCILLATIONS

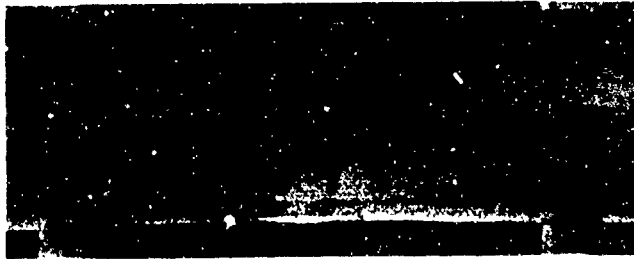
FIGURE 6



0.75R  $\alpha = 4.1^\circ$   
 $Re = 0.91 \times 10^6$   
 $V = 283 \text{ FT/SEC.}$

HOVERING TEST

$\theta = 8^\circ$  600 RPM.



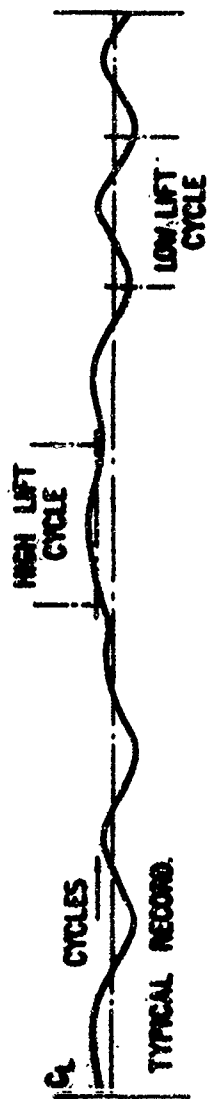
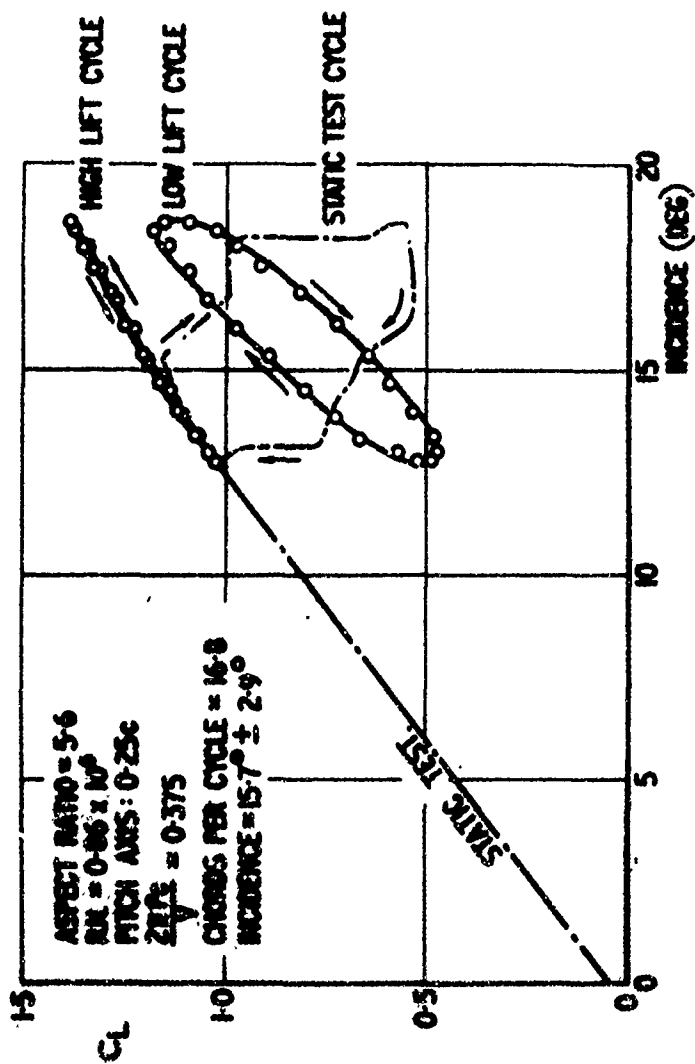
TUNNEL TEST

$\alpha = 3\frac{1}{2}^\circ$   $V = 280 \text{ FT/SEC.}$   
 $Re = 0.90 \times 10^6$

COMPARISON OF BOUNDARY LAYER TRANSITION POINTS  
 IN HOVERING AND IN SMOOTH AIRFLOW  
 WIND TUNNEL CONDITIONS.

FIGURE 7





HIGH INCIDENCE PITCH OSCILLATIONS.  
 NACA 0012 SECTION.

**SOME RESULTS FROM  
THE ARMY LOW ALTITUDE, HIGH-SPEED  
FLIGHT PROGRAM (MAN-MACHINE)**

**John E. Yeates  
TRECOM, Virginia**

**Some Results From the Army  
Low-Altitude, High-Speed Flight Program (Man-Machine)**

**by**

**John E. Yeates \***

**U. S. Army Transportation Research Command  
Fort Eustis, Virginia**

**To Be Presented**

**at the**

**U. S. Army - Cornell Aeronautical Laboratory  
Dynamic Loads Symposium**

**at**

**Buffalo, New York, 26-27 June 1963**

## SUMMARY

As part of a program to extend the Army's capability for combat surveillance and target acquisition in the field army area, flight tests were conducted in 1960 and 1961 to aid in establishing operational requirements for aircraft that might be required to operate at high speed and low altitude.

This paper reports on the tests and some of the results that were obtained in the field relative to gust accelerations experienced while flying at very low altitudes and at speeds approaching 550 knots. In addition, some of the problems that occurred relative to man-machine compatibility are discussed.

## INTRODUCTION

Means for improving and extending the Army's capability for combat surveillance and target acquisition throughout the field army area are currently under serious study. In 1959, the Army Aircraft Development Plan 1960-1970, prepared by the Chief of Research and Development, indicated the desirability of developing a new surveillance aircraft for battlefield surveillance missions. To aid the Army in its thinking, many industrial organizations investigated possible aircraft configurations and submitted many design concepts as solutions to the stated requirements. In 1960, an Army Aircraft Review Board (Rogers' Board) was established to review industry's design concepts and to explore possible courses for future action. The evaluation of industry's design concepts pointed to the desirability of conducting surveillance missions in the low-altitude, high-speed flight regime. The Rogers Board called particular attention to the effects of gust loadings on the aircraft and crew and recommended that studies and tests be conducted to aid in establishing operational requirements for aircraft that might be required to operate at high speed and low altitude.

Subsequently, the Army Aviation Board was assigned the task of conducting such studies and tests (Reference 1). The Aviation Board was assisted in the tests by the U. S. Navy, which provided personnel, material (some of the aircraft), and maintenance facilities; by the U. S. Army Aviation School, which provided observer personnel; by the U. S. Army Transportation Research Command, which provided instrumentation, personnel, technical assistance, and photographic support; by NASA's Langley Research Center, which provided instrument equipment and advice; by the U. S. Army Human Research Unit, which accomplished the

human factors portion of the flight test program; by the U. S. Army Hospital, Fort Rucker, Alabama, which conducted the physiological portion of the flight test program; and by various industrial organizations, which provided technical advice and assistance for their respective aircraft.

During the early stages of the program, it was determined that little measured and correlated objective flight test data pertaining directly to the man-machine compatibility design problem was available. Several low-level flight programs had previously been conducted by the Air Force and Navy to gather turbulence data for use in the analysis of aircraft structures. However, data were not available for correlated man-machine compatibility for a low-level, high-speed surveillance-type mission. The Army's flight program was designed to gather information in the human factors area which would provide background for future laboratory studies and to obtain data to aid in establishing the technical characteristics for future aircraft that may be required to operate at high speed and low altitude.

This paper reports on the 1961 tests and some of the results that were obtained in the field relative to gust accelerations while flying at very low altitudes and at speeds approaching 550 knots. In addition, some of the problems that occurred relative to man-machine compatibility are discussed.

## TEST EQUIPMENT AND INSTRUMENTATION

### TEST EQUIPMENT

The following aircraft were used in the 1961 flight test program (Reference 2):

1. The A4D-2N (Figure 1), a single-place, high-performance, lightweight Navy attack airplane with a modified delta wing. It is powered by an axial-flow turbojet engine which develops 7700 pounds of static thrust.
2. The G-91 R/1 (Figure 2), single-place, swept-wing, high-performance strike reconnaissance fighter. It is powered by an axial-flow turbojet engine which develops 5000 pounds of static thrust.
3. The N-156 (Figure 3), a single-place, supersonic fighter powered by two axial-flow turbojet engines which develop 2500 pounds of static thrust each and 3850 pounds of static thrust with afterburner.
4. The YAO-1 (Figure 4), a side-by-side, two-place, tactical surveillance airplane. It is powered by two turboprop axial-flow gas-turbine engines which develop 1005 equivalent shaft horsepower each.
5. The T-38, a two-place version of the N-156, used as an Air Force supersonic trainer. It was used as a chase plane for low-altitude, high-speed flights of the N-156.

### INSTRUMENTATION

The A4D, G-91, and N-156 aircraft were instrumented with NASA-VGH recorders to measure the following quantities:

1. Vertical acceleration (range - 2g to 4g)
2. Airspeed (range 0 to 460 knots), for speeds above 460 knots the aircraft airspeed systems were used.
3. Pressure altitude.

The YAO-1 was instrumented with a CEC 5-114-P3 18-channel oscillograph to measure the following quantities:

1. Stick position
2. Pitch attitude
3. Angle of attack
4. Pitch rate
5. Norman acceleration (cockpit)
6. Lateral acceleration (cockpit)
7. Norman acceleration (cg)
8. Lateral acceleration (cg)
9. Sideslip angle

An absolute altimeter (radar altimeter) was used on most of the test aircraft for maintaining the required altitude above the ground.

In addition, physiological studies consisted of preflight and postflight weighing of the pilot and observer; inflight records of pulse rate, respiration rate, heart activity (EKG), and body temperature were systematically sampled during the missions. Throughout the test period, a general evaluation was made of the pilot's mental attitude in an effort to determine the psychological effects of flight stress and fatigue. The human factors portion of the tests will be only briefly mentioned in this paper.



## TEST PROGRAM

### SCOPE

The A4D, G-91, N-156, and YAO-1 aircraft were flown for sustained periods at low altitudes and high speeds over various types of terrain under daylight visual flight conditions (VFR). In compliance with the regulations governing the use of the low-level test routes, a chase airplane accompanied each flight. The test airplanes were instrumented to measure the response to turbulence; the pilots were instrumented to measure selected physiological changes occurring during the flight; observers were used in the chase airplane (T-38) and in the YAO-1 to determine psychomotor ability during turbulence. The pilots and observers were given standardized debriefings, the results of which were correlated with airplane acceleration response data.

### TEST CONDITIONS AND PROCEDURES

#### Location

The flight test program was conducted at the following locations to obtain representative turbulence data over the various types of terrain indicated:

1. Naval Air Station, Jacksonville, Florida (flat land, swamps, water).
2. Naval Air Station, Memphis, Tennessee (rolling land, foothills).
3. Marine Corps Auxiliary Air Station, Yuma, Arizona (desert, mountains).

#### Terrain Clearance

The absolute altitudes at which the flights were flown depended upon the type of terrain and were as follows:

Surface TerrainAverage Absolute Altitude (ft)

Water	50
Flat land and swamps	200
Rolling land and mountains	400

The chase airplane maintained an altitude of 800 feet above that of the test airplane.

Aircraft Speeds

The airplanes were flown in the following speed ranges in order to provide correlation of the data between the jet aircraft at the lower speed limits and to exploit the individual capabilities of the airplanes at the upper speed limits.

AirplaneIndicated Airspeed (knots)

A4D	350 - 425
G-91	350 - 500
N-156	350 - 575
AO-1	200 - 220

Flight Duration

The duration of the individual flights was a function of the airplane characteristics, course layout, and flight objectives. The mission times varied from 30 to 80 minutes.

Method of Evaluation of Acceleration Data

The acceleration traces of the flight records from the test airplanes were evaluated to obtain the magnitude of all gust acceleration increments from the steady-state, or 1g, datum. The evaluation was limited to single peaks, positive or negative, between any two consecutive intersections of the acceleration trace with the "g" reference line. The traces

were read in such a manner as to eliminate the acceleration due to maneuvers. A threshold of 0.2g was used, with the acceleration peaks read to the nearest 0.1g increment.

Gust velocities,  $U_{DG}$ , were calculated from acceleration data using the derived gust velocity formula contained in Reference 3. For these calculations, the airplane weight and wing loading were adjusted during the flight to compensate for the fuel consumed. The lift-curve slopes used in the calculations were furnished by the aircraft manufacturers.

## TEST RESULTS

### Atmosphere Encountered

In Figure 5, derived gust velocity,  $U_{DE}$ , is plotted against miles to exceed a given gust velocity for all the 1960 and 1961 tests along with results from the Air Force B-66 low-level gust program (Reference 4).

In general, slightly higher gust velocities were experienced during the 1961 tests than during the 1960 tests. The 1961 test results show good agreement with the B-66 data. Most of the 1961 tests results presented were obtained in the Yuma test area; however, a limited amount of data was obtained in the Jacksonville and Memphis test areas.

### Measured Gust Data

In Figure 6, miles to exceed a given normal acceleration is shown for the A4D, G-91, N-156, and YAO-1 in the Yuma test area. It can be seen that the N-156 experienced the highest gust accelerations of the three high-speed aircraft while the YAO-1 experienced the lowest acceleration (this is to be expected since the maximum speed of the YAO-1 was only about one-half the speed of the other aircraft). The acceleration data of Figure 6, along with other aircraft parameters, are used to calculate a derived gust velocity,  $U_{DE}$ . Figure 7 shows the derived gust velocity so obtained, plotted against miles to exceed a given gust velocity for the test aircraft. It can be seen that of the three high-speed aircraft, the A4D encountered the highest gust velocity while the N-156 experienced the lowest gust velocity. Comparing Figures 6 and 7, it would appear that for the three high-speed aircraft, the N-156 had the highest gust sensitivity while the A4D had the lowest gust sensitivity. Figure 8 shows the acceleration data of Figure 6 plotted against time. As an example,

a 1-hour mission would on the average encounter one incremental gust of 1g intensity.

### Terrain Clearance

Minimum safe terrain clearance is dependent upon a number of interacting factors. Some of these are: visibility, turbulence, speed, terrain variation, orientation with respect to terrain variations, aircraft response characteristics, obstacle spacing, obstacle visibility, sun or station, pilot fatigue, reference cues, in-cockpit tasks, density altitude, wind direction, familiarity with route and airplane, mission time, and general experience level. With good visibility and a minimum of cockpit tasks, the parameters of terrain variation, turbulence, mission duration, and speed are the main factors affecting safe terrain clearance. Minimum desirable terrain clearances for missions of  $\frac{1}{2}$  hour duration as determined by subjective evaluation of the pilots immediately following the test flights are presented.

In Figure 9, terrain clearance is plotted against speed for flat terrain, where terrain clearance is thought of as the distance above obstacles, such as trees, houses, etc. It can be seen that as the speed was increased from 200 knots to 500 knots or more, the desired terrain clearance increased from 25 to 50 feet for smooth to mild turbulence. As the turbulence levels increased, the terrain clearance amounts increased accordingly.

In Figure 10, terrain clearance is plotted against speed for rolling hills. It appears that the introduction of moderate relief changes (rolling hills) to the flight mission changes the type of flying from contour following to peak-to-peak flying as a function of speed and altitude. It can be seen

from the figure that an extra margin of about 200 feet altitude over that required for flat terrain is needed for rolling terrain.

It was the opinion of the pilots that terrain clearance for each type of terrain would have to be increased by 50 - 100 percent if the mission duration were increased to 2 hours.

#### Physiological Effects

The physiological studies consisted of preflight and postflight weighing of the pilot and inflight recordings of body temperatures, heart activity, and respiration. Throughout the test period, a general evaluation was made of mental status, attitude, and fatigue. The findings of this portion of the tests are covered in Reference 2 and will not be discussed in this paper.

### CONCLUSIONS

It is concluded that the program:

1. Acquainted the Army with the problems associated with the operation of high-speed aircraft at very low altitudes (LAHS).
2. Showed the pilots could satisfactorily complete a  $\frac{1}{2}$ - to 1-hour simulated LAHS mission while flying through light-to-moderate turbulence.
3. Pointed out the need for future research that would establish the effect of longer missions and higher turbulence levels on pilot performance.
4. Showed a possible need for gust alleviation for future aircraft, to make the ride more tolerable for the pilot and to provide a more stable platform for the electronic equipment.
5. Provided data which showed that the turbulence encountered at extremely low altitudes was not nearly as severe as had been predicted.

#### REFERENCES

1. "Man-Machine Environment Compatibility Studies and Test in Support of Surveillance Aircraft Development", Report of Project No. AVN 4860, U. S. Army Aviation Board, 14 December 1960.
2. "Phase III of Man-Machine Environment Compatibility Studies and Test in Support of Surveillance Aircraft Development", Report of Project No. AVN 4860, U. S. Army Aviation Board, 28 May 1962.
3. Pratt, K. G., and Walker, W. C., "A Revised Gust-Load Formula and a Reevaluation of V-G data Taken on Civil Transport Airplanes from 1933 to 1950", NACA TR 1206, 1954.
4. Sanders, K. D., et al, "B-66B Low Level Gust Study", Vol 1, WADD Technical Report 60-305, March 1961.



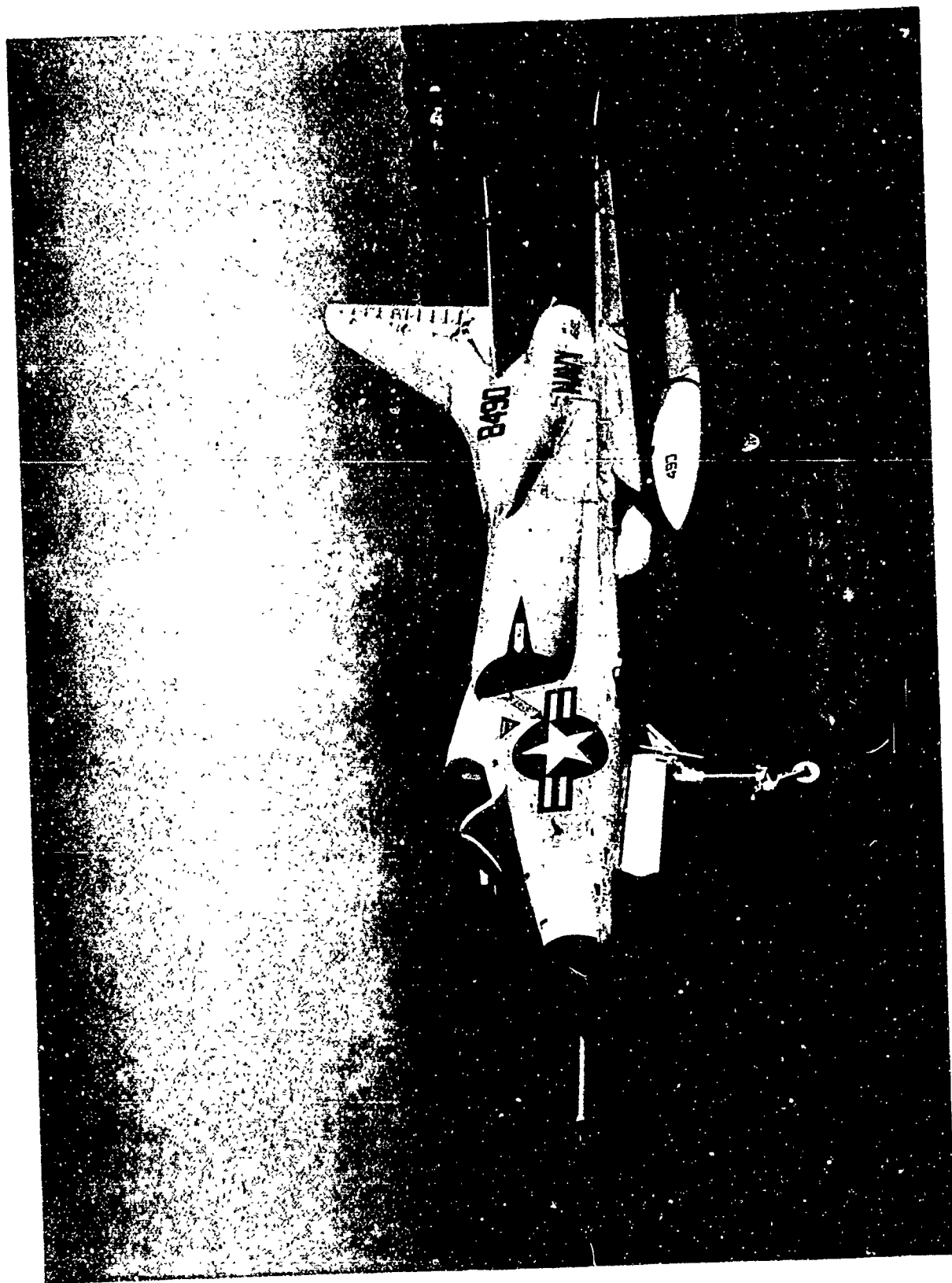


Figure 1 - A4D-2N

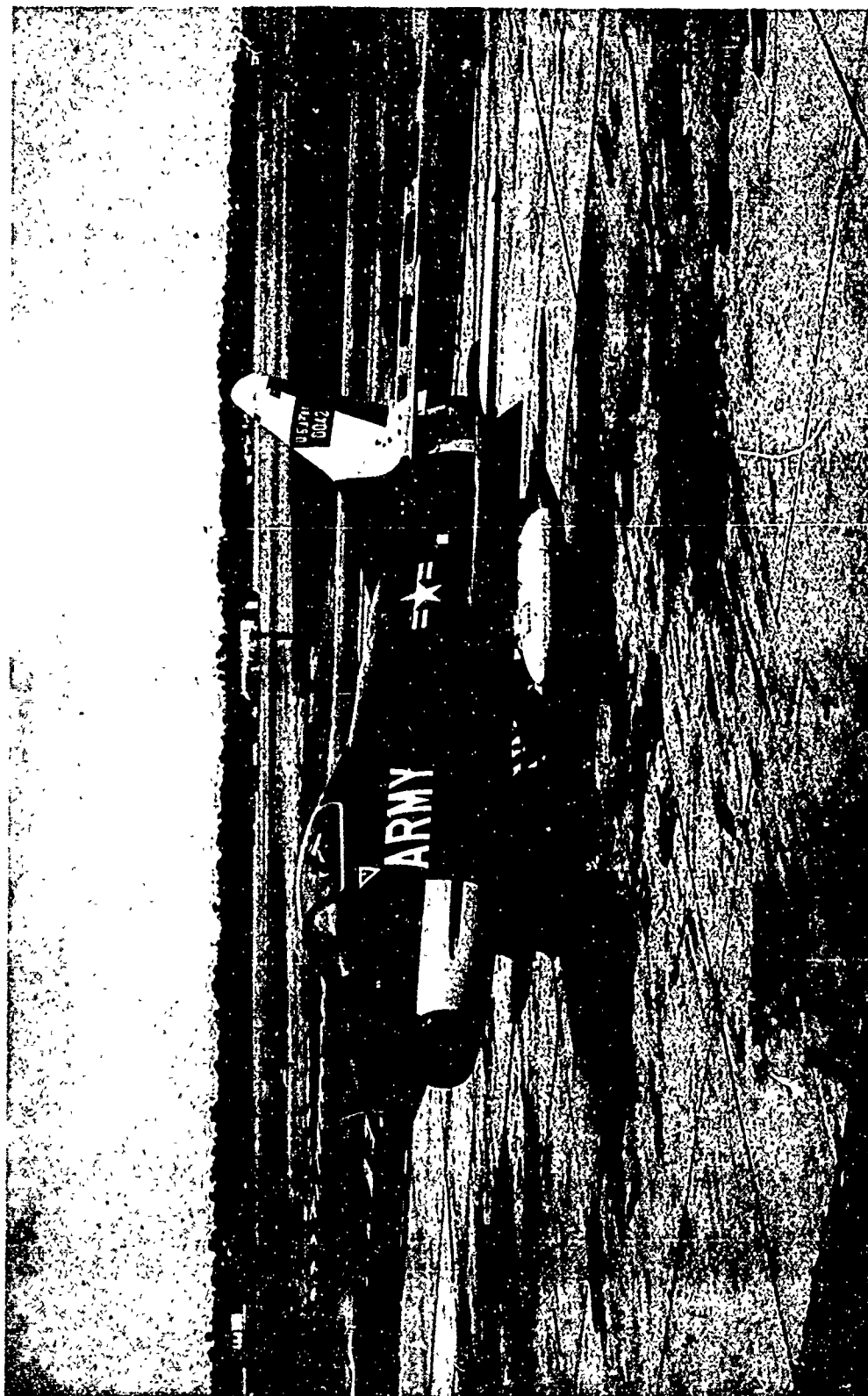


Figure 2 - G-91R/1

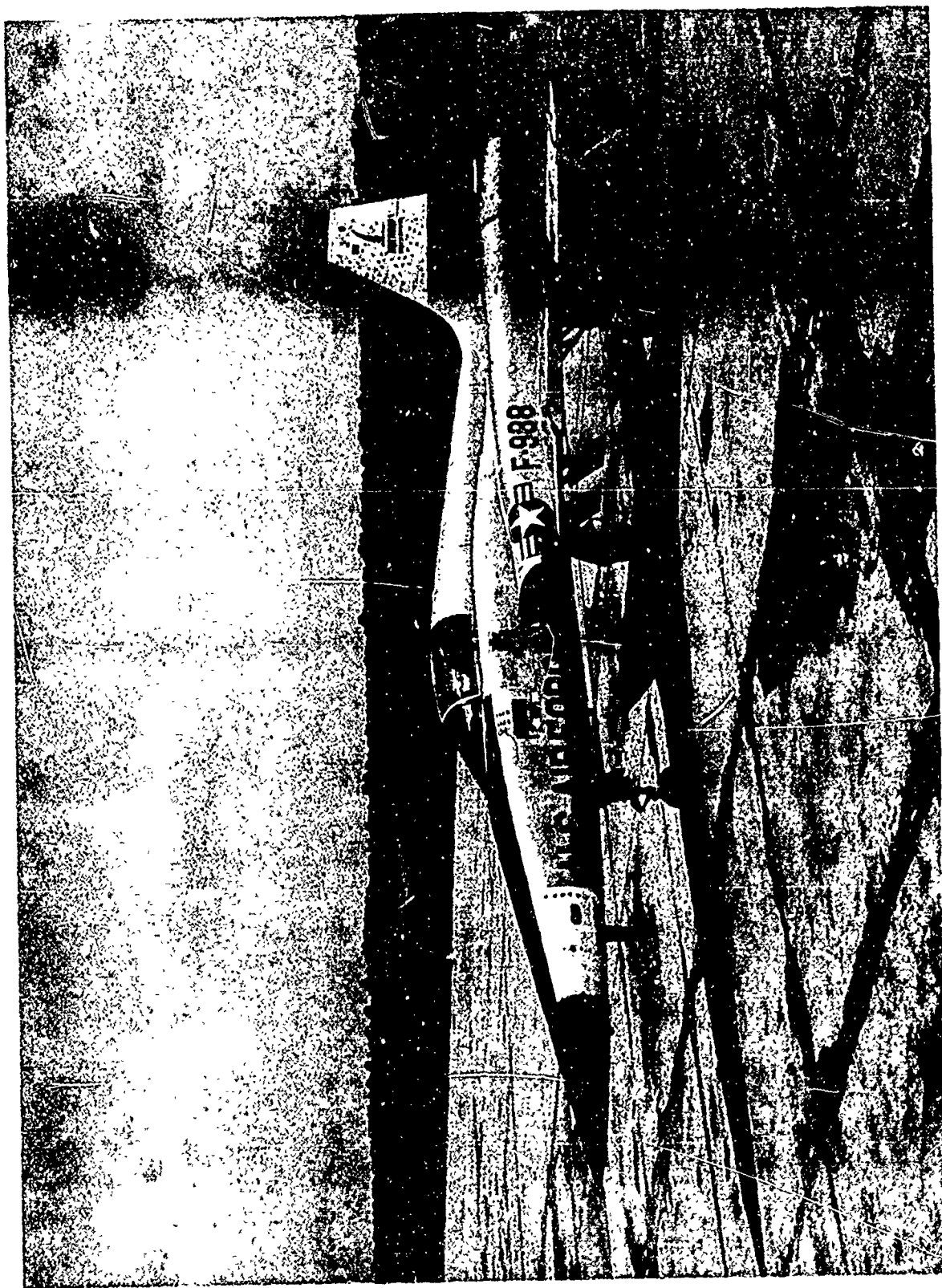


Figure 3 - N-156



Figure 4 - YAO-1

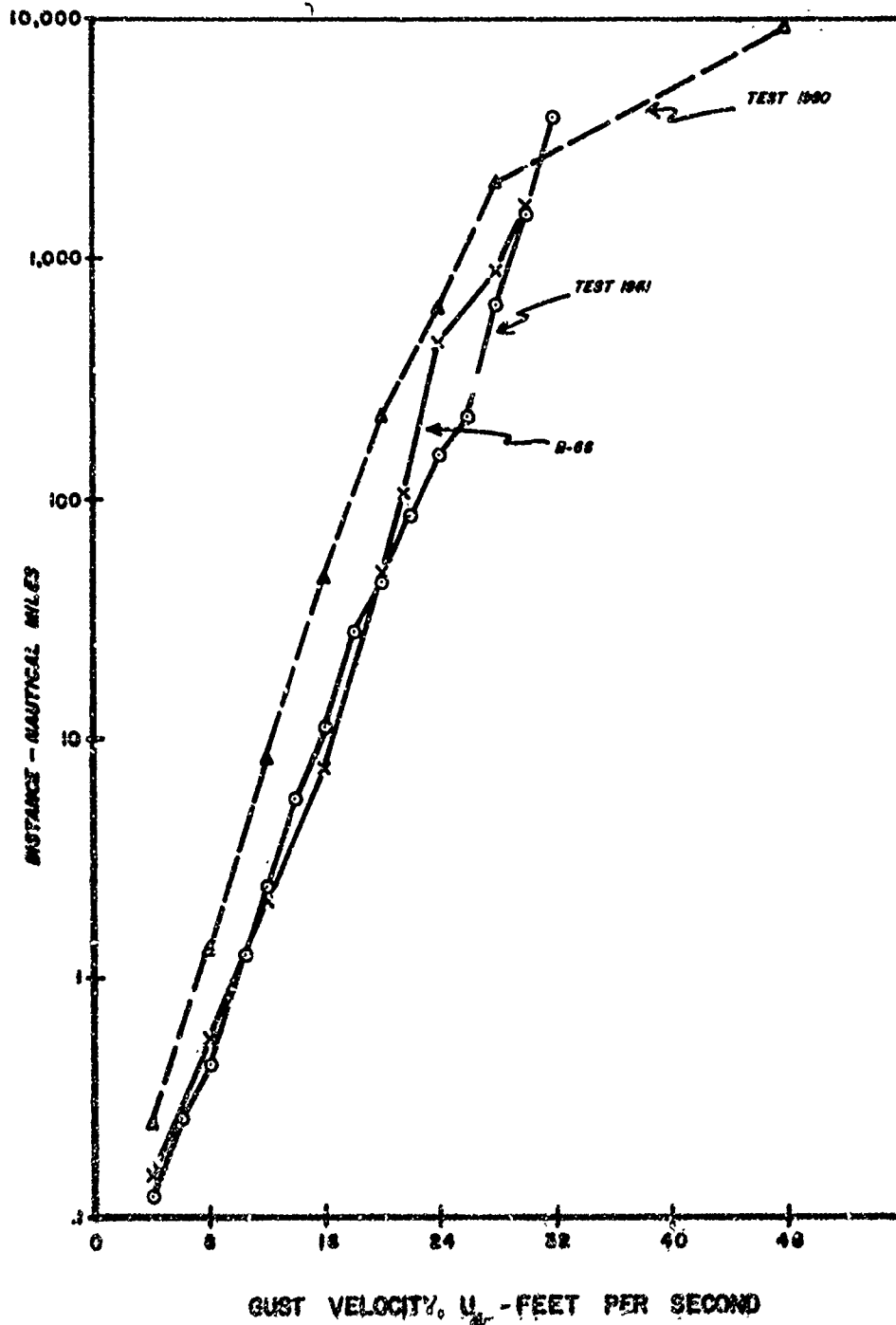


FIGURE 5- NUMBER OF MILES TO EXCEED A GIVEN GUST VELOCITY,  $U_{gs}$  -TOTAL ATMOSPHERIC SAMPLE COMPARED WITH OTHER LOW LEVEL DATA.

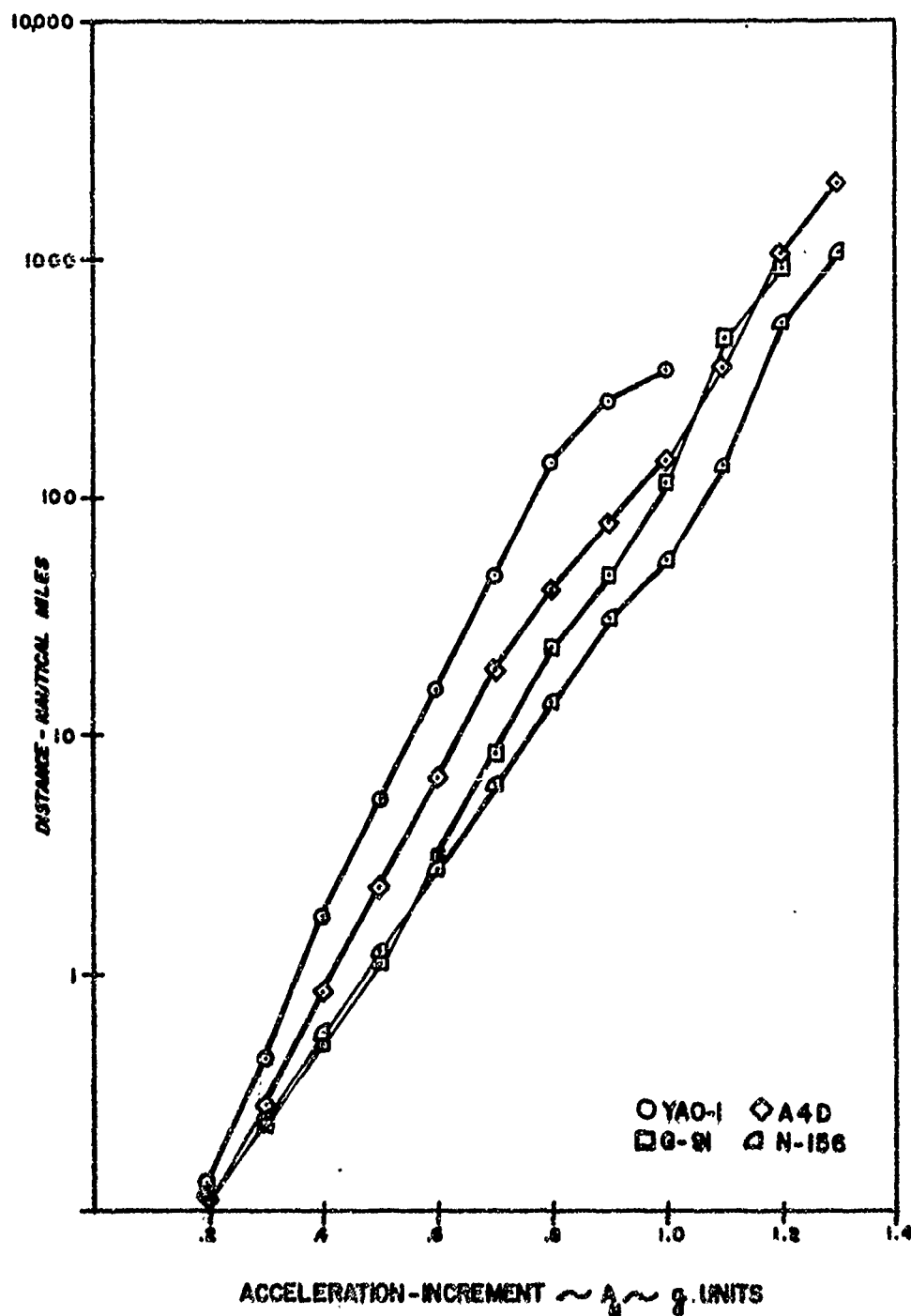


FIGURE 6- NUMBER OF MILES TO EXCEED A GIVEN NORMAL ACCELERATION,  $A_n$ , FOR THE TEST AIRCRAFT (YUMA DATA).

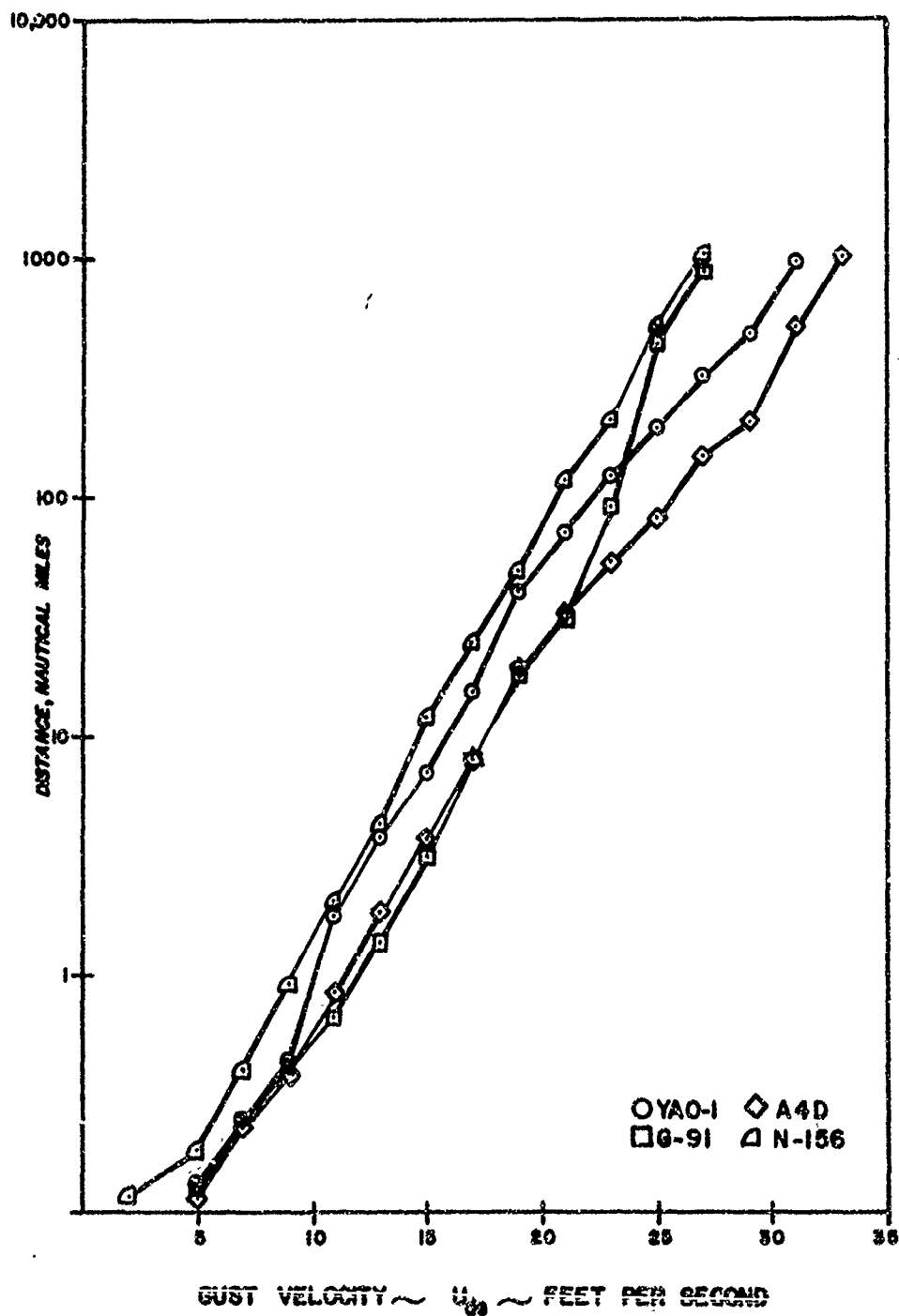


FIGURE 7- NUMBER OF MILES TO EXCEED A GIVEN GUST VELOCITY,  $U_0$ , FOR THE TEST AIRCRAFT (YUMA DATA).

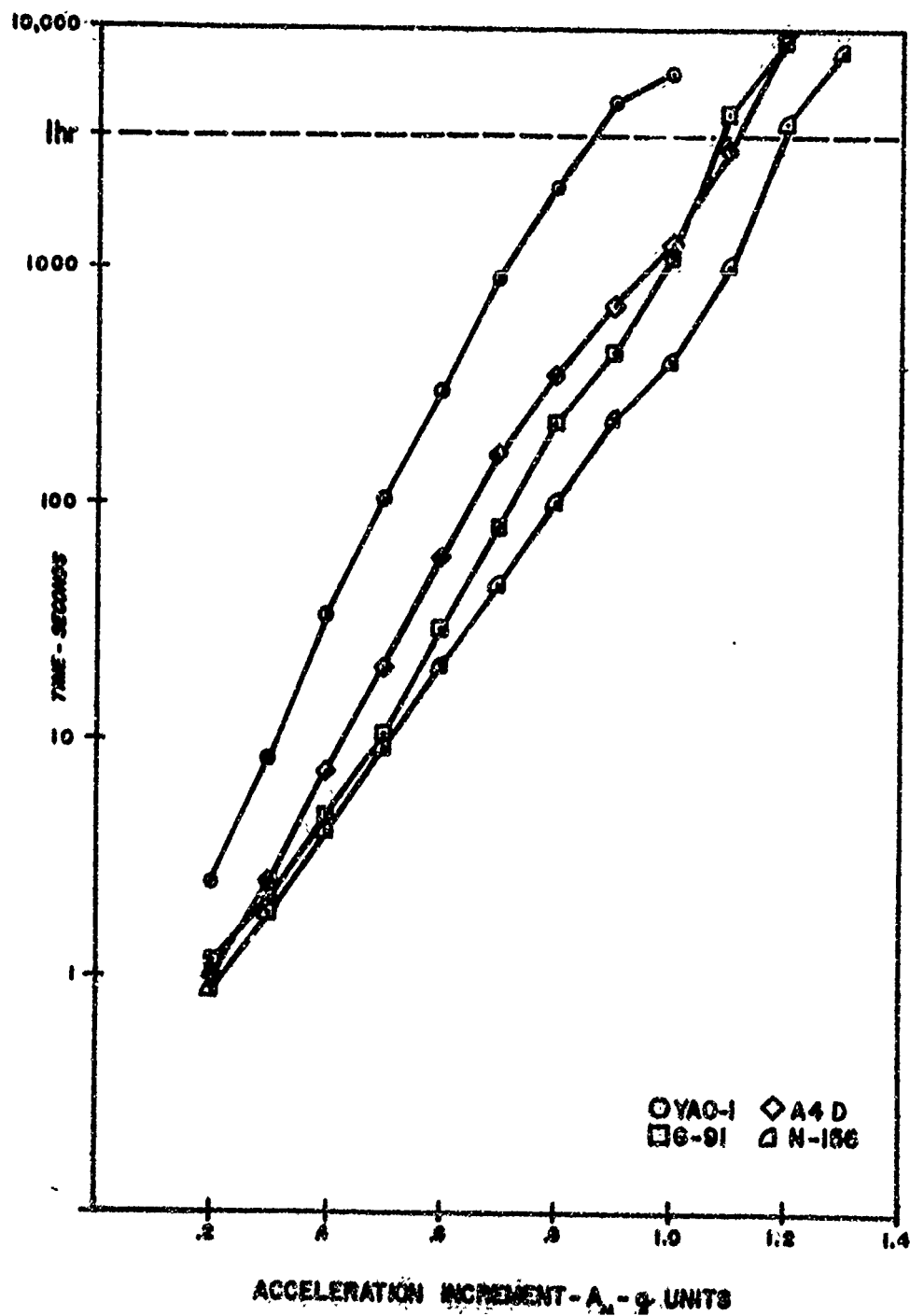


FIGURE 8- NUMBER OF SECONDS TO EXCEED A GIVEN NORMAL ACCELERATION,  $A_n$  FOR THE TEST AIRCRAFT (YUMA DATA).



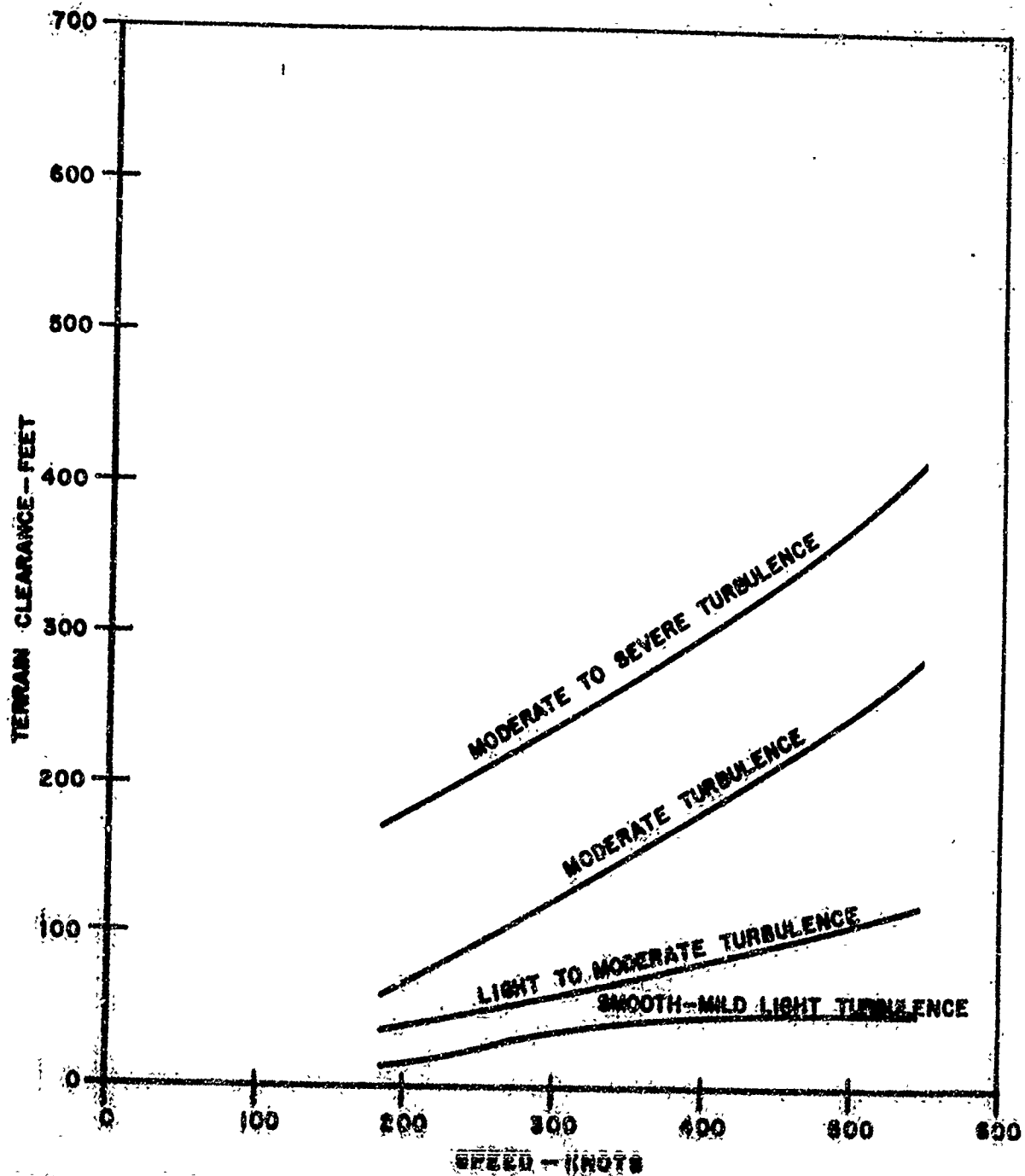


FIGURE 2- MINIMUM DESIRABLE TERRAIN CLEARANCE FOR 1/2 TO 1 HOUR FLIGHTS AS DETERMINED BY SUBJECTIVE EVALUATION DURING POST FLIGHT BRIEFING.

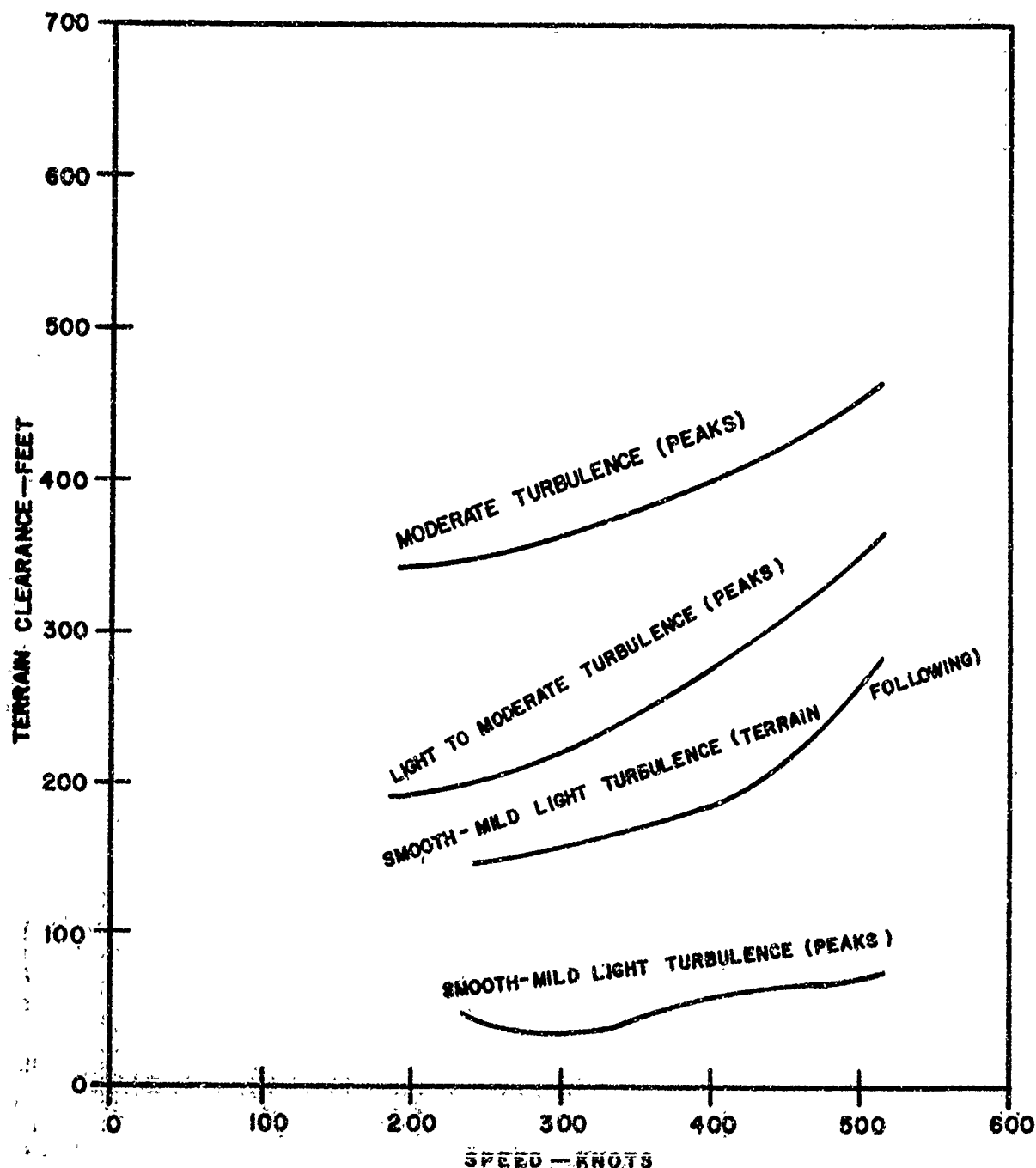


FIGURE 10— MINIMUM DESIRABLE TERRAIN CLEARANCE FOR 1/2 TO 1 HOUR FLIGHTS AS DETERMINED BY SUBJECTIVE EVALUATION DURING POST FLIGHT BRIEFING.

**HUMAN FACTOR PROBLEMS  
ASSOCIATED WITH LOW ALTITUDE,  
HIGH-SPEED (LAHS) FLIGHT**

**H.E. Rawson, and B. Schohan  
North American Aviation, Inc., Columbus, Ohio**

Paper to be Presented to CAL/TRECON Symposium on Dynamic  
Load Problems Associated with Helicopters  
and V/STOL Aircraft

"Human Factor Problems Associated with Low-Altitude, High-Speed Flight"

by

H. E. Rawson, Ph.D.

B. Schohan

In order to minimize the probability of detection and increase survival probability, the mission of an advanced U.S. Army surveillance aircraft is being defined in terms of flying at very low altitude and at relatively high air speeds for extended durations. This type of mission raises the possibility of human operator performance decrements due to the buffeting experienced under low-altitude, high-speed (LARS) conditions. Two distinct operator problems may arise: first, the problem of accomplishing the system's primary mission, that is, surveillance, reconnaissance, etc.; and, second, the problem of maintaining the vehicle flight path -- specifically altitude -- within a set of restrictive bounds.

The study to be reported was sponsored by the U. S. Army Transportation Research Command to investigate pilot and observer performance in piloting, navigational, and surveillance tasks under simulated low-altitude, high-speed flight conditions.

The study was performed on the North American Aviation Dynamic Flight Simulator, or G-Seat, as it is commonly called. A subject seated in

this device can be subjected to positive or negative accelerations in the vertical axis, and patterns of accelerations can be programmed through an analog computer to produce acceleration time-histories similar to those experienced in an aircraft flying at low altitudes and high speeds.

The report will be presented in three parts. First, a brief summary of the simulation procedures will be given. Second, the results obtained will be reviewed; and, third, the conclusions drawn from analysis of these results will be presented.

#### SIMULATION PROCEDURES

At the beginning of the study, a typical Army surveillance mission was defined and then analyzed in terms of the various operator task components required, and in terms of the times in which these essential tasks needed to be performed. From this mission-task analysis, those tasks essential for successful completion of a typical Army low-altitude, high-speed surveillance mission were determined so that human performance measurements could be made under varying buffeting conditions that could be expected under low-altitude, high-speed flight conditions.

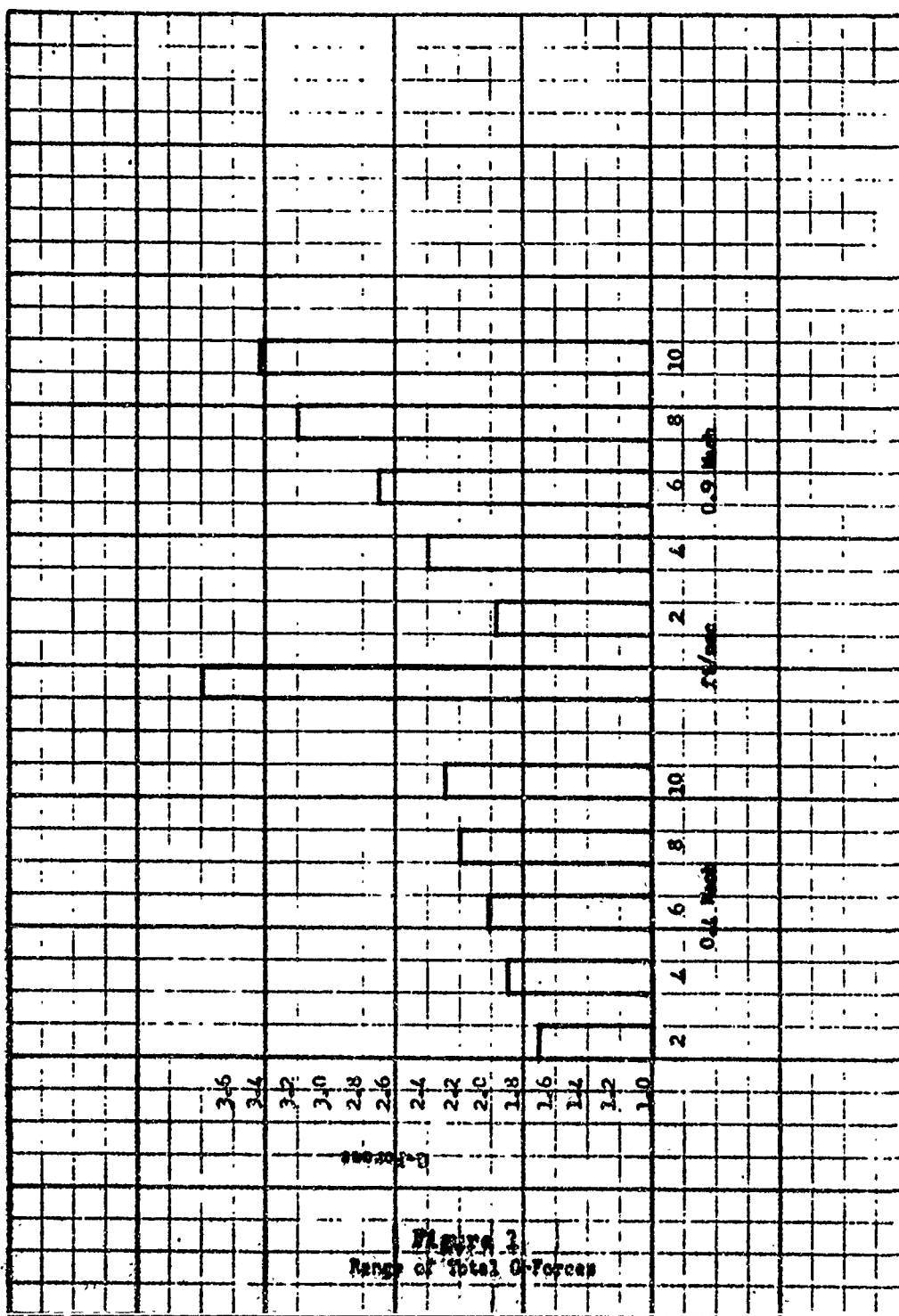
To simulate realistic LAES bulleting, the aerodynamic and control characteristics of a proposed advanced surveillance aircraft were defined. Gust data obtained from the Douglas RB-66 flights were then used to determine acceleration time histories for root mean square gust velocities of 2, 4, 6, 8 and 10 ft/sec at velocities of 0.4 Mach and 0.9 Mach. These acceleration time histories were programmed for the G-seat.

The equations of motion of the vehicle were set in an analog computer for the flight simulation. Thus, the simulator and its supporting computer complex enabled the pilot to fly a closed-loop simulation. The mean of the root mean square G's ranged from .05 to .41 G, with peak accelerations reaching  $\pm 3.5$  G. Figure 1 shows the range of G-forces imposed on the pilot at each of the gust intensity levels introduced during this study.

The experimental runs consisted of the simulated surveillance missions. These missions were three hours long, consisting of an 80-minute cruise to the target at 0.4 Mach, followed by a 20-minute dash at 0.9 Mach, and again followed by an 80-minute return cruise at 0.4 Mach. Figure 2 shows one of the simulated missions used during the study. The dash segment of the mission is over suspected hostile territory.

The study was conducted in two phases - a pilot study phase and an observer study phase. Six Army pilots whose experience ranged from jet to helicopters were used as subjects in the pilot study, while four Army observers, who also had experience piloting L-19's, were used in the observer study. Each pilot and observer flew the simulated mission under a variety of acceleration time histories at both air speeds.

The pilots' tasks during these missions were held constant. These tasks consisted of terrain tracking over a variable terrain, out-of-cockpit target identification; in-cockpit multi-sensor target identification utilizing simulated IR, radar and TV displays; and ECM monitoring.



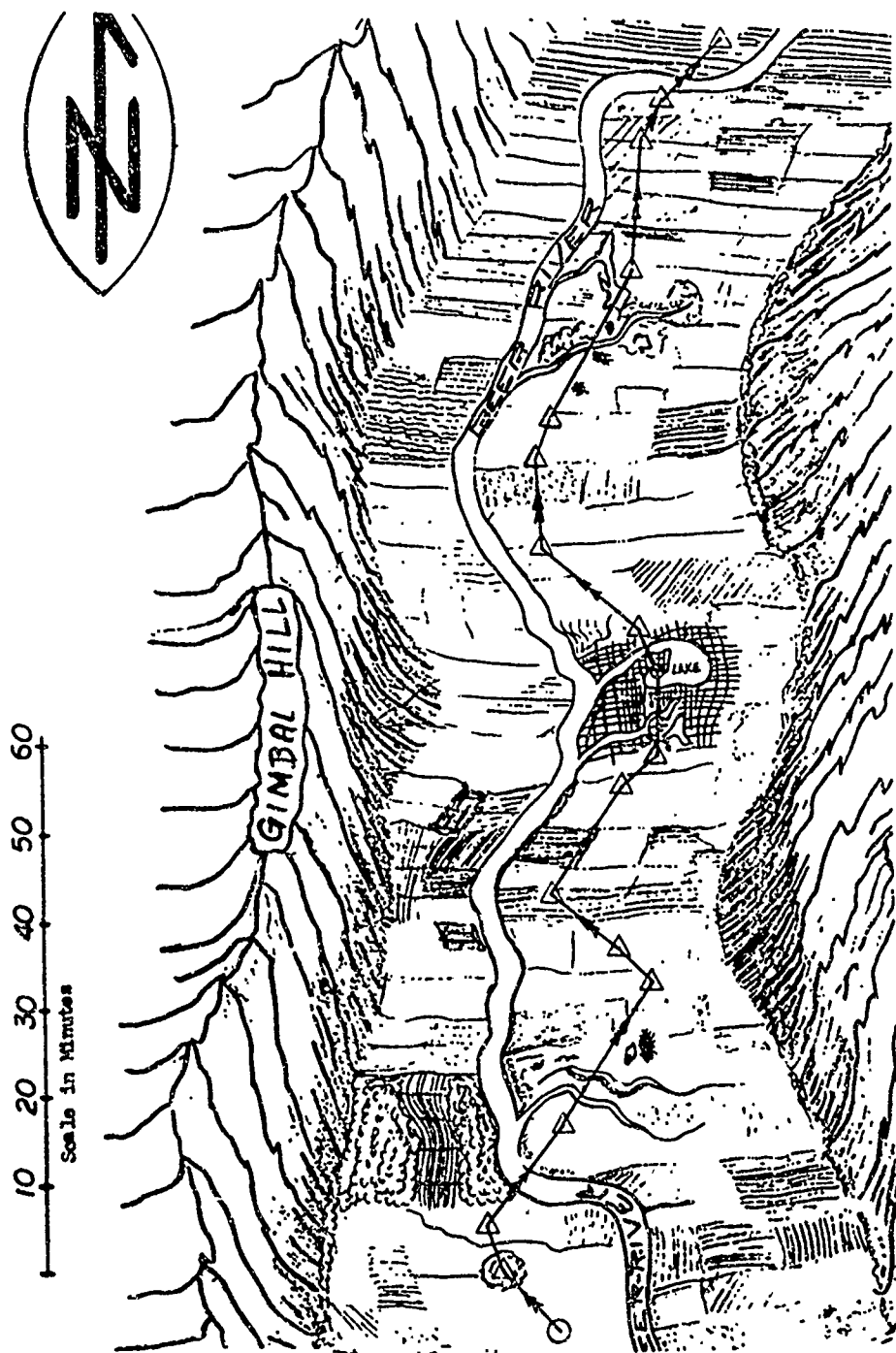


Figure 2  
Mission Profile



The observer tasks, which were also held constant throughout the missions, consisted of out-of-cockpit target identification, in-cockpit target identification, ECM monitoring, navigation and fuel consumption computations.

Four of the pilots and all of the observers flew approximately seven three-hour missions following briefing and practice runs. In addition, a few "endurance" runs were made in which a pilot and observer were asked to fly up to three hours under continuously severe turbulence conditions, that is, at 0.9 Mach under vertical gust accelerations representative of those encountered in thunderstorms. Approximately 260 simulator hours were devoted to the conduct of both studies.

### RESULTS

For the pilot, terrain following under LAHS conditions is a full-time job. Performance on this task is satisfactory at 0.4 Mach, but falls off at the higher air speed of 0.9 Mach (Table 1). As this table shows, the altitude error increases generally as a function of increasing rms gust velocity at the higher air speed.

At 0.9 Mach, the pilots incurred a large number of "missile kills" - that is, they exceeded 1,000 feet altitude above the terrain, and they also incurred a large number of "crashes" - that is, they hit the "ground". Table 2 lists the average number of missile kills at the different gust intensity levels during different segments of the mission, and Table 3 lists the median number of crashes for the same conditions.

TABLE 1

MEAN RMS ALTITUDE ERROR AS A FUNCTION OF TOTAL RMS  
VERTICAL GUST ACCELERATION

RMS Gust Velocity	Mission Segment		
	Cruise (0.4 Mach)	Dash (0.9 Mach)	Final Cruise (0.4 Mach)
2 ft/sec	*M = 149.12 **S = 21.13	M = 109.50; S = 12.27	M = 110.62; S = 9.96
4 ft/sec	M = 108.62; S = 18.59	M = 132.00; S = 24.86	M = 162.00; S = 10.70
6 ft/sec	M = 99.50; S = 8.86	M = 121.50; S = 46.44	M = 127.00; S = 19.02
8 ft/sec	M = 132.88; S = 12.90	M = 348.00; S = 106.68	M = 104.87; S = 11.66
10 ft/sec	M = 134.75 S = 9.52	M = 152.50; S = 152.50	M = 101.38 S = 14.92

\* M represents the mean rms altitude error

\*\* S represents the standard deviation of rms altitude error.

TABLE 2  
AVERAGE NUMBER OF 'MISSILE KILLS' (6 SUBJECTS)

MISSION SEGMENT			
Gust Intensity Level	Initial Cruise 0.4 Mach	Dash 0.9 Mach	Final Cruise 0.4 Mach
2 ft/sec - 0.4 Mach	9.99	-	3.69
4 ft/sec - 0.4 Mach	2.81	-	13.00
6 ft/sec - 0.4 Mach	1.67	-	5.31
8 ft/sec - 0.4 Mach	5.24	-	3.54
10 ft/sec - 0.4 Mach	5.25	-	2.08
2 ft/sec - 0.9 Mach	-	1.25	-
4 ft/sec - 0.9 Mach	-	3.75	-
6 ft/sec - 0.9 Mach	-	4.17	-
8 ft/sec - 0.9 Mach	-	38.75	-
10 ft/sec - 0.9 Mach	-	13.33	-
Total =	24.96	61.25	27.62
Mean =	4.99	12.25	5.52
SD =	8.18	192.40	15.01

TABLE 3  
MEDIAN NUMBER OF CRASHES (6 SUBJECTS)

Quest Intensity Level	MISSION SEGMENT		
	Initial Cruise 0.4 Mach	Dash 0.9 Mach	Final Cruise 0.4 Mach
2 ft/sec - 0.4 Mach	4	-	1
4 ft/sec - 0.4 Mach	1	-	3
6 ft/sec - 0.4 Mach	0	-	0
8 ft/sec - 0.4 Mach	0	-	4
10 ft/sec - 0.4 Mach	0	-	2
2 ft/sec - 0.9 Mach	-	0	-
4 ft/sec - 0.9 Mach	-	0	-
6 ft/sec - 0.9 Mach	-	0	-
8 ft/sec - 0.9 Mach	-	4	-
10 ft/sec - 0.9 Mach	-	1	-
Total	5	5	10

Finally, the altitude error records indicated a marginal degree of aircraft control at high turbulence levels which is not reflected in the rms altitude error records.

As you adjust the total number of crashes for the time intervals of the mission segments, there were twice as many crashes in the final cruise as in the initial cruise, suggesting a fatigue effect which does not show up in rms altitude error. Also, again adjusting percentages for the shorter time intervals of the dash (20 minutes for the dash as compared to 80 minutes for the cruise segments), there were considerably more crashes per min<sup>+</sup> during the dash portion than in either of the cruise portions of the mission: there were 6 1/4% crashes during the initial cruise, 25% during the dash, and 12 1/5% during the final cruise.

Table 2 shows that there were considerably more "missile kills" in the dash segment than in either cruise segment. It is also interesting to note that "missile kills" in the final cruise were slightly higher than in the initial cruise, again indicating a fatigue factor. Differences due to gust intensity levels alone are not significant at the lower airspeeds in the cruise segment. In the dash portion, however, the higher gust intensity leads to significantly more "missile kills".

#### CONCLUSIONS

Based on the results of this study and on a predicted configuration of an Army surveillance aircraft, it appears that LARS flights at 0.9 Mach or higher should be considered only under conditions of rather mild

turbulence. Higher speeds or flights in heavy turbulence should be considered only if gust alleviation devices can reduce significantly the total G loadings on the operator.

Since the pilot is fully occupied with terrain following, two operators will be essential for satisfactory conduct of this type of mission. The pilot should be assigned the task of terrain following and aircraft operation only. The results indicated that any additional tasks imposed on him tended to degrade his performance in these crucial operations. The observer, or second man, should handle all the other tasks such as navigation, in-cockpit electronic sensor surveillance, out-of-cockpit visual surveillance, and ECM monitoring and jamming operations. The results obtained in this study supported this allocation of tasks. The pilot can perform his tasks quite well except at high subsonic speeds. Under these latter conditions, missions should probably be aborted except in emergencies unless gust alleviation devices provide significant relief in jostling. The pilot's handling tasks, in addition to piloting tasks, resulted in erratic piloting and poor performance on the newly assigned task. Observers, relieved of the heavy piloting load, completed their assigned tasks in a satisfactory manner despite the G-loads imposed in this study. Increased speed, with its shorter viewing time, did affect their surveillance performance, however, as would be expected. Navigation tasks, performed on a manual computer (E6B), proved in general to be less than satisfactory. The observers were slow and often inaccurate in their calculations which resulted in their being 'lost' a good deal of the time. Furthermore, these computers could not be held in the observer's

hands at the higher turbulence levels. Out-of-cockpit surveillance and in-cockpit electronic sensor surveillance was handled satisfactorily, at least to the level of proficiency that this study measured. More complex task assignments for the observer might lead to deterioration of performance under severe conditions. It should be pointed out, however, that all four observers flew one continuous three-hour mission at the highest turbulence levels used in the study with no noticeable performance decrements or significant ill effects. This seems to indicate that observers could handle very heavy task loadings with no serious effects on mission effectiveness. In summary, it appears that navigational and surveillance tasks should be assigned to observers, leaving the pilots as few tasks as possible other than terrain following.

In regard to crew training, it should be mentioned that the study results revealed strong training effects due to the acceleration environments prevalent under LAHS conditions. These effects seem to center around three phenomena:

1. A decrease in anxiety as the operator becomes psychologically conditioned to this environment.
2. A quick learning effect of new control, visual reading, and comfort techniques which greatly enhance his performance.
3. A physiological conditioning in which muscles used in tensing the body under high turbulence become effective in enabling the pilot to perform his task with greater ease.

Intensive short-term specialized training under dynamic buffeting conditions should greatly enhance performance on the IAMS mission. This training program should include proper restraint system adjustment, visual scanning techniques, control response under heavy turbulence, relaxation techniques, and physiological conditioning. In such a program the operator should be instructed to use fine motor movements rather than gross motor movements in instrument and control adjustments.

Next, some mention should be made about the standard Navy integrated torso harness that was used for restraint. Many complaints were made after the pilot or observer had been exposed to turbulent conditions continuously for approximately one hour, and the complaints centered around the level of discomfort caused by the harness rather than from the adequacy of restraint. As a matter of fact, some observers loosened the harness after an hour so that they could twist and bend into a more comfortable position. This practice, although undoubtedly allowing more comfort, is extremely dangerous from a physiological safety viewpoint. The fact that observers loosened their restraint systems, knowing the dangers involved, points to the importance of this problem. For long duration missions, new restraint systems should be developed which would offer adequate restraint, but would, at the same time, be comfortable.

The instrument panel in the G-seat is rigidly mounted, i.e., it is undamped. Pilots frequently had difficulty reading the instruments because of vibrations of the panel. Since operator error must be held



to a minimum under LAES conditions, all cockpit displays should be as vibration free as possible to avoid this kind of error. A dampened cockpit panel should be investigated for this purpose. Dial faces and markings should be larger to aid in the quick processing necessary under LAES conditions, and alternate mode displays, that is, displays which can be switched to special low-altitude calibration, should be investigated.

To minimize the danger of inadvertent control stick inputs by the pilot under LAES conditions, special controls should be designed. For example, a pencil- or ball-type side-arm controller and arm support should be investigated for flight control in lieu of a center-stick controller, and, as previously mentioned, manual navigational aids will probably have to be built into the cockpit. The use of electronic navigational aids and read-outs, which require little manual adjustment, should be explored.

Some mention should be made of the special endurance runs in which three of the pilots and all of the observers were asked to fly missions at the highest acceleration time histories utilized in the study. The pilots were instructed to fly as long as they felt comfortable. One pilot flew for one and one-half hours at this level, another flew one hour and fifty minutes, and a third flew a full three hours under these severe conditions. The pilots flying these endurance runs felt that the experience was extremely fatiguing. In fact, one pilot experienced extreme observable fatigue. He kept falling asleep for about 48 hours after experiencing this endurance run and felt

dissoy for about 24 hours. This would indicate that three-hour missions at high subsonic speeds under heavy turbulence would be extremely hazardous and very fatiguing. The chance of successfully repeating such a mission soon after the first mission would be quite low. It should be pointed out, however, that the pilots actually performed slightly better in their terrain following under these severe conditions than during our normal simulated mission. This can probably be attributed to the high level of motivation and competition surrounding these special flights.

Consequently, even though specialized LANS training and psychological and physiological conditioning should greatly enhance performance under these conditions, special human factor items will have to be considered such as the design of gust alleviation devices, specialized cockpit displays, and improved restraint systems.

**EFFECT OF GUST ALLEVIATION SYSTEM  
ON DYNAMIC AIRLOADS**

**J.D. Balducci, F.L. Adams, and M.A. Schwartzberg**  
**Autonetics**

**EFFECT OF GUST ALLEVIATION SYSTEMS  
ON DYNAMIC AIR LOADS**

By

J. D. Balducci, F. L. Adams, and M. A. Schwartzberg

**Autonetics**

A DIVISION OF NORTH AMERICAN AVIATION, INC., ANAHEIM, CALIFORNIA



EFFECT OF GUST ALLEVIATION SYSTEMS  
ON DYNAMIC AIR LOADS

By

J. D. Balducci, \*

F. L. Adams, \*

and

M. A. Schwartzberg\*\*

SUMMARY

This paper describes various system methods of alleviating air loads due to gusts. The effects of these gust alleviation systems on the dynamic air loads are presented and the analysis tools and techniques, and the criteria used for evaluation are described.

\*Research Engineer, Autonetics, A Division of North American Aviation, Inc.

\*\*Senior Engineer, Columbus, A Division of North American Aviation, Inc.

## INTRODUCTION

This paper discusses the results obtained from the gust alleviation feasibility study conducted by the Autonetics and Columbus Divisions of North American Aviation, Inc., under contract with the U.S. Army Transportation Research Command (TRECOM).

The study was conducted in order to obtain a realistic appraisal of the capabilities of known gust alleviation techniques and to determine the feasibility of utilizing these systems in future Army aircraft intended for sustained low-level high subsonic speed operations.

Gust alleviation systems are herein considered to be in one of two categories:

1. Active systems. Those systems using feedback control to activate aircraft control surfaces. Among these are autopilots, pitch dampers, normal acceleration or angle-of-attack sensing systems, and those systems which employ dynamic sensors to attempt simulation of the gust.
2. Passive systems. Those systems which alter the aircraft geometry during flight. No sensing devices are employed. Included in this category are variable sweep wings, telescoping wings, folding wings, spoilers and deflectors, and freely-floating surfaces.

The various systems are evaluated in terms of load alleviation capability, pilot tolerance and endurance, aircraft performance, stability and control, structural effects, weight, cost, reliability and fail-safety.

The study results indicate that a variable sweep wing design or a normal acceleration feedback system commanding flaps and elevators offers the most attractive method of alleviation.

## THE ALLEVIATION PROBLEM

Penetration of enemy defenses and territory can be considerably enhanced by flight at high speeds and minimum altitudes. High speed coupled with the natural masking afforded by the terrain and earth curvature, significantly decreases the probability of detection and kill. The low altitude high speed (LAHS) flight, however, results in a greatly increased probability of clobber and an attrition due to degradation in pilot and equipment performance. A nominal altitude, determined as a function of speed and terrain, can be achieved, resulting from a trade off between clobber and detection-kill. At this altitude, the severity of atmospheric turbulence contributes to the aforementioned attrition. The probability of success of an LAHS mission is determined to a great extent by the aircraft sensitivity to turbulence or gusts.

The study was restricted to longitudinal response to vertical gusts because the vertical gust component impinges on the largest surface area and the wing span is small compared to the average eddy size. The vertical acceleration sensitivity to gusts can be defined as

$$\text{Sensitivity } \mathcal{L} = \frac{\sigma_N}{\sigma_w} \frac{z}{g} \text{ in g's/fps.} \quad (1)$$

A vehicle can be designed with a low gust sensitivity, normally sacrificing performance and maneuverability at low dynamic pressures. The parameters of aircraft design which effect a low gust sensitivity are discussed later. LAHS missions cannot tolerate gust alleviation through aircraft velocity reduction or weather detection and course changing techniques, both of which prove effective in commercial aircraft or for less critical military missions. Consequently, some sort of gust alleviation system or device that can be incorporated into the basic design becomes desirable.

A gust alleviation system must decrease the sensitivity by altering the acceleration response to gust disturbances. The approximate response over the short period frequency range can be given in Laplace transform notation as:

$$N_z / w_g = \frac{Z_\alpha (s^2 - 2 M_q s)}{g V (s^2 + 2 \zeta \omega_n s + \omega_n^2)} \quad (1)$$

where

$$\frac{Z_\alpha}{g V} = - \frac{\rho V C_{L\alpha}}{2 W/S} \quad (2)$$

The effect of the time lag for gust incidence on wing and tail, and downwash effects are included. Although response outside of this frequency range was also considered in the study, presentation from the limited frequency range standpoint allows a more simplified discussion of system concepts and feasibility.

Gust alleviation systems must be so designed as to alter Eq 2 and provide attenuation of the acceleration. Past efforts may not have considered this equation directly, but all alleviation schemes must necessarily result in its alteration.



## TURBULENCE

The random vertical gust component can be characterized statistically by the power spectral or mean square density. Since extensive atmospheric research in recent years has contributed to a reliable representation of this quantity, a statistical approach to the representation of turbulence is desirable.

Among the most comprehensive analyses of atmospheric turbulence are those discussed in Ref 1 and 2. The spectra are illustrated in Figure 1.

The vertical motion of the air can be considered to result in a change in angle of attack, whereby for small angles  $\alpha_g = \frac{w}{V}$ , expressed in radians.

Atmospheric turbulence generally may be considered to be a stationary Gaussian random process. The turbulence encountered for a given time or flight is, of course, limited by the duration, flight course, and weather conditions. The turbulence history can be reduced to a non-stationary Gaussian process that varies only in intensity. For localized investigations, a root mean square gust velocity can be assumed. This rms value can then be considered to vary according to some cumulative probability distribution as shown in Figure 2.

The power spectral density, or more properly, mean square density, as provided by Ref 1 and employed in this study is given by

$$\Phi_{w_g}(\Omega) = \sigma_{w_g}^2 \frac{L}{\pi} \frac{(1 + 3\Omega^2 L^2)}{(1 + \Omega^2 L^2)^2} \quad (3)$$

where

$$\Omega = \frac{\omega}{V} \quad (4)$$

The spectrum of Ref 2 differs from the chosen one only in that slightly more power is evidenced at high frequencies for the former. The analog representation of this spectrum corresponds to that of Ref 1 for a turbulence scale L equal to 600 ft.

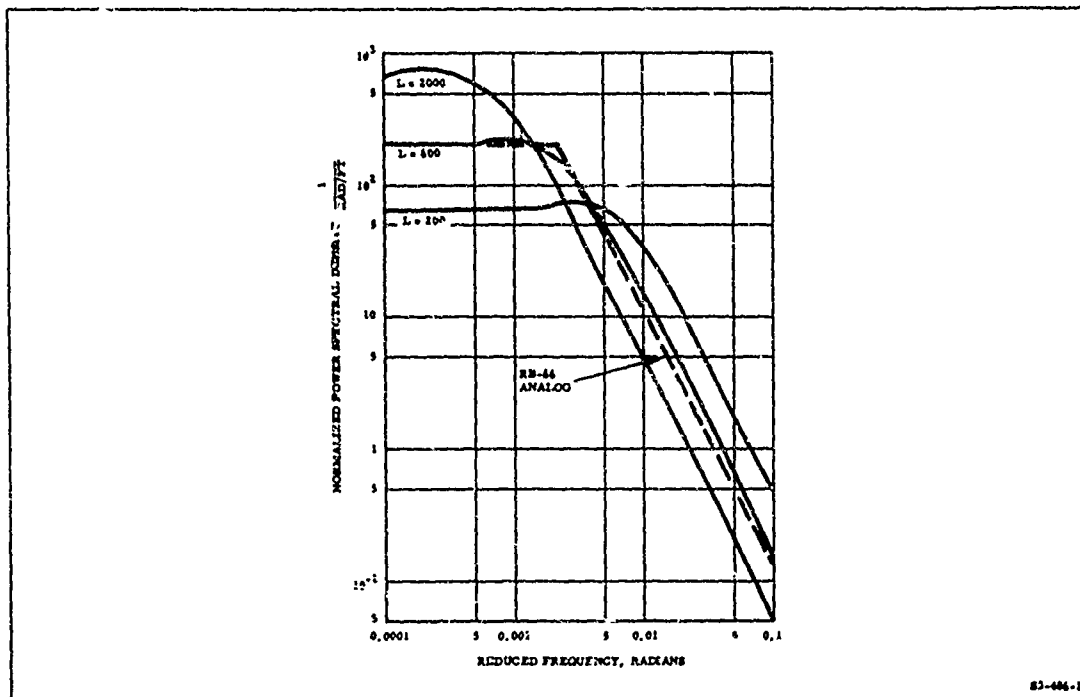


Figure 1. Analytic Turbulence Representation

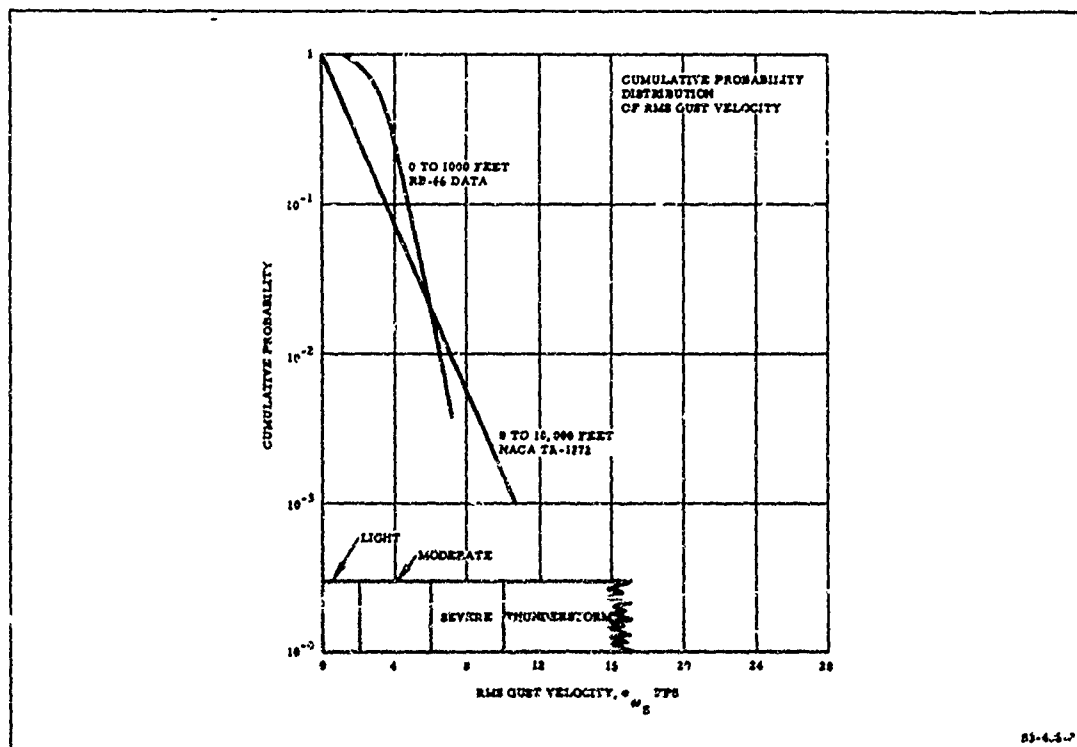


Figure 2. Cumulative Probability Distribution of RMS Gust Velocity

The load spectra can then be determined by use of the relationship

$$\phi_{N_z} = \phi_{w_g} \left| \frac{N_z}{w_g} \right|^2 \quad (5)$$

## CRITERIA

The primary function of any gust alleviation system is to reduce the loads on the aircraft and to provide a less fatiguing ride. A system designed to perform this function necessarily introduces considerations other than the direct ability to alleviate, and the feasibility criteria must cover these factors as well.

### ALLEVIATION

Statistical approaches have frequently been employed in gust alleviation analyses, yet different forms for the measurement of alleviation capability have been assumed. Among these are the measurement of peak or rms accelerations at a particular frequency or over a band of frequencies, or the maximum value of the acceleration power spectral density (PSD). Care must be taken in evaluating alleviation study results. For example, Ref 3 indicates 91 percent alleviation using peak PSD values, and 75 percent based on rms values, as applied to the Mohawk YAO-1. The measure adopted herein for determining the ability of a gust alleviation system to perform its design function is its effect on the aircraft's sensitivity,  $\mathcal{L}$ , based on rms measurements.

The sensitivity of an alleviated vehicle at a particular flight condition can be directly compared to that of the vehicle without an alleviation system. The sensitivity criterion can also be used to compare various alleviation systems as applied to a given vehicle. Systems may also be compared on a percentage alleviation basis for a vehicle under the same flight conditions. Percent alleviation is herein defined as:

$$\text{Percent A} = 100 \left( 1 - \frac{\mathcal{L}_A}{\mathcal{L}_U} \right) \quad (6)$$

Where  $\mathcal{L}_A$  is the sensitivity with alleviation and  $\mathcal{L}_U$  is the sensitivity without alleviation.

The normalized vertical acceleration power spectral density and percentage of alleviation based on peak values of this spectrum are also utilized. The spectra serve to illustrate the frequency content of the acceleration response.

#### PILOT TOLERANCE AND ENDURANCE

Vertical acceleration at the pilot fuselage location is given by

$$N_{Z_P} = N_{Z_{cg}} - \frac{l_P}{57.3 \text{ g}} \ddot{\theta} \quad (7)$$

Some investigations have utilized a tolerance or endurance criterion consisting of a minimization of pitch rates as well as accelerations. (See Ref 4.) Quantitative information on human reaction to angular rates is scant although current studies may lead to useful conclusions in this area. It is the opinion of the authors that use of angular rate criteria at this time would be unjustified. Of more importance are the angular accelerations which contribute to the accelerations at the pilot's fuselage station. In general, the tendency is to reduce the total accelerations because of the resultant pitching action of a statically stable vehicle.

##### 1. Tolerance

The best available information on human reaction to complex vibrations encountered in flight through rough air is contained in Ref 5. For purposes of data analysis, this reference groups acceleration levels into several categories.

The following generalizations are made for each of the behavior categories depicted in Figure 3:

1. Category 1a: Smooth - No performance impairment. Lack of stimulation could produce lethargy.
2. Category 1b: Practically smooth - No appreciable performance impairment. Precise manipulations are performed easily and quickly.

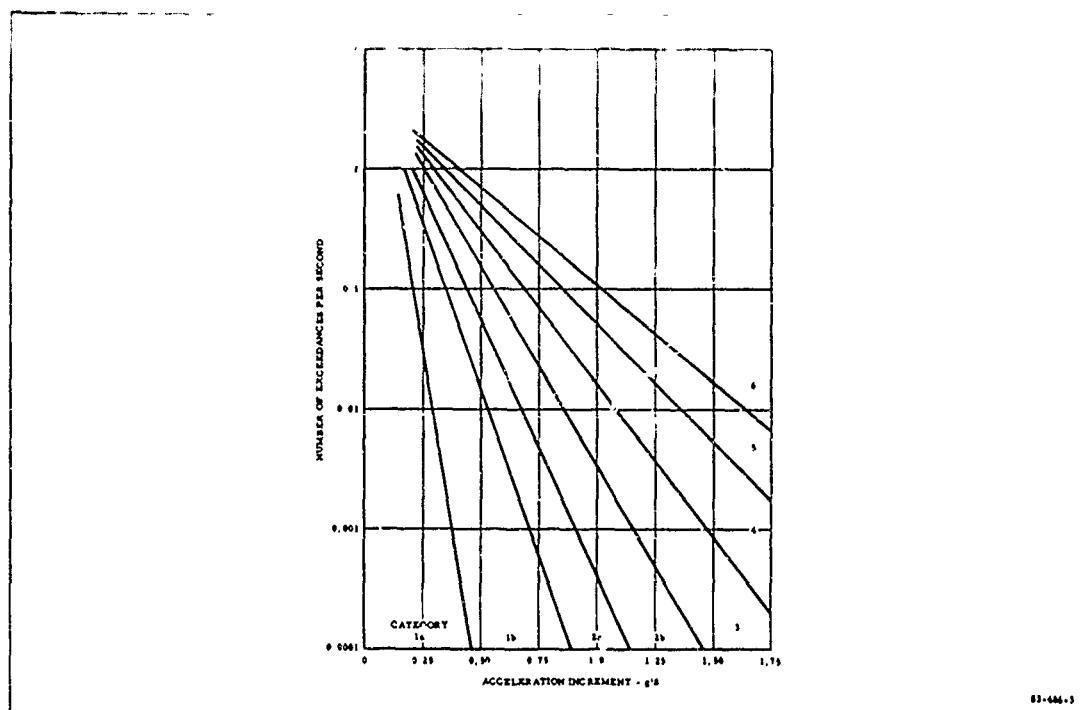


Figure 3. Behavior Categories

3. Category 2a: Mild light - Most tasks are performed easily. Interference with precise manipulations such as writing is noticed, but is not appreciable.
4. Category 2b: Light - Effects may be bothersome at upper levels, but do not markedly interfere with the performance of most tasks. Marked interference occurs with precise tasks such as writing.
5. Category 3: Light to moderate - In cockpit psychomotor coordinations suffer an increased decrement in this category, with a marked increase in time to read and adjust instruments. The task of controlling the airplane requires a considerable portion of the pilot's attention.
6. Category 4: Moderate - Instruments become difficult to read, and manipulations with the outstretched hand are quite difficult at the upper levels of this category. As the upper levels are approached, it becomes necessary to support the arms on the legs

or brace them in some manner in order to avoid inadvertent stick movements.

7. Category 5: Moderate to severe - Manipulations other than those with the stick and throttle are practically impossible, and control of the aircraft requires the full attention of the pilot to the virtual exclusion of glances inside the cockpit. Pilot control of the aircraft becomes increasingly marginal.
8. Category 6: Severe - Pilot control is submarginal a considerable portion of the time. The pilot takes a severe physical pounding, and exposure of more than 5 to 10 min might result in physiological damage.

The preceding categories are determined by the number of exceedances of various acceleration levels, (peaks), in 1 sec. This value for a Gaussian random process is approximated by the formula

$$N = \frac{1}{2\pi} \left[ \frac{\int_0^\infty \omega^2 \phi_{N_z}(\omega) d\omega}{\int_0^\infty \phi_{N_z}(\omega) d\omega} \right] e^{-N_z^2 / \sigma_w^2 g^2} \quad (8)$$

A discussion of this formula and its relationship to the power spectral density is included in Ref 1. Study data are interpreted in terms of this criterion to allow greater appreciation for alleviation, sensitivity, and gust velocity parameters.

## 2. Endurance

Pilot endurance of accelerations as a function of flight duration has been investigated by Cornell Aeronautical Laboratory, Inc. and the Columbus Division of North American Aviation, Inc. The results of these studies in terms of pilot proficiency as a function of mission duration and rms g levels is shown in Figure 4.

The endurance herein is calculated on constant vehicle velocity, and sensitivity values based on a mean weight airplane (half-fuel load). The

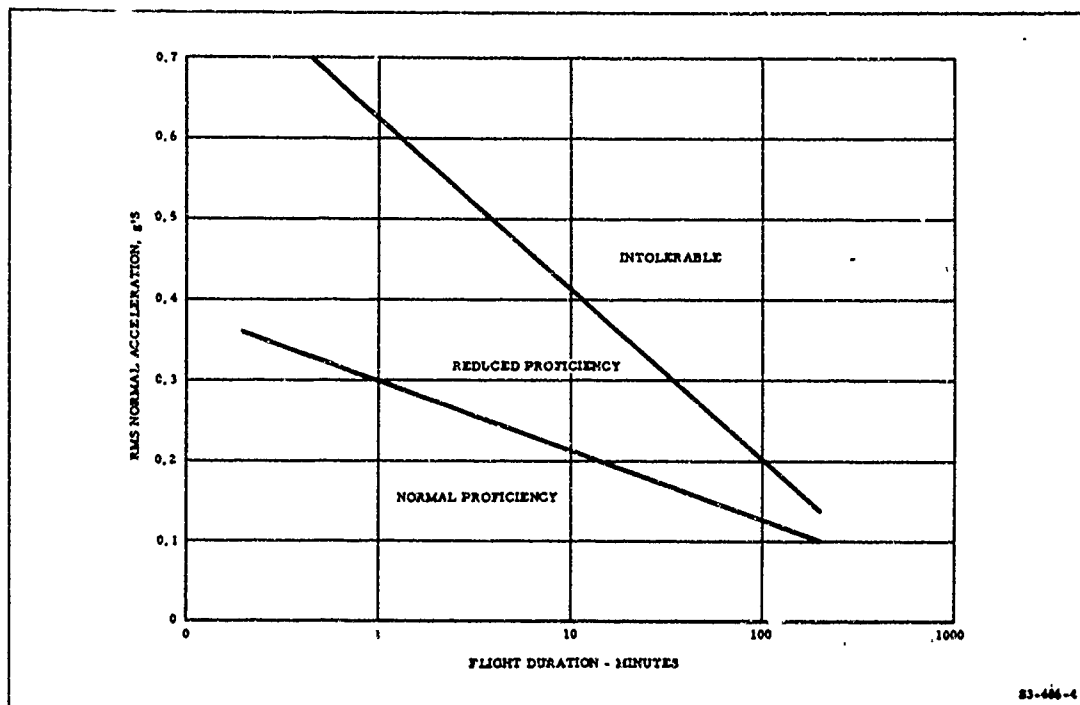


Figure 4. Endurance Boundaries

actual sensitivity, varying inversely with weight, would be lower at the beginning of the mission and higher toward the end. The mean value gives a good indication of probable endurance.

The frequency content of the acceleration spectrum is also an important factor in the determination of tolerable vibration levels, and the data in Figure 4 must be qualified. The rms values indicated are based on spectra corresponding to the frequency response of a rigid airplane having a well damped short period natural frequency of about 0.8 cps.

#### PERFORMANCE

For a given flight speed, weight, and full load, the range of an aircraft is inversely proportional to the drag. The range ratio of the alleviated vehicle to the unalleviated one can be expressed as

$$\frac{R_A}{R_U} = \frac{(C_D S)_U}{(C_D S)_A} \quad (9)$$



With this equation no fuel load reductions are considered necessary because of the added weight of a system. Calculations of range variation resulting from any necessary weight changes and subsequent fuel supply reduction are also calculated. For those systems which involve continual surface deflections, drag due to the surface motion is taken into account.

#### STABILITY AND CONTROL

Reference 6 requires that short period damping shall be such that the normal acceleration response to a stick impulse shall damp to one-tenth amplitude in one cycle; i. e., have a damping ratio,  $\zeta$ , greater than 0.34. Normal stability augmentation system design requirements are more stringent; a much-used criterion corresponding roughly to that resulting from CAL studies is shown in Figure 5. Also shown, are results of handling qualities investigations conducted at North American Aviation, Inc., Columbus Division, indicating that pilot preferences allow a much looser criteria in the higher frequency areas. Below 0.9 cps, the results agreed well with CAL data. Above 0.9 cps, the pilot acceptance boundary was a line of constant time of one sec to damp to one-tenth amplitude, independent of actual damping ratio. The incorporation of an alleviation system should not seriously degrade the rise time or steady-state value of the response to stick commands.

#### STRUCTURAL EFFECTS

A gust alleviation system may adversely affect the vehicle aeroelastic modes and effects on flexibility should be considered. Added airframe stress resulting from alleviation system incorporation and subsequent necessary structural weight changes are estimated.

#### WEIGHT

The total weight penalty attributable to a gust alleviation system is a consequence of (1) weight difference caused by incorporation of the system

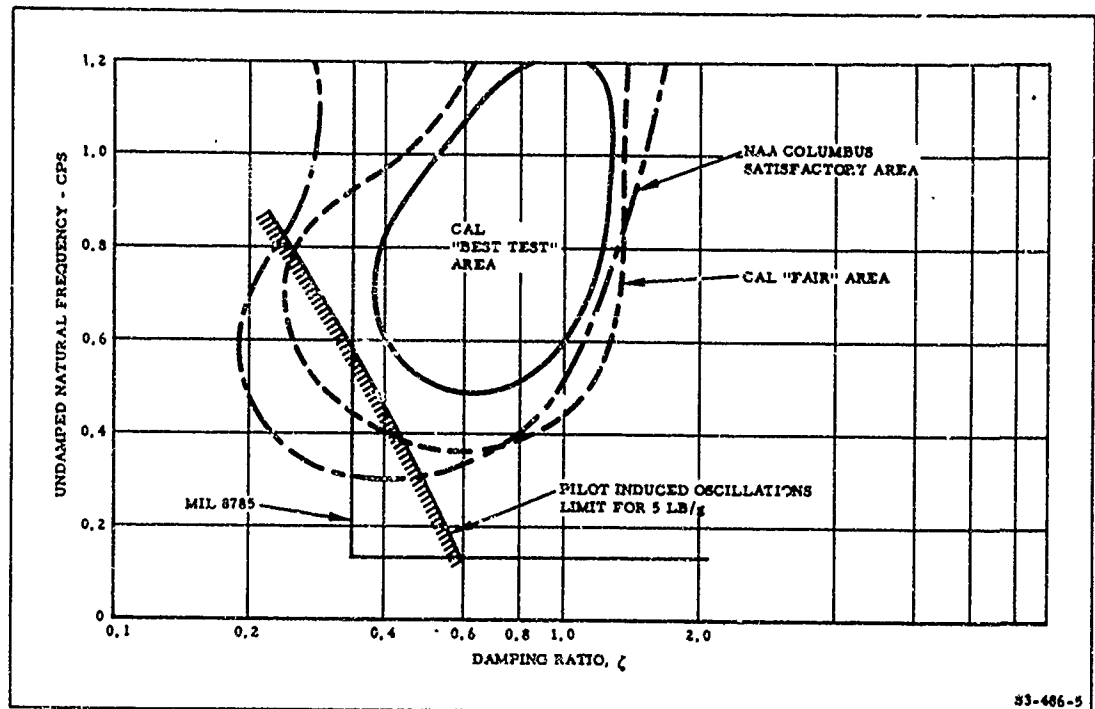


Figure 5. Short Period Damping and Frequency Criterion

itself, and (2) possible structural weight increases. It is also conceivable that a decrease in vehicle structural weight may be permissible with a reduction of the gust loads and consequent design to a lower load factor.

#### COST

The relative cost for each alleviation system has been estimated. Maintenance cost was also considered.

#### RELIABILITY AND FAIL-SAFETY

System reliability figures are calculated wherever possible. Equipment mechanizations are considered to take maximum advantages of state-of-the-art techniques for enhancing reliability and fail-safety. Some of these techniques are presented in Ref 6.

## BASE-POINT AIRPLANE

An aircraft, called the base-point airplane (BPA), was designed to perform a LAHS surveillance mission and to provide the basis for system comparison.

### SPECIFICATIONS

The aircraft specifications for this study are defined as follows:

1. At sea level maximum velocity will occur at Mach 0.9.
2. At 500-ft altitude cruise velocity will occur at Mach 0.4.
3. Gross weight is 18,000 lb.
4. Takeoff distance over 50-ft obstacle is 2,000 ft.
5. Maximum load factor is 7.33.
6. Surveillance equipment weight is 1500 lb.
7. Two engines.
8. Two-man crew.

### AIRCRAFT MISSION

The aircraft mission consists of the following:

1. Cruise to and from the surveillance site will occur at Mach 0.4 at an altitude of 500 ft for approximately 300-naut mi radius.
2. Dash at the surveillance site will occur at Mach 0.9 at an altitude of 500 ft for 20 min.

### GEOMETRY

The geometry of the BPA is illustrated in Figure 6 and listed in Table 1. The BPA, although not optimized, provides a reasonable and conventional design.

Handling qualities at all flight speeds for a wide range of center of gravity travel are indicated in Figure 7. These handling qualities are acceptable within the criteria of Ref 7.

The gust sensitivity of the BPA as a function of Mach number is shown in Figure 8.

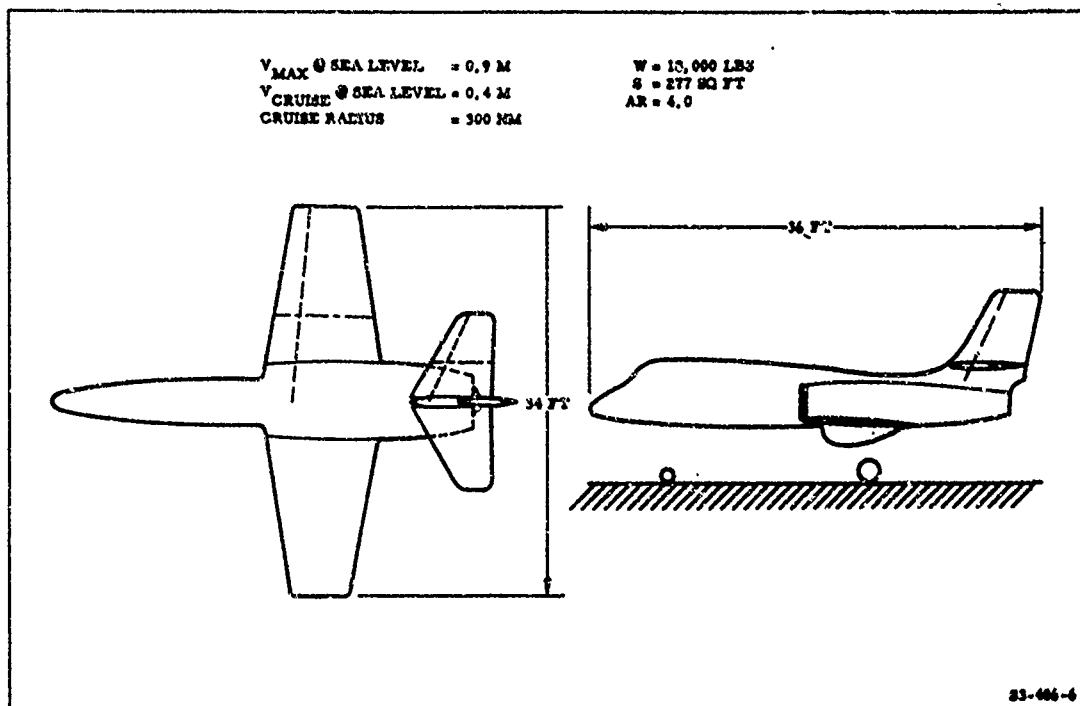


Figure 6. Base-Point Aircraft (BPA)

Table 1. BPA Geometry

Wing area	277.0
Aspect ratio, wing	4.0
Taper ratio	0.5
Sweep of C/2	0
Airfoil section	64A206
Wing span	33.3
Chord, root	11.1
Chord, tip	5.55
Chord, mean aerodynamic	8.625

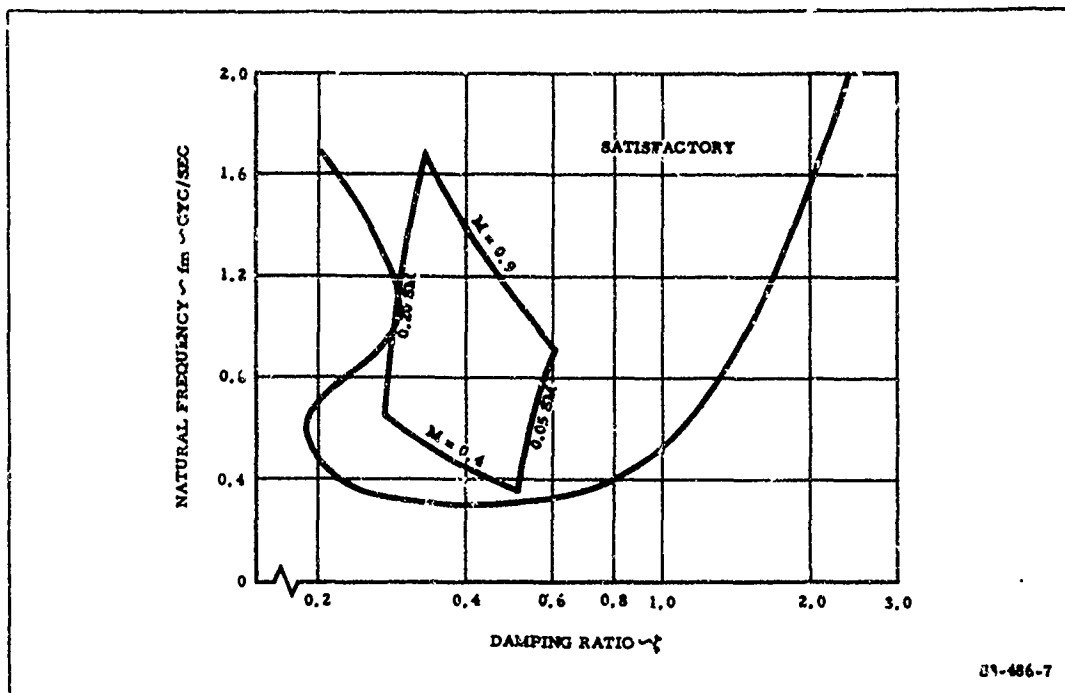


Figure 7. Short Period Stability Characteristics of BPA

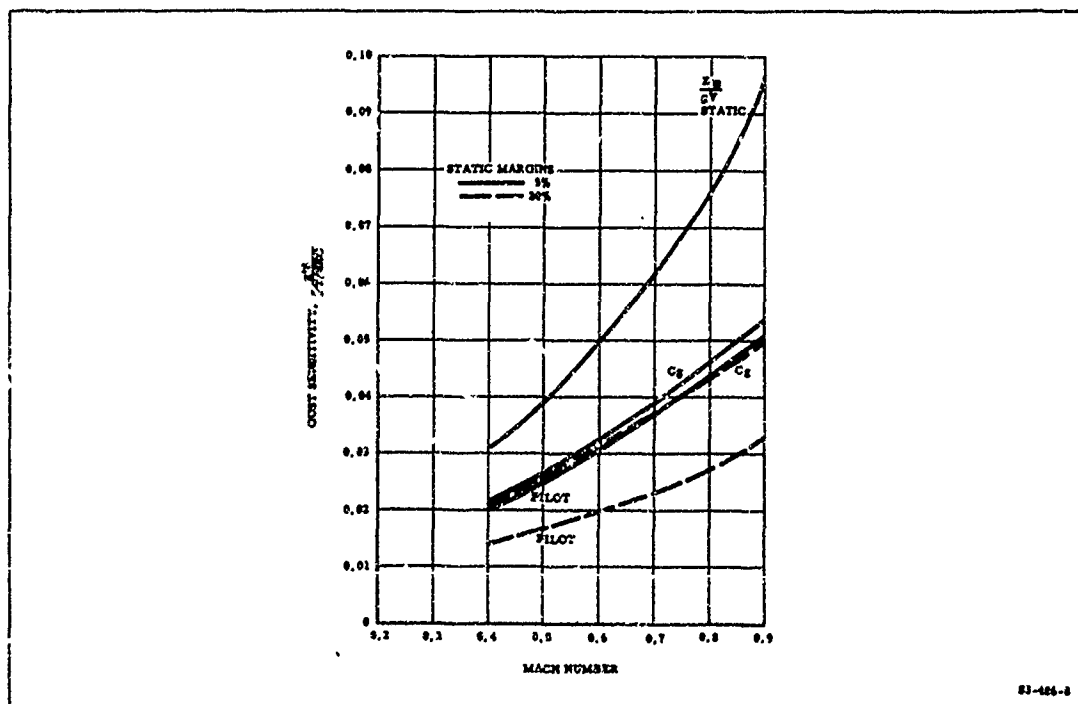


Figure 8. Gust Sensitivity of BPA

## ALLEVIATION THROUGH AIRCRAFT DESIGN

Examination of Eq 2 will serve to illustrate how the basic aircraft characteristics can be altered to provide a reduction in gust sensitivity.

It can be seen that a reduction in vehicle forward velocity results in a decrease in gust-induced loading. In addition, the dynamic response is altered, so that the resultant sensitivity is not exactly a linear function of velocity.

An increase in altitude (reduction of  $\rho$ ) also results in a loading reduction. This effect is independent of the fact that the turbulence decreases in intensity with increasing altitude.

Other important parameters that can directly result in load reductions are increased wing loading ( $W/S$ ) and decreased lift curve slope  $C_{L_\alpha}$ . The lift-curve slope of an aircraft is determined primarily by the planform, airfoil section and flexibility of the wing. The aircraft wing loading for a given aircraft weight is directly related to the wing area. As previously mentioned, changes in wing loading or lift curve slope, in an attempt to reduce the gust sensitivity, are incompatible with performance at low dynamic pressure conditions where a large lift coefficient is required. Passive systems that alter the vehicle geometry in flight are attempts to provide alleviation through changes in one or both of these parameters.

Changes in aircraft dynamic stability, i. e., variations in  $\zeta$  and  $\omega_n$ , also result in alteration of the gust response. The gust sensitivity of a vehicle having the BPA characteristics and variable short period dynamics is illustrated in Figure 9. Note that decreased sensitivity is achieved through an increase in the short period natural frequency and/or an increase in damping.

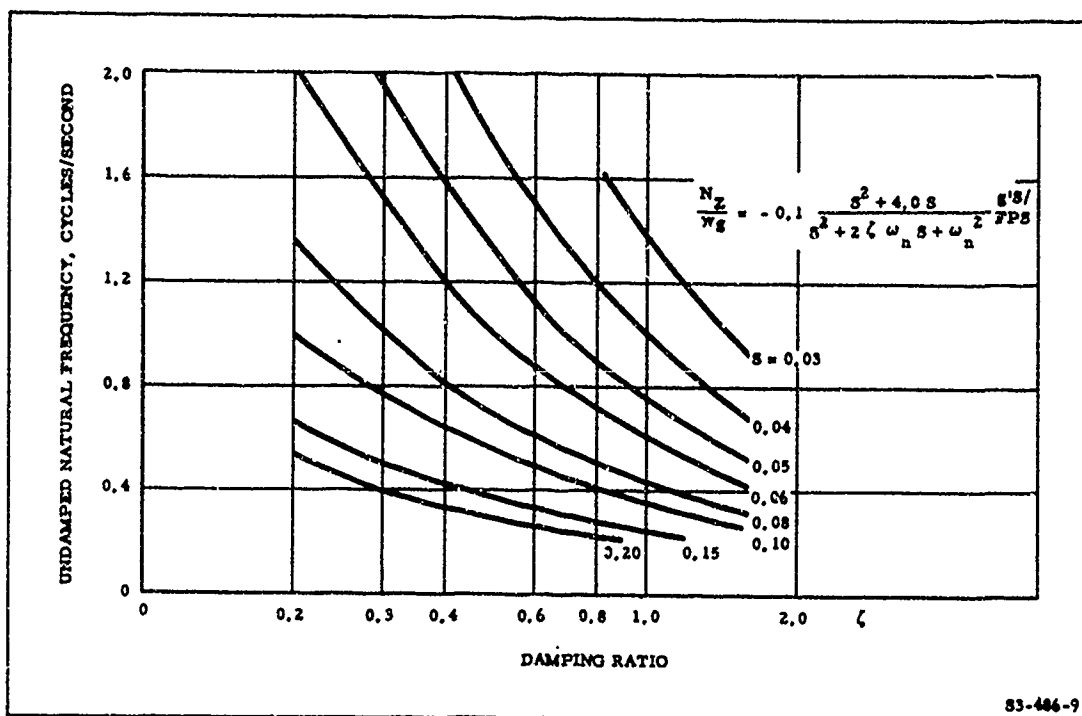


Figure 9. Gust Sensitivity of BPA Having Variable Short Period Characteristics

Short period frequency is determined primarily by  $M_\alpha$ , the equivalent of static margin. The higher static margin vehicle pitches more rapidly into the relative wind, thus nullifying the change in lift more quickly. The faster response vehicle provides a more noticeable reduction in total accelerations at positions forward of the center of gravity. As a result, pilot proficiency improves with increase in static margin.

Changes in aircraft design to effect alleviation through improved damping do not readily result in the expected sensitivity reduction. This is true since the damping ratio is determined primarily by  $M_q$ . Therefore, a change also occurs in the numerator of Eq 2 which tends to offset the improvement gained by increased damping.

Damping ratio changes can also be effected through a change in  $M_{\alpha}^{\dot{}}$ . Increases in this parameter are obtainable through design involving lengthening of the tail moment arm and a corresponding reduction in horizontal tail surface area.

It should also be pointed out that decrease in the lift curve slope will also decrease the damping ratio, although the change in the latter has a much less significant effect on sensitivity than has the static change.



## PITCH DAMPERS AND AUTOPILOTS

Autopilots and pitch dampers or stability augmentation systems (SAS) are considered as active system techniques which artificially alter the aircraft dynamic response. Pitch dampers and SAS utilize inertial sensors, electronic computation, and servo actuators to augment the aircraft short period stability. Autopilots, in addition to providing short period stabilization, employ outer-loop or pilot relief modes such as attitude hold, altitude hold, Mach hold, and automatic terrain following. The alteration in short period response as provided by these systems may alleviate or aggravate the response due to gusts.

For aircraft operating over an extreme range of flight conditions, a SAS must either be designed specifically for the vehicle, or must contain adaptive ability, i.e., the ability to alter the control system parameters as a function of the environment or measured response. Most SAS utilize a pitch rate signal as obtained from a rate gyro to control the elevator for improved damping. Normal design employs short-period criteria such as that indicated in Figure 5 (CAL studies).

A pitch SAS that would result in acceptable qualities is shown in functional form in Figure 10. This system employs a compensated pitch rate signal. The compensation employed was not necessarily optimum, but is used to indicate the normally desired trend of SAS design, and to allow evaluation as a gust alleviator. The choice of compensation allowed evaluation over a large range of static margin.

The cancellor or washout circuit employed on the rate gyro output serves to wash out or eliminate the steady-state pitch rate value from the feedback signal, thus allowing maneuverability. The washout time constant must be short enough to allow the commanded rate to be reached within a reasonable time, yet long enough so as not to interfere with the short-period stability. This can be accomplished for the BPA with a 2-sec time

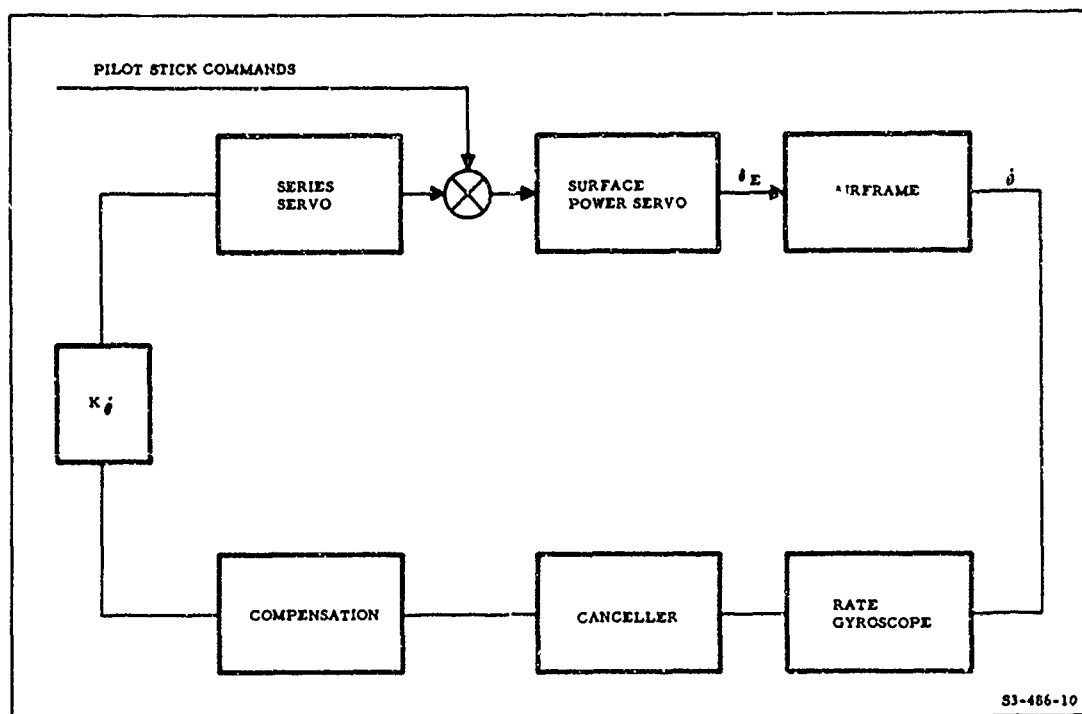


Figure 10. Pitch Stability Augmentation System

constant. Vehicles having a short period response that would be adversely affected by a short time constant are forced to employ control stick pick-offs in addition to a longer term washout.

The root loci plots of Figure 11 illustrate the change in damping and frequency obtainable with the SAS for 5 percent and 20 percent static margin vehicles as a function of the gain,  $K_{\delta}$ .

The increase in damping afforded by the SAS is accompanied by a decrease in the natural frequency. Hence, little or no alleviation occurs (see Figure 9).

An alternate approach to stability augmentation and alleviation would appear to be the feedback of a pure pitch rate signal. The locus plot of Figure 12 illustrates that an increase in natural frequency would result with no change in damping ratio. This would appear to effect a sensitivity reduction. Unfortunately, pitch rate feedback acts in the same way as a

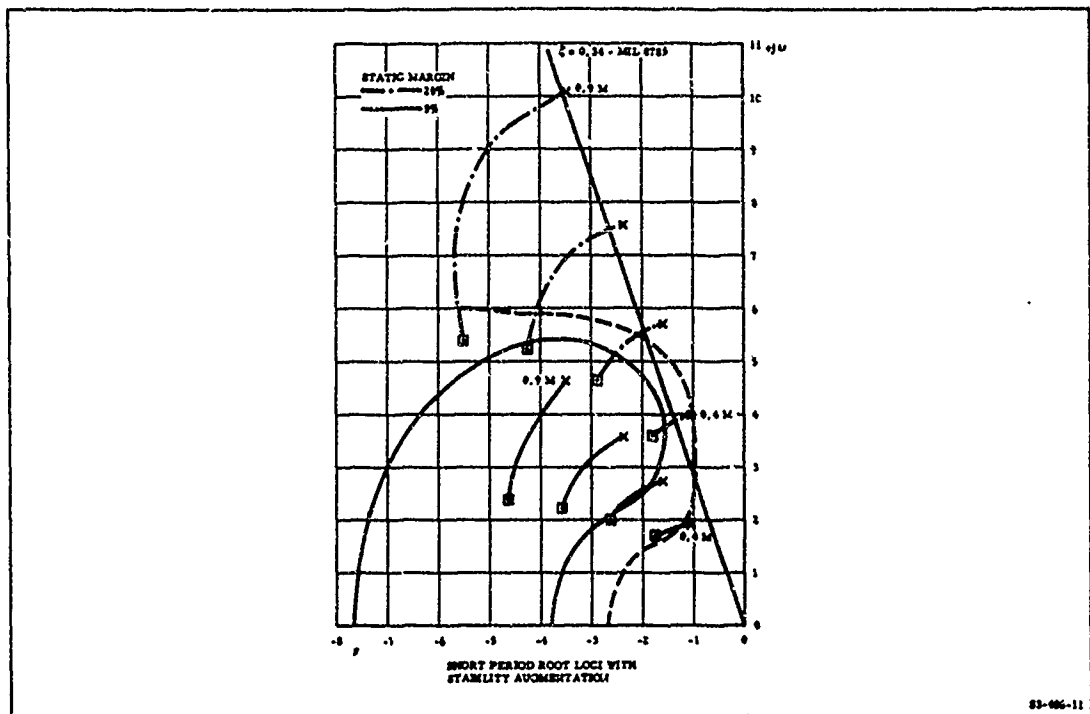


Figure 11. Short Period Root Loci With Stability Augmentation

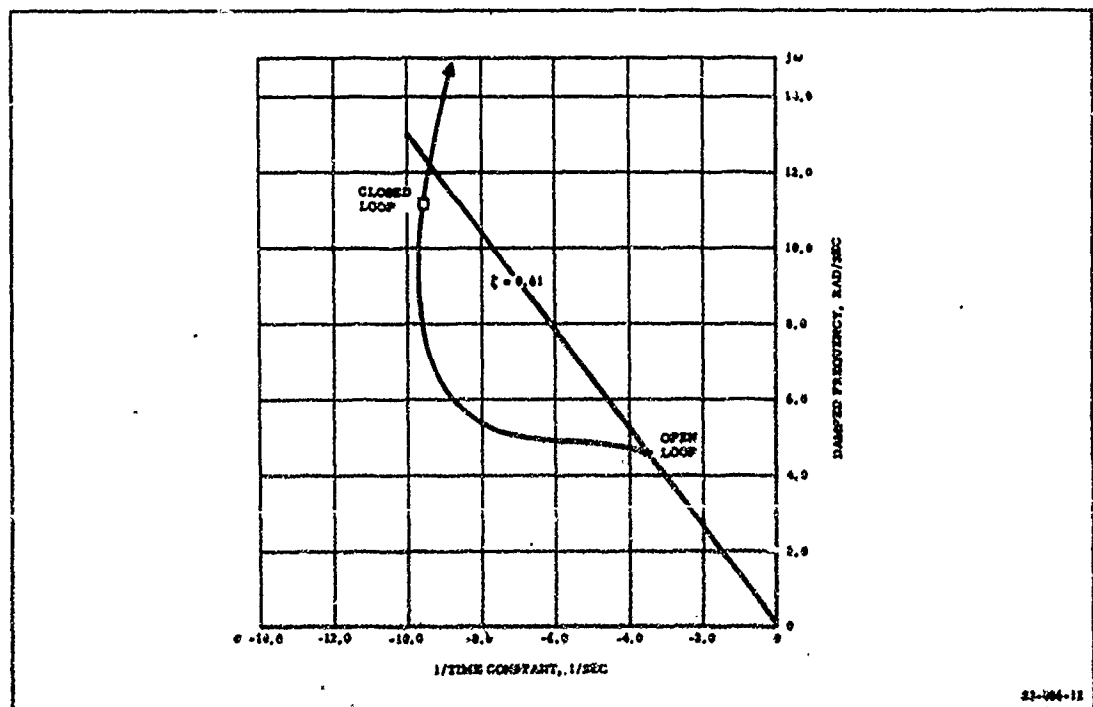


Figure 12. Short Period Locus Pitch Rate Feedback

change in  $M_q$  and the numerator of Eq 2 is also altered, resulting in little or no change in sensitivity.

Autopilots provide the same sort of change in short period dynamics. Most other outer loop commands operate under slowly changing conditions, and therefore, affect the gust response negligibly. An exception to this may be the case of an automatic terrain following mode. Terrain following-gust alleviation compatibility appears to be an area worthy of further investigation.

Autopilots or dampers operating with normal acceleration in conjunction with pitch rate are a design possibility. Acceleration feedback acts to alter frequency and damping with no change in the numerator of Eq 2. Acceleration feedback to the elevator alone tends to be destabilizing, particularly so for the BPA, and some form of pitch rate is needed for good stability. Overall alleviation obtained with such a system may be better than a pitch rate system, however, significant changes are unlikely to occur.

Systems employing mechanical damping, such as the mass-overbalanced elevator of Ref 8, provide essentially the same results.

## ACCELERATION CONTROL

Some proposed alleviation systems have used normal accelerometer sensing and flap deflection to provide gust alleviation. Flap-produced pitching moments can be significant, and moment counterering is necessary. The generated moment is a function of the center of pressure and center of gravity locations, and also, of the flap deflection and rate. Only very small gains and flap deflections are possible with a flap-only system. With this system, phugoid motion easily becomes excited.

A frequently proposed gust alleviation system (Ref 9 and 10) employs vertical acceleration feedback to both flaps and elevators. Non-differentially deflecting ailerons may be used in place of flaps. The two surface acceleration system is shown in Figure 13. Proper moment counterering is obtained with a ratio of gains,  $K_{Nz_E} / K_{Nz_F}$  equal to  $M_{\delta_F} / M_{\delta_E}$ . The moment due to deflection rate is small.

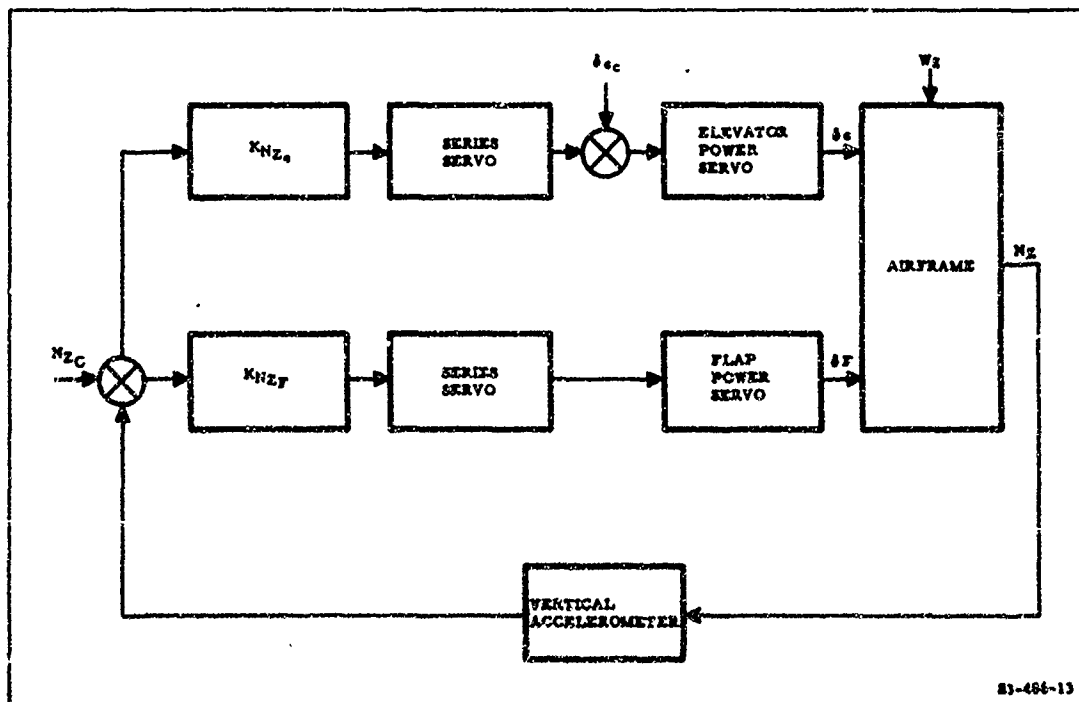


Figure 13. Normal Acceleration Alleviator

If the accelerometer is mounted at the center of gravity, the gust response equation is altered to

$$\frac{N_z}{W_g} = \frac{Z_{\alpha} (s^2 - 2M_q s)}{gV \left[ 1 - K_{NZ_F} \left( Z_{\delta_F} - \frac{M_{\delta_F}}{M_{\delta_E}} Z_{\delta_E} \right) \right] \left[ s^2 + 2\zeta \omega_n s + \omega_n^2 \right]} \quad (10)$$

Because the moment ratio is a function of aircraft velocity, best results at constant gain may be realized at only one condition of flight. The adjustment can be made for the high-speed case where sensitivity is highest, providing the system remains effective (though not optimum) for lower speeds. The damping ratio,  $\zeta$ , changes as a function of  $K_{NZ_F}$  but the frequency  $\omega_n$  remains essentially as for the basic aircraft, providing the gain ratio is maintained. Figure 14 is a root locus plot for the system with SAS used to regain damping.

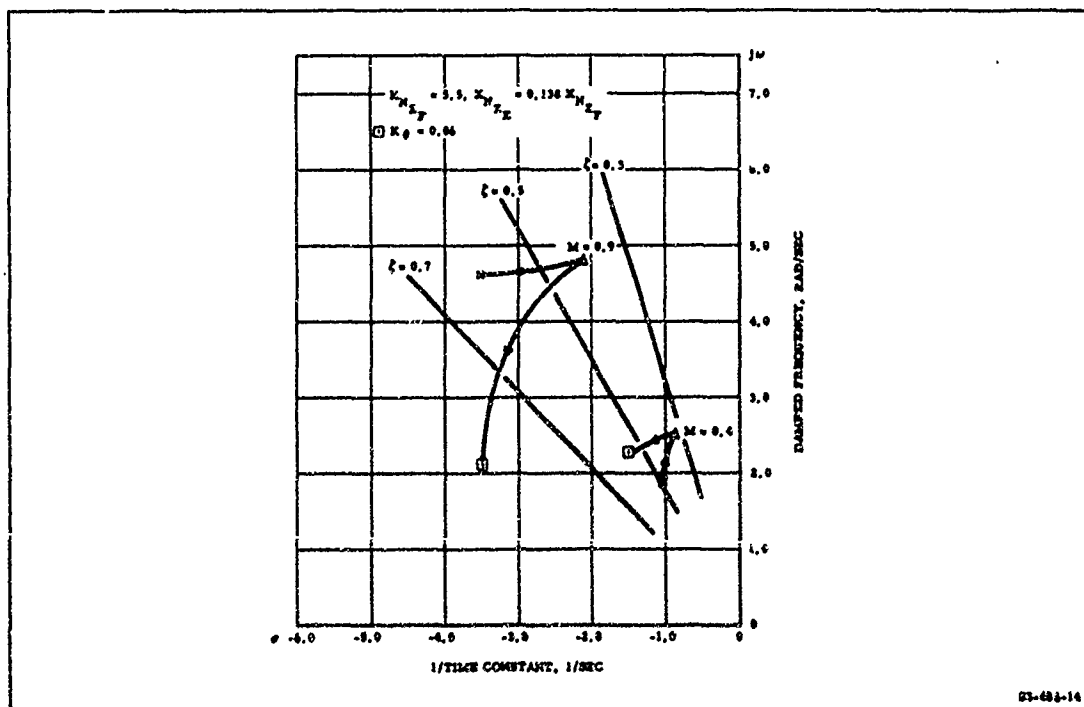


Figure 14. Short Period Loci, Normal Acceleration and Stability Augmentation System

The alleviation provided by a theoretical normal acceleration feedback system, i. e., linear with unity sensor and actuation dynamics, should continuously increase as a function of  $K_{N Z_F}$ , except for the change contributed by the reduction in damping. This static decrease in sensitivity is shown in Figure 15 as a function of  $K_{N Z_F}$ .

The effect of the damping change, servo, and sensor dynamics are also shown in Figure 15. Inclusion of linear sensor and servo dynamics alters the sensitivity very little at low gain. Variation in linear flap servo dynamics over a wide range showed little effect on the alleviation capabilities of the system. At high gains, servo dynamics play a more important role. The SAS has little effect on the sensitivity.

A linear servo response necessarily assumes some maximum displacement. Increased amplitudes of commanded motion with no change in frequency must eventually result in actuator rate limiting. Flap power

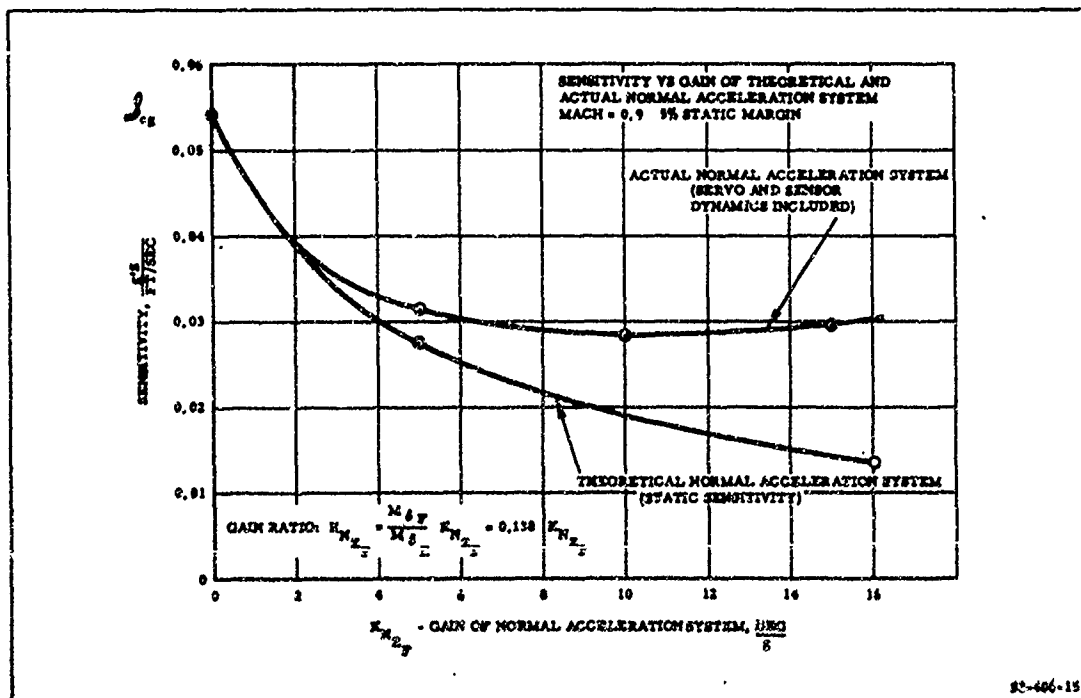


Figure 15. Sensitivity vs Gain of Theoretical and Actual Normal Acceleration System Mach 0.9, 5 Percent Static Margin

servo rate limiting becomes pronounced at high gust velocities with high system gains. A high gain system provides better alleviation at low gust velocities, but results in both sensitivity and stability problems at higher gust velocities. A low gain system, while less effective as an alleviator, assures significant sensitivity reduction well beyond the thunderstorm range.

Elevator deflections and rates are sufficiently small, in that no problems arise from elevator servo non-linearities.

The product  $K_{N_{Z_F}} Z_{\delta_F}$  is an important factor in determining alleviation capability as seen from Equation 10. Since the value of  $K_{N_{Z_F}}$  is limited by the non-linear servo effects as discussed, it would appear that the largest control force possible ( $Z_{\delta_F}$ ) would be the most desirable. This implies the use of larger surfaces which result in a reduction of servo rate, and consequently in a lower value of  $K_{N_{Z_F}}$ .

Maneuverability and response to pilot commands is best obtained if an artificial stick feel system is used wherein g-load commands are proportional to the applied control stick force. Alleviation is accomplished about the maneuver commands.



## ANGLE OF ATTACK CONTROL

A system employing a type of wind flow sensor to generate an error signal for flap and elevator commands has been presented in Ref 11 and 12. The sensors studied have been either a vane or a pressure-probe, usually mounted on a nose boom. Both serve to generate a signal

$$\alpha_v = \alpha_o + \alpha + \alpha_g \left(1 + \frac{1}{U} \frac{c_p}{v} s\right) - \frac{1}{v} \frac{c_g}{v} \dot{\theta} \quad (11)$$

where

$$1 + \frac{1}{U} \frac{c_p}{v} s \text{ approximates the gust transportation lead, } e^{st}$$

The functional diagram for such a system is shown in Figure 16. The steady component of angle-of-attack,  $\alpha_o$ , must be cancelled out so that changes in the trim angle-of-attack with velocity or weight will have no

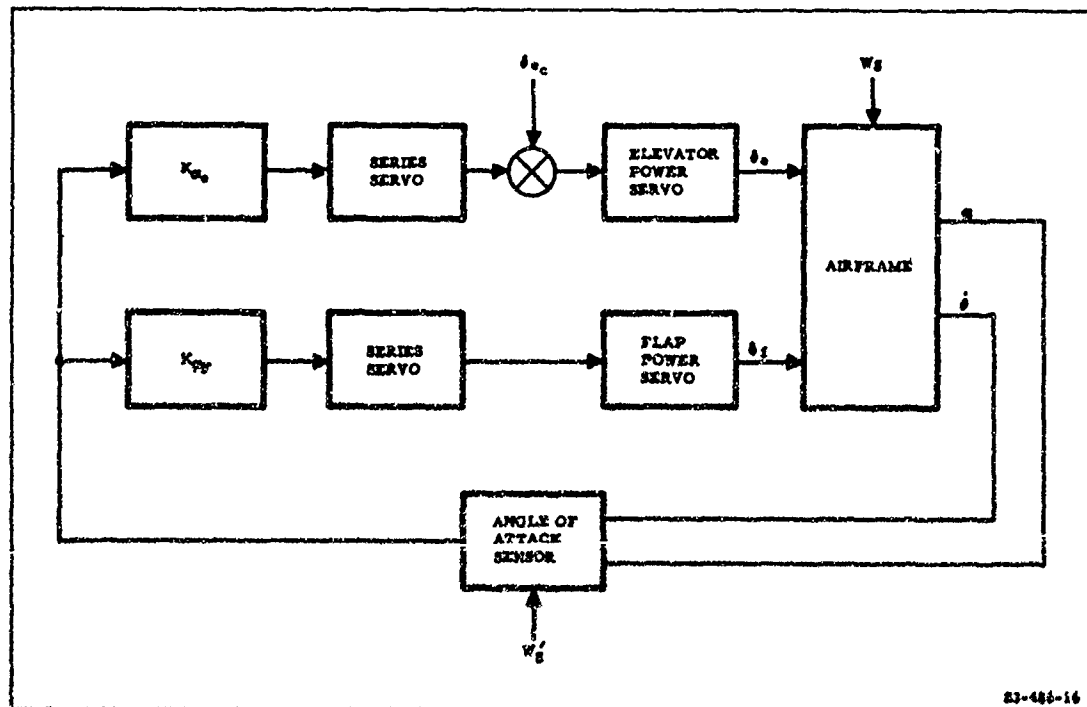


Figure 16. Angle of Attack Alleviator

effect on the sensed signal. The effect of this system on the gust response equation is not as apparent as for the accelerometer system. In general, the  $\alpha$  and  $\dot{\theta}$  terms alter the dynamic response and the  $\alpha_g$  term tends to minimize the numerator. As for the  $N_Z$  system, the sensed signal is used to actuate the flaps and elevator. As long as the gain ratio  $K_{\alpha_E}/K_{\alpha_F}$  is varied and maintained equal to the surface moment ratio  $M_{\alpha_F}/M_{\alpha_E}$ , a single value of flap gain ( $K_{\alpha_F} = 4.5$ ) will serve to provide good alleviation. The results hold throughout the aircraft velocity range. Figure 17 illustrating the effect of varying the gain ratio at  $M = 0.9$  and  $M = 0.725$ , shows that no single gain ratio will serve over the flight speed regime. In fact, no constant ratio will result in a stable system over the range of velocities.

With the gain ratio adjusted for optimum operation at Mach 0.9 and stability augmentation added, damping at lower aircraft velocities remains far from optimum. Higher gaining on the pitch rate signal as an attempt

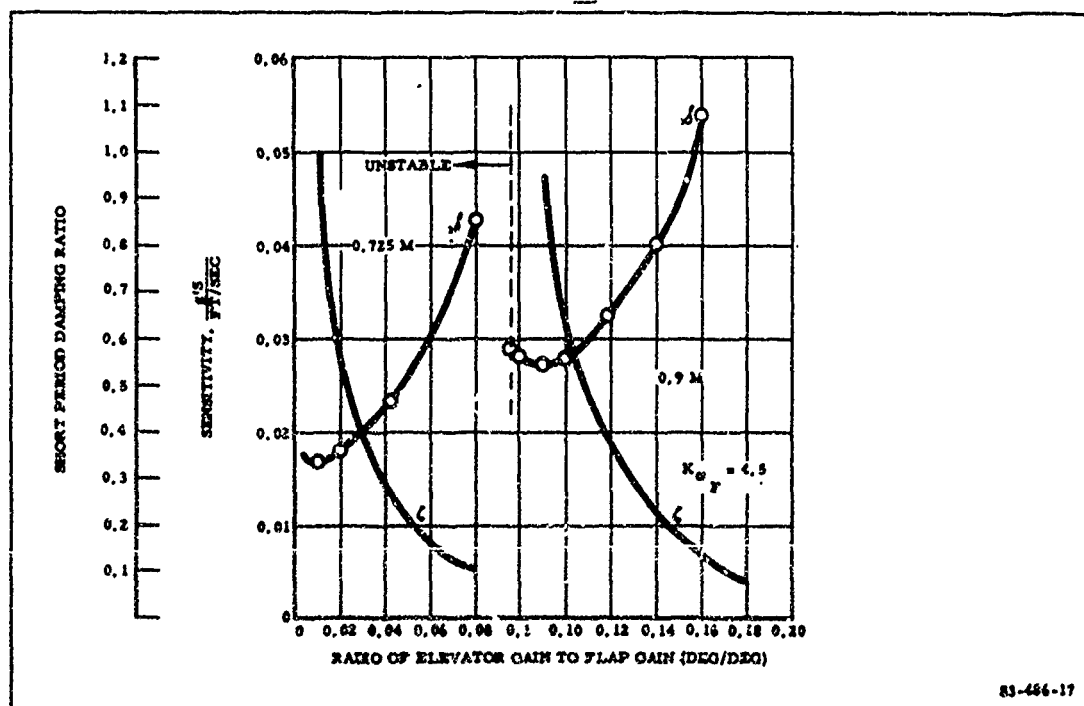


Figure 17. Angle of Attack System, Sensitivity and Short Period Damping Ratio vs Gain Ratio

to provide increased low-speed damping results in poorly damped or unstable servo modes. In addition, the short period response at Mach 0.9 becomes seriously degraded, becoming highly overdamped. It is conceivable that a SAS could be designed to provide satisfactory short-period characteristics for all flight conditions. The stabilization difficulties, nevertheless, appear to be an inherent deficiency of the angle-of-attack system if significant vehicle velocity ranges are to be satisfied.

A noteworthy advantage of the angle-of-attack sensing system is its relative independence of servo-rate limiting. Control surface motion is less with the angle-of-attack system than for the acceleration system. This can be attributed to the lead provided by sensor location at the nose. Improved alleviation is also attributed to the inherent lead. If the sensor were located near the center of pressure, the sensitivity would be increased by 15 percent at Mach 0.9 and by 25 percent at Mach 0.4.

A washout on the probe or vane signal cannot be successfully employed to provide desired handling qualities. The short time constant required, adversely affects the present stability problem. Longer time constants interfere with the ability to sense low-frequency gusts. An integrating actuator or other type canceller is needed for trim.

Stick pickoffs provide a possible method of obtaining pilot control, but gaining and possible shaping of stick force or displacement pickoff signals are functions of the flight conditions. Optimization for a particular flight case could be obtained, but control over a range of conditions would be compromised.

## SIMULATED GUST SYSTEM

Several active gust alleviation schemes that have been considered and discussed attempt to simulate the actual gust. Most analyses have employed a signal corresponding to  $\alpha_g$ . The systems of Ref 13 and 14 fall into this category. A combination of inertial sensors and surface pickoffs can be employed for gust-signal simulation. The lift and moment equations are solved simultaneously, and the approximate equation obtained as

$$\alpha_g \approx -K_{N_z} N_z - K_{\delta_F} \delta_F - K_{\delta_E} \delta_E - \frac{K_{\dot{\theta}} \dot{\theta}}{s+a} \quad (12)$$

The lagged  $\theta$  term here is a low frequency approximation of  $\alpha$ . Wind-flow and inertial sensors may be used to obtain

$$\alpha_g \approx \alpha_v - \alpha + \frac{1}{V} \frac{c.g.}{V} \dot{\theta} \quad (13)$$

$\alpha$  is approximated, either by lagged  $\dot{\theta}$  as above, or by programming as a function of airspeed as follows:

Since

$$\int N_z dt = V \sin \gamma \quad (14)$$

and

$$\gamma = \theta - \alpha \quad (15)$$

then for small angles

$$\alpha = \theta - \frac{N_z}{V s} \quad (16)$$

Rate gyros are usually employed and approximately integrated to obtain  $\theta$ . The integration of  $N_z$  is also an approximate integration. Programming as a function of airspeed introduces some error since the velocity term involved here is actually an inertial or groundspeed.

The gust transportation lead is neglected in this equation. A time delay may be used on the control signal for equalization. The time delay must also be programed as a function of airspeed for operation over a range of flight conditions.

The simulated gust signal approach theoretically results in the ideal gust alleviator. Alleviation is accomplished by surface commands from this signal, however, no change occurs in the basic vehicle stability or response to control inputs. This point can be seen if a matrix is formed of the airframe perturbation equations of motion and the control system equations, and the closed loop transfer function obtained by matrix expansion. The closed loop gust response is seen to be of the form

$$\left. \frac{N_z}{w_g} \right|_{CL} = \left. \frac{N_z}{w_g} \right|_{OL} + F_1 \left. \frac{N_z}{\delta_F} \right|_{OL} + F_2 \left. \frac{N_z}{\delta_E} \right|_{OL} \quad (17)$$

where  $F_1$  and  $F_2$  are the mechanized gains and shaping that operate on the control signals. This expansion assumes perfect simulation of the gust. The subscripts CL and OL denote closed loop and open loop respectively. Since the denominators of each of the open loop transfer functions is the system characteristic equation that determines stability, it is obvious that the control system does not alter the stabilization characteristics.

Through a similar expansion it can be seen that

$$\left. \frac{N_z}{\delta_E} \right|_{CL} = \left. \frac{N_z}{\delta_E} \right|_{OL} \quad (18)$$

and thus the response to control stick inputs is also unaltered.

The question of alleviation capability remains to be answered. Setting Eq 17 equal to zero and solving for  $F_1$  and  $F_2$  yields system parameters necessary for perfect alleviation. Two basic fallacies exist with such a development:

1. The system parameters determined are a function of flight condition.

2. The parameters are obtained by what amounts to forcing the difference of two large numbers equal to zero.

Thus, a small error can result in a large differential, consequently, the amount of alleviation obtainable with such a system becomes a critical function of system parameters and tolerances. In addition, the aerodynamic parameters which combine to make up the transfer functions are usually determined by wind tunnel tests and are accurate only to within approximately 20 percent.

System parameters were determined for the BPA on this basis and a subsequent analog computer simulation was conducted. As a basic test, the actual gust input utilized for disturbance was also used as a control signal. The resultant sensitivity as a function of the elevator signal gain is shown in Figure 18. The critical characteristics are obvious, the system is extremely gain sensitive.

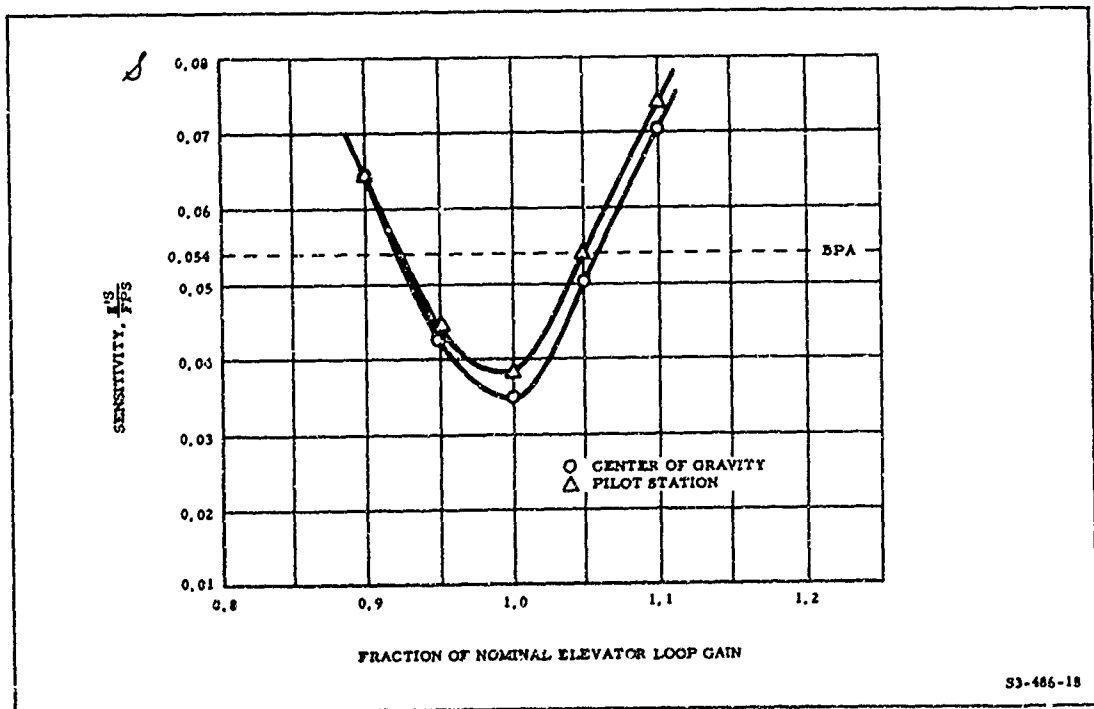


Figure 18. Sensitivity vs Gain-Simulated Gust System

Simulation of the Mach 0.4 flight condition, coupled with the control system parameters determined for Mach 0.9, actually resulted in aggravation rather than alleviation.

The authors' conclusion is, while the simulated gust approach allows maximum alleviation with known and fixed airframe dynamics, its use under practical conditions is questionable. It is highly probable that good alleviation could be obtained over a small range of flight conditions with the use of empirical adjustments as determined in flight test. Alleviation over a limited flight regime is possible with a number of systems and the high degree of sophistication appears to preclude this scheme from use.

The system appears to lend itself ideally to an adaptive approach, and hence, operation over a wide flight regime. This approach provides several interesting aspects for further investigation.

## FOLDING WING

The passive system concept of folding a portion of each wing tip of an aircraft when gusts are encountered has as its objective a reduction of the aircraft's gust sensitivity through a decrease in the exposed wing area (increased  $W/S$ ), and a reduction of wing aspect ratio (decreased  $C_{L\alpha}$ ). The effective aspect ratio of a folded wing, which determines its aerodynamic characteristics, is not the same as its geometric aspect ratio because of the end-plating effect of the folded tips on the load carrying portion of the wing. Little, if any, change is indicated in the effective aspect ratio except for extreme taper ratios. This relative independence of  $C_{L\alpha}$  on wing folding, when based on projected wing area, is apparently the case for partial wing folding (tip dihedral). Since there is no reduction of  $C_{L\alpha}$  with wing folding, the only gust alleviating capabilities of this system result from increased wing loading and altered dynamic characteristics.

Evaluation of the gust sensitivity with folded wing tips was conducted for an assumed folding of the outboard 40 percent of the wing span. The configuration is thereby altered as shown in Figure 19. The projected wing area is 188.5 sq ft, a 32-percent reduction from that of the BPA with wing unfolded.

The structural weight penalty ( $0.035 \times$  gross weight) estimated is considered and compensated for by a corresponding decrease in the available fuel. If the 20-min dash occurring at Mach 0.9 is performed with the wings folded, and the cruise portion of the mission is flown at Mach 0.4 with the wings in their extended position, there will be a 21-percent resultant decrease in aircraft range.

It should be noted that whereas folding the wing tips decreases the aircraft's sensitivity to vertical gusts, the sensitivity to lateral gusts is increased because of the larger vertical surface area.



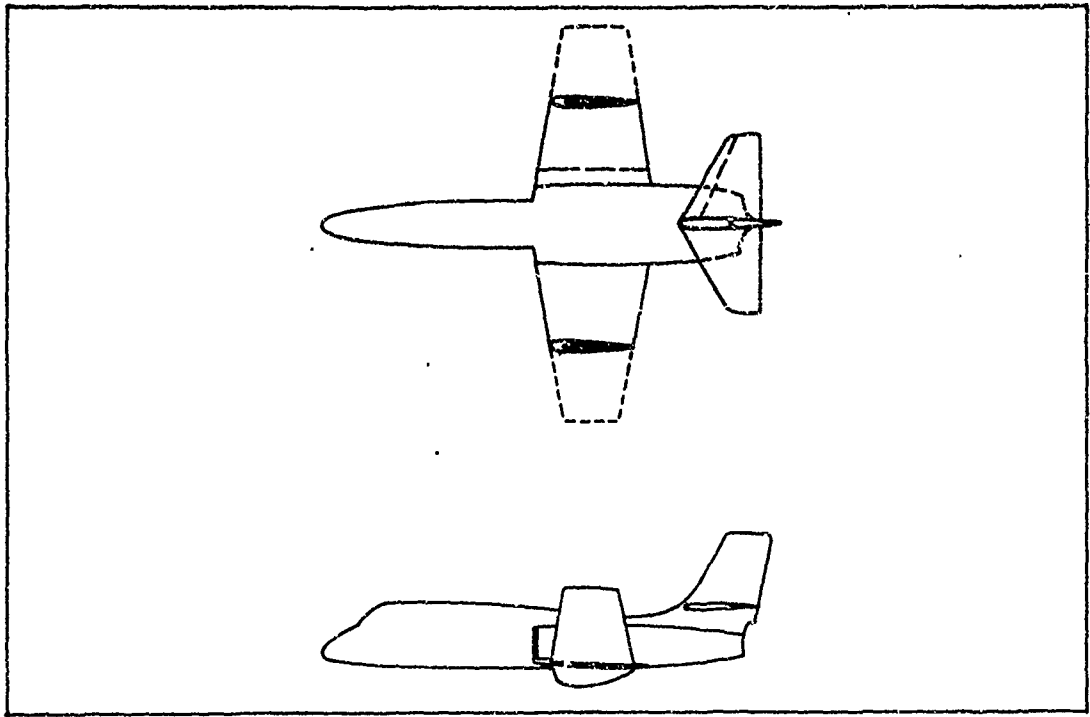


**Figure 19. Folding-Wing Aircraft (FW)**

## TELESCOPING WING

The telescoping wing system retracts a portion of the normal wing tip into the inboard wing contour without any influence on the aircraft's aerodynamic characteristics. The objectives in this case are a decrease of the exposed wing area (increased  $W/S$ ), and a reduction of wing aspect ratio (decreased  $C_{L_\alpha}$ ).

Application of wing telescoping alters the geometric aspect ratio and wing area in the same manner as wing folding. The geometric aspect ratio in this case is also the effective aspect ratio.

The BPA with telescoping wing was evaluated for gust sensitivity with an assumed telescoping of the outboard 40 percent of the wing. This allows 10 percent of the wing to house the telescoping mechanism. The altered configuration is shown in Figure 20.

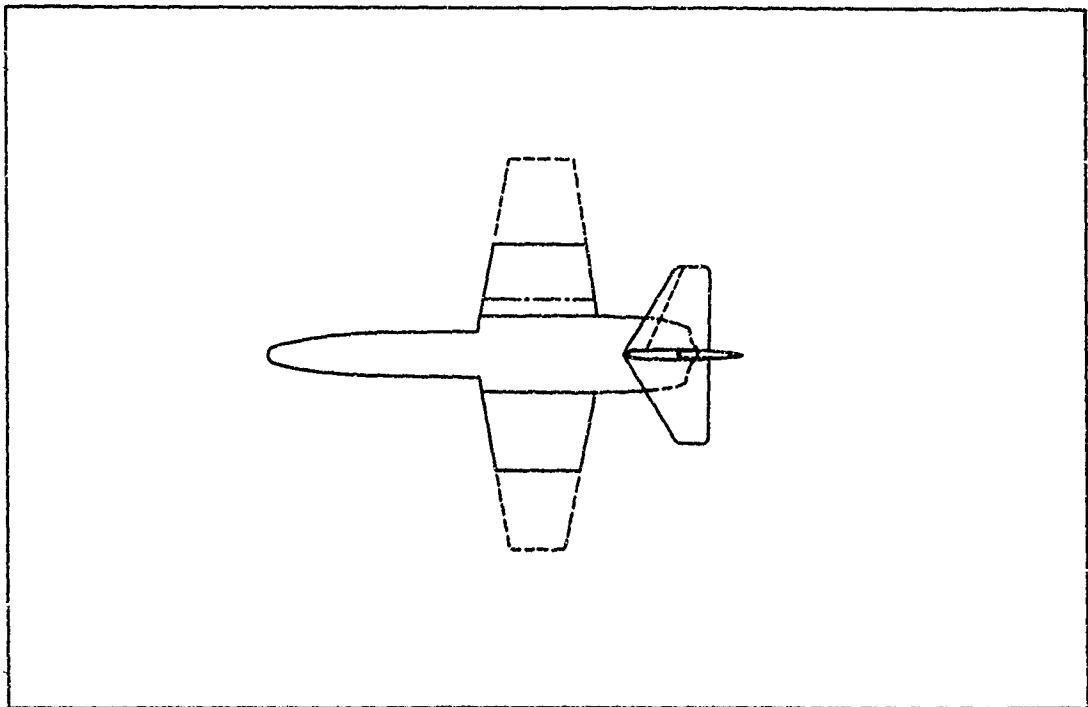


Figure 20. Telescoping-Wing Aircraft (TW)

The higher induced drag with telescoped wing at Mach 0.4 is detrimental to aircraft range whereas the reduced profile drag at Mach 0.9 results in increased range capability at that speed. A structural penalty is associated with the ability to telescope the wings ( $0.067 \times$  gross weight). Reducing the fuel load and maintaining the same takeoff gross weight (18,000 lb), there is a net loss in cruise range of 32 percent even with the wings extended during the cruise portion of the mission. This discussion is based upon the assumption of no discontinuities in wing contour although the degree of error caused by this assumption was considered in detail in the study.

## VARIABLE SWEEP WING

A variable sweep wing offers several possibilities for reducing gust sensitivity. The wing lift-curve slope can be decreased due to the increased sweep angle of the wing and its reduced aspect ratio. The possibility exists that the wing area can be reduced by using sweepback.

The BPA has been assumed to incorporate variable sweep as shown in Figure 21. This configuration is designated  $VS_1$ . A low aspect ratio (wide-chord) wing is not a desirable plan form for variable sweep purposes, and is used here only for comparison.  $VS_1$  requires the addition of a wing glove at the leading edge and a rounded section at the trailing edge of the inboard portion of the wing. Sweep has been limited to 60 deg of the leading edge for the outboard wing panel and 45 deg for the glove.

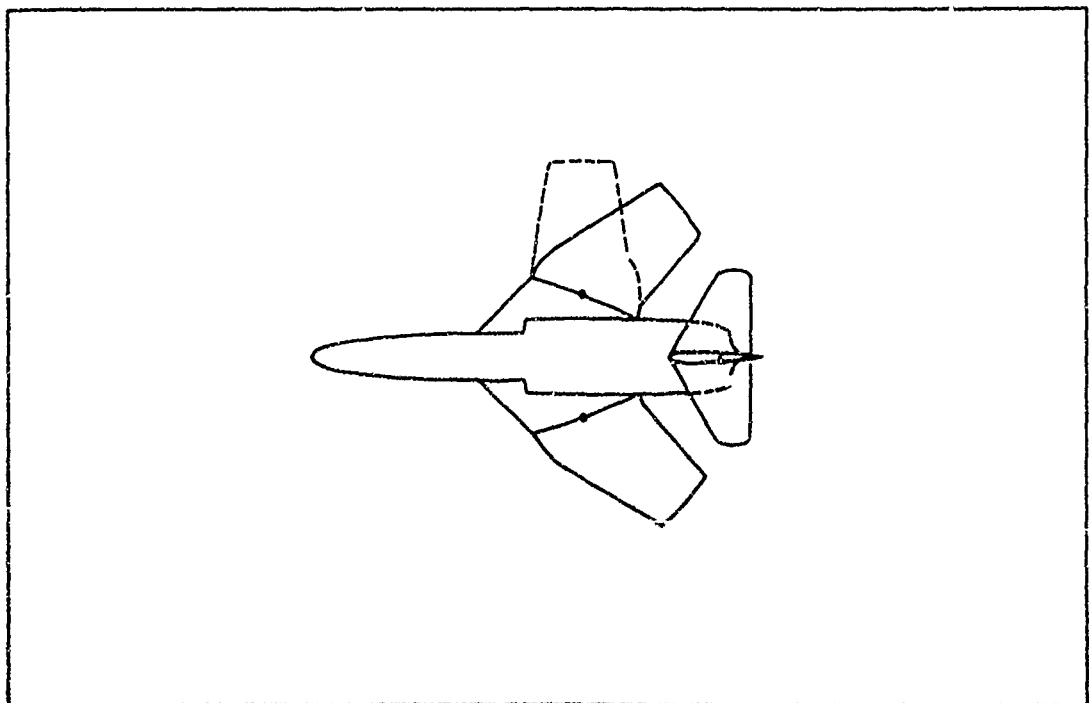


Figure 21. Variable Sweep Aircraft ( $VS_1$ )

The higher induced drag of the swept version is detrimental at cruise Mach numbers, but is outweighed by the profile drag reduction at the dash speed. More economical high-speed flight is thus possible with the wings swept. The structural weight penalty ( $0.048 \times$  gross weight), when compensated for by a reduced fuel weight, decreases range at cruise speed by 21.5 percent.

A further consideration for a variable sweep configuration is elimination of the necessity for a thin wing. If the wing of  $VS_1$  is increased in thickness from 6 to 12 percent, the wing structural weight decrease will enable the aircraft to carry a greater fuel load. The range decrease is 21.5 percent for the thin-wing  $VS_1$  as opposed to 9 percent for a thick-wing version. The range decrement now is due largely to the increased profile drag of the thicker wing. Takeoff distance over a 50-ft obstacle at a wing loading of 65 will be reduced from 2000 to 1740 ft.

This analysis of variable sweep can prove somewhat misleading because of the limited applicability of this concept to the BPA configuration. In order to indicate the more desirable characteristics achievable by means of variable sweep, an additional, although less extensive, analysis was made of an alternate configuration. For this purpose, an entirely new wing is incorporated on the basic airplane, and the configuration is designated as  $VS_2$ . Figure 22 illustrates the geometry of  $VS_2$ . In order to retain some basis for comparison, the wing area in the unswept position (excluding the glove) has been maintained at 277 sq ft.

The high unswept aspect ratio of  $VS_2$  permits considerable sweepback of the wing while retaining a smooth wing contour for high speed flight. By comparison with  $VS_1$ , the increased sweepback of  $VS_2$ , reduced swept wing aspect ratio, and smaller wing area are conducive to decreased gust sensitivity. There is a corresponding reduction in  $Z_{\alpha}$  of 55 percent, indicating a gust alleviation potential of 55 percent

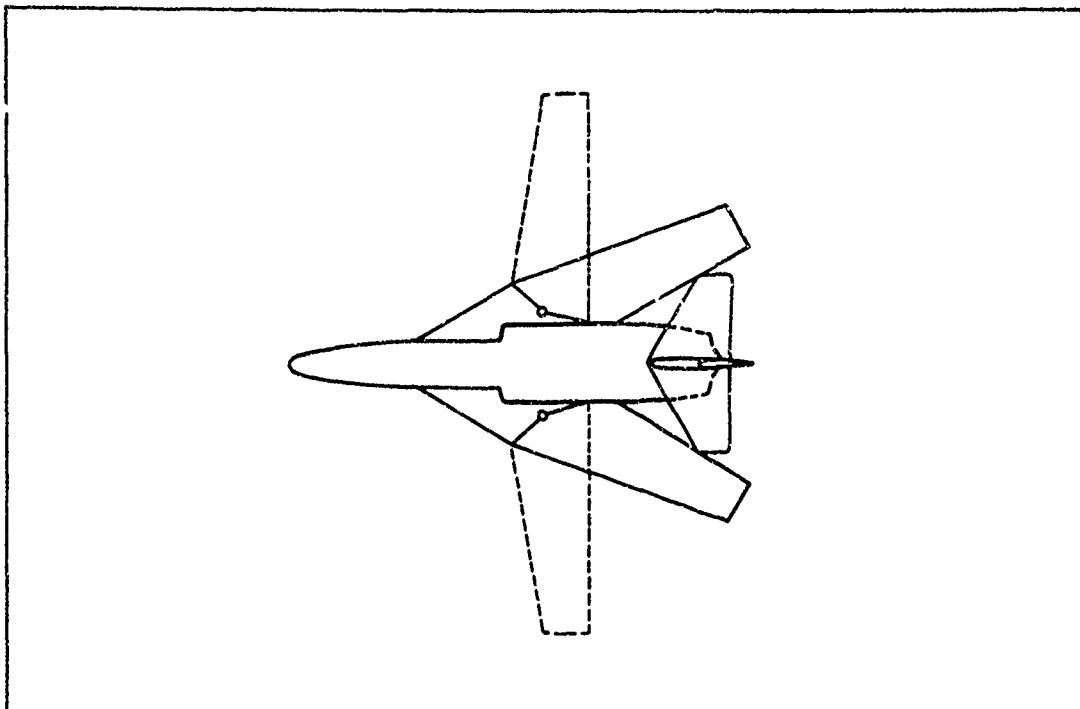


Figure 22. Variable Sweep Aircraft (VS<sub>2</sub>)

in contrast to 35 percent for VS<sub>1</sub> calculated on the same basis. Considerations of aircraft dynamics and the turbulence spectrum will reduce these percentages, but the relative comparison should remain substantially the same. It is estimated that the aircraft structural weight will be 17 percent greater than that of the BPA. With a 20-min dash occurring at Mach 0.9, the cruise range with wings unswept is estimated to be 13 percent less than that of the BPA.

The wing planform of VS<sub>2</sub> provides improved low-speed performance over the BPA. The thicker wing, in an unswept position, combined with the higher aspect ratio reduces takeoff distance from 2000 ft to 1665 ft for the same gross weight.

Another possible design approach would be to maintain the 2000-ft takeoff distance and decrease the wing area with the planform of VS<sub>2</sub>

unchanged. The resulting configuration will exhibit reduced gust sensitivity, and have a reduced structural weight so that its fuel load and range will be greater than that of VS<sub>2</sub>. The possible variable sweep designs are sufficiently numerous to require further study.

## FREE-FLOATING SURFACES

Many gust alleviating concepts can be classified as free-floating or rotatable surfaces. This classification covers those systems which can release a portion of the load-carrying wing surface from its rigid continuity with the remainder of the wing and permit it to float freely with the relative wind. The surfaces released can be the trailing edge flaps, the ailerons, or a portion of the main wing, generally the outer span, specifically constructed to permit freedom of rotation about either a spanwise or chordwise hinge. In any of these approaches, the basis of the concept is to reduce the load-bearing surface area in the presence of gusts (increased  $W/S$ ).

A sizeable portion of the wing tips conceivably can be permitted freedom to rotate about a chordwise hinge line at the inboard end of the releasable tip. In calm air, the tips will then tend to float at some known dihedral angle, determined by the balance between the moment due to the weight of the tip and the lift on the tip. The maximum achievable reduction in gust sensitivity by this means is the same as that of the folding wing. However, since turbulent air encompasses both up and down gusts, the resultant tip action will consist of a limited, and essentially equal, range of vibration angles about its normal position. Small net changes in tip dihedral, about 10 deg, have relatively little effect upon the overall wing lift. Consequently, this particular concept offers little potential for gust sensitivity reduction.

If the wing tip is designed to float freely about a spanwise hinge line ahead of the tip aerodynamic center, its maximum potential for gust alleviation purposes is similar to that of the folding wing. For a given size of wing tip effected in either concept, the same area of wing will be unloaded. However, the presence of the tip whether in the vertical plane as for the



folded wing, or the horizontal plane as for the rotating tip, will serve to end-plate the remainder of the wing and thus maintain a high effective aspect ratio. The rotating tip can be treated as a full-chord flap, as shown in Eq 19,

$$(C_{L_{\alpha}})_R = C_{L_{\alpha}} (1 - K) \quad (19)$$

where K is a function of tip span.

In accordance with the preceding equation, the effective lift curve slope with different extents of free-floating tips can be calculated. The alleviation factor of the rotating wing tip is very similar to that of the folded wing as expected. It is slightly less effective than the folding wing for reasons not discussed here. It is also noted that the folded wing will have less drag than a rotating tip of equivalent size. A weight analysis of a 40-percent semi-span rotating tip on the BPA indicates a 17-percent increase in the aircraft structural weight in contrast to an 11-percent increase for the folded wing.

The analysis indicates that the rotating wing tip concept will provide gust alleviation and aircraft performance somewhat similar, but inferior, to that achievable with a folding wing. The possibility of wing tip flutter also exists.

## DEFLECTORS AND SPOILERS

The passive alleviation method of projecting a spoiler or deflector, lower surface spoiler, similar to split flap, from a wing surface will reduce the lift curve slope of the wing if the projection is at a forward chordwise station of the wing. Spoilers and split flaps in their more commonly used locations, 70 or 80 percent of the wing chord, do not appreciably effect the wing lift curve slope.

The forward located spoiler or deflector induces flow separation from the wing surface behind it, thereby altering the airfoil characteristics and effectively reducing the section lift curve slope,  $C_{L_\alpha}$ . Three dimensional test data obtained with these devices in a forward wing location, Ref 15 through 18, have been analyzed and used to determine the effect of deflectors on section  $C_{L_\alpha}$ .

Devices which reduce wing lift curve slope by causing flow separation from the wing also introduce additional drag. It is noteworthy that a spoiler will produce some negative shift of the lift coefficient at which minimum drag occurs,  $\Delta C_{L_0}$ , whereas a deflector will produce a positive shift.

In order to maintain the lowest possible drag level while achieving maximum alleviation, it appears desirable to use a maximum of deflector projection with a minimum of deflector span. The permissible spanwise extent of the deflector, as used on the BPA, is limited to an inboard location,  $0.45 b_w$ , that will not result in excessive buffeting of the tail, and an outboard location,  $0.65 b_w$ , that will not interfere with the effectiveness of the aileron. The test data also suggest that the deflector be located well forward on the wing where the drag contribution is less but no degradation in alleviating capability,  $\Delta C_{L_\alpha}$ , is apparent.

Sensitivity comparisons of the BPA with and without deflectors projected can be limited to consideration of the parameter,  $Z_a/gV$ , which is a direct function of the changes in lift curve slope.

Large decrements in aircraft range capability are also found as a consequence of the  $dra_g$  introduced by the deflectors. The indications are that reduced maximum flight speeds and large decreases of aircraft range will result, with relatively little reduction in sensitivity.

The preceding discussion has been based upon information available for forward-located deflectors. The same conclusions are generally applicable to similarly located spoilers or combinations of these devices, with or without associated slots in the wing. It is evident from symmetry that either a spoiler or a deflector, of similar size and location on a wing, will provide identical reductions in  $C_L$  and increments in  $C_{D_o}$ . Combinations of these devices will lead to the same pattern of results.

## MISCELLANEOUS

A number of possible alleviation techniques that have received some attention are briefly presented here.

### CHORDWISE WING SLOTS

The concept of chordwise slots opened at one or more spanwise stations along the wing is discussed in Ref 19, 20, and 21. Simplifying assumptions made in developing the theory, and the lack of knowledge concerning viscous effects and slot structural carry-through interference effects, suggest that theoretical results be viewed with caution.

The opening of chordwise slots at one or more stations along the wing span permits air flow from the lower to the upper wing surface at the slot when the aircraft is in level flight. The result is a local equalization of pressure similar to that normally occurring at the wing tip. In that respect, it is also similar to an aspect ratio reduction. The wing is effectively divided into wing segments, each of reduced aspect ratio, leading to a net decrease in wing lift curve slope. The theory indicates the possibility of about 20-percent gust alleviation for an aircraft such as the BPA on the basis of lift curve slope reduction alone.

Associated with the effect of chordwise wing slots on lift will be some drag increase and stability changes. These effects depend considerably upon the contouring of the slots, and the exposed carry-through wing structure.

### AIR JET SPOILERS

Consideration is given to spoilers consisting of airjets from the wing surface to serve as gust alleviators in Ref 22 and 23. Indications are given of reasonable promise for this system when it is considered in place of mechanical spoilers. The effect of an airjet deflector on the wing aerodynamic characteristics is the same as that of a mechanical

wing aerodynamic characteristics is the same as that of a mechanical spoiler. That is, any decrease in lift curve slope due to wing flow spoilage will be associated with the same large drag increases which prove detrimental as in the case of mechanical deflectors. In view of the high drag penalty, the appreciable power required and the ducting and nozzle requirements, it appears that an airjet spoiler or deflector system is less attractive than the mechanical deflector system.

#### FLEXIBLE WING SPAR

A gust alleviation system which has been tested in flight is discussed in Ref 24, 25, and 26. The system operates to counteract the effect of a gust upon the aircraft by aileron deflection determined by and geared to the bending of the wing. For the system as flight tested, alleviation of aircraft accelerations was about 9 percent at flight Mach numbers of the order of 0.2. Higher aileron deflection to wing bending gearing ratios resulted in an unstable system. Surface inertia and response time requirements for satisfactory in-phase operation at high flight speeds are extremely difficult to achieve. Instability can easily result.

#### ALLEVIATION AIRPLANE

The gust alleviation airplane described in Ref 27 is a rather interesting development of an airplane designed specifically to alleviate the effect of gusts. This approach appears to utilize the floating characteristics of the flaps and an auxiliary empennage mechanically linked to flaps and elevators. Maneuverability is obtained because of the linkage, but it appears to be limited in application to a small flight regime. Detailed alleviation analysis is difficult with the limited information available on the system. The detailed design problems, system weight, and lack of promise of considerable alleviation appear to prohibit utilization of such a system for the purposes considered here.

## DIRECT SEARCH OPTIMIZATION

The problem of attaining the optimum active gust alleviator was subjected to a unique digital computer program called Direct Search Optimization, under the constraints of stability, controllability, and alleviation. This approach results in the simulated gust system.

## WIENER OPTIMUM FILTER THEORY

A theoretical study employing the Wiener optimum filter theory was conducted and reported in Ref 4. The theoretical requirements included a minimization of a combination of acceleration and pitch rate. The derived filter in this case corresponds to the characteristics of the system to be obtained. The author assumes that a gust sensing device is available, and that independently operating force and moment can be applied. A system based on this analysis would effectively be a simulated gust system with optimum shaping.

## RESULTS AND CONCLUSIONS

Alleviation capabilities of the various systems are summarized in Figure 23, where sensitivity is shown as a function of Mach number for a heavy weight vehicle. The sensitivities shown, however, are obtained on a linear basis; both the angle of attack and the low gain acceleration systems are little affected by servo rate limiting at rms gust velocities up to about 18 fps. From an endurance standpoint, assuming a mean weight vehicle, half-fuel load, it can be seen from Figure 24 that a considerable increase in pilot proficiency is possible with alleviation system incorporation. The normalized acceleration power spectral densities at the pilot location are illustrated in Figure 25 for the BPA, telescoping wing and acceleration system, at Mach 0.9.

Passive systems generally exhibit the same spectral characteristic as the BPA, with a reduction in loading in the short period frequency

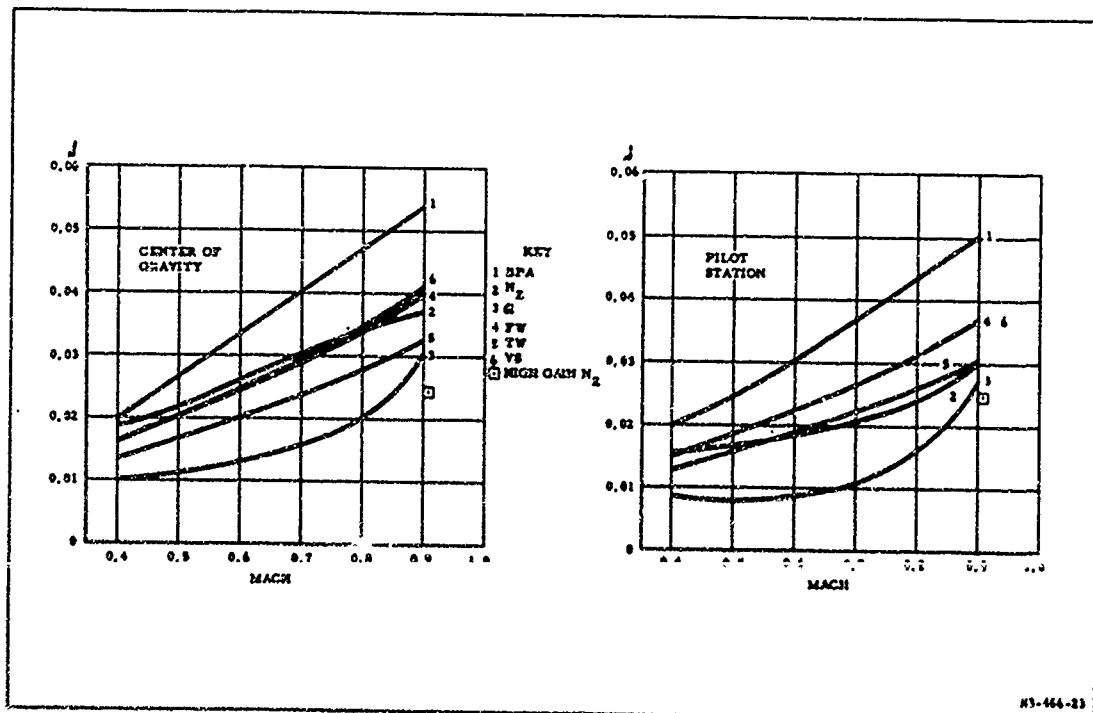


Figure 23. Center of Gravity and Pilot Station Charts

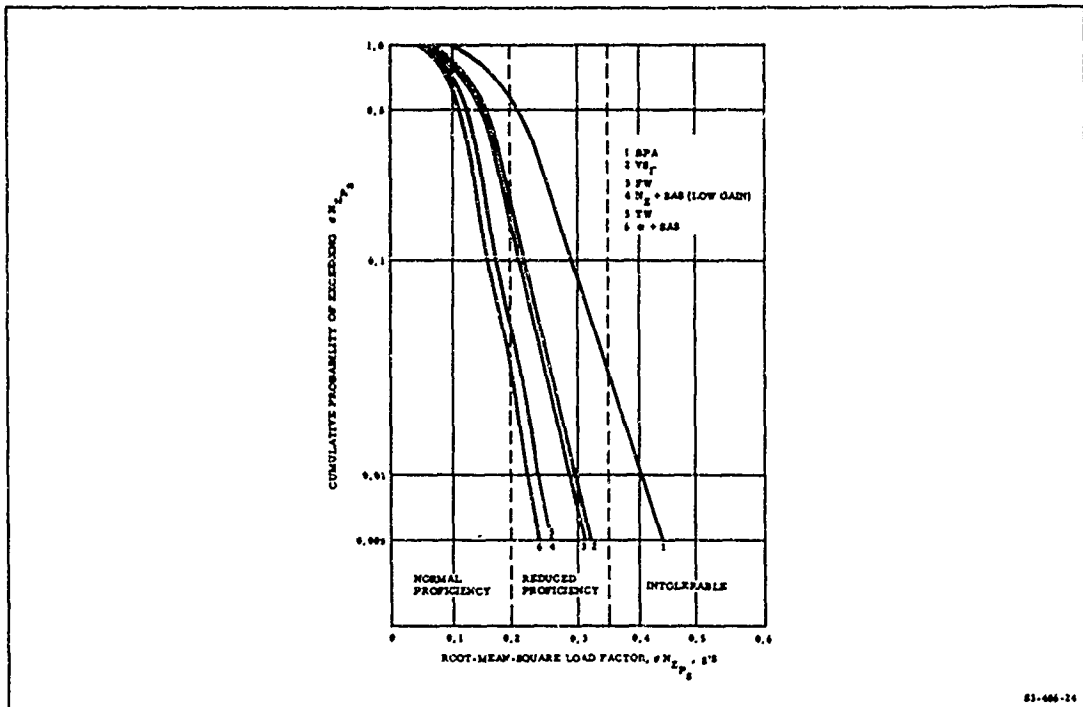


Figure 24. Cumulative Probability of Exceeding RMS Load Factor-Dash,  $M= 0.9$

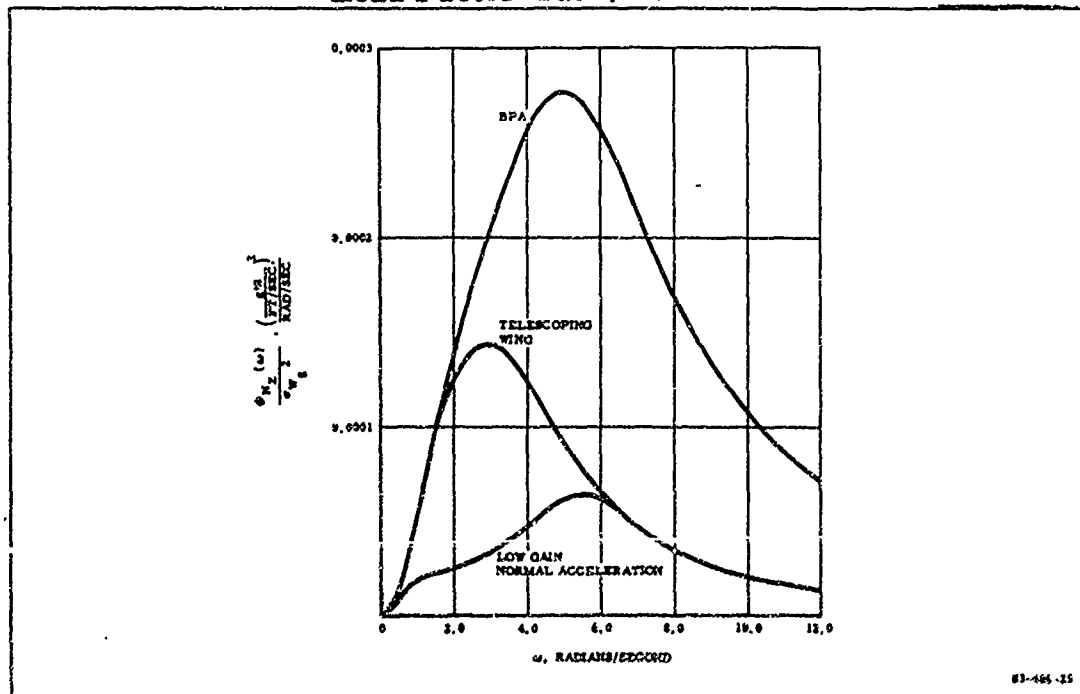


Figure 25. Power Spectral Density of Normal Acceleration at Pilot Station



range. Active systems, while maintaining rms values similar to the passive configurations, show a marked decrease in the short period frequency range, and an associated increase at higher frequencies. This characteristic is further illustrated in Figure 26. It should be noted that the telescoping wing and acceleration systems have similar sensitivities. The result of this high frequency acceleration content is noted in Figure 27, where the number of exceedances of peak g's is compared to the pilot behavior categories. Therefore, the active systems appear to result in a decreased pilot tolerance. The actual effect on pilot behavior is somewhat nebulous when the frequency content is such that the exceedance curves pass through a number of behavior categories. Are pilots more disturbed by high frequency and low amplitude vibrations or by low frequency and large amplitude oscillations in acceleration? More study in the area of human reaction is clearly indicated. The high frequency acceleration content as evidenced for the

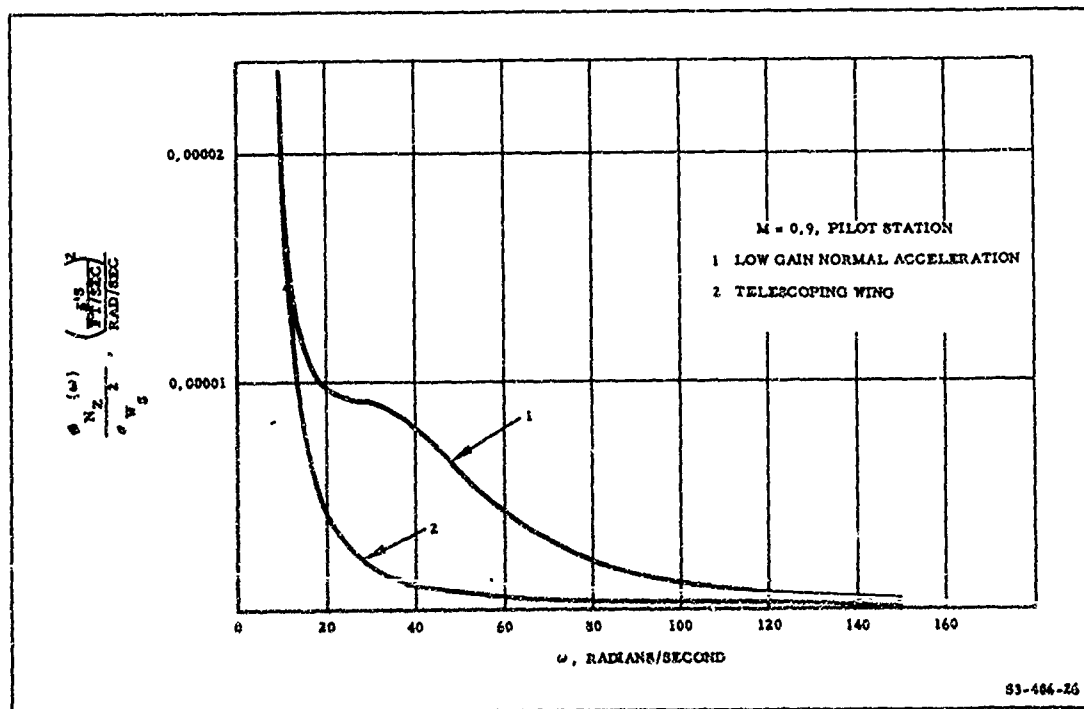


Figure 26. Power Spectral Density of Normal Acceleration at Pilot Station

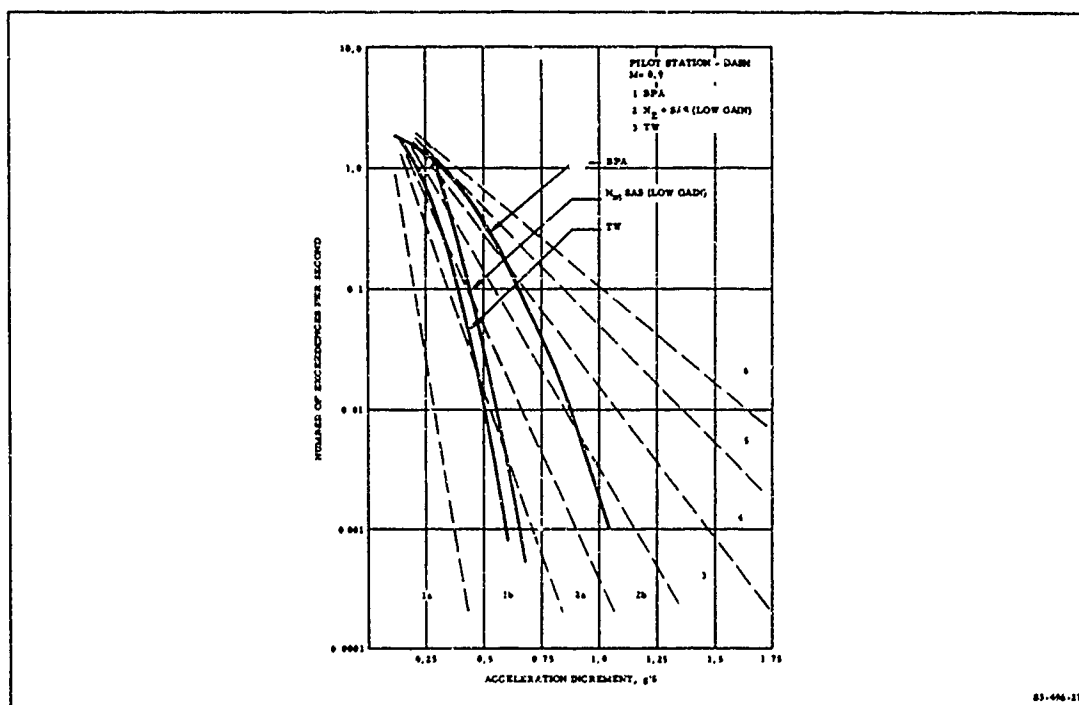


Figure 27. Exceedances Per Second for Gust Alleviation Systems Pilot Station-Dash,  $M = 0.9$

active systems, rises from peaking at the servo frequencies. Though transient lift buildup on the wing was not considered in this study, it appears that perhaps such refinements are necessary in view of the high frequency reactions. A further refinement also appears necessary in the area of time lag in gust incidence and downwash variations. A truncated exponential series expansion was utilized and leads to investigation difficulties at structural modes frequencies.

An actual increase in sensitivity must occur when structural mode oscillations are considered. Alteration of vehicle geometry in passive configuration generally has little effect on the structural mode frequency and damping, with the possible exception of a variable sweep wing. This configuration should result in a decrease in structural vibrations as a result of the decreased effect of wing flexibility.

Structural mode excitation with active system incorporation is, of course, a distinct possibility. Care must be taken as with the design of any autopilot in location of sensors and subsequent vibration pickup. Additional high frequency filtering may be necessary but remains a problem unique to the individual aircraft structural design and subsequent structural mode frequencies. Sensor location also has an effect on the low frequency sensitivity.

All active systems discussions have assumed the trailing edge flaps as lifting devices. Ailerons may be used instead, with signal mixing such that differential motion remains for roll control but non-differential displacement is utilized for alleviation. Flaps, being nearer the wing root, allow for greater stress. Aileron use may limit roll maneuverability during severe turbulence. If flaps are used a relatively slow screwjack actuator will still be necessary, in parallel with the alleviation servo, to obtain the large deflections necessary for conventional operation. Range decreases, resulting from active system operation and continuous flap deflection, are minor, roughly equal to 1-percent for rms gust velocities of 16 fps. Rms flap deflections at this intensity are approximately 1-deg. Range decreases for passive systems are shown in Table 2. Also given are system weights, production costs, and reliability figures.

Both active and passive systems are capable of providing adequate alleviation. Production cost figures are comparable, but development costs are difficult to assess, the active systems are most likely to incur the greater cost in this area. Reliability is comparable when modern redundancy techniques are utilized in electronic subsystems. (See Ref 6.)

Active systems are appreciably lighter in weight and offer less range degradation. The high frequency acceleration content may prove to be bothersome. System maintenance is negligible when combined with normal autopilot maintenance, with the exception of the additional servos which

Table 2. System Summary

	BPA	FW	TW	VB <sub>1</sub>	VB <sub>2</sub>	SAS	N	G
ADDED WEIGHT*	—	630	120	860	635	7	45	55
COST	1.0	1.005	1.023	1.016	—	1.005	1.011	1.010
PROBABILITY OF FAILURE (3 hr mission)	—	0.00045	0.00045	0.00035	0.00035	0.00040	0.00023	0.00025
RANGE	1.00	0.79	0.68	0.78 to 0.91	0.86	1.00	0.98	0.98
SENSITIVITY**	0.051	0.027	0.030	0.037	0.30	0.052	0.030	0.028

\* ACTIVE SYSTEM WEIGHTS INCLUDE 30 LBS FOR ESTIMATED  
STRUCTURAL WEIGHT INCREASES.

\*\*SENSITIVITY AT PILOT STATION FOR 0.9 M, SEA LEVEL, 5% STATIC  
MARGIN.

require periodic replacement. Stability and control characteristics are altered by active system incorporation and only the normal acceleration system appears to be capable of providing acceptable qualities over a range of flight conditions. With active systems, the ratio of gains to flaps and elevator is important. Failures resulting in large deviations of this ratio require signal monitoring of the ratio to ensure fail-safety.

Passive systems provide a reduction in sensitivity and allow for possible shorter takeoff distances. Little alteration of stability and control characteristics occurs but active stability augmentation remains a necessity as with all modern higher performance aircraft. System maintenance consists of periodic seal and bearing replacement, and perhaps track adjustment.

It is the conclusion of the authors, based upon the study results presented here, that the normal acceleration feedback to flaps and elevators or the variable sweep wing concept offer the most practical means of providing suitable alleviation of turbulence induced loads during the low altitude high speed mission.

# NOMENCLATURE

$\alpha$	Acceleration sensitivity to gusts	g/fps
$\sigma$	Root mean square value	----
$w_g$	Vertical gust velocity	ft/sec
$N_z$	Normal acceleration	g's
$s$	Laplacian operator	1/sec
$S$	Wing area	ft <sup>2</sup>
$\omega_n$	Natural frequency	rad/sec
$f_n$	Natural frequency	cps
$\zeta$	Damping ratio	----
$V$	Aircraft velocity	ft/sec
$\rho$	Air density	slugs/ft <sup>3</sup>
$g$	Gravitational acceleration	ft/sec <sup>2</sup>
$Z$	Lift force coefficient	----
$C_{L_\alpha}$	Lift curve slope	1/deg
$\alpha_g$	Angle of attack due to gust incidence	deg
$\Phi$	Power spectral density	----
$L$	Scale of turbulence	ft/
$\Omega$	Normalized frequency	1/ft
$cp$	Center of pressure	----
$cg$	Center of gravity	----
$\theta$	Pitch angle	deg
$A$	Alleviated or alleviation	----
$U$	Unalleviated	----
$l$	Distance	ft
$\omega$	Frequency	rad/sec
$N$	Number of exceedances per second	----
$C_D$	Drag coefficient	----

R	Range	miles
M	Mach number or moment coefficient	----
c	Chord	ft
K	Gain factor	deg/deg
$\delta_F$	Flap deflection	deg
$\delta_E$	Elevator deflection	deg
$\alpha$	Angle of attack	deg
$\gamma$	Flight path angle	deg
o	Denotes trim or steady value	----
.	Denotes derivative with respect to time	----
$\alpha_v$	Angle sensed by vane or probe	deg
W	Weight	lb
q	Pitch rate	deg/sec

## REFERENCES

1. NACA TR-1272, A Re-Evaluation of Data of Atmospheric Turbulence and Airplane Gust Loads for Application in Spectral Calculations, H. Press, M. T. Meadows and I. Hadlock, 1956.
2. WADD Technical Report 60, 305, B-66B Low Level Gust Study, K. D. Saunders, March 1961.
3. NAA Report, A Preliminary Gust Alleviation Study for the Mohawk Aircraft (YAO-1), J. M. Johnson, Jr. and G. M. Andrew.
4. NACA TN 3290, On the Minimization of Airplane Responses to Random Gusts, Murracy Tobak, 1957.
5. Report of Test Project No. AVN 4860, 1/16 Phase III of Man Machine Environment Capability Studies and Test in Support of Surveillance Aircraft Development, U.S. Army Aviation Board, Ft. Rucker, Alabama, May 28, 1962.
6. A. S. Escobosa, "Unit Redundant Scheme for Higher Control System Reliability," IRE Proceedings of the 6th National Convention on Military Electronics, June 1962.
7. NA 62H-397, An Investigation of Low-Altitude High Speed Flying and Riding Qualities of Aircraft, R. C. A'Harrah, R. P. Schulze, NAA Columbus Division.
8. NACA TN 4173, An Analytical Investigation of the Gust-Alleviating Properties of a Simple Pitch Damper, N. A. Crabill, December 1957.
9. NAA IOL 60-3441-64-FCS-46, CESSNA 310 Gust Alleviation Study, W. G. Watt and J. T. Nishimi, December 8, 1960.
10. NACA TN 2416, Theoretical Study of Some Methods for Increasing the Smoothness of Flight Through Rough Air, William H. Phillips and Christopher C. Kraft, Jr., 1951.
11. NASA TN D-532, A Flight Investigation of an Automatic Gust-Alleviation System in a Transport Airplane, Paul A. Hunter, Christopher C. Kraft, Jr., and William L. Alford.



12. NACA TN 3612, Initial Results of a Flight Investigation of a Gust Alleviation System, Christopher C. Kraft, Jr., 1956.
13. NAA TM 3441-12-50, Gust Alleviation Study for the B-70 Aircraft, J. M. Johnson, Jr., G. M. Andrew, and R. Olshausen.
14. EM-0362-258, Bending Suppression and Gust Alleviation Concept Study (Proposal), CDS, September 4, 1962.
15. NACA TN 3705, An Investigation of Forward-Located Fixed Spoilers and Deflectors as Gust Alleviators on an Unswept-Wing Model, D. R. Croom, C. C. Shufflebarger, and J. K. Huffman, June 1956.
16. NACA TN 4006, Investigation at Transonic Speeds of Deflectors and Spoilers as Gust Alleviators on a 35° Swept Wing, D. R. Croom, J. K. Huffman, June 1957.
17. NACA TN 4057, Investigation at Low Speeds of Deflectors and Spoilers as Gust Alleviators on a Model of the Bell X-5 Airplane with 35° Swept Wings and on a High-Aspect Ratio 35° Swept-Wing-Fuselage Model, D. R. Croom and J. K. Huffman, June 1957.
18. NACA TN 4175, Investigation of Deflectors as Gust Alleviators on a 0.09 Scale Model of the Bell X-5 Airplane with Various Wing Sweep Angles from 20° to 60° at Mach Numbers from 0.40 to 0.90, D. R. Croom and J. K. Huffman, November 1957.
19. SM-14819, (ASTIA AD-65091), Some Aerodynamic Aspects of Gust Load Alleviation, Douglas Aircraft Company, June 1953.
20. WADC Report 57-750, Part I (ASTIA AD-2081-143), Estimation of the Control Derivatives for Flaps, Spoilers, and Other Control Devices Intended for Use as Gust Alleviators, Fluidyne Engineering Corp., January 1958.
21. WADC Report 57-750, Part III (ASTIA AD-2081-145), Prediction of the Alleviation of Gust Loads on a Rigid Restrained Wing Utilizing Wing Installed Alleviator Devices, Fluidyne Engineering Corp., January 1958.
22. RDO No. 451-374 (ASTIA AD-50757), An Analysis of the Effectiveness of a Gust Alleviating Device, Wright Air Development Center, Aircraft Laboratory, July 1, 1953.

23. SM-14456, Dynamic Analyses for the C-47 Airplane Gust Load Alleviation System, Douglas Aircraft Company, July 29, 1952.
24. DOCAERO No. 42, Études Et Essais D'un Avion Absorbeur De Rafales (Studies and Tests on a Plane Which Absorbs Strong Wind Gusts), René Hirsch, January 1957.

## ACKNOWLEDGMENT

The authors wish to thank Mr. John E. Yeates of U.S. Army TRECOM, the authorized representative of the contracting officer, for his full cooperation and understanding during conduct of the study, and at whose suggestion this paper was written. Fullest appreciation is given to Mr. Harold L. Ehlers and Mr. Ralph A'Harrah for their superior cooperation and program direction and to Mr. Edward C. Bridges for his technical direction. Special gratitude is extended to Dr. Gustave Andrews, Mr. Carl Rasmussen, Mr. Richard Olshausen, and Mr. Ehlers for allowing us the benefit of their experience in the field of gust alleviation and for giving of their time for consultation. Mr. Charles H. McKinley deserves the highest recognition as a participating engineer on the program, although we regret that he could not be with us for preparation of the paper.

**AN ANALYTICAL INVESTIGATION  
OF AIRCRAFT LOADS  
INDUCED BY ROUGH TERRAIN LANDINGS**

**Fred C. Allen, and Lane B. Mosby**

**Douglas Aircraft Company**

# **AN ANALYTICAL INVESTIGATION OF AIRCRAFT LOADS INDUCED BY ROUGH TERRAIN LANDINGS**

*By*

**F. C. ALLEN**

**L. B. MOSBY**

**Structural Mechanics Section  
Aircraft Division  
Douglas Aircraft Company, Inc.**

## **ABSTRACT**

As part of a program to establish landing loads criteria for aircraft whose mission requires landing and takeoff from unprepared areas, a dynamic analysis was made of the loads induced in an Army observation airplane by rough terrain landings. These loads were subsequently used to compute weight and performance penalties as a function of the magnitude of the surface irregularity. The analytical methods are described herein, and the results of the load analysis are summarized.

The investigation provided an understanding of the required characteristic of landing gear which are to be used in rough terrain operations. Suggestions are presented for reducing the loads associated with such usage by the proper choice of shock strut and tire configuration.

## INTRODUCTION

The problem of landing area roughness has been of concern for many years to both military and civil organizations responsible for the operation and maintenance of aircraft. It has been recognized, for example, that normal irregularities in the surface of commercial landing fields contribute to the fatigue damage of transport aircraft landing gear and that failures of carrier-based aircraft have been caused by running over an arresting cable during landing impact. Design criteria to account for these conditions are appearing in current structural specifications.

The terrain roughness encountered by Army aircraft whose mission involves operating in and out of unprepared areas is of greater magnitude, and there is an urgent need for the development of design criteria which will provide adequate strength for these conditions. Current Army aircraft are designed to meet Air Force, Navy, or Federal Aviation Agency requirements. These requirements are not adequate to predict the loads which will be imposed by the Army's specialized mission.

The problem of designing airplanes for rough terrain landing operations can be divided into the following steps:

1. Definition of the design landing surface,
2. Analysis of loads induced by the rough terrain, and
3. Design of the optimum landing gear configuration.

If these steps were successfully accomplished, there would remain one additional major problem, namely, that of providing ground personnel with a means of determining whether a given landing surface does or does not exceed the permissible roughness specified in the design. Presumably such a determination would be necessary before the landing of the first aircraft at a forward base.

As part of the program to establish the landing loads criteria, a dynamic analysis was made of the loads induced in an Army STOL observation plane by landings on terrains of varying degrees of roughness. The load increments obtained by this analysis were used to compute the amount of additional structural weight required to prevent failure. These weight increases, in turn, were used to determine the loss in performance (range) of the aircraft, and, as a final step, the degree of terrain roughness at which the performance of the STOL aircraft became equal to that of a VTOL aircraft of equal weight was determined.

Definition of the design landing surface (Step 1 above) is a particularly difficult problem. Obviously, terrain can have any degree of roughness imaginable. It is equally obvious that an airplane with a finite landing speed cannot be designed for all degrees of landing area roughness. The philosophy adopted in this investigation was that the limiting roughness would be that which made an STOL aircraft economically unfeasible, i.e., that which made its performance equal to or less than that of a comparable VTOL aircraft. Because the investigation was made on an aircraft whose landing gear contained few provisions for rough terrain landings other than high sinking speed, the surface roughness limits that were determined are quite conservative. For this reason, emphasis is placed herein on the methods of analysis employed, the loads generated and the general knowledge obtained of the desired characteristics of the optimum landing gear configuration.

## METHOD OF ANALYSIS

### GENERAL APPROACH

To determine analytically the variation of loads in the aircraft with terrain roughness, computations were made using a computer program which simulated the operational characteristics of the gear and the elastic properties of the gear and airplane structure. Essentially, the computing program consisted of a mathematical model of the aircraft in which the gear and structure were considered as mutually interacting dynamic systems. The input to the program consisted of the initial velocities (both horizontal and vertical), the attitude of the airplane, and the contour or character of the ground. The output gave time histories of gear loads, and accelerations and loads at numerous selected points on the structure.

The loads and accelerations thus derived were entered into a second computing program which determined the change in weight of the airplane. The resulting curves of weight increase versus magnitude of surface irregularity were utilized in established aerodynamic procedures to obtain the effect on airplane performance.

### THE AIRPLANE

Figure 1 shows the Army observation airplane that was used as a basis for these calculations. The landing gear configurations are shown in Figures 2 and 3. The gears are conventional hydro-pneumatic shocks struts, equipped with metering pin-orifice arrangements characteristic of airplanes designed for high sink speed landings. The ultimate design sinking speed for the airplane was 20.8 feet per second at a gross weight of 10,715 lbs.

### THE TERRAIN REPRESENTATION

Landing surface irregularities were represented by the types of terrain shown in Figure 4. These consist of:

- (a) Slopes in the direction of airplane motion
- (b) Soft earth as indicated by various sliding and rolling coefficients of friction
- (c) Single bumps
- (d) Continuous identical undulations, and
- (e) Series of discrete bumps.

The protuberances investigated under (c), (d) and (e) consisted of cylindrical, one minus cosine bumps of various heights and lengths, oriented at right angles to the direction of airplane motion. The magnitudes of surface irregularities were progressively increased until the weight increments resulting therefrom brought the performance of the STOL airplane down to that of the VTOL airplane. The investigation was limited to protuberances with concave radii equal to, or greater than, the radius of the tire. Computational difficulties arose when bumps outside this range were considered because the tire then made contact with the ground at two locations.

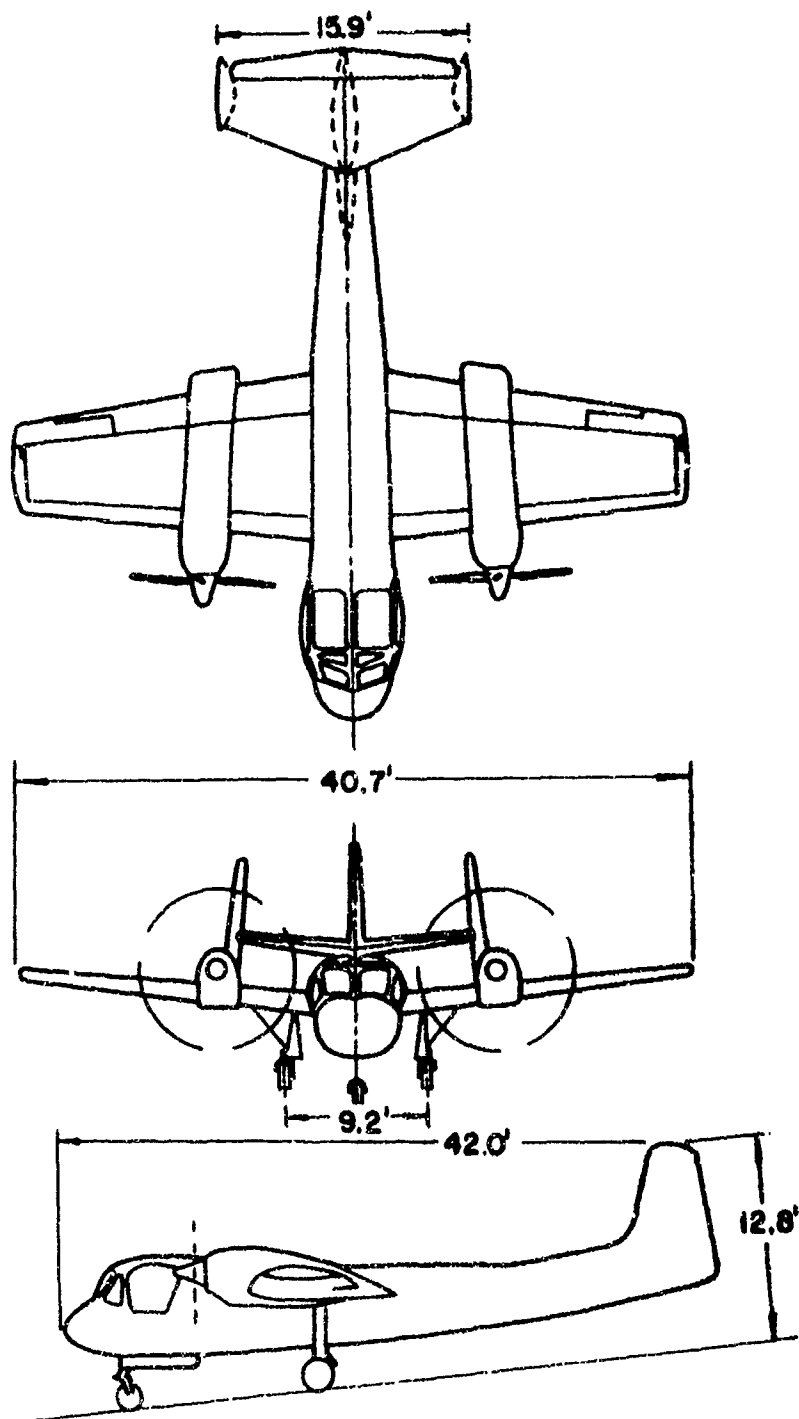


FIGURE 1. AC-1 MOHAWK AIRPLANE GENERAL CONFIGURATION



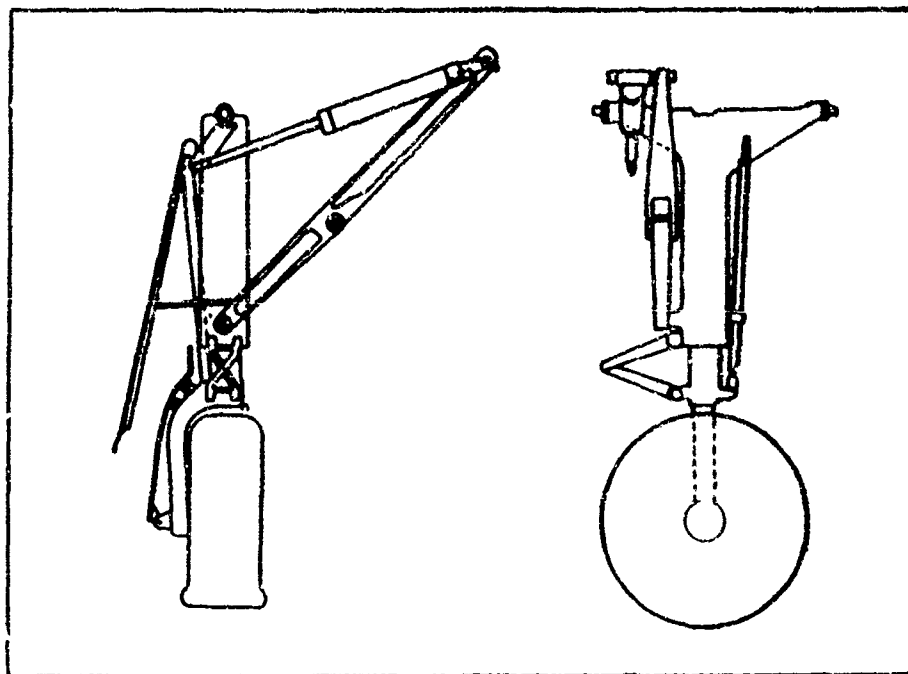


FIGURE 2. MAIN GEAR

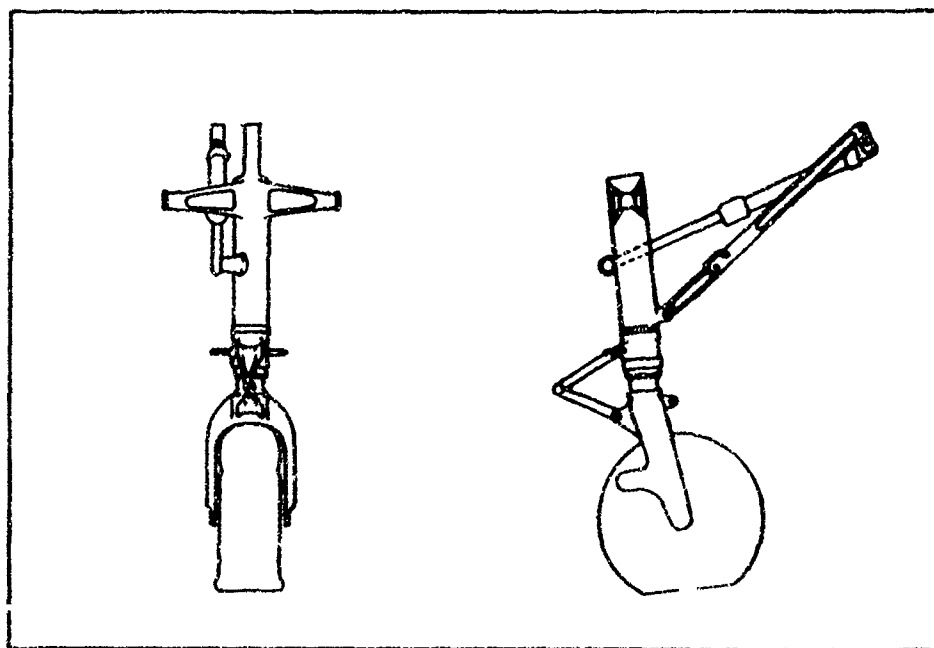


FIGURE 3. NOSE GEAR

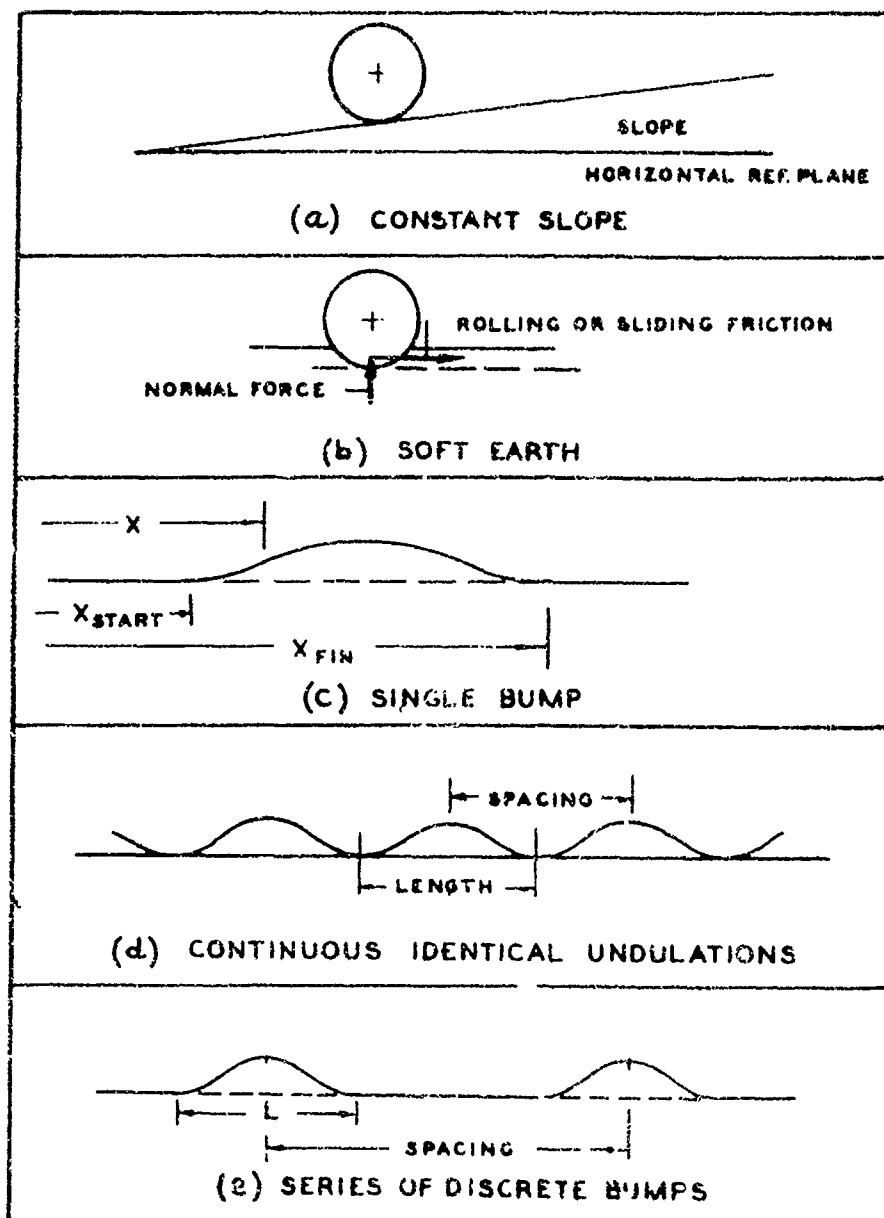


FIGURE 4. TERRAIN REPRESENTATION

The number of cycles of "continuous" undulations considered in each landing was a function of wavelength. Thus, ten cycles were used when the length was 27.4 inches; five cycles were used with a 45-inch wavelength; and three cycles were used at 137-inch wavelength. To a large extent, this limit was created by the computing machine time required to run each case; however, some justification for this procedure lies in the anticipated character of the terrain. The short undulations may be likened to a plowed field, the furrows of which are both uniform and continuous. The long undulations might be considered natural irregularities. The probability of encountering more than three such protuberances of equal wavelength is rather remote.

The frequency of the continuous undulations\* started at 125 cps ( $L = 25"$ ) and extended down to 12.5 cps ( $L = 137$ ), a value just below the highest of the structural frequencies used in the analysis. The series of discrete bumps were spaced farther apart and were designed to excite the lower structural modes. Each of these series contained two identical bumps.

#### Basic Assumptions:

The following basic assumptions were made in this investigation:

1. All landings and all surface irregularities were symmetrical with respect to the airplane centerline. Hence, side loads resulting from asymmetric initial conditions were not determined.
2. The airplane was assumed to land once in the two-point attitude and once in the three-point attitude on each surface. Loads were obtained for both main and nose gear in the latter case.
3. The airplane, just before impact, was assumed to be in a steady state condition, i.e., accelerations were assumed equal to zero. Sinking speeds were 8, 12, and 17 feet per second (ultimate).
4. The forward velocity was assumed constant at 84.5 knots through the interval of impact.
5. The first four symmetrical airplane flexible modes were used in describing the elastic characteristics of the structure. Their frequencies were 7.06, 7.76, 9.04, and 13.6 cps. These frequencies and mode shapes were obtained from ground vibration tests (Reference 1) on the airplane and corresponded to first, wing bending, wing torque, nacelle pitching; and second, wing bending modes, respectively.
6. Weight increments were based on strength requirements. (No weight increments were provided for fatigue.)
7. Rigidities were assumed to be constant at their original values. (No adjustment was made as weight increased.)

Items 2, 3 and 4 need no justification since the assumptions deviate little from the facts. The use of symmetrical conditions (Item 1) and the neglect of fatigue loadings (Item 6) are permissible only if it is acknowledged that supplementary investigations will be necessary to establish side load and fatigue criteria.

\*Frequency of the undulations is defined as  $\frac{V}{L}$  where  $V$  is the landing speed in inches per second and  $L$  is the wavelength in inches.

The frequencies and mode shapes included all the symmetrical values that could be derived from the available ground vibration data. The effect of assuming constant rigidities was a loss of accuracy as the loads increased. However, since, a major portion of the load and weight increments is dependent upon rigid body considerations, the loss of accuracy assignable to this assumption is not as great as might be expected. Additional discussion on this point will be found on Page 22, Paragraph "G."

#### Secondary Assumptions

Numerous secondary assumptions were made, most of which follow rationally from a knowledge of the physics involved in the problem and which have only a minor effect on the results. Several assumptions, however, are of special interest to those working with landing gear computations. These are associated with the operation of the gear as an energy absorbing device and have substantial effect on the primary loads.

The first of these is the tire load-deflection curves (Figure 5) which, in this case, were derived from manufacturer's test data. The curves were obtained under dynamic conditions, a procedure

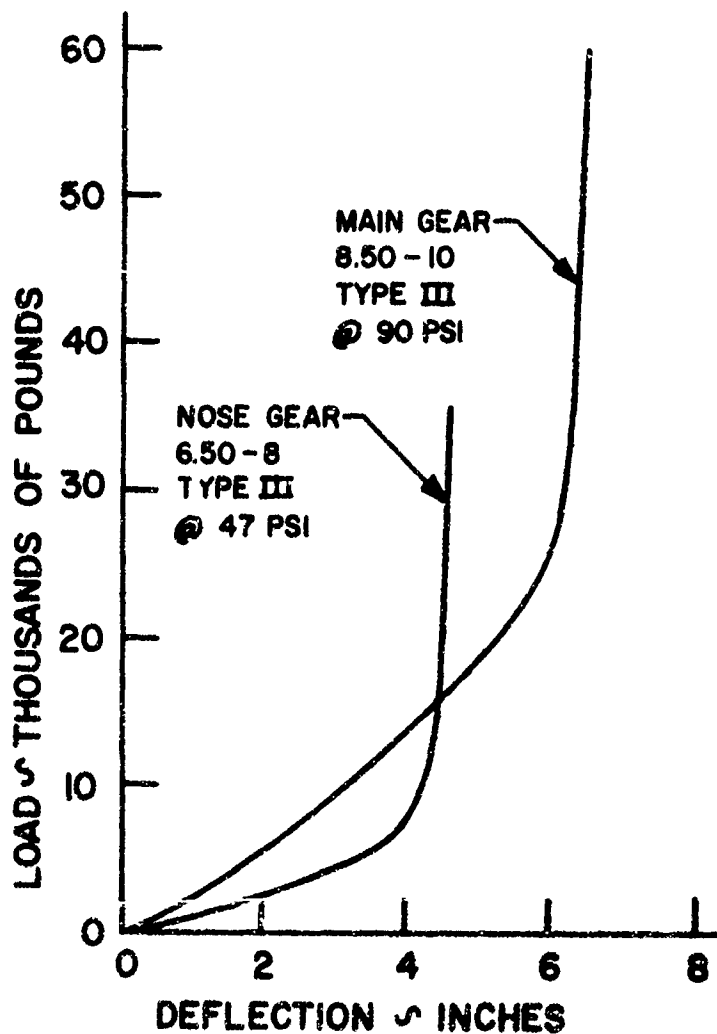


FIGURE 5. TIRE LOAD DEFLECTION CURVES

which appears to be essential to . . . They were obtained by the impression of the tires on a flat surface. It seems evident that a substantial error would be introduced if the same curve were used for landing or rolling over objects of small radius, such as a log or boulder. In the present investigation, this problem was avoided to some extent by limiting the obstacles to one minus cosine shapes of a reasonable minimum length. Since tire deflection data are not available for tires bearing on objects of varying radii of curvature, the error introduced in this program cannot be determined at this time.

The discharge coefficient for the metering pin-orifice was assumed to be 0.85. This value was obtained from tests on an A-4B (A4D-2) gear under actual landing conditions (Reference 2).

The polytropic exponent "n" for the air compression equation was assumed to be 1.12. This compares to experimental values of 1.01 to 1.10 obtained by Walls (Reference 3) on a small gear with a simple orifice.

#### Equations of Motion

The equations of motion and other aspects of the loads computing program are provided in the Appendix for those who are interested in the details. The output was computed at time intervals of 0.0001 second and printed at intervals of 0.002 second. In a three-point landing, the printed output contained 96 items; in a two-point landing, 68 items. Each normal landing required 5 minutes of 7090 computer machine time. Landings on continuous undulations and series of bumps required 12 minutes of machine time. The present equipment, which is the 7094 computer, reduces these times by approximately one-third. A total of approximately 600 landings was computed.

#### The Check-out

To be certain that the computations were successfully duplicating the actual gear and airplane operation, calculations were made, using initial conditions of drop tests (Reference 4), and the computed loads were compared with the measured loads. Results of this investigation are shown in Figure 6 for the 17-fps sinking speed. Comparable agreement was found at sinking speeds of 7 and 11 fps.

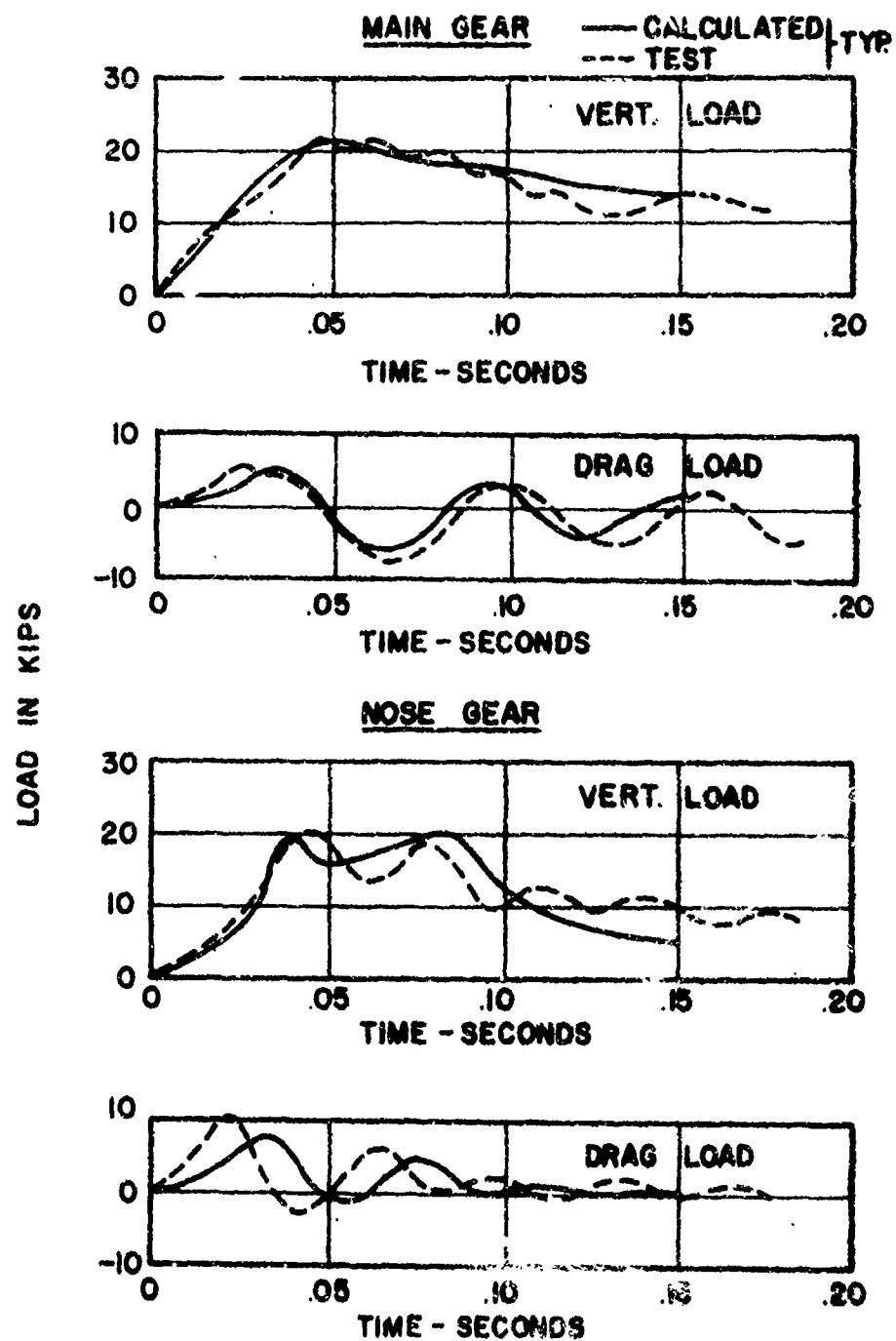


FIGURE 6. COMPARISON OF THEORY WITH DROP TEST,  $V_v = 17$  FT/SEC

## RESULTS

Because of the large amount of data generated, it is possible here only to summarize the results. As previously stated, emphasis will be placed on the loads, rather than weight or performance changes. Results will be categorized according to the surface irregularities shown in Figure 4.

### A. Terrain Slope

In computing the loads for landings on runways which sloped upward, in the direction of airplane motion, it was assumed that the pilot could adapt the airplane attitude to the local slope, but that the flight path, and, hence, the horizontal and vertical velocities established by reference to the horizon, remained unchanged. Under these conditions, slopes created an effective increase in sinking speed equal to

$$\Delta V_v = 1.689 V_A \sin \theta \quad (\text{feet per second})$$

where  $V_v$  is in feet per second and  $V_A$  is in knots. At the airplane landing speed,  $V_A$ , of 64.5 knots, each degree of slope created an increment of vertical speed of 2.5 feet per second. The variation of maximum vertical and horizontal landing gear loads with slope is shown in Figure 7.

It is possible to consider a uniform slope as the limiting case of a long bump. Hence, the results are approximately applicable to long smooth bumps, with maximum slopes as shown. A long bump can be defined for these purposes as one in which the half-length (distance from beginning to the apex) is longer than the distance traveled during the period of impact. For this aircraft, high gear loads exist for approximately 0.2 second, and a long bump has a half-length of roughly 30 feet.

### B. Soft-Earth Landings

Soft-earth landings have been investigated by the simple process of varying the static and rolling coefficients of friction which are used in the computations. The problem of relating the coefficients to measurable characteristics of the soil is left to other investigators. In this regard, it would appear that considerable work remains to be done inasmuch as rolling coefficients of friction which have been obtained under slow moving conditions probably are not applicable to the relatively high aircraft landing speeds.

Intuitively, one realizes that the important load in this case is the drag load on the gear. Figure 8 shows the variation of maximum drag load with rolling coefficient for the three initial sinking speeds, together with the corresponding vertical loads. From these charts it is apparent that main gear vertical loads are not significantly increased by increases in coefficient of friction, but that the drag load is increased substantially. Nose gear vertical loads are increased because of the nose-down airplane pitching moment created by the higher drag forces.

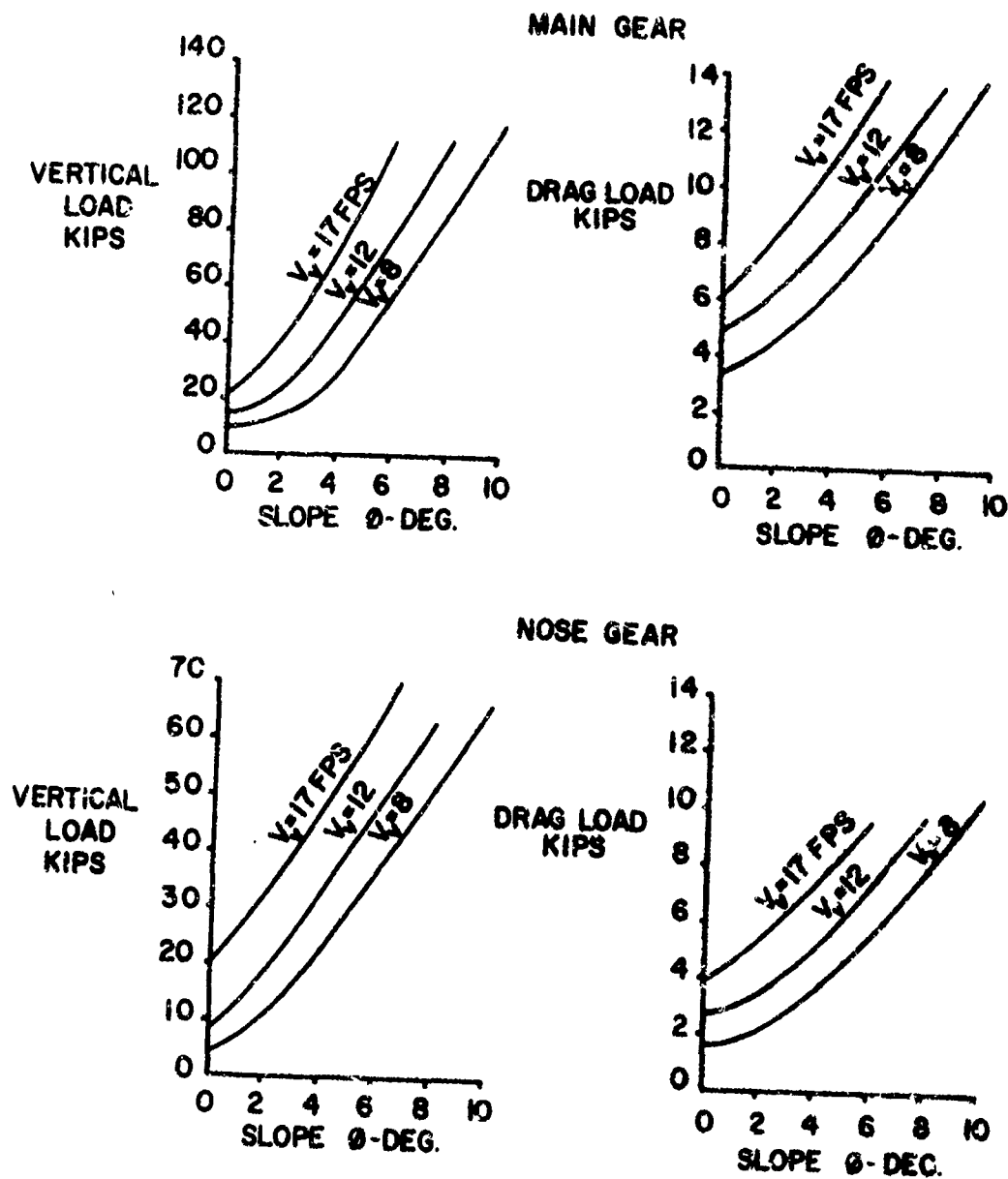


FIGURE 7. VARIATION OF MAXIMUM LOADS WITH GROUND SLOPE



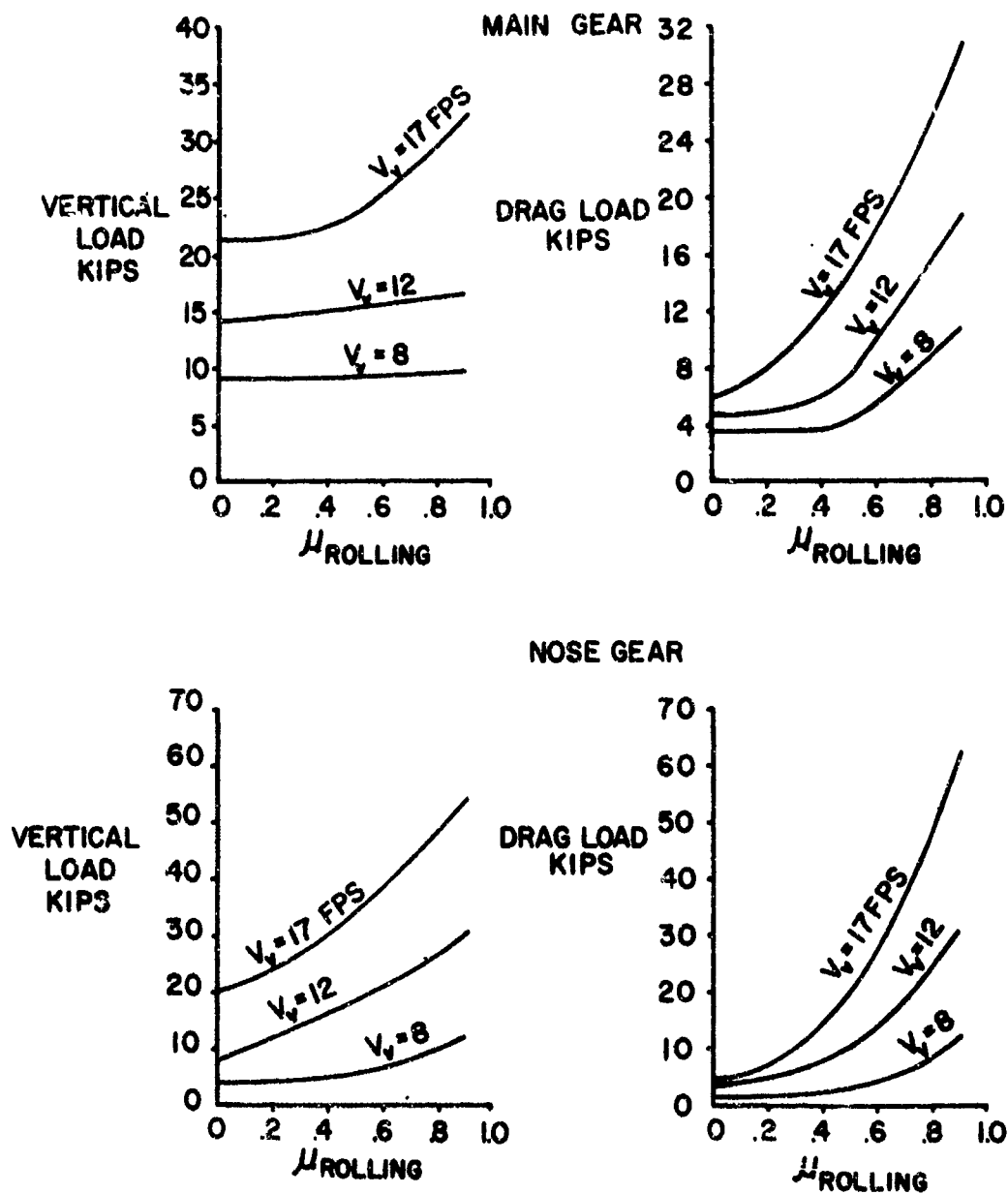


FIGURE 8. VARIATION OF MAXIMUM LOADS WITH ROLLING COEFFICIENT OF FRICTION

### C. Single Bumps

The magnitude of the vertical gear load increment obtained when the airplane landed upon a single bump, was dependent not only on the height of the bump, the sharpness or wave length, and the initial sinking speed but also upon the position of the airplane's initial touchdown relative to the bump. The last consideration made it necessary to determine the critical point of touchdown for each landing before proceeding with the rest of the investigation. Figure 9 shows the effect of point of touchdown upon the maximum vertical gear load. Figure 10 shows the detailed time relationship between the vertical gear load and the bump contour for a landing at 17 fps on a three-inch bump, 137 inches long. Figure 11 shows the effect of wave length, sink speed, and bump height on the magnitude of the maximum vertical load. In these charts all landings were made at the critical point of touchdown.

The large magnitude of the load increment caused by relatively small bumps, when the initial sinking speed is high, requires special comment. Examination of other portions of the computer program output shows that the tire bottoms (or becomes flat) during a normal 12 fps landing. If the wheel encounters a bump during the period when the tire is flat, a sharp, high velocity pulse is imparted to the gear, which is additive to that caused by the airplane's sinking speed. Since the metering pin-orifice dimensions are not designed for this condition, the oil flow is essentially blocked, and the gear becomes a rigid strut. This phenomenon has been noted with carrier aircraft where severe damage was incurred when the gear rolled over an arresting cable at the time of maximum tire deflection. Figure 12 shows the recorded load from such a landing. In this case, the bump consisted of a  $1\frac{3}{8}$  inch, multistrand arresting cable which undoubtedly compressed somewhat under load.

Although the highest gear loads were experienced with short bumps, the wing loads were often maximum when the frequency of the bump approached that of the structure. This is illustrated typically by the following comparisons which show the relationship between maximum main gear vertical load and maximum wing moment for two three-inch bumps of different length:

3" Bump Length ( $V_v = 17$ fps)	Max. Vertical Gear Load Lbs.	Max. Wing Mom. - Sta. 40 In. - Lbs.
27.4	111,500	1,862,000
137	62,620	2,677,000

This result is not surprising since an analogy can be drawn to the response of a single degree of freedom system in which the response to a pulse is a function of the ratio of frequency of the pulse to the frequency of the system.

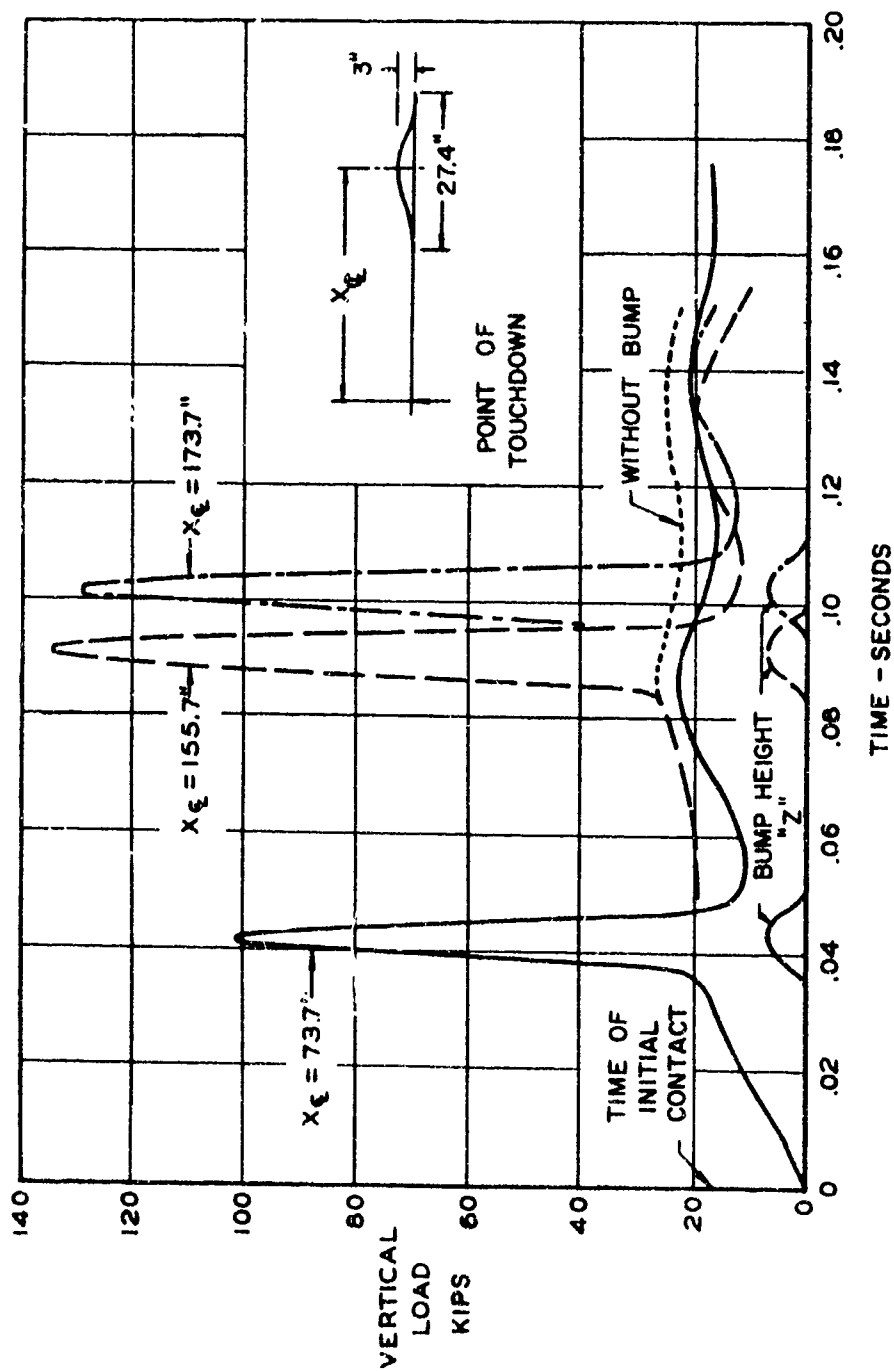


FIGURE 9. VERTICAL LOAD ON MAIN GEAR FOR BUMPS IN DIFFERENT LOCATIONS  
RELATIVE TO POINT OF INITIAL TOUCHDOWN ( $V_v = 17$  FT/SEC)

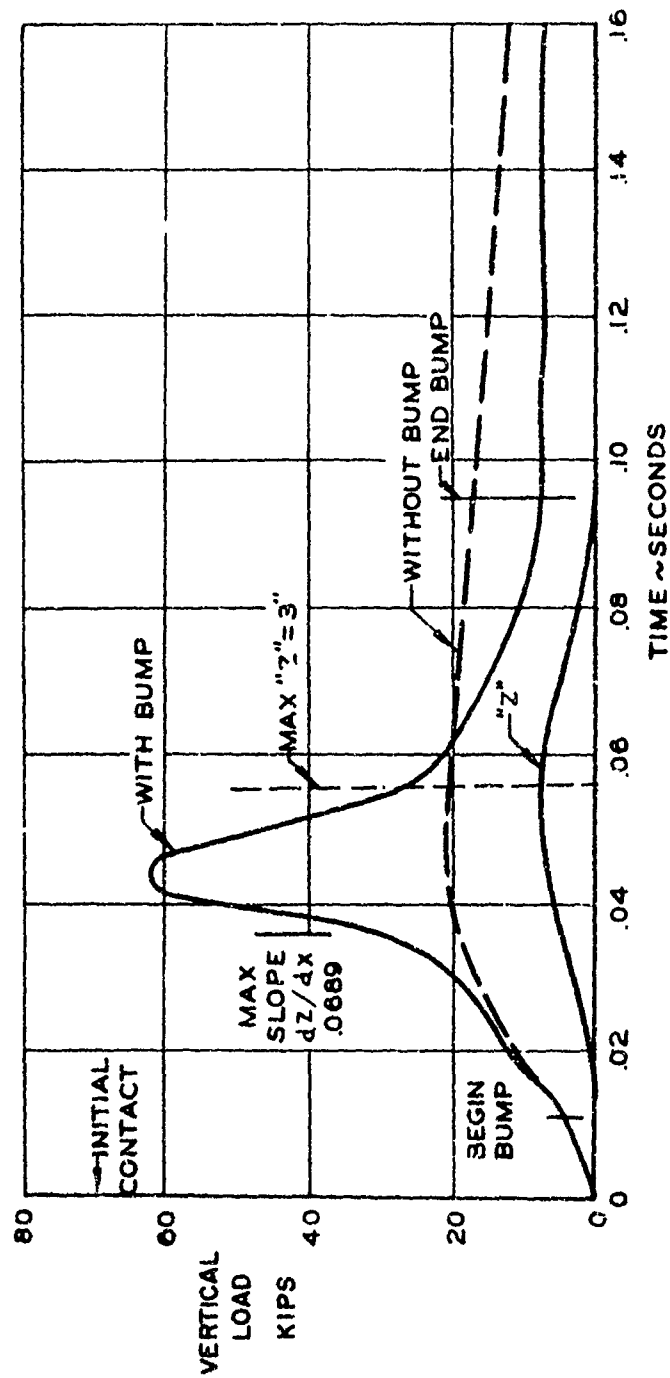


FIGURE 10. MAIN GEAR LOAD VS. TIME FOR A THREE-INCH BUMP 135 INCHES LONG  
( $V_v = 17$  FT/SEC)

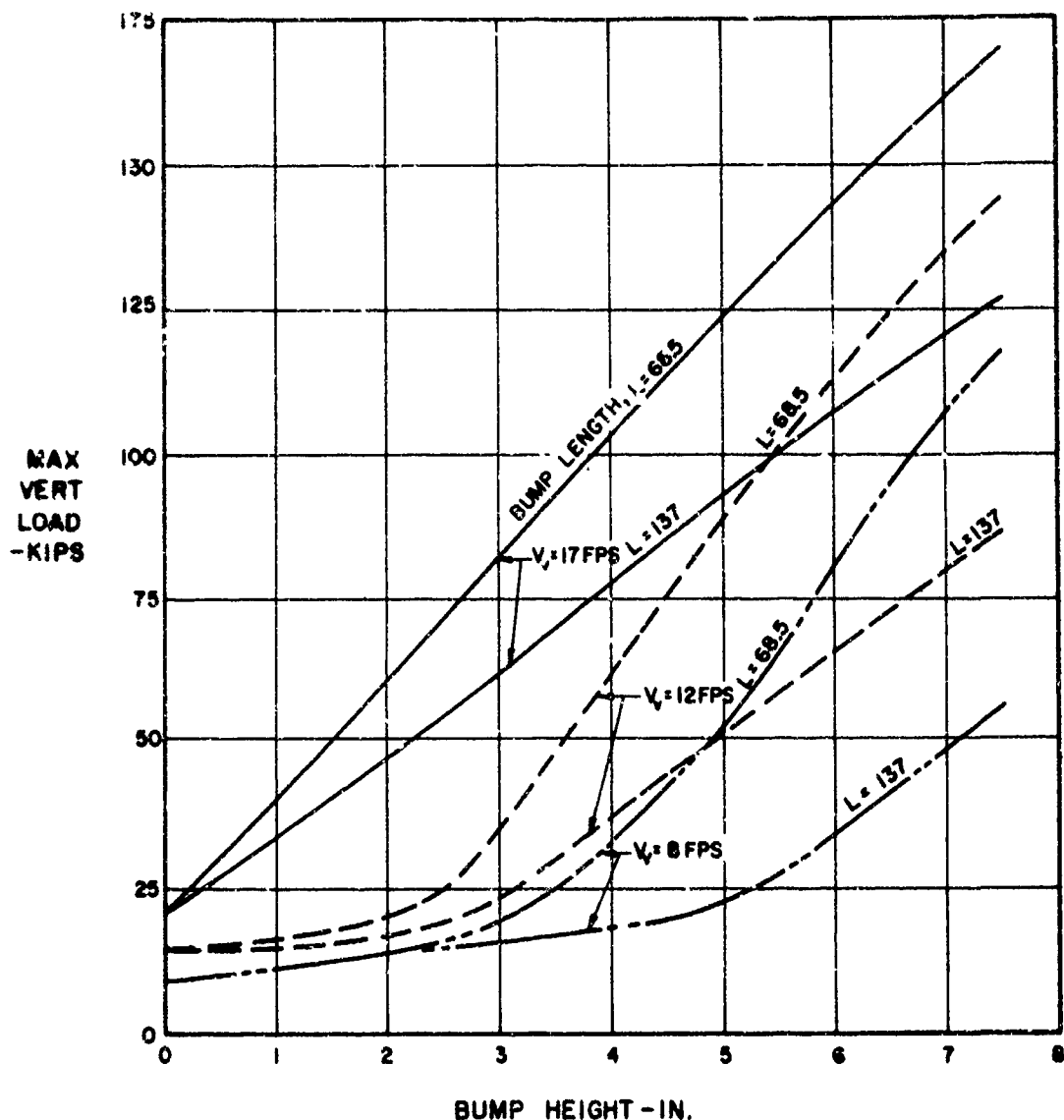


FIGURE 11. MAXIMUM MAIN GEAR VERTICAL LOAD VS. BUMP HEIGHT, BUMP LENGTH AND SINKING SPEED

#### D Continuous Undulations

All landings on continuous undulations were made with the point of initial touchdown at the start of a wave, in other words, at the bottom of a trough. It was also assumed, in effect, that the undulation preceding the point of touchdown did not exist, inasmuch as contact with this protuberance was ignored. The first undulation did not produce as high a load as the maximum from a single bump of the same shape because initial touchdown was not in the most critical location.

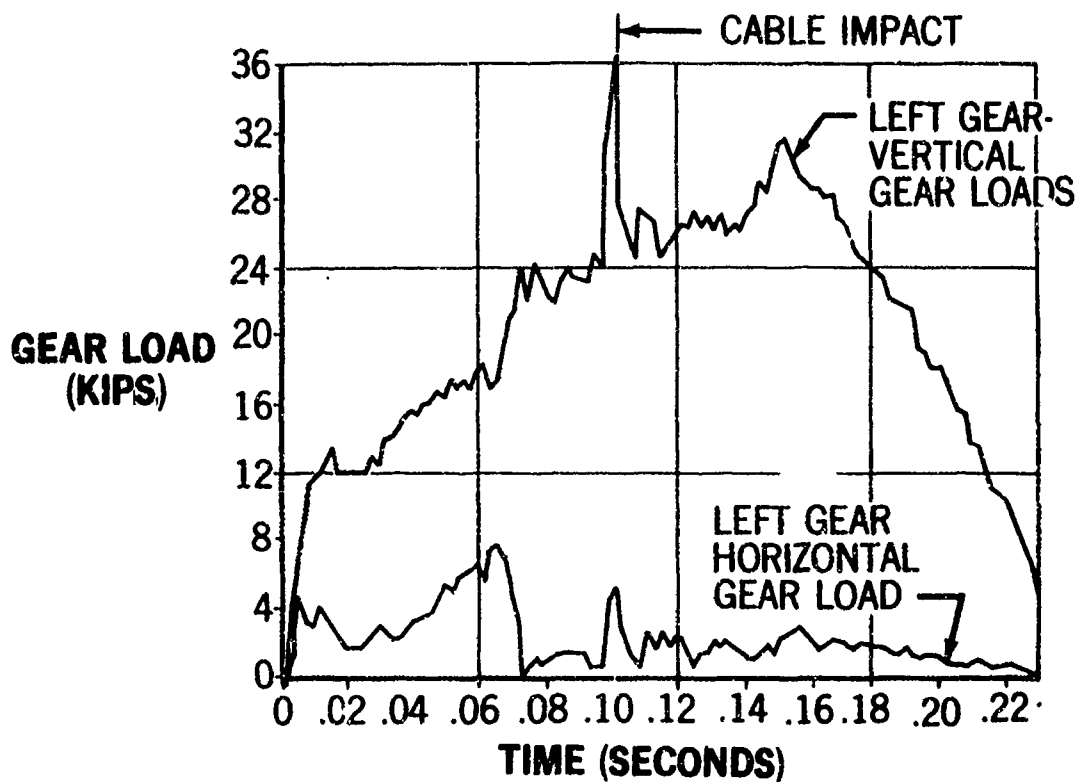


FIGURE 12. EFFECT OF CABLE IMPACT ON A-4B GEAR LOADS

Typical time histories of gear loads and wing bending moments are shown in Figures 13 through 16. Figures 13 and 14 are for continuous undulations three inches high and 27.4 inches long. The comparable loads for a smooth field landing with the same sinking speed are shown by the dashed line. Although the second and third undulations produce loads higher than the first, it can be seen that this occurs when the smooth field landing load is increasing and that it is not a diverging phenomenon.

Similar data for undulations 137 inches long are shown in Figures 15 and 16. This spacing corresponds approximately to the highest structural mode considered (second wing bending). As previously stated, calculations were carried out to the end of the third undulation only at this wave length. The gear loads and wing moments are maximum at the first undulation. It will be noted that the maximum wing moment exceeds the maximum for the shorter undulation by approximately 20 percent. It is apparent again that maximum loads are obtained at a time when the energy of initial impact is being absorbed. No evidence of load reinforcement on the second and third undulations can be seen.

#### E. Series of Discrete Bumps

The point of touchdown for these landings was chosen so as to make the gear load from the first bump maximum, as was done with the single bump. The second bump was spaced so as to supply load pulses at the natural frequencies of the structure.

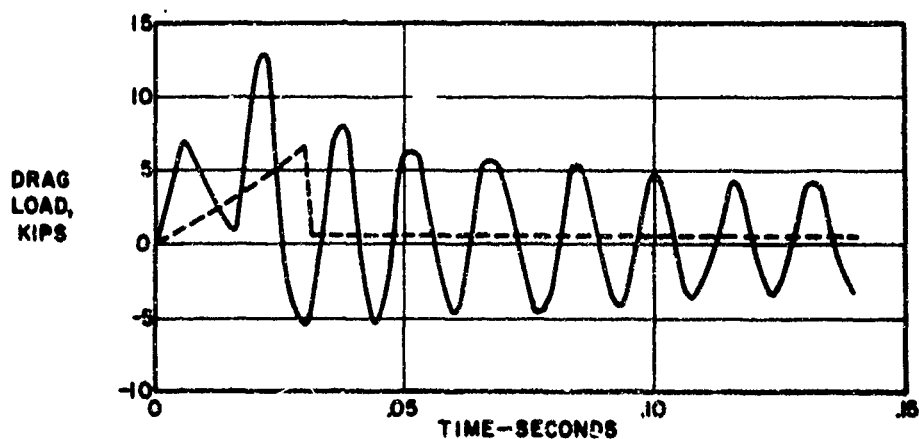
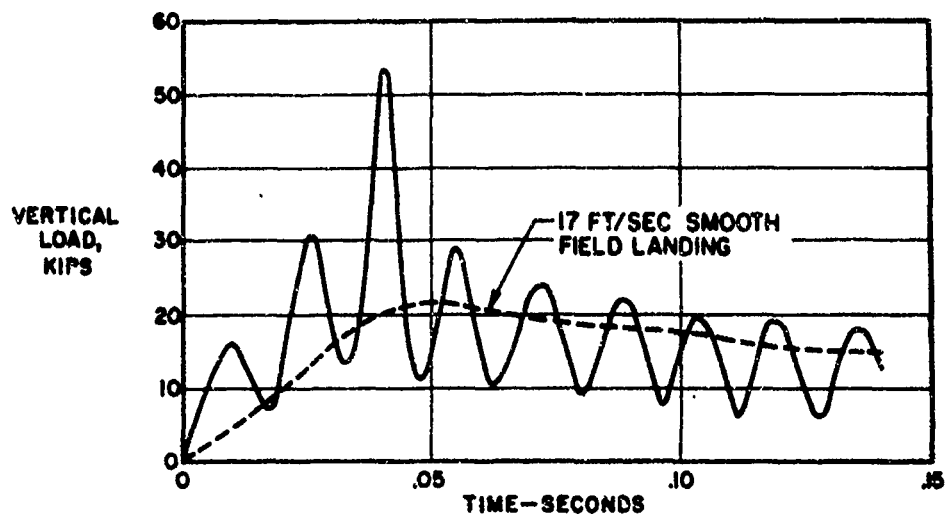


FIGURE 13. GROUND LOADS FOR A 17 FT/SEC LANDING ON CONTINUOUS 3" x 27.4" UNDULATIONS

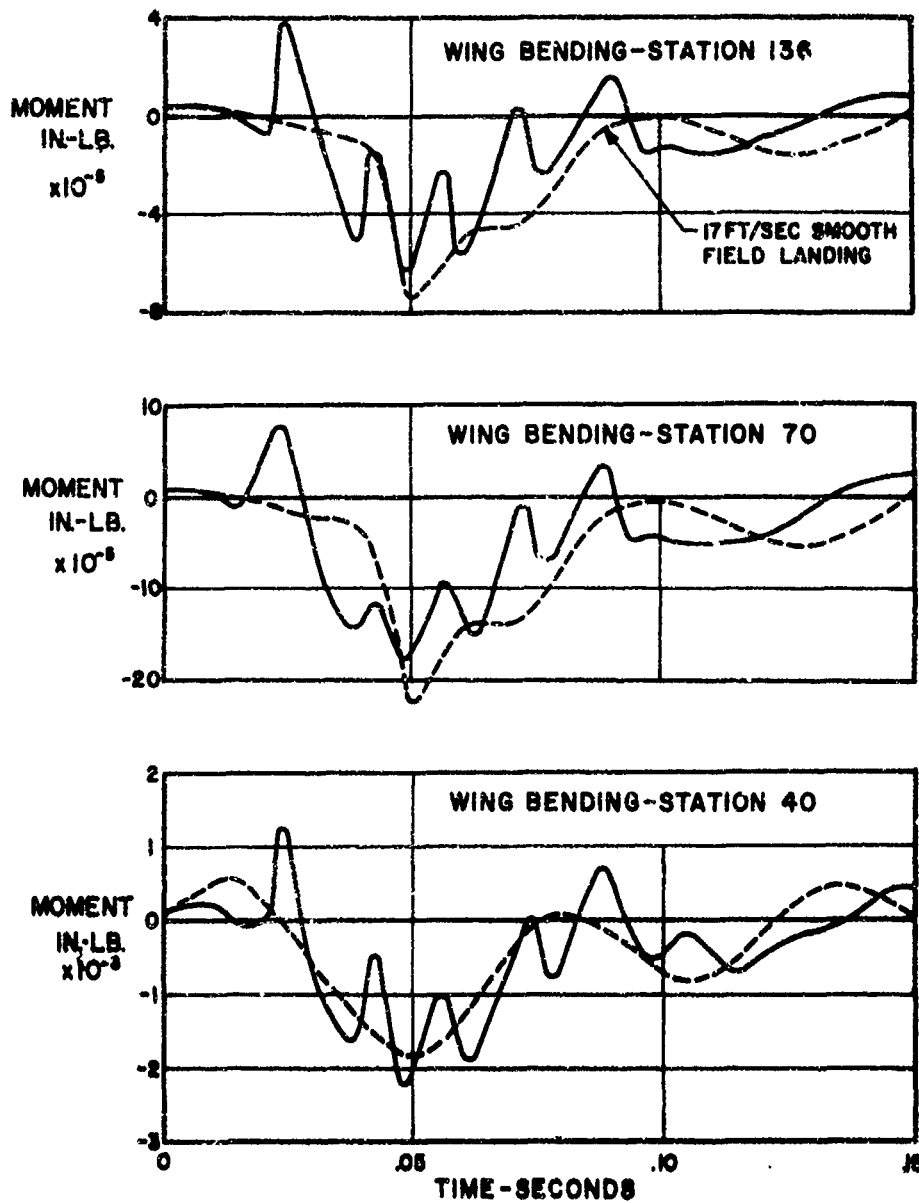


FIGURE 14. WING BENDING MOMENT FOR A 17 FT/SEC LANDING ON 3"  $\times$  27.4" CONTINUOUS UNDULATIONS



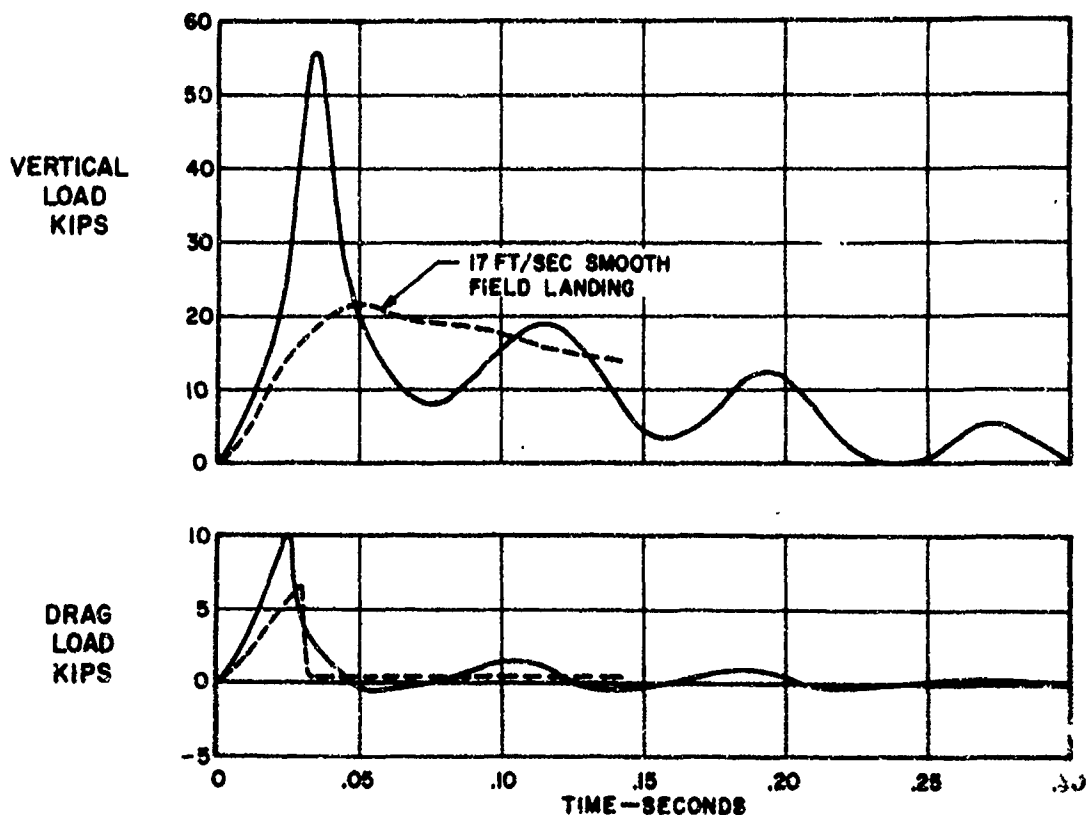


FIGURE 15. GROUND LOADS FOR A 17 FT/SEC LANDING ON CONTINUOUS 3' x 13' UNDULATIONS

Typical time histories of gear and wing loads are shown in Figure 17. It was found that in no case did the second bump gear load exceed that of the first nor did a structural load from the second pulse exceed that of the first. Thus, maximum loads and weight penalties for the series of bumps were identical with those from the single discrete bumps.

#### F. General Comment on the Multiple Bump Cases

The lack of load reinforcement in both the continuous undulation and series of bump cases was quite unexpected. In retrospect, however, it now becomes obvious that the superposition of primary energy absorption with the bump effect must produce maximum loads in the early part of the load-time history. Undoubtedly, substantial resonance would be introduced if the multiple bump cases were carried out over a longer distance; however, this procedure would, in the estimation of the author, be rather unrealistic and unnecessarily conservative as a design criterion. It would appear prudent nevertheless, to include a precautionary note to the effect that landings on terrain with many uniformly spaced bumps or undulations should be avoided.

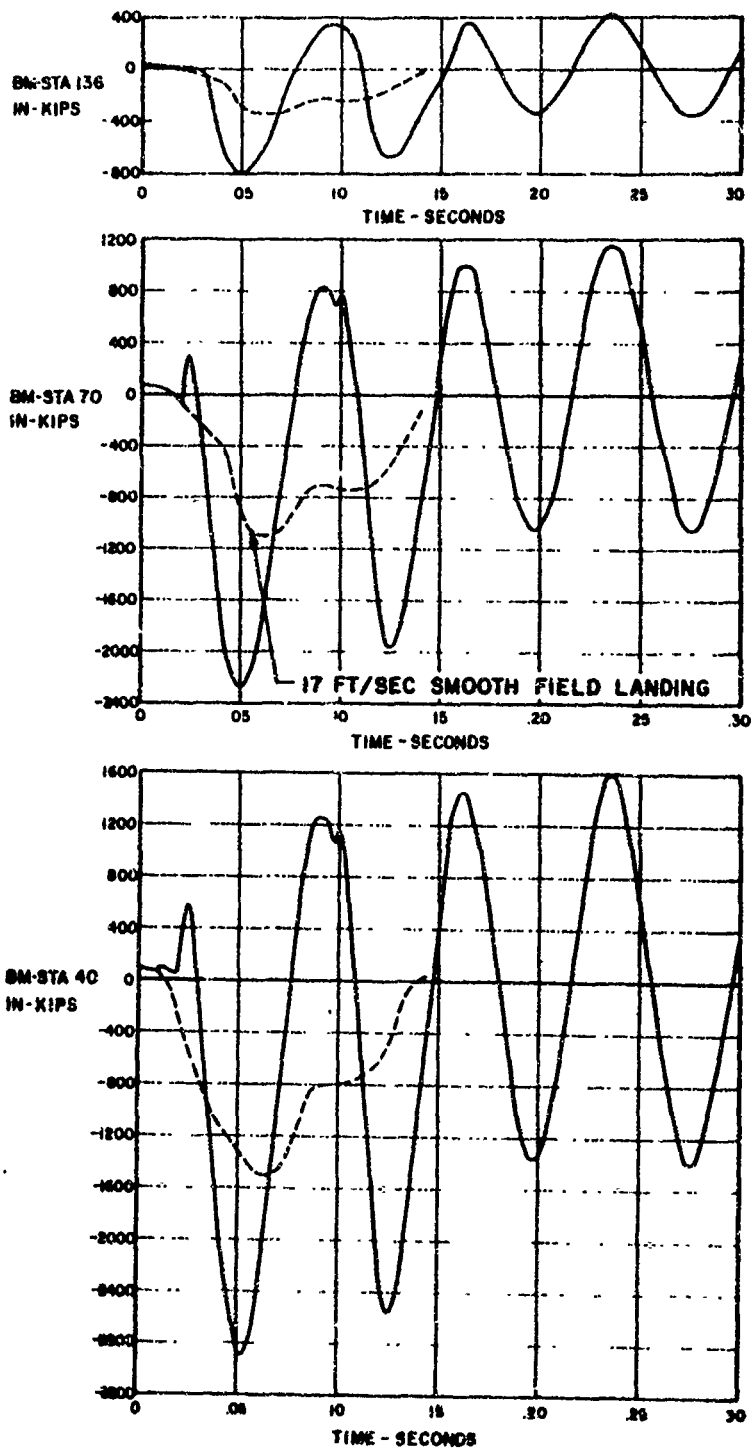


FIGURE 16. WING BENDING MOMENTS FOR A 17 FT/SEC LANDING ON 3" x 137" CONTINUOUS UNDULATIONS

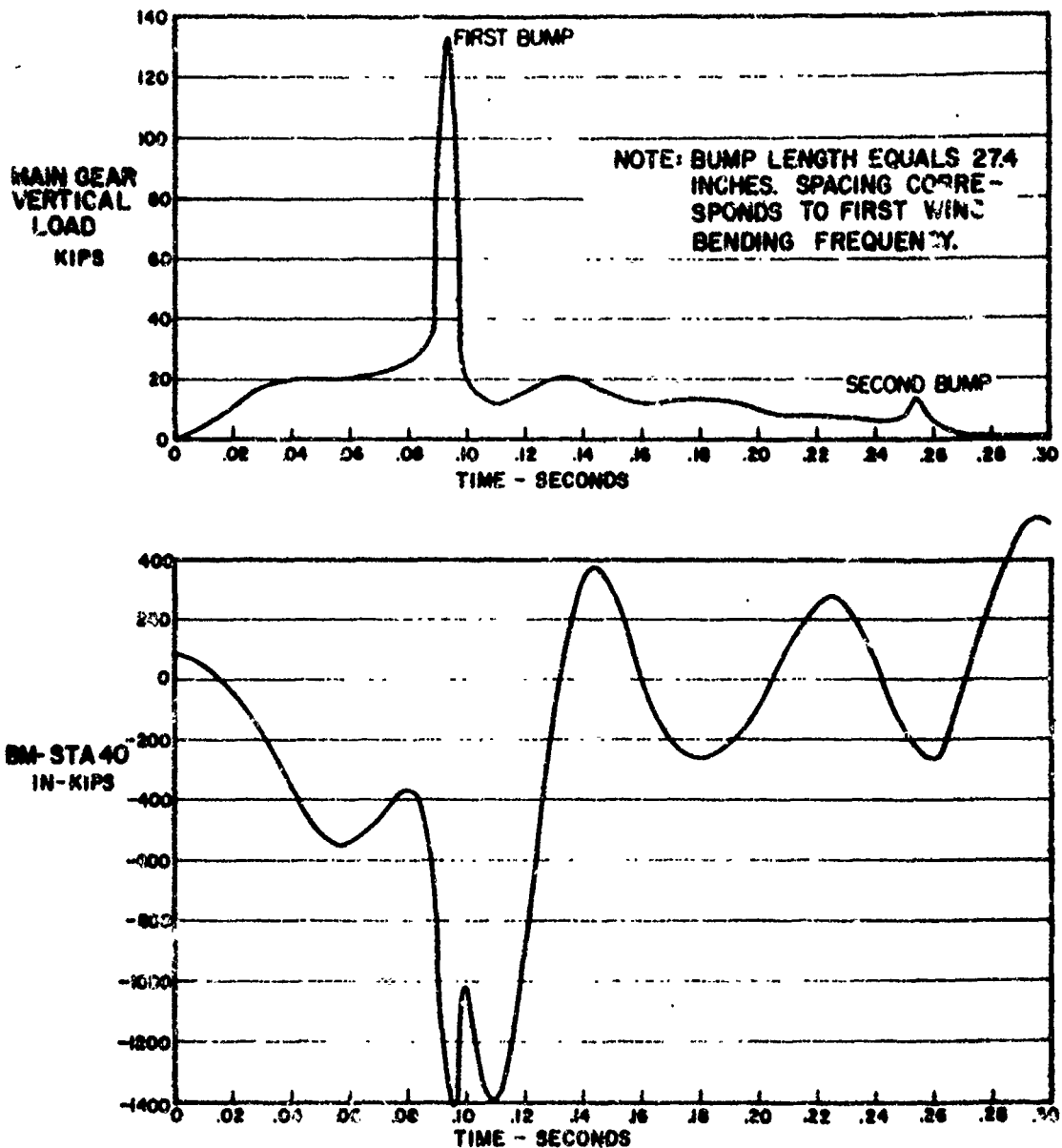


FIGURE 17. VERTICAL GEAR LOAD AND WING BENDING MOMENT FOR A 17 FT/SEC LANDING ON A SERIES OF TWO 2-INCH BUMPS SPACED 242 INCHES APART

#### G. Effects of Airplane Flexibility

The effects of airplane flexibility were investigated for several cases by comparing the loads computed in the standard manner with those computed for a rigid airplane. The latter loads were obtained by removing the modal data from the computing program. A comparison of the flexible versus rigid loads for two discrete bump cases is shown in Figures 18 and 19. It will be noted that the gear loads are changed very little by airplane flexibility but that substantial

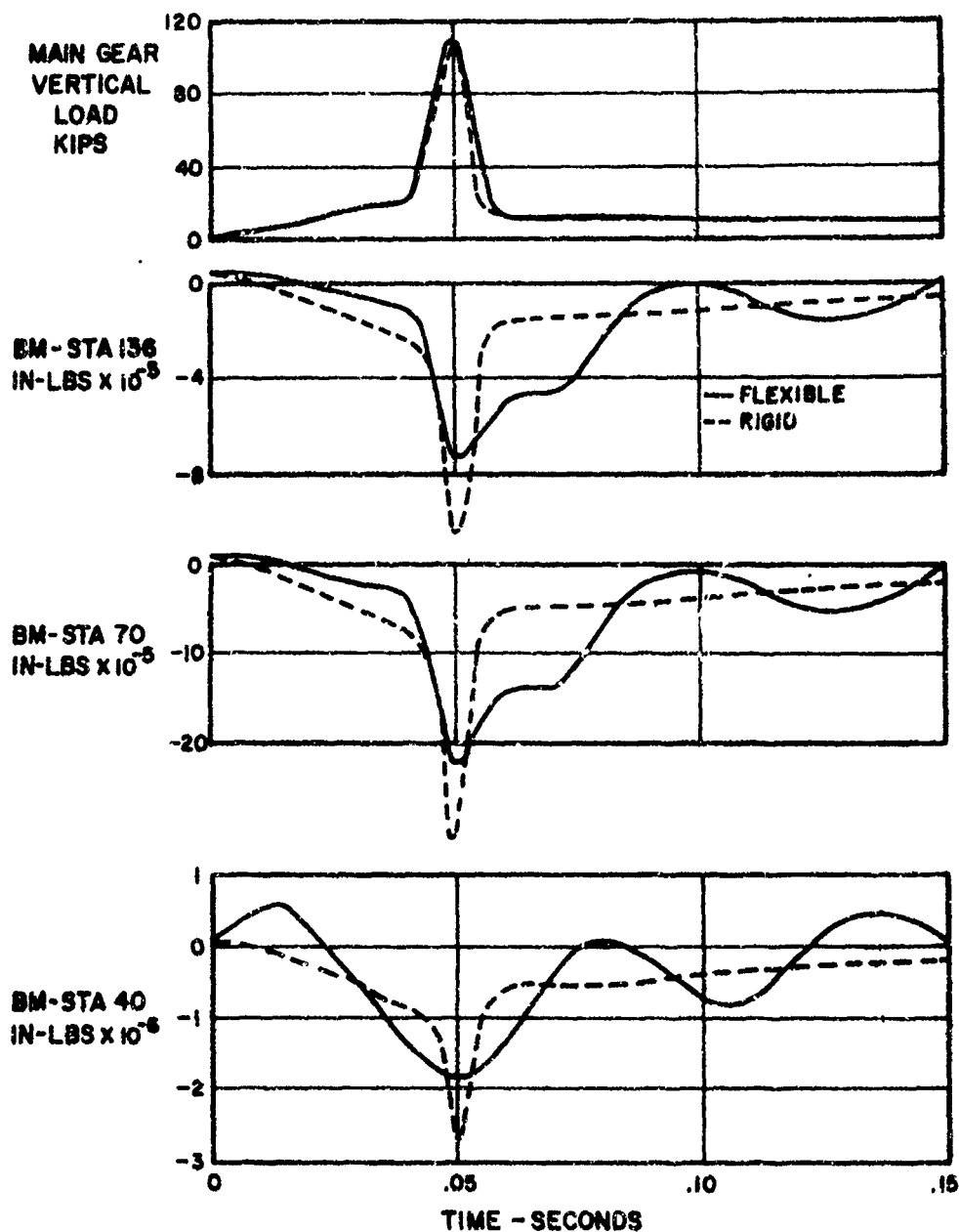


FIGURE 18. COMPARISON OF RIGID AND FLEXIBLE AIRCRAFT LOADS FOR A 17 FT/SEC LANDING ON A 3" BUMP 27.4" LONG

dynamic effects are noted in the internal structural loads. When the bump is short, wing moments for the flexible airplane are less than for the rigid airplane. When the bump is long, wing moments for the flexible airplane are higher than for the rigid airplane. Dynamic amplification up to 1.5 was computed on wing moments at the longer wave lengths.

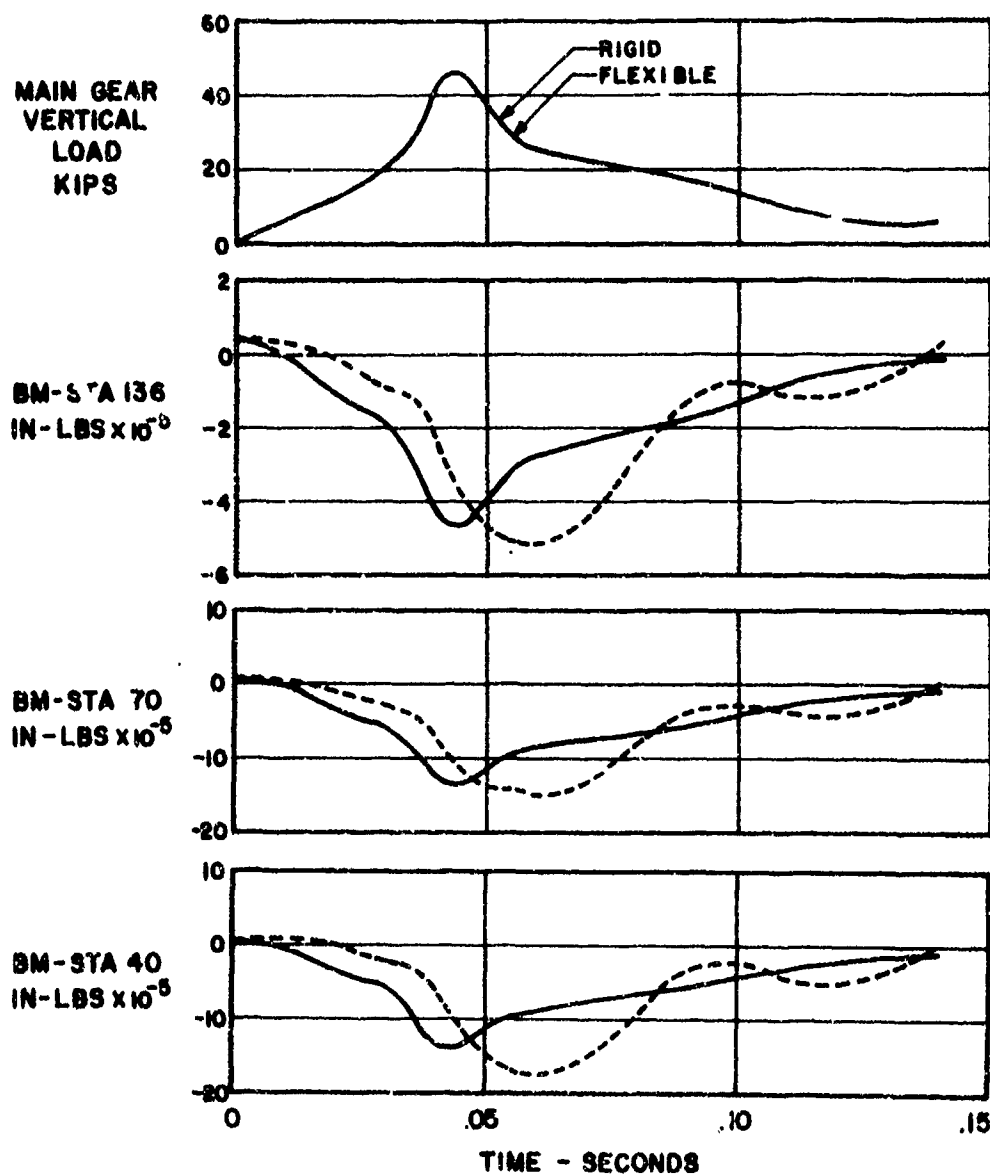


FIGURE 19. COMPARISON OF RIGID AND FLEXIBLE AIRCRAFT LOADS FOR A 17 FT/SEC LANDING ON A 3-INCH BUMP 242" LONG

## OBSERVATIONS REGARDING BUMP LOADS AND LANDING GEAR REQUIREMENTS

Having noted that large loads are developed when the gear traverses bumps of short wavelength at the time when the tire is flat, a simplified concept of the phenomenon can be constructed which will shed some light on the requirements of the landing gear.

Assuming that high-frequency pulses cannot be alleviated by the metering pin-orifice design, energy absorption must be accomplished by the deflection of the tire and the local structure. The load-deflection curve of Figure 20 has been prepared by adding to the tire deflection curve the computed structural deflection of the fork. Considering the case of a 12 fps landing, the normal smooth field vertical load has been determined to be 14,300 pounds. A sharp three-inch bump will require an additional three inches of deflection and, according to our simplified concept, will produce a load increment of 51,200 pounds for a total load of 65,500 pounds. The corresponding load from the more detailed calculations for a three-inch bump 27.4" long is 53,000 pounds. The following table shows a comparison of the approximate with the more detailed loads for several other initial sinking speeds and bump heights.

$V_v$ fps	Height In.	Length In.	$P_v$ Approximate (A)	$P_v$ Exact (B)	Ratio (B)/(A)
12	1.5	13.7	21,300	19,959	.94
17	1.5	13.7	66,000	61,002	.92
8	3	27.4	23,400	22,000	.94
12	3	27.4	65,500	53,000	.81
17	3	27.4	137,000	111,000	.81
8	5	45.7	105,000	67,900	.65
12	3	137	65,500	23,600	.36
17	3	137	137,000	62,600	.46

As might be expected, the agreement is fair with short bumps but poor with longer bumps. The approximate method gives a ballpark figure which would be useful for preliminary design for the limiting case of short bumps.

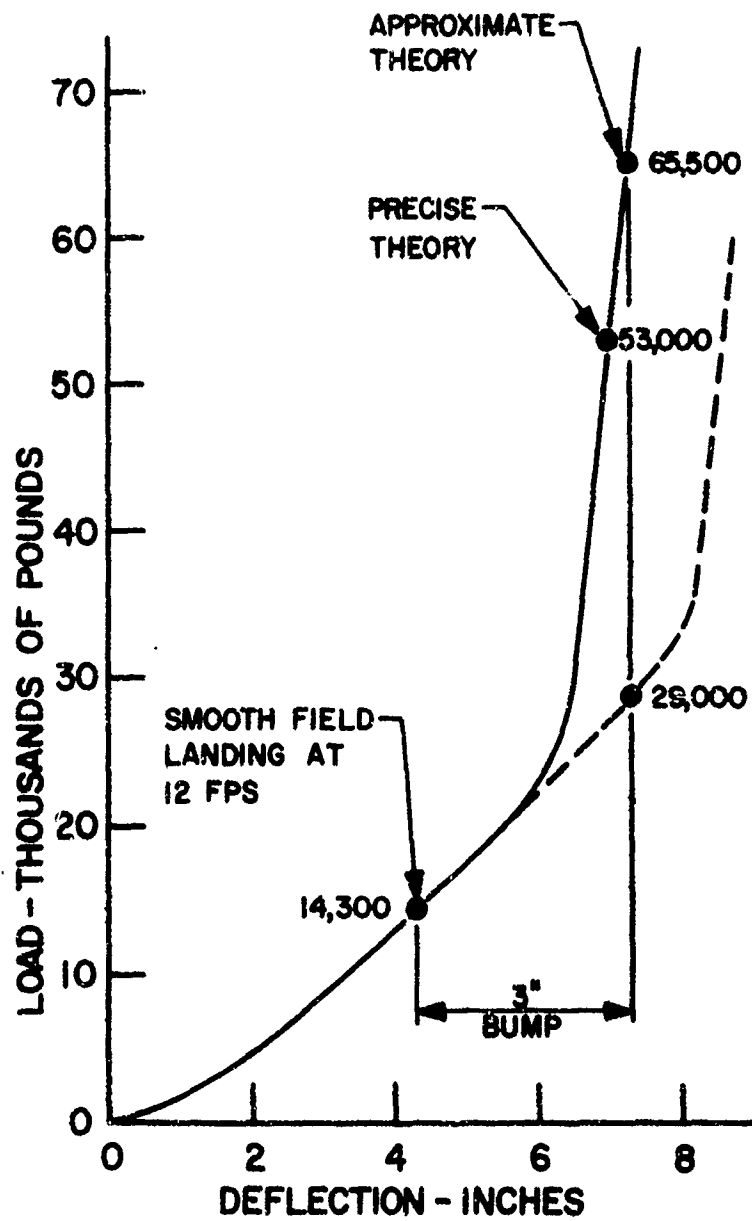


FIGURE 20. TIRE PLUS LOCAL STRUCTURE DEFLECTION CURVE

It becomes evident from the foregoing exercise that tolerance for rough terrain may be increased by shifting the knee of the load deflection curve by some manner to the right. If, in the 12 fps landing example above, the knee were extended as shown by the dotted line in Figure 20, the load resulting from a three-inch bump would be 29,000 pounds as compared with the original 53,000 pounds. An obvious conclusion is that an increase in tire size, specifically, an increase in the difference between tire radius and rim radius (which will be called tire depth), will aid greatly in alleviating the detrimental effects of rough terrain.

It has been recognized for some time that a large tire with low footprint pressure has been needed to prevent sinking into soft soil. Are the requirements for soft soil and the requirements for bumps compatible? If the width of the tire is increased simultaneously with the depth, improvement will be obtained for both types of terrain. However, a low tire pressure is desirable for soft soil, and a high tire pressure for bumps. In this regard, there is a conflict of requirements and a compromise must be achieved.

In many actual designs, a large tire cannot be used because of limited stowage space, and in any case, as the degree of terrain roughness is increased, the tire size eventually becomes impractical. To further alleviate the effects of bumps, two suggestions for modification of the shock strut have been advanced. The first involves the use of a relief valve in the oil pressure chamber and the second involves the use of a floating metering pin. These configurations are shown schematically in Figure 21.

The relief valve in the orifice plate is a device which has been explored by Bendix (Reference 6) and NASA (Reference 7) for the purpose of alleviating the previously mentioned cable impact loads for carrier-based aircraft. Although simple in concept, it is rather difficult to accomplish because of the need for extremely high frequency response characteristics. In principle, such a relief valve would not permit the oil pressure to build up beyond a certain value, but to accomplish this purpose successfully, it must open fully in a fraction of the load pulse time.

The floating metering pin appears to have certain practical advantages. In essence, the air chamber below the pin provides the same type of protection in the same way as the deep tire. The reaction to a sharp bump can, in fact, be computed by the approximate manner described in the previous section, by constructing a load deflection curve for the tire plus the air spring. A more precise calculation would, of course, be necessary to determine the dynamic characteristics of the complete system. Additional length to the shock strut must be added in either case.



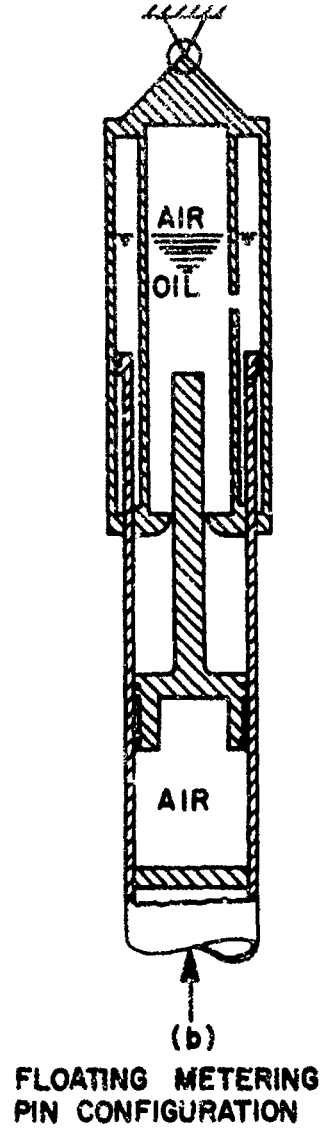
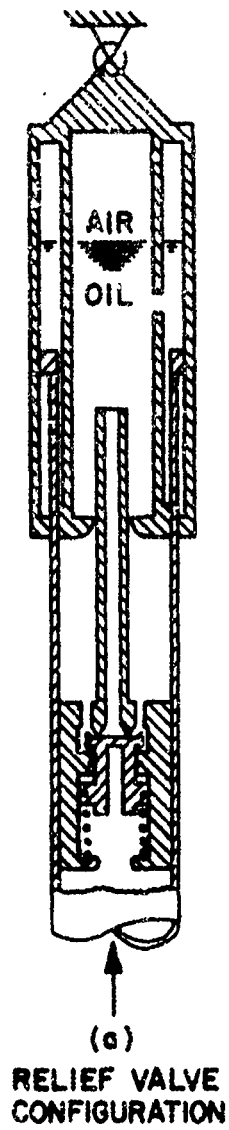


FIGURE 21. SCHEMATIC DIAGRAMS — ROUGH TERRAIN GEAR

## CONCLUDING REMARKS

The investigation reported herein attempted to determine the effect of rough terrain on the loads, weights, and performance of an Army observation airplane by analytical methods in which numerous simulated landings were made on surfaces of varying slope, softness, and roughness. The results must be used with discretion, as with any investigation in which an infinite number of possibilities are explored by a finite number of conditions.

In regard to the computing program used, it can be said that this method or one similar to it can be very useful in the investigation of landing load phenomena. To obtain accurate results, however, accurate input data must be available including a knowledge of the tire deflections curve, fundamental gear characteristics, and structural deflection data. A checkout against drop test results is also desirable.

As a further check on this program, a series of tests will be run in the near future on the NASA moving drop rig at Langley Field, Virginia, in which the loads on the main gear will be measured while it is traversing landing areas of varying degrees of roughness. At that time, data will also be obtained on the side loads induced when the gear traverses a bump obliquely.

Subject to the assumptions and limitations stated herein, the following conclusions regarding the effects of rough terrain can be made:

1. Slopes, or long bumps, in the direction of airplane motion created an effective increase in sinking speed equal to the forward velocity times the sine of the angle of slope. A rough terrain gear should, therefore, incorporate provisions for sinking speeds in excess of the estimated maximum airplane sinking speed.
2. Soft soil produces high rolling coefficients of friction which will produce maximum drag loads on the gear. Work needs to be done to relate the rolling coefficient of friction to measureable characteristics of the soil.
3. During landing impact on rough terrain, protuberances produce load pulses which the standard hydropneumatic shock strut cannot alleviate because of their high frequency. The magnitude of the load developed depends to a large extent upon the tire deflection available at the time the gear traverses the bump.
4. Short bumps produce the highest ground loads. Longer bumps, whose load pulse has a period near that of the structural natural frequency, produce highest internal structural loads.

5. Under the assumptions used in this analysis, multiple, uniformly spaced protuberances did not create loads in excess of those obtained from single bumps located at the most critical distance from point of touchdown.
6. Structural flexibility had little effect on the magnitude of the maximum gear loads. Structural flexibility had a pronounced effect on maximum internal structural loads causing an amplification of up to 1.5 times rigid body loads.
7. The detrimental effect of rough terrain can be alleviated by the proper choice of tire and by the incorporation of special features in the shock strut design. Two special features which warrant consideration are the oil pressure chamber relief valve and the floating metering pin.

## REFERENCES

1. Zentgraf, John K., "Ground Vibration Survey of the YAO-1 Airplane with External Stores," Grumman Aircraft Engineering Corporation Report DA184-521.3, October 14, 1960.
2. Allen, F.C. and Mosby, L.B., "An Investigation of the Landing Loads Experienced by the A4L-2 Airplane During Flight Tests and Drop Tests and a Comparison with Theory," Douglas Aircraft Company, Inc. Report No. LR-21038, October, 1962.
3. Walls, James H., "Investigation of the Air Compression Process During Drop Tests of an Oleo-Pneumatic Landing Gear," NACA TN 2477, 1951.
4. Morrison, A., "Results of Main Gear Dynamic Tests, Model YAO-1," Grumman Aircraft Engineering Corporation Report No. 3934.13, December 16, 1960.
5. Morrison, A., "Results of Main Gear Dynamic Tests, Model YAO-1," Grumman Aircraft Engineering Corporation Report No. 3934.23, December 9, 1960.
6. Black, R.J. and Palmer, E.M., "Band Pass Development Program, Phase I Report. Analytical Study of Low Band Pass Shock Strut," Bendix Report SH-61-1, August, 1961.
7. Schnitzer, Emanuel, "Experimental Evaluation of Low-Band-Pass Landing-Gear Shock Absorber for Pulse Loadings," NACA TN 4387, September, 1958.

# APPENDIX A - EQUATIONS OF MOTION

## NOTATION

## NOTATION (Cont'd)

Theory	Portran	Definition	Units	Theory	Portran	Definition	Units
$\delta, \dot{\delta}, \ddot{\delta}$	A	Motion at axle parallel with strut of unsprung mass of rolling assembly, positive down.	in., sec.	$F_H$	$F_H$	Load on airplane from gear, $\perp$ to reference plane, positive down	lb.
$\bar{z}$		Distance from lower piston bearing to axle parallel to strut with strut fully extended.	in.	$F_1$	$F_1$	Normal force on upper piston bearing, positive aft	lb.
$A_0$		Gross orifice area w/o reduction for pin.	in. <sup>2</sup>	$F_2$	$F_2$	Normal force on lower piston bearing, positive aft	lb.
$A_1$		Internal area of oleo piston	in. <sup>2</sup>	$g$		Gravitational constant	in./sec <sup>2</sup>
$A_2$		Piston area based on i, d. of lower bearing	in. <sup>2</sup>	$ G_1 $		Coefficient of moment from gear	
$A_p$	AP	Metering pin area, function of strut stroke	in. <sup>2</sup>	$ M_1 $		Coefficient of force from gear	
$a_1$		Slopes of line equation for pin diameter	-	$I_R$		Mass moment of inertia of rolling assembly	lb.in.sec <sup>2</sup>
$[A_{1j}]$		Aerodynamic damping coefficients	1/sec.	$K_1$		Strut influence coefficient, deflection fwd. due to force acting down parallel to strut	in/lb
$\alpha, \dot{\alpha}, \ddot{\alpha}$	Alpha	angular motion of rolling assembly	RAD., Sec.	$K_{32}, K_{33}$		$K_{32} + \delta K_{33}$ is deflection aft due to force acting aft perpendicular to strut	in/lb, l/lb.
$b_1$		Intercepts of line equations for pin diameter	in.	$k_1, k_2$		Coefficients of gear force for horizontal accelerations	-
$\bar{b}$		Distance from upper to lower piston bearing parallel to strut, strut fully extended	in.	$\lambda$		Instantaneous skidding velocity	ft/sec.
$[B_{1j}]$		Coefficients of displacements in airplane equation of motion	1/sec. <sup>2</sup>	$\lambda/V_L$	EA	Slip ratio	-
$\delta$	$\delta$	Tire deflection	in.	$\ell_1$		Intercepts in lines for tire load	lb.
$\ddot{\delta}$		Damping coefficient perpendicular to strut	lb-sec/in.	$m_1$		Slopes in lines for tire load vs. deflection	lb/in.
$C_D$		Coefficient of discharge	-	$n$		Polytropic exponent for strut air load	-
$C_C$		Discharge coefficient for compression	-	$o$		Subscript to denote initial conditions	-
$C_E$		Discharge coefficient for extension	-	$F_A$	$F_A$	Strut air load	lb.
$C_M$		Maximum allowable tire deflection	in.	$F_D$	$F_D$	Drag load in horizontal plane	lb.
$ G_1 $		Coefficient of force from gear	1/lb.sec <sup>2</sup>	$F_E$	$F_E$	Airload in oleo with strut extended	lb.
$\delta, \dot{\delta}, \ddot{\delta}$	D	Motion at axle perpendicular to strut of unsprung mass of rolling assembly, positive aft	in., sec.	$F_F$	$F_F$	Bearing friction force on strut	lb.
$\delta, \dot{\delta}, \ddot{\delta}$	ED	Motion at axle in relative coordinates	in., sec.	$F_O$	$F_O$	Strut oil load	lb.
$\bar{s}$		Distance from axle to gear attach point with strut fully extended	in.	$F_P$	$F_P$	Force at axle (relative coordinates) perpendicular to strut positive fwd.	lb.
$D_0$	EO	Coefficient of oil damping force in oleo	lb/sec <sup>2</sup> /ft <sup>2</sup>	$F_T$	$F_T$	Tire load	lb.
$ E_1 $		Coefficient of moment from gear	1/ft.lb.sec <sup>2</sup>	$F_V$	$F_V$	Vertical ground reaction load	lb.
$\bar{q}$		Distance from axle to strut $\bar{q}$ normal to strut, positive for axle forward	in.	$[F]$		Coefficients of generalized displacement	ft or in.
$[E_1]$		Vector column of constants	1/sec <sup>2</sup>	$q, \dot{q}, \ddot{q}$	A	Airplane motion, generalized coordinates	-, 1/sec, 1/sec <sup>2</sup>
$\theta$		Angle of strut with vertical, positive for strut forward of gear attach point		$\rho_0$		Mass density of hydraulic fluid	lb.sec <sup>2</sup> /in. <sup>3</sup>
$F_A$	EA	Load on axle parallel to strut, positive down	lb.	$r_0$		Radius of undeflected tire	in.
$F_A$	EP	Load on axle $\perp$ to strut, positive aft	lb.	$R$	R	Instantaneous rolling radius of tire	in.
				$[R]$		Coefficients of generalized acceleration	-
				$\delta, \dot{\delta}, \ddot{\delta}$	S	Strut motion measured from full extension	in., sec.
				$R_0$		Maximum strut stroke	in.
				$R_1$		Values of $\delta$ associated with pin constants	in.

## NOTATION (Cont'd)

Theory	Program	Definition	Units
[S]		Coefficients of Q in equation for airplane loads	-
$\Delta t$		Time	sec.
$\Delta t$		Interval of numerical integration	sec.
$\Delta t$		Step of integration	sec.
$ T_{M1} $		Generalized airplane coefficients of force at gear attaching point	in/lb. sec. <sup>2</sup>
$ T_{M1} $		Generalized coefficients of moments at gear attaching point	1 lb./sec. <sup>2</sup>
$M$		Coefficients of friction identified (numerically) by its subscript	-
$M_1$		Bearing coefficients friction before strut moves - static friction	-
$M_2$		Bearing coefficients after strut moves	-
$M_0$	GRND	Ground coefficient sliding friction	-
$M_R$	GRND	Ground coefficient rolling friction	-
[u]		Arbitrary constants in equation for loads on airplane	-
$V_E$		Air volume in shoe strut extended	in. <sup>3</sup>
$V_L$		Forward velocity of airplane	in./sec.
[V]		Coefficients of generalized velocities	in. or ft.
$W_G$		Weight of gear	lb.
$W_H$		Airplane net weight supported by gear	lb.
X	X	Horizontal coordinate of ground contact point for rough terrain function	in.
$X_1$		Arguments in table of terrain roughness, $0 = 1 = 700$	in.
$X_A$	XA	Axle coordinate, horizontal displacement along terrain roughness	in.
$X_1, X_2, X_3, X_4$		Coordinates used to define terrain	in.
$X_0$		Initial (starting value) of X	in.
$Y_B, \dot{Y}_B, \ddot{Y}_B$	YB	Motion at top of strut	in., sec.
Y	Y	Vertical coordinate of ground contact point for rough terrain function	in.
$Y_A$	YA	Axle displacement from touchdown, positive down	in.
$Y_0$		Initial (starting value) of Y	in.
$\theta$		Ground slope	Rad.
$Y_{M1} \theta$	YMX	Printed for instantaneous value of ground slope	-
$A, B, C, D$		Amplitudes of terrain roughness entered in X-table, positive down	in.
$Z_G$	AG	Eupent from gear, positive airplane nose up	ft. lb.

## NOTATION (Cont'd)

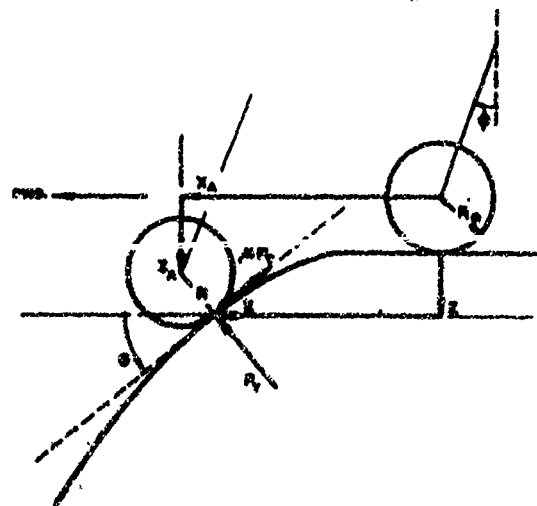
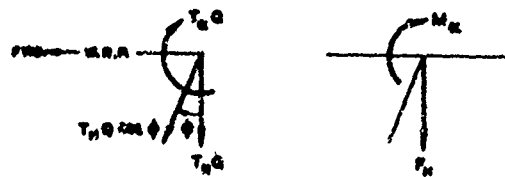
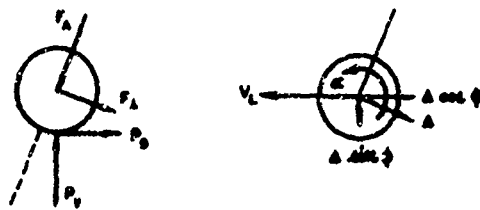
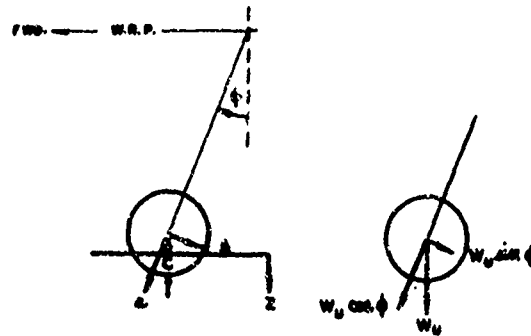
Theory	Program	Definition	Units
$\gamma$		Multiple of $\Delta t$ at which printing of program output takes place	-
VA		Vertical accelerations	-
PA		Pitching acceleration	-
SM		Shear	-
BM		Bending moment	-
TQ		Torque	-
AA		Airplane angle of attack	-
AV		Airplane pitching velocity	-
APA		Airplane pitching acceleration	-
VP		Airplane vertical position	-
VV		Airplane vertical velocity	-
AVA		Airplane vertical acceleration	-
HA		Airplane horizontal acceleration	-

## SIGN CONVENTION

VA	Vertical accelerations - Positive upward (resulting in demand inertia forces)
PA	Pitching accelerations - Positive leading edge up
SM	Shear - Positive shear produces positive bending moment
BM	Bending moment - Positive moment produces compression in upper elements of wing and fuselage
TQ	Torque - Positive torque produces nose up twist of wing
AA	Airplane angle - Positive nose up
AV	Airplane pitching velocity - Positive nose up
APA	Airplane pitching acceleration - Positive nose up
VP	Vertical position of airplane C.G. - Positive up
VV	Vertical velocity of airplane C.G. - Positive up
AVA	Vertical acceleration of airplane C.G. - Positive up
HA	Horizontal acceleration of C.G. - Positive forward

Cont. on following page

# DIRECTION OF POSITIVE DISPLACEMENTS AND FORCES



# EQUATIONS OF MOTION

## GRAB EQUATIONS

$$\ddot{A} = \left[ -P_y \sin \phi + P_D \cos \phi - P_A + W_U \sin \phi \right] \div \frac{W_U}{g}$$

$$\ddot{B} = \left[ -P_y \cos \phi - P_D \sin \phi + P_A + W_U \cos \phi \right] \div \frac{W_U}{g}$$

$$= [T_{H1}] \left| \ddot{Q}_1 \right| \cos \phi \text{ Before the strut moves}$$

$$\ddot{B} = \mu P_y \left( R_0 - \frac{g}{g} \right) \div I_R$$

$$P_A = \left[ \ddot{A} - \mu_1 P_A \right] \div \left[ K_{y2} + \delta K_{y3} \right]$$

$$P_A = -P_A + U \dot{A}$$

$$P_A = P_A + P_D + P_y$$

$$= \frac{W_U}{g} \ddot{A} + P_y \cos \phi + \mu P_y \sin \phi - W_U \cos \phi$$

Before the strut moves.

$$P_1 = \frac{P_A (R-S) - P_A (S-S)}{S + S}$$

$$P_R = P_1 + P_A$$

$$P_y = \left| \mu_1 P_1 \right| + \left| \mu_1 P_2 \right| \quad \delta > 0, P_y \text{ positive}$$

$$\delta < 0, P_y \text{ negative}$$

$$\mu_1 = \mu_1 \text{ Before strut moves}$$

$$= \mu_2 \text{ After strut moves}$$

$$V_D = [T_{H1}] \left| \dot{Q}_1 \right|$$

$$\ddot{B} = \ddot{A} - V_D \sin \phi + (\delta - S) [T_{H1}] \left| \ddot{Q}_1 \right|$$

$$\ddot{B} = [T_{H1}] \left| \ddot{Q}_1 \right| \cos \phi - \ddot{A}$$

$$P_A = (P_R + 14.7A_2) \left[ \frac{V_R}{V_S - 3A_2} \right]^n - 14.7A_2$$

44

$$P_D = D_0 \dot{A} \left| \dot{A} \right| \quad D_0 = \frac{P_0 (A_1 - A_p)^3}{2 [D_0 (A_0 - A_p)]^2}$$

$$A_p = \frac{1}{2} (a_1 R + b_1)^2$$

$$C = R_0 - R$$

$$P_T = R_1 + W_1 C$$

$$\lambda_{VL} = 1 - \frac{(R_0 - \frac{g}{g}) \dot{A} + \dot{A} \cos \phi}{V_L}$$

$$\mu = \mu_B \text{ Before spinup}$$

$$= \mu_R \text{ After spinup}$$

$$P_y = P_T \cos \phi + \mu P_T \sin \phi$$

$$P_D = -P_T \sin \phi + \mu P_T \cos \phi$$

$$\text{Criteria for strut motion } P_A > P_R + P_y$$

$$H_A = X_0 + V_L t - A \cos \phi + a \sin \phi$$

$$Z_A = Z_0 + \Delta \sin \phi + a \cos \phi$$

$$X = X_A - R \sin \phi$$

$$Z = -A \left[ 1 - \cos 2\pi \frac{X - X_1}{X_2 - X_1} \right] + 0$$

$$\tan \phi = \frac{2aA}{X_2 - X_1} \sin 2\pi \frac{X - X_1}{X_2 - X_1} + 0$$

$$R = \left[ (X - X_A)^2 + (Z - Z_A)^2 \right]^{1/2}$$

$$\sin \phi = \frac{2\pi A}{(1 + 7A^2)^{1/2}}$$

$$\cos \phi = \frac{1}{(1 + 7A^2)^{1/2}}$$

## AIRPLANE EQUATIONS

$$\left| \ddot{Q}_1 \right| = [A_{1j}] \left| \ddot{Q}_1 \right| + [D_{1j}] \left| \dot{Q}_1 \right| + P_{H1} \left| \dot{Q}_1 \right| + P_{H2} \left| \dot{Q}_1 \right|_2$$

$$+ M_{O1} \left| \dot{Q}_1 \right| + M_{O2} \left| \dot{Q}_1 \right|_2 + \left| E_1 \right|$$

$$P_H = -P_A \cos \phi - P_1 \sin \phi$$

$$M_O = (S - S) P_A$$

$$[A_{1j}] = -[T^*WT + T^*A_1T]^{-1} [T^*A_2T] \quad (\text{SEE NOTE BELOW})$$

$$[D_{1j}] = -[T^*WT + T^*A_1T]^{-1} [T^*WT + T^*OT + T^*A_3T]$$

$$[C_1] = [T^*WT + T^*A_1T]^{-1} [T^*H_1]$$

$$[D_1] = [T^*WT + T^*A_1T]^{-1} [T^*O_1]$$

$$[E_1] = -[T^*WT + T^*A_1T]^{-1} \left\{ W_{U1} [T^*H_1] + W_{U2} [T^*H_1] \right.$$

$$- S_1 W_{U1} \sin \phi_1 [T^*O_1] - S_2 W_{U2} \sin \phi_2 [T^*O_2]$$

$$\left. - [T^*A_2T] \left| \ddot{Q}_1 \right|_{t=0} \right\} \text{ when } \left| \ddot{Q}_1 \right|_{t=0} = 0$$

## INTERPOLATION EQUATIONS

$$\text{Prediction } X_{N+1} = X_N + \Delta t \dot{X}_N + .5 \Delta t^2 \ddot{X}_N$$

$$\ddot{X}_{N+1} = \ddot{X}_N + 1.5 \Delta t \ddot{X}_N - .5 \Delta t \ddot{X}_{N-1}$$

$$\text{Correction } X_{N+1} = X_N + \Delta t \dot{X}_N + .5 \Delta t^2 \ddot{X}_{N+1}$$

$$\ddot{X}_{N+1} = \ddot{X}_N + .5 \Delta t \ddot{X}_{N+1} + .5 \Delta t \ddot{X}_N$$

$$\text{where } X = a, \Delta, a, Q$$

## EQUATIONS FOR LOADS

$$\text{Accelerations} = [R_{1j}] \left| \ddot{Q}_1 \right|$$

$$\text{Shear, Bending Moment,}$$

$$\text{Torque} = [S_{1j}] \left| \dot{Q}_1 \right| + P_{H1} \left| \dot{Q}_1 \right| + P_{H2} \left| \dot{Q}_1 \right|_2$$

$$+ M_{O1} \left| \dot{Q}_1 \right| + M_{O2} \left| \dot{Q}_1 \right|_2 + \left| u_1 \right|$$

$$\text{Displacement} = [P_{1j}] \left| Q_1 \right|$$

$$\text{Velocities} = [V_{1j}] \left| \dot{Q}_1 \right|$$

$$\text{Horizontal Acceleration} = (K_1 P_{D1} + K_2 P_{D2}) \div M_H$$

NOTE: FOR DEFINITION OF  $A_1$ ,  $A_2$ , AND  $A_3$  SEE FOLLOWING PAGE UNDER "AERODYNAMIC LIFT AND MOMENT".



# AERODYNAMIC LOADS FOR LANDING

The following formulas for lift, "L", and moment, "M", take into account the change in aerodynamic forces during landing and taxi. It is assumed that the air stream velocity is constant, and that the contribution to lift of circulation lag is negligible.

$$L = -\rho b^2 \Delta X \left[ v \dot{a} + \dot{a} h - v \dot{a} \dot{a} \right] - 2 \rho v \Delta X v^2 \dot{a} \\ - 2 \rho v \Delta X v \dot{a} h - 2 \rho v \Delta X v \dot{a}^2 (1.5 - a) \dot{a} \\ - \gamma \rho \left[ b^2 \Delta X \dot{a} h - b^2 \Delta X \dot{a} \dot{a} \right] - \gamma \rho v \left[ b^2 \Delta X \dot{a} \dot{a} \right] \\ - \gamma \rho v^2 \left[ b \Delta X \dot{a} h + b^2 (1.5 - a) \Delta X \dot{a} \right] - \gamma \rho v^2 \left[ b \Delta X \dot{a} \right] \\ M = -\rho b^2 \Delta X \left[ v (1.5 - a) v \dot{a} + v \dot{a}^2 (1/8 + a^2) \dot{a} - a \dot{a} h \right] \\ + 2 \rho v \Delta X v^2 (a + .5) \left[ v \dot{a} + h + b (1.5 - a) \dot{a} \right] \\ - \gamma \rho \left[ -a b^2 \Delta X \dot{a} h + b^2 (1.25 + a^2) \Delta X \dot{a} \right] \\ - \gamma \rho v \left[ b^2 (1.5 - a) \Delta X \dot{a} \right] \\ - \gamma \rho v^2 \left[ -h^2 (a + .5) \Delta X \dot{a} + b^2 (a^2 - .25) \Delta X \dot{a} \right] \\ - \gamma \rho v^2 \left[ -b^2 (a + .5) \Delta X \dot{a} \right]$$

The aerodynamic coefficients occurring in the equations of motion are  $A_1, A_2, A_3$ . In the form given below, these coefficients are equivalent to those shown above.

Coefficient of  $\dot{h}, \ddot{h}$

$$- \left[ A_1 \right] = - \gamma \left[ V_1 \right]$$

Coefficient of  $\dot{a}, \ddot{a}$

$$- \left[ A_2 \right] = - \gamma \rho v \left[ V_2 \right] - \gamma \rho v^2 \left[ U_1 \right]$$

Coefficient of  $a$

$$- \left[ A_3 \right] = - \gamma \rho v^2 \left[ U_2 \right]$$

Where

$$\left[ U_1 \right] = \left[ \frac{\Delta X b}{\Delta X b^2} (1.5 + a) \frac{\Delta X b^2}{\Delta X b^2} (1.25 + a^2) \right] \\ \left[ U_2 \right] = \left[ 0 \quad \frac{\Delta X b}{\Delta X b^2} (1.5 + a) \right] \\ \left[ V_1 \right] = \left[ 0 \quad \frac{\Delta X b}{\Delta X b^2} (1.5 - a) \right] \\ \left[ V_2 \right] = \left[ \frac{\Delta X b}{\Delta X b^2} \quad - \frac{\Delta X b^2}{\Delta X b^2} (1.25 + a^2) \right]$$

$d_1$  is the slope of the lift curve over  $v$ . In Theodoreson's expressions  $d_1 = 2\pi/v = 2$ , which is infinite aspect ratio. For the general case in which  $d_1$  is experimentally determined,  $d_1 = dC_L/d\alpha$ . The generalized coefficients are  $\left[ \frac{\Delta X b}{\Delta X b^2} \right], \left[ \frac{\Delta X b^2}{\Delta X b^2} \right], \left[ \frac{\Delta X b^2}{\Delta X b^2} \right]$ .

## LOADS ON THE AIRPLANE STRUCTURE

The airplane may be fully represented in the generalized coordinate system. A maximum of eighteen generalized coordinates,  $q$ , may be used. In the sectional coordinate system,  $X$ , the airplane is divided into as many mass-bays as desired. Each bay may have six degrees of freedom: translation along  $x$ , rotation about three axes. The transformation from generalized to sectional coordinates is given by  $x = [T] q$  where  $[T]$  is a modal transform matrix. In the landing impact analysis the

through the use of the modal transform matrix, the sectional displacements, velocities, and accelerations at all points on the airplane structure are available for computing loads.

## DATA OUTPUT

The following were printed for each of two gears at time intervals of .002 sec. or less:

$F_A$	Strut air load	lb.
$F_O$	Strut oil load	lb.
$F_F$	Strut friction force	lb.
$F_A$	Axle load    strut	lb.
$F_{A \perp}$	Axle load $\perp$ strut	lb.
$F_{A \perp}$	Axle load $\perp$ strut in relative coordinates	lb.
$F_1$	Aft normal force on upper bearing	lb.
$F_2$	Forward normal force on lower bearing	lb.
$F_T$	Tire load	lb.
$F_V$	Vertical ground load	lb.
$F_D$	Horizontal drag load	lb.
$F_H$	Gear force on airplane	lb.
$M_H = AM$	Gear pitching moment on airplane	ft.-lb.
$A_p$	Area of metering pin	in. <sup>2</sup>
$B_p$	Oil force damping coefficient	lb sec <sup>2</sup> /in. <sup>2</sup>
$\lambda/V_L = \mu$	Slip ratio	-
$X_A, Z_A$	Coordinates of axle	in.
$X, Z$	Coordinates of ground contact point	in.
$TAN \theta$	Slope of terrain at ground contact point	-
$\delta$	Tire deflection	in.
$R$	Rolling radius of ground contact point	in.

## DATA OUTPUT (cont'd)

$\mu_{R,S}$	GRW, ground coefficients of friction	-
$a, \dot{a}, \ddot{a}$	Strut motion in strut direction	in., sec.
$a, \dot{a}, \ddot{a}$	Axle motion in strut direction	in., sec.
$a, \dot{a}, \ddot{a}$	Axle motion $\perp$ strut	in., sec.
$a, \dot{a}, \ddot{a}$	Axle motion $\perp$ strut in relative coordinates	in., sec.
$v_{A, \dot{A}, \ddot{A}}$	Motion at top of strut	in., sec.
$\alpha, \dot{\alpha}, \ddot{\alpha}$	Angular motion of rolling assembly	rad., sec.
$V_A$	Vertical acceleration at 10 stations	in/sec <sup>2</sup>
$F_A$	Pitching acceleration at 6 stations	rad/sec <sup>2</sup>
$M_H$	Stress at 7 stations	lb.
$M_H$	Bending moment at 7 stations	in.-lb.
$T_Q$	Torque at 3 stations	in.-lb.
$\theta$	Airplane pitch angle	rad.
$\dot{\theta}$	Airplane pitching velocity	rad/sec
$\ddot{\theta}$	Airplane pitching acceleration	rad/sec <sup>2</sup>
$V_V$	Vertical position of airplane G.C.	in.
$\dot{V}_V$	Vertical velocity of airplane G.C.	in./sec.
$\ddot{V}_V$	Vertical acceleration of G.C.	in./sec. <sup>2</sup>
$\ddot{H}$	Horizontal acceleration of G.C.	g's

\* THE NOTATION IN THIS SECTION IS THAT OF THEODORSEN (REF. NACA TN 406).

\* These quantities are not computed before the strut moves. They are printed as zero.